Volume 2 · Issue 3
September 2023
ISSN: 2810-9635 (Online)

Materials Science in Additive Manufacturing

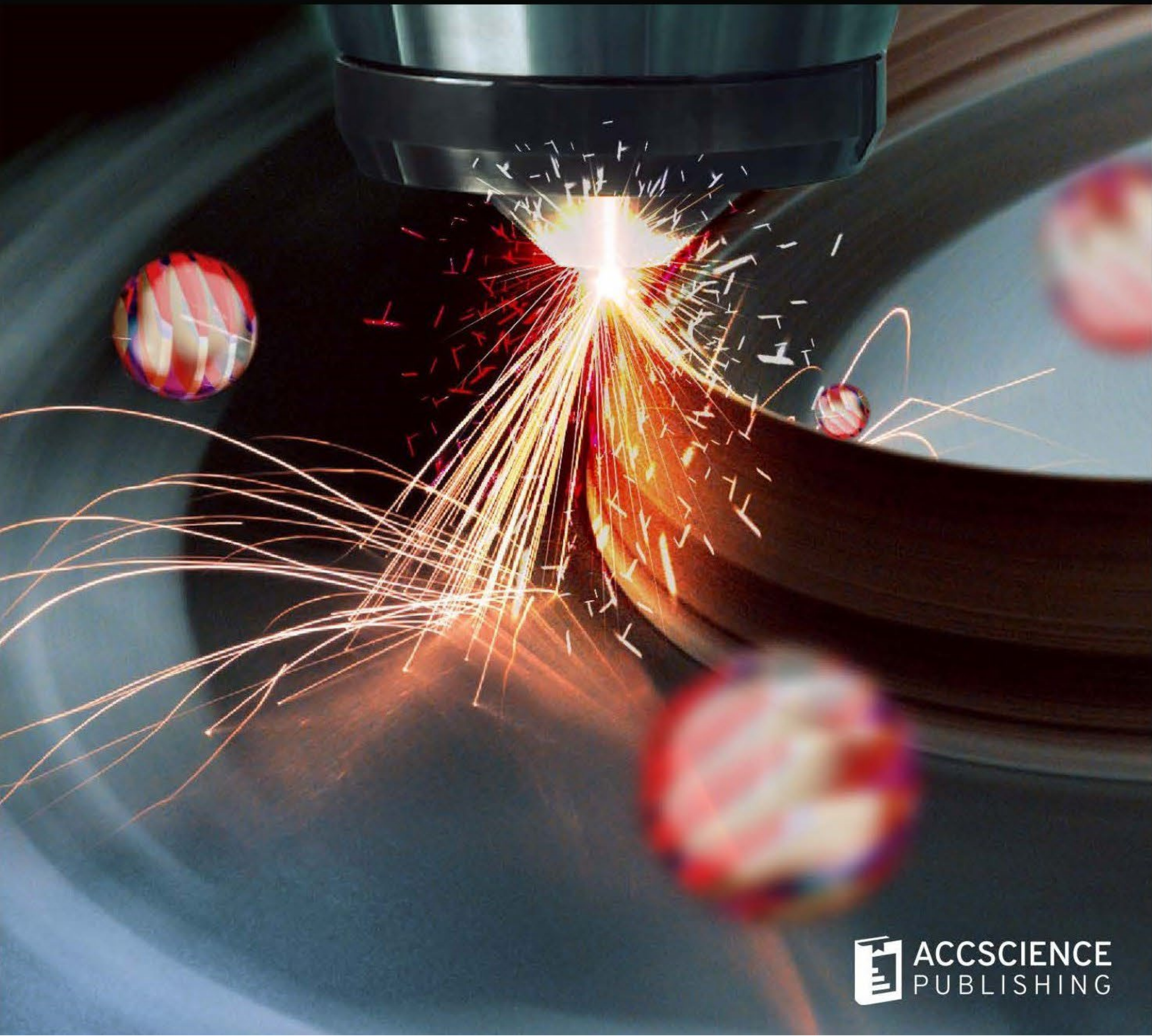

ACCSCIENCE PUBLISHING

ACCSCIENCE
PUBLISHING

Materials Science in Additive Manufacturing

Online ISSN: 2810-9635

Materials Science in Additive Manufacturing aims to bridge the cutting-edge research between additive manufacturing and the entire spectrum of materials science. The journal covers all applied and fundamentals of processing, synthesis, structure, composition, properties and performance of materials designed or manipulated for additive manufacturing. The journal covers a wide scope of innovative techniques, processes, methods, and applications.

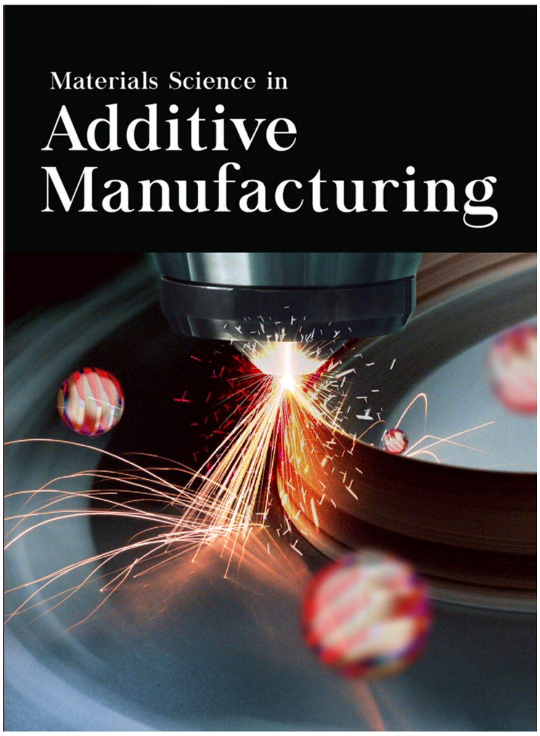

About the Publisher

AccScience Publishing is a publishing company based in Singapore. We publish a range of high-quality, open-access, peer-reviewed journals and books from a broad spectrum of disciplines.

Contact Us

Managing Editor
msam.office@accscience.sg

AccScience Publishing
8 Burn Road, #15-03 Trivex, Singapore 369977.

Volume 2 • Issue 3 • September 2023
ISSN 2810-9635 (online)

MATERIALS SCIENCE IN ADDITIVE MANUFACTURING

Editor-in-Chief

Chee Kai Chua

Singapore University of Technology and Design, Singapore

ACCSCIENCE PUBLISHING

ACCSCIENCE
PUBLISHING

Full issue copyright © 2023 AccScience Publishing
All rights reserved. Without permission in writing from the publisher, this full issue publication in its entirety may not be reproduced or transmitted for commercial purposes in any form or by any means, electronic or mechanical, including photocopying, recording, or any information storage and retrieval system. Permissions may be sought from msam.office@accscience.sg.

Article copyright © Respective Author(s)
See articles for copyright year. All articles in this full issue publication are open-access. There are no restrictions in the distribution and reproduction of individual articles, provided the original work is properly cited. However, permission to reuse copyrighted materials of an article for commercial purposes is applicable if the article is licensed under Creative Commons Attribution-NonCommercial License. Check the specific license before reusing.

MATERIALS SCIENCE IN ADDITIVE MANUFACTURING

ISSN: 2810-9635 (online)

Editorial and Production Credits

Publisher: AccScience Publishing
Editorial Assistant: Flora Kang
Production Editors: Ian Wong, Chi Tat Poon
Article Layout and Typeset: Sinjore Technologies (India)
Cover Design: BUTTON GRAPHIC DESIGN STUDIO (Malaysia)

For all advertising queries, contact msam.office@accscience.sg.

Supplementary file

Supplementary files of articles can be obtained at https://accscience.com/journal/MSAM/2/3.

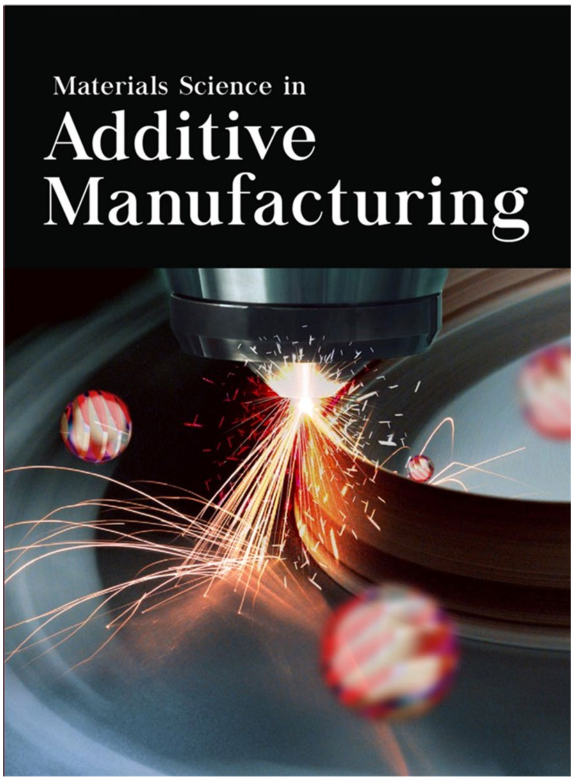

About the Cover

Directed energy deposition in progress

Disclaimer

AccScience Publishing is not liable to the statements, perspectives, and opinions contained in the publications. The appearance of advertisements in the journal shall not be construed as a warranty, endorsement, or approval of the products or services advertised and/or the safety thereof. AccScience Publishing disclaims responsibility for any injury to persons or property resulting from any ideas or products referred to in the publications or advertisements. AccScience Publishing remains neutral with regard to jurisdictional claims in published maps and institutional affiliations.

Materials Science in Additive Manufacturing

Editorial Board

Volume 2 | Issue 3 | September 2023 |

Materials Science in Additive Manufacturing

https://accscience.com/journal/MSAM

CONTENTS

ACCSCIENCE PUBLISHING

Materials Science in Additive Manufacturing

REVIEW ARTICLE

A review of advances in additive manufacturing and the integration of high-performance polymers, alloys, and their composites

Yanting Liu, and Swee Leong Sing*

Department of Mechanical Engineering, National University of Singapore, Singapore

Abstract

In recent years, additive manufacturing (AM) has emerged as the most revolutionary technology in manufacturing, playing an indispensable role in many important areas due to its outstanding precision, ability to fabricate complex structures, and short production cycles. At the same time, the development of this technology has been accompanied by a constant search for materials suitable for it. These materials play important roles in the industry, have excellent properties but are difficult to process using traditional manufacturing methods, or are newly developed materials specifically for AM. While these explorations are being undertaken, attention to standards in the field will ensure that research is accelerated and on the right track. This paper presents each of the seven technique categories of AM. The focus of this paper is on the emerging materials for AM, such as polyetheretherketone, polyimide, high entropy alloys, and composites. Finally, international standards in the field of AM with perspectives on research in this area are also presented.

Keywords: Additive manufacturing; 3D printing; Polyetheretherketone; Polyimide; High entropy alloys; Standards

***Corresponding author:**
Swee Leong Sing
(sweeleong.sing@nus.edu.sg)

Citation: Liu Y, Sing SL, 2023, A review of advances in additive manufacturing and the integration of high-performance polymers, alloys, and their composites. *Mater Sci Add Manuf*, 2(3): 1587.
https://doi.org/10.36922/msam.1587

Received: August 12, 2023

Accepted: September 8, 2023

1. Introduction

With the progress and development of science and technology, people are increasingly investing in and paying attention to cutting-edge key areas such as aerospace, biomedical, and so on. The development is accompanied by the increasing complexity of the structure of the parts and the increasing requirements for strength, corrosion resistance, biocompatibility, etc., of the parts. Therefore, upgrading and improving manufacturing technology and actively expanding the adaptability with high-performance materials are the focus of prevailing research.

Additive manufacturing (AM) has caught the attention of researchers and the industry in recent years due to its rapid prototyping capabilities and design flexibility[1-3] compared to traditional manufacturing. These interests have led to the development of many types of AM methods, with significant results for a wide range of materials. As a key component of Industry 4.0, AM has been endowed with the ability to prepare products for the future with higher customization, shorter cycle times and costs, and more outstanding capabilities than traditional manufacturing processes.

According to the ISO/ASTM52900-21 standard[4], AM techniques are classified into seven categories, as shown in Figure 1, namely, binder jetting (BJT), directed energy deposition (DED), material extrusion (MEX), material jetting (MJT), powder bed fusion (PBF), sheet lamination (SHL), and vat photopolymerization (VPP). The technical characteristics, application scenarios and applicable material types vary among these techniques. Given that, these techniques have developed in different aspects in recent years, culminating in the current status. The current summary and overview of these seven technologies is relatively rare, which is unparalleled to the rapid development of the industry.

On the basis of continuous technological advances, the adaptability of high-performance raw materials is another key issue, and even, empowering and trying to further explore the potential of materials through AM technology will be the focus of attention of the application end of AM field in the future. This review focuses on two core classes of materials, namely polymers and metals, and highlights a representative high-performance material from each of them. The review also focus on those materials that have a fit with AM technology in terms of application areas and have already demonstrated significant research value in conventional processing to explore their latest developments in the AM field as well as further possibilities for the future. Engineering plastics such as polyimide and polyetheretherketone (PEEK), as well as alloys such as high entropy alloys (HEAs), are among the star materials that fit this profile. We believe that tracking the development of these high-performance materials in the AM field will help us further understand the growth trajectory of AM technology.

Therefore, the final section of the review includes the relevant, up-to-date standards in the AM field. This multidimensional summary is intended to provide another perspective on the development of the technology.

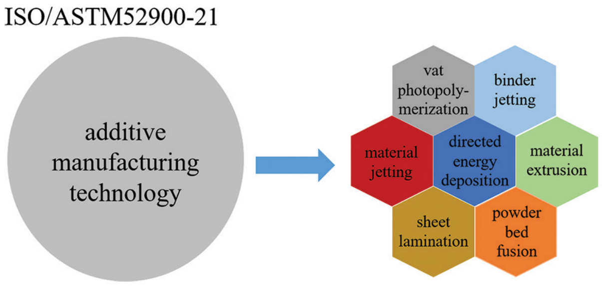

Figure 1. Seven different categories of AM techniques[4].

2. Additive manufacturing techniques

2.1. Binder jetting

Binder jetting additive manufacturing (BJT) is an inexpensive AM technique that uses liquid adhesives to bond and cures specific parts of a powdered material layer by layer into the green state, followed by different types of post-processing to obtain a finished product, depending on the nature of the material[5,6].

The BJT technology is an AM process conducted entirely at room temperature. As there is no deformation due to thermal effects, it can be used to build large parts and there is no need to design additional support structures when using BJT technology. In some cases, it is even possible to fabricate colored products. This technology is now used to print finished parts with complex internal structures and geometries in a variety of materials including metals[5,6], ceramics[7], and polymers[8].

The major disadvantage of BJT as compared to several other AM technology is that it is uncompetitive in many commercial cases due to shrinkage problems when machining metals and the difficulty of achieving fully dense parts directly[9]. Furthermore, the fabricated products are very fragile in their green state before post-processing, limiting the use of the AM process to a certain extent. Figure 2 clearly reflects several typical product defects when using BJT techniques[10].

Improvements and refinements to address this feature are ongoing. One of the main treatments is the use of additives to provide additional treatment to the green parts before sintering. This process modifies the internal structure of the green parts, increasing the number of particle alignments and the size of inter-particle contacts to make it denser and more stable[11]. This approach has been demonstrated with several different types of additives, including metal salts[12], metal-organic inks[13], and sol-gel[14].

Building on this foundation, related research to gain insight into the effects of reactive binders on the creep and densification mechanisms of binder-jet 3D printed parts has also been conducted recently. Grant *et al.* investigated the intrinsic mechanism of aqueous titanium bis-ammonium lactato dihydroxide (TALH) as a binder to alter the creep of the samples and achieved significant deformation improvement[11].

2.2. Directed energy deposition

DED technology melts metal powders or wires during the manufacturing process and deposits them layer by layer onto specified areas and cooled them to form the

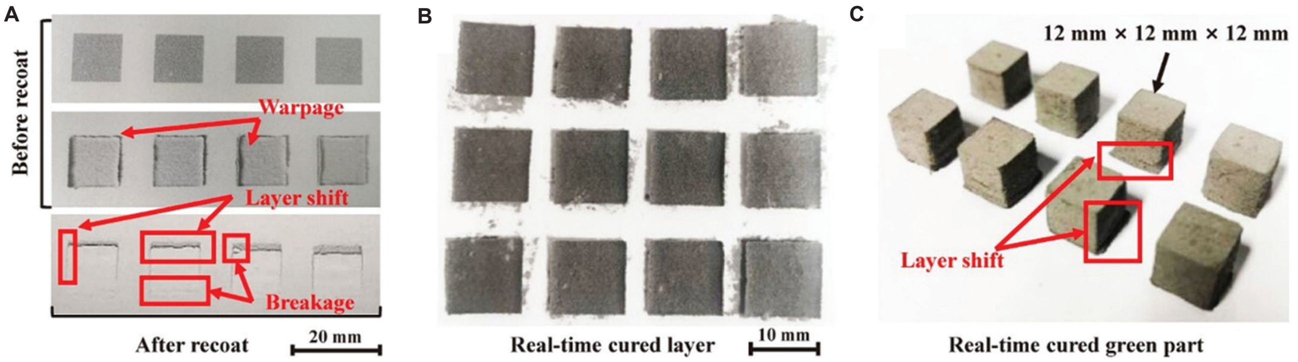

Figure 2. Typical vital defects in real-time curing binder jetting additive manufacturing. (A) Real-time cured layers during printing (inside powder bed). (B and C) Real-time cured layers and green parts after an ultraviolet irradiation (outside powder bed)[10].

structure. The molten material is released through the nozzle and the direction of deposition is changed in the process by adjusting the relative movement of the platform or nozzle[15,16]. Figure 3 presents the working principle of a general laser powder DED (LP-DED) system[17].

DED technology is well suited for the preparation of high-performance metallic materials and is also suitable for the processing of some ceramic materials[18]. Compared to other AM technology, DED technology offers a number of advantages, including faster build rates, the capability to produce large parts, the ability to fabricate under non-horizontal conditions, the ability to print in weightless environments under certain conditions, and the ability to deposit multiple materials simultaneously on some models[18,19]. This makes DED technology a promising technology for a wide range of applications.

The DED technology can also be used for the repair and addition of materials onto existing components. With DED technology, it is possible to achieve higher precision, lower residual stresses and a more flexible repair process than with conventional welding repair methods[20]. Research into DED technology is becoming increasingly advanced due to its outstanding advantages, with recent studies showing, for example, that the final performance of products can vary considerably under different scanning strategies[21]. Nonetheless, there are disadvantages of using DED technology. In most cases, the components formed by DED technology have a relatively low resolution and often require post-processing to complete the final product. The anisotropy of the product itself is significant and requires dynamic adjustment of parameters to reduce the impact of this on the performance of the fabricated product[20,22].

In response to the above problems, researchers have also attempted to solve them in recent years by improving and perfecting the hardware of DED devices. Novel devices such as rolling-assisted laser directed energy deposition (L-DED) have emerged. With the aid of *in situ* rolling, the product has a unique initial microstructure, which results in relatively low uniform elongation and relatively high ultimate tensile stress[23].

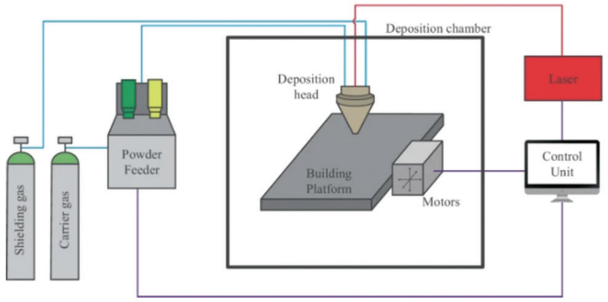

Figure 3. Demonstration of the working principle of a general laser powder directed energy deposition system[17].

2.3. Material extrusion

MEX technology is a very established AM technique. It builds 3D parts by heating a linear composite or thermoplastic material to soften it, followed by depositing and curing it layer by layer[24]. In particular, while printing biomaterials by means of MEX, the material is extruded from the nozzle and then forms the structure[25]. The process is shown in Figure 4.

MEX technology is well suited for use in domestic or non-professional applications, and it also has applications in the medical field due to its high degree of customizable flexibility[26]. At present, this technology has proven to be very compatible with more than 20 thermoplastics, such as acrylonitrile butadiene styrene (ABS), polyamide 66 (PA66), and aliphatic polyamides (PA, also known as nylon). New research has shown that MEX technology is also suitable for polymers such as PEEK or ceramic materials, which will be described in more detail in subsequent sections of this paper[24].

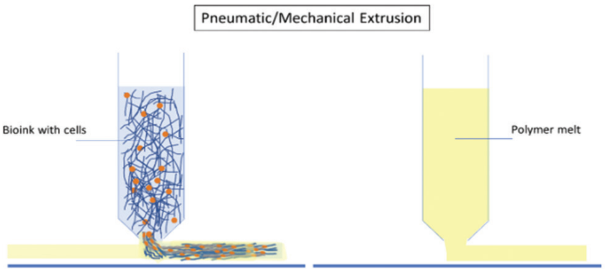

Figure 4. Illustration of material extrusion with or without cells (permission obtained from authors)[25].

One of the advantages of MEX technology is that it is inherently less restrictive in terms of raw materials. Most of the feedstocks are very inexpensive, and a considerable proportion of the model material is open source, reducing the cost of learning for the user themselves, and making it highly adaptable and relevant for the home market. At the same time, 3D printers using MEX technology are generally less expensive to maintain and run and are therefore used in some commercial scenarios to produce prototypes.

On the other hand, there are limitations to the strength of the finished products printed by MEX technology, especially for the perpendicular Z-axis direction (along the build direction), where there is a large deficit in strength. At the same time, if the user tries to increase the accuracy of a 3D printer using MEX technology, the corresponding fabrication time increases, which limits the value of this technology to a certain extent.

Most importantly, the thermoplastic material in a MEX process can be heated to a maximum of 500°C, thereby emitting harmful gases and ultrafine particles that can lead to a reduction in indoor air quality in domestic scenarios. This poses a potential health problem for the occupants of the house, considering that some components take more than a few hours to fabricate[27].

It is worth noting that MEX technology may be developed for medical applications because it is compatible with most materials. This certainly broadens the potential market for this easy-to-use technology. Recent studies have successfully used medical-grade polyamide (PA)12 polymer as matrix material to complete the print; it was also found that by adding silver nitrate, polyethylene glycol or polyvinylpyrrolidone, the printed samples could further exhibit higher tensile strength or sterilization properties[28].

2.4. Material jetting

MJT technology is an AM technology that is somewhat similar to conventional 2D printers[29]. 3D printers using this technology build complex 3D structures by spraying a photosensitive liquid material layer by layer over a specified area with a nozzle and curing it with ultraviolet light.

This technology offers high cost-efficiency and application potential. In addition to being suitable for traditional thermoset photopolymers, MJT has shown adaptability to a variety of materials such as gels and bio-based materials[30]. It has also received increasing interest from the market as well as industry in recent years because it can be used in informal settings such as office scenarios due to its similar working characteristics to traditional printers[29]. On the other hand, the ability to print simultaneously with multiple materials is a major advantage of MJT technology. The high dimensional accuracy and low surface roughness of the finished products fabricated using MJT technology make it potentially useful in areas such as cutting-edge customized medicine, aerospace, and other applications[31].

The current shortcomings of MJT technology are divided into two principal areas: material and technology. The layer-by-layer method has gaps and defects that can have a significant impact on the final performance of certain elastomeric materials, such as fatigue life[32]; on the other hand, the raw materials used in MJT technology are photosensitive, the mechanical properties of the finished product could potentially deteriorate over time[33].

Targeted research has been followed up. By studying the aging of different color resins printed by MJT over time, the researchers found that the stiffness of the material first increased and then decreased over time, and the aging process has a potential relationship with the color and appearance of the product itself[34]. At the same time, various tests were carried out; the structure of the whole experiment is shown in Figure 5.

These studies provided the basis for understanding the long-term factors affecting the changes in the appearance and performance of objects printed using MJT technology. In the future, on this basis, through a series of research on the parameters of the entire industry chain and product design, it may be possible to greatly increase the lifespan of the product and enhance the actual application value of the technology.

2.5. Powder bed fusion

Powder bed fusion (PBF) technology is an important branch of AM. Especially in the field of metal additive manufacturing, PBF occupies an absolute advantageous position. Figure 6 illustrates the market share held by different technologies in the metal additive manufacturing segment in 2019[17]. PBF technology, as

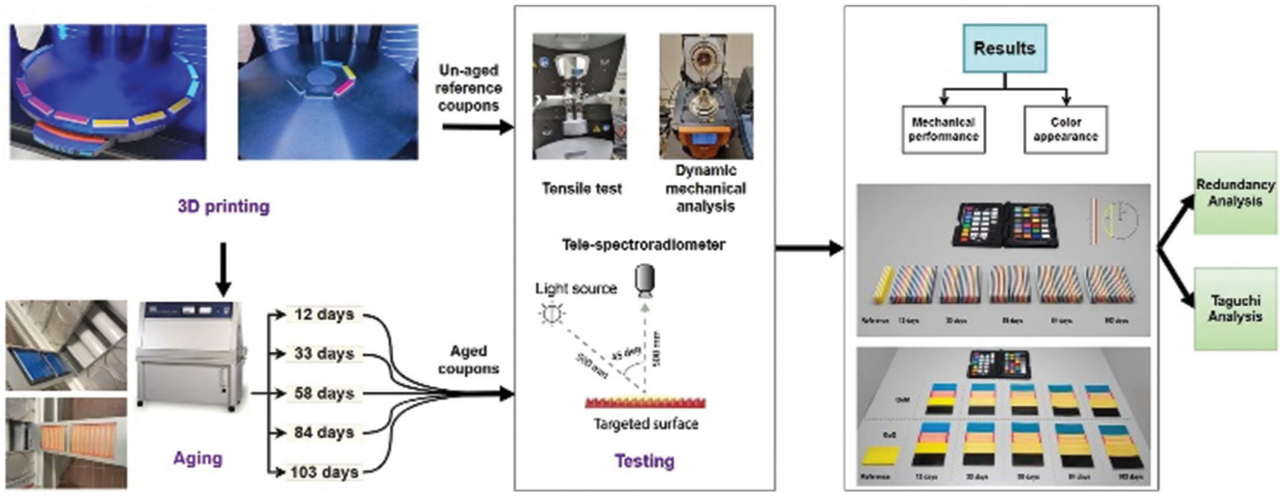

Figure 5. Schematic diagram of the experimental framework[34].

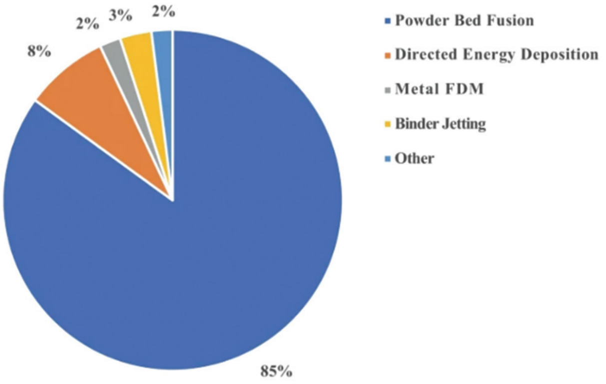

Figure 6. Schematic representation of the market share held by different technologies in the metal additives manufacturing segment in 2019[17].

the name suggests, is a technique in which various parts of the powder laid on a bed are heated by different heat sources to sinter or melt the powder and then solidified to form a 3D structure[35].

Over time, four derivatives of PBF technology have been developed to suit different raw materials and heat sources for applications; these are selective laser sintering (SLS), selective laser melting (SLM)[36], electron beam melting (EBM)[37] and multi jet fusion (MJF).

These four technologies are different in their technicalities and use different raw material form. For thermoplastics, SLS and MJF are used[37]. Of these, SLS is by far the most established PBF technology for polymers[38]. The main difference between SLS and MJF lies in the heat source, with the SLS technology using a laser for powder sintering and the MJF technology using an infrared (IR) lamp to activate the solidification process. Both types of technology are currently limited by the range of polymers available and researchers are expanding their database of raw materials to continue exploring their potential applications in industry[37,38].

Another category within the PBF technique comprises the SLM technique and the EBM technique. These two techniques are suitable for most types of metal powders[39]. The heat source for SLM technology is a laser, while the heat source for EBM technology is an electron beam[40]. Figure 7 illustrates the basic working principle and structure of SLM technology by presenting a schematic of the working process of SLM technology.

The EBM technology has a larger scanning beam diameter and a faster scanning rate, allowing for the rapid construction of larger volumes and the processing of thicker powder layers compared with the SLM technology. At the same time, the EBM technique produces products with better fineness and surface roughness compared to the SLM technique[41,42].

Both techniques are currently attracting significant interest in the academic circles, for their complex thermal processes during processing and their eventual impact on the microstructure of the finished product[43]. In fields such as aerospace, medical, and military defense, these two technologies have been more widely researched and applied due to their suitability for finished complex structures and the ability to rapidly prepare prototype products[44].

The extensive development of LPBF is matched by the ongoing development of targeted and applicable alloys to raise the application value of this technology. For instance, by adding Ti, Cr, and Fe to the Al-Cu alloy, a

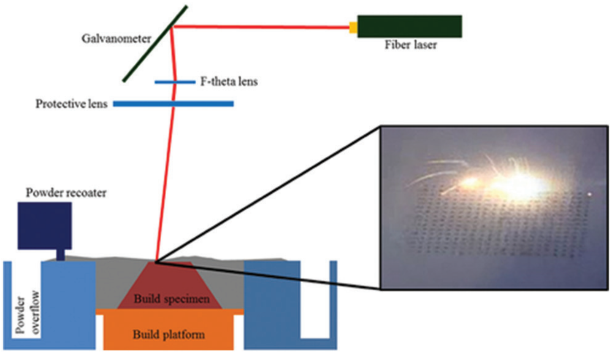

Figure 7. Schematic of selective laser melting build chamber and process[36].

new aluminum alloy with low thermal crack sensitivity suitable for PBF printing technology was fabricated and was shown to achieve the highest strength currently known for aluminum alloys printed by PBF[45]. For other aluminum alloys such as Al-Zn-Mg-Cu-Nb alloys, the effect of Zn content on the formability and aging precipitation that may result from LPBF preparation has also been studied[46]. It has been demonstrated that the content of the Zn element affects the aging kinetics, the order of elemental precipitation and the crystal size of the alloy, provided that the PBF printing technique is used. It was also explored how the processing window changes as the Zn content rises to ensure that it can be stabilized for fabrication[46].

There are numerous studies exploring in this regard, indicating that the intensive investigations of the PBF technology are a testament to its current dominance.

2.6. Sheet lamination

Sheet lamination (SHL) technology is known to be the first commercialized AM technology, but its market share is still very limited today[47,48]. The raw material requirement for SHL technology is sheet or plate. During the process, these raw materials are stacked layer by layer and tooled to cut out specific sections for gluing or welding, which are combined to form the structure.

Over the years, SHL technology has evolved into various sub-categories including selective deposition lamination, ultrasonic additive manufacturing and selective lamination composite object manufacturing, depending on the type of raw materials used and the bonding process, which vary in detail but are based on the same principle[49].

Due to these adaptable variants, SHL technology can process a wide range of materials such as metals, paper, polymers, textiles, ceramics, and composites and can be used to build very large finished products[47,49]. Some of the 3D printers using SHL technology can also be deployed in office environments to fabricate paper models. The problem with SHL technology, however, is that it cannot be used to print complex structures, so the practical value of this technology is limited.

A similar technique called electron beam sheet lamination (EBSL) has recently been attempted in the manufacture of turbine disk alloys with good results[50]. EBSL technology utilizes electron beams to achieve rapid melting and solidification between multiple layers of material. This feature helps control the segregation of the alloy itself and removes impurities in the alloy to obtain products of higher purity. The alloy prepared by EBSL has a finer structure and exhibits good creep rate.

2.7. Vat photopolymerization

VPP technology is incredibly special compared to other AM technology. During the process, a light source of a specific wavelength is selectively directed at a specific part of a barrel of photosensitive liquid material to induce a curing reaction, during or after which the build platform is lowered and the surrounding liquid material re-submerges the platform and a new layer is cured[51]. Depending on the light source used and the way the platform is lowered, VPP technology can be classified as continuous direct light processing, direct light processing, stereolithography (SLA), etc.[52,53].

The principle of this technique therefore limits the range of materials that can be applied to VPP. The usual raw material is photosensitive liquid resin, but fillers such as ceramics can be added to enhance the mechanical properties of the finished product[54]. In addition, a new study has offered a solution to the problem of switching raw materials during the process, enabling the use of multiple materials in printing embedded complex structures[55].

Compared to other AM technology, VPP technology offers the advantages of high precision, fast forming, smooth surfaces and low material waste[56]. However, this technology has a few disadvantages, such as high costs, limited adaptability of raw materials and potential instability in the performance of the finished product. The field of bioprinting based on VPP technology is currently gaining traction. By varying the type of photo initiator used, VPP technology can produce finished products that are simultaneously reliable and highly biocompatible. VPP technology also has considerable potential for application in the field of tissue engineering and regenerative medicine[57].

The application of VPP technology improves the scalability and also eases the replication and manufacture of organs-on-a-chip[58,59]. Two sub-types of VPP technology – SLA and DLP – have proven to be the most favorable fabrication methods for future in-depth research in the field of organs-on-a-chip. Recent studies have demonstrated that DLP printing technology is suitable for organs-on-a-chip fabrication and development, and with the improvement and specificity optimization of the equipment hardware and preparation parameters, it is even possible to consistently reproduce them in tens of microns of printing accuracy[59].

3. High-performance polymers and polymer composites for additive manufacturing

The rapid development of AM technology will continue to revolutionize and reshape all areas of human life. The emergence of AM technology will also provide more possibilities for the application of PEEK and polyimide, which are already commonly used in aerospace, biomedical and other fields, as high-performance materials. On the other hand, the continuous experimentation with these materials has also enriched the database of materials applied in various AM technologies in different fields, further strengthening the potential of AM technologies. The following section focuses on high-performance engineering plastics – PEEK and polyimide – and their combination with AM technology.

3.1. Polyetheretherketone

PEEK, under the trademark of Victrex[60], shares many characteristics with polyether sulfone and is a semi-crystalline thermoplastic polymer with tough properties[61]. This material, which was developed in the last century, has shown enormous potential and value in several fields since its introduction.

With a high melting point of over 300°C[62], high abrasion resistance, chemical resistance, competitive dielectric strength, excellent mechanical properties[63], and potential biomechanical properties[64], PEEK is ideal for use in a wide range of industries, including military, medical, electrical and electronic. Among these, PEEK is particularly promising for medical applications as it has been demonstrated that PEEK does not exhibit cytotoxicity to biological cells, nor does it induce cancerous necrosis in cells, and therefore, it has good biocompatibility[65].

However, the progress of this field, which has been explored since 1987[66], does not stop there, and many studies exploring composite reinforcement of PEEK materials are still underway. Among the more important of these are PEEK composites containing bioactive particles such as hydroxyapatite (HA) to cater for the repair of active cells in living organisms[67] and the modification of the elastic modulus of the PEEK material by means of carbon fiber reinforcement[68]. Studies have shown that the mechanical properties of PEEK-based composites reinforced by carbon fibers have a high resemblance to those of the most pristine state of human bone than other biocompatible metals such as titanium, thus minimizing the problem of stress shielding and making them an ideal raw material for human bone repair techniques[60].

The enormous potential of PEEK and its composites has also led researchers to investigate its application in the field of AM technology. By combining the two, it will be possible to expand the prospects for both. The combination of the two is first and foremost seen in the manufacture of complex medical components such as dentures, biological scaffolds, and implants, where the rapid prototyping capabilities of AM technology for complex structures are being put to great use. Several studies have recently demonstrated the successful printing of pure PEEK materials using MEX technology and good performance was observed in the printed item[69-71].

In parallel, experiments on PEEK-based composites are underway. The previously mentioned PEEK-HA composites containing HA nanoparticles[72] and PEEK-carbon fiber (CF) composites containing carbon fibers[73], as well as PEEK composites containing carbon nanotubes and graphene nanosheets[74], have all been experimented in combination with MEX technology. These experiments were generally successful; for example, biocompatible PEEK-HA composites with sufficient mechanical strength were successfully processed by AM technology[53], PEEK-graphene nanoplate (GNP) and PEEK-carbon nanotube (CNT) nanocomposites printed by AM technology also exhibited unique multiple properties, reflecting their promising applications in multiple fields such as oil extraction, automotive manufacturing, and space exploration[74], while the PEEK-CF composites processed by AM technology exhibit a controlled adjustment of the anisotropy of the thermal properties to suit potentially specific application requirements[73]. Alternative trials have also been conducted for titanium implants. Figure 8 is a schematic representation of the MEX process for replacing existing titanium products by processing PEEK as a mesh in cranioplasty[75].

Another development idea is to modify the surface of PEEK to overcome its biological inertness and further broaden its potential applications. Surface bisphosphonation of PEEK has been successfully accomplished using alendronate, and this newly obtained material has been shown to be able to direct the biological behavior of macrophages and further improve the cellular microenvironment[76]. This could significantly improve

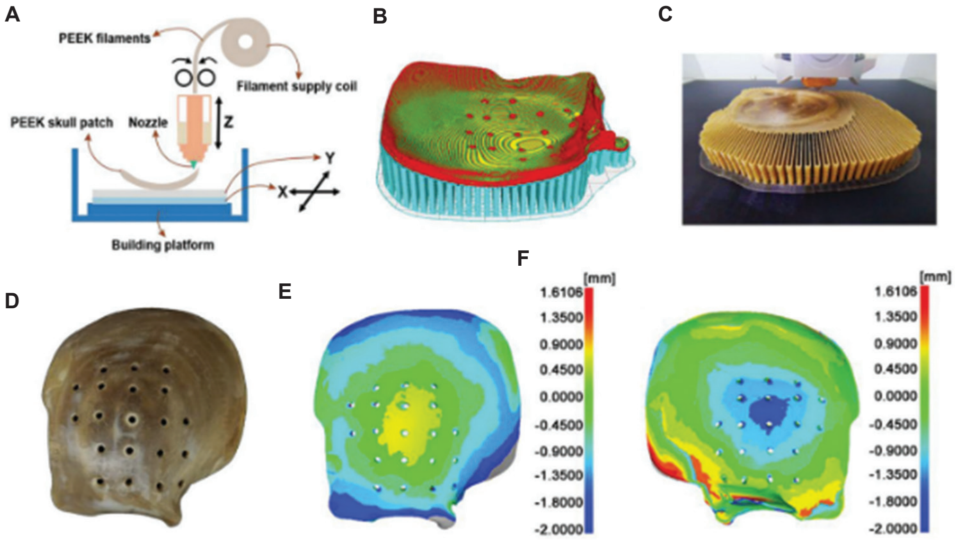

Figure 8. Schematic illustration of the process to fabricate the material extrusion (MEX)-printed polyetheretherketone (PEEK) skull implant. (A) Flow chart of the MEX printing of PEEK skull implant. (B) Printing data processing and acquiring control parameters. (C) MEX printing of the PEEK skull implant. (D) The MEX-printed PEEK prosthesis of the skull. (E and F) Comparison between the MEX-printed PEEK skull implant and the patient-specific designed PEEK skull prostheses. The front (E) and back (F) views of the printing accuracy are shown[75].

the treatment of inflammation in patients as well as the regenerative bone repair of implants at a later stage.

Similar modifications can also yield sulfonated PEEK (SPEEK), which can be adhered to other antimicrobial substances to achieve an improved inflammatory environment in implanted soft tissues. The antimicrobial peptide HHC36 has been shown to provide up to 10 days of extended sterilization effect on SPEEK by a simple solvent evaporation method (HSPEEK)[77], which opens further possibilities for minimally invasive bone and joint grafting and repair in the elderly. The flowchart of the synthesizing HSPEEK is shown in Figure 9.

However, the integration of this novel material obtained by modification with AM technology has yet to be further explored, but its promising future in the biomedical field will undoubtedly point to the need for complex structures, making this area highly explorable.

3.2. Polyimide

Polyimide, a material that predates PEEK, is one of the most heat-resistant polymers currently available[78]. It has a rigid aromatic molecular structure and therefore exhibits excellent corrosion and heat resistance, mechanical and electrical properties[79] and can be used at extreme operating temperatures. It is currently of great value in many fields such as space exploration, defense and security, electronics, and electrical appliances.

On the other hand, given its stability at high temperatures, it is difficult to fuse polyimide in conventional processing methods, limiting the value of this material in cutting-edge applications. AM technology allows the polyimide material to be processed with precision, enabling it to be used in more complex scenarios[79].

The precursors of polyimide materials can be used for manufacturing by means of VPP technology due to their ability to conveniently bind photocurable functional groups[80]. In 2017, researchers prepared photosensitive polyimide oligomers into solvent-free photocurable inks and processed them using VPP technology, successfully obtaining products with excellent mechanical properties[81]. In the same period, the printing of insoluble engineering thermoplastic polyimides was also successfully accomplished with the VPP technology using soluble precursor polymers for chemical cross-linking under light induction and post-printing heat treatment[82].

These early studies have demonstrated that the polyimide materials are compatible with AM technology. It also paves the way for the subsequent use of AM technology to improve the functionality as well as the practical value of polyimide and polyimide-based composites. For example, new research has begun to focus on greening the AM process and has incorporated this concept into the research process, resulting in an alternative to the harmful organic solvents required for the AM process for polyimide materials[83]. On the other hand, in response to the low strength, poor thermal stability and high curing shrinkage of photocurable resin materials currently available on the market, new light-curable polyimide inks for the

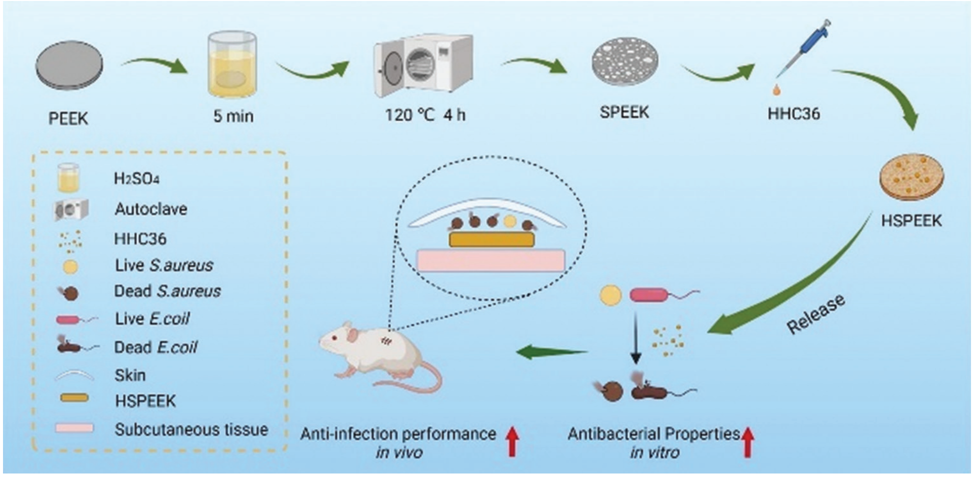

Figure 9. Synthesis of HSPEEK and summary of the experimental procedure[77].

manufacture of polyimide materials using AM technology are being innovated to increase thermal stability and may be used in special applications with higher operating temperatures[84].

Blending polyimide-based composites with CNT is a popular research topic, and researchers are exploring the processing of polyimide-CNT composites in MEX technology after overcoming the problems of inhomogeneous mixing associated with conventional sonication and other methods[85]. After optimizing the process parameters during the process and the filling level of CNT, finished complex structures with exceptional electrical and mechanical properties and anti-electromagnetic shielding were successfully prepared by MEX technology, offering new possibilities for the application of this new composite material in cutting-edge fields such as aerospace[86].

In the future, research into improving the accuracy and stability of polyimide materials in AM technology will continue, and this important polymer material and its complexes will play an even more significant role in future developments.

4. High entropy alloys and its composites for additive manufacturing

It has always been a research focus to investigate new alloys, which are commonly employed in AM technology and are essential materials for human society. There is an increasing demand for metal components with high-performance and ultra-complex structures, but traditional manufacturing techniques are limited by their metal processing capabilities. Thus, this highlights the need for rapid commercialization of new alloys and innovation of manufacturing technologies.

In the field of metals, the study of HEAs and their processing methods is currently the focus of research. This unique type of alloy is gradually becoming the most dominant material in future, and its unique value compels researchers to devote greater attention to it; therefore, this section will focus on this unique metal concept, the current status of development and application of HEAs, the composites involved, and the integration of HEAs with AM technology. This section summarizes the work of researchers in recent years and analyzes future directions of research and development.

4.1. Concept and current development

The concept of alloys has been around for a long time and since the discovery of metal materials, the process and method of adding different elements to pure metals to improve metal properties have been explored by generations of researchers.

The concept of HEAs was first introduced by Yeh *et al.* in 2004[87], and its original definition requires that it comprises at least five principal elements and that the atomic concentration of each principal element is between 5% and 35%. Subsequent researchers have expanded the concept of HEAs[88] to also include alloys containing three or four principal elements. Although the concept of HEAs has been promulgated for less than two decades, this concept has already disrupted the traditional framework of alloy research and has grown into a major research hotspot in metallic materials science.

The “entropy” in the “high entropy alloy” refers to the constitutive entropy of the alloy and according to Equation I, an increase in entropy at high temperatures will result in a significant decrease in Gibbs free energy, which, in turn, will show the stability of the phases in the material[89].

$$G = H - TS \quad \text{(I)}$$

where H is the enthalpy, T is the absolute temperature, and S is the entropy.

Compared to conventional alloys, HEAs have several outstanding core effects such as diffusion hysteresis effect and cocktail effect. These effects associated with solid solution strengthening can lead to a variety of unique properties, including microstructural stability and oxidation resistance. Different studies have been carried out to investigate the mechanical, electrical, and other properties of HEAs[90], and new HEAs are also constantly developed for use in a variety of applications and in special advanced fields[91]. HEAs can also be used as metallic materials under extremely high or low temperature operating conditions.

In their application as refractory materials, HEAs can maintain structural stability at high temperatures due to lattice distortion, high entropy effects, and diffusion hysteresis[92,93]. Since 2010, few research groups have successfully produced NbMoTaW and VNbMoTaW that can withstand temperatures of up to 1600°C[92,94]. Since then, through the incessant innovations and breakthroughs made by the researchers, the practical value of HEAs in the field of refractory materials has been increased by reducing their density and improving many of their properties, including ductility[93,95,96]. In the field of cryogenic applications, research into HEAs has also yielded impressive results. A recent study on CrCoNi-based medium- and high-entropy alloys demonstrated that CrCoNi with excellent damage tolerance exhibits high fracture toughness at temperatures as low as 20 K and shows a deformation structure different from that at higher temperatures[97].

This unique property is due to the synergistic effect of multiple microstructures such as dislocation slip and twin structure, and the performance of HEAs beyond that of other conventional materials once again demonstrates the extraordinary potential of HEAs for future high-performance alloys[97].

4.2. Integration with additive manufacturing

As HEAs are promising materials in many applications, studies have been conducted to investigate their processing by AM technology. As a metallic material, the suitability of HEAs as a raw material for AM technology has been relatively well studied, and subsequent research has begun to investigate the effect of the different parameters applied in the processing by different AM technologies on the performance of the final product.

In the case of the CoCrFeNi alloy system, for example, which is the most frequently used system to study the fabrication of bulk HEAs using AM technology[98], the influence of process parameters such as scanning speed and laser power on the final microstructure of the finished product has been investigated in both the PBF and DED techniques[99,100]. Further attempts have been made to optimize the temperature gradients and cooling rates during material fabrication by means of improved scanning strategies or the use of ultrasonic assistanc[99].

For another frequently used alloy system in research, AlxCoCrFeNi, a new study published is equally exciting[98,101]. This study, using the LPBF technique, succeeded in preparing a high-strength alloy with a layered microstructure consisting of body-centered cubic and face-centered cubic nanospheres layer by layer from AlCoCrFeNi alloys, making it stronger and more ductile than other alloys[101].

In addition, two popular research directions in the field of HEAs processing by AM technology are *in situ* alloying and *in situ* strengthening. *In situ* alloying is the direct *in situ* synthesis of HEAs by AM technology without pre-alloying. Through such studies, it has been found that the AM technique allows the costly pre-alloying process to be bypassed in favor of the direct preparation of HEAs from different pure metal powders, with acceptable densities and excellent mechanical properties[102]. *In situ* strengthening, on the other hand, refers to the generation of strengthening particles directly in the process through *in situ* chemical reactions between different elements or compounds during processing. In this way, a more homogeneous and detailed particle distribution, which is indicative of a better strengthening performance, can be obtained, as compared with the particle distribution obtained with conventional methods[103,104]. The emergence of these two research directions means that both AM technology and HEAs materials are refining each other, which is beneficial to devising a manufacturing method of greater value.

4.3. Processing of high entropy alloys composites and future directions

The HEA composites can be prepared by two methods: (i) The addition of other substances to the HEAs matrix to form metal matrix composites, and (ii) the addition of HEAs particles to a conventional alloy matrix to form metal-metal composites[105,106]. Both of these categories have been studied specifically for manufacturing with the application of AM technology, and it has been verified that the composites possess, for example, improved tensile and friction resistance properties[107].

In the future, as more unique properties of HEAs are explored and exploited, the synergy between HEAs and AM technology will become even stronger, and it is expected that this material will play a valuable role in more fields and serve the practical needs of cutting-edge fields better with the help of AM technology.

5. Standards in additive manufacturing

As AM technology flourishes, standards are needed for all aspects of the development, use, and refinement of the varied materials that are applied to this technology. Industry standards are the foundation for development, the beacon that inspires researchers to make breakthroughs and the guide for those trying to make the most out of this revolutionary technology. This section will therefore focus on the internationally recognized material standards currently used for AM technology, with a view to informing research in this area.

It should be noted that an early effort to formulate standards in the field of AM technology was undertaken by the American Society of Automotive Engineering (SAE) in the USA, which launch a standard on laser-deposited titanium products in 2002[108]. This standard is no longer valid and has been reaffirmed by the SAE as AMS4999A in 2016[109]. This has been updated with regard to the requirements for raw materials.

In 2008, the ASTM International started to engage became in this important endeavor and in 2009, the ASTM Committee F42 on Additive Manufacturing Technology was formed and divided into eight technical subcommittees to oversee the development of standards for different parts of the AM technology field[110]. Of the 22 standard headings currently listed on the F42 website, the more important ones include F42.01 Test Methods, F42.04 Design and F42.05 Materials and Processes[111]. In turn, F42.05 includes a dozen standards that define the requirements and characterization of polymer and metal powder raw materials for specific types of processing[112,113], performance specifications for specific products[114-117], as well as specific procedures and specifications for different processes[118]. On the other hand, ISO also formally established Committee TC261 in 2011 to work specifically on the standardization issues throughout the entire process of additive manufacturing[119]. In its 1st year since inception, it started a partnership with the F42 committee and has been working on the definition of terms, coordinate system definitions, data formats, etc., in the following years.

In 2021, ASTM and ISO have again jointly published the harmonized standard ASTM ISO/ASTM52903-1-20 for raw materials for MEX technology, including unfilled, filled, and reinforced plastic materials suitable for processing into parts and taking into account the influence of components that may contain flame retardants or stabilizers[120].

The European Union and China have also started to formulate their own AM standards. For example, the European Union launched the SASAM (Support Action for Standardization in Additive Manufacturing) project in 2015[121] and China established the TC562 National Technical Committee for Additive Manufacturing Standardization in 2016[122]. They have also started to develop standards in a number of key areas of AM technology, some of which are related to the requirements for raw materials.

As can be understood from the above history of development, the most influential standards in the field of AM technology are still those developed by ASTM and ISO, and they have developed some standards for constraints and characterization of metals as well as polymeric raw materials. Table 1 provides a summary of information on these material standards that are still in force.

However, as stated in ASTM's February 2022 article on materials suitable for AM in construction, there are

Table 1. Summary information on ASTM standards for raw materials in the AM sector

Standard no.	Applicable material	Applicable technology	Date of update
ASTM F2924-14 (2021)	Ti-6Al-4V	Full-melt powder bed fusion	October 20, 2021
ASTM F3001-14 (2021)	Ti-6Al-4V (extra low interstitial)	Full-melt powder bed fusion	October 22, 2021
ASTM F3049-14 (2021)	Metal powders	Powder-based additive manufacturing processes	October 25, 2021
ASTM F3055-14a (2021)	Nickel alloy (UNS N07718)	Powder bed fusion	October 29, 2021
ASTM F3056-14 (2021)	Nickel alloy (UNS N06625)	Powder bed fusion	October 29, 2021
ASTM F3091/F3091M-14 (2021)	Plastic materials	Powder bed fusion	October 29, 2021
ASTM F3184-16	Stainless steel alloy (UNS S31603)	Powder bed fusion	October 10, 2017
ASTM F3213-17	Co-28-Cr-6-Mo	Powder bed fusion	January 11, 2018
ASTM ISO/ASTM52901-16	General raw materials	Not specified	April 03, 2017
ASTM ISO/ASTM52903-1-20	Plastic materials	Material extrusion	March 09, 2021
ASTM ISO/ASTM52925-22	Polymers	Laser-based powder bed fusion	April 11, 2022

no standards regarding raw materials for many of AM's new applications, such as building houses, to meet the requirements of these applications[123].

6. Conclusions and future development

This paper introduces the seven major AM methods and their respective working principles, the types of raw materials that are compatible with the different technologies, and the advantages and disadvantages of each technology. This is followed by a description of the emerging materials used in AM technology, namely, PEEK, polyimide and HEAs, and the development of and adaptation to AM technology involving these composites. Finally, we present the international standards in the field of AM, focusing on their requirements for raw materials used in AM technology and categorizing them by time and geography.

The summary and outlook for the above are as follows:

(i) The AM technology can be divided into several subcategories driven by different processing principles. These technologies are mainly applicable to the manufacture of polymers as well as metallic materials and have emerged to correspond to application scenarios and targeted machining of component features. It is worth noting that while popular technologies such as DED and PBF are attractive options among the researchers and industries in recent years, the sub-technologies still possess the potential and value in their respective application areas and neither one of them will be phased out.

(ii) PEEK is a popular, new material for use with AM technology and has exceptional performance. The disadvantages that it exhibits with conventional processing methods are no longer present in AM technology. Research into PEEK and its composites is ongoing, and there is still much to be explored in this regard. Similarly, the integration of polyimide materials (including the composites in which they constitute) with AM technology has also passed the feasibility stage. In the next few years, research on employing these two materials in printing will move towards increasing precision, controlling defect, allowing full control of the AM process, and thus further improving the print quality.

(iii) HEAs are currently a type of popular material for researchers to experiment with until the next revolutionary alloy is introduced in the future. Since they are metallic in nature, HEAs possess several advantages in combination with AM technology. The concepts of *in situ* alloying and *in situ* strengthening adopted in the field of AM technology confer this class of alloys even more possibilities, and it is expected that more harmonious integration of these two fields will happen in the future.

(iv) The AM technology sector has been the focus of international associations since 2002, and a series of standards have been released, which have been enriched and improved since 2008 due to the rapid development of the AM technology. However, as AM technology becomes a more prevailing technique, the issue of standards for raw materials for specific industries needs to be addressed and this will be a key issue in future.

In the future, the deeper integration of AM technology with more materials will continue to accelerate, and the application of the technology will continue to expand towards more complex and refined directions. For example, by combining it with machine learning, it will greatly accelerate the optimization of the generation of different structures for different metals with different process parameters under the PBF technique[124,125]. A variety of models, including decision trees, have been demonstrated to learn and predict the performance of products printed with PBF technology[126]. We also look forward to the good news in this area. In other areas, electronic additive manufacturing is also an emerging research direction. This direction, which requires higher printing accuracy, has also been shown to be realized using MJT technology[127-129]. It is believed that as the AM technology starts to influence more application scenarios, the incentives of interdisciplinary integration will speed up the entry of this processing tool into a virtuous cycle to benefit different application aspects in a more effective manner.

Acknowledgments

The authors acknowledge the support of National University of Singapore for providing the research resources.

Funding

The authors would like to acknowledge the funding support from Singapore Ministry of Education Academic Research Fund Tier 1 (Award No.: 22-3721-A0001).

Conflict of interest

The authors declared no potential conflict of interest with respect to the research, authorship, and/or publication of this article.

Author contributions

Conceptualization: Swee Leong Sing
Project administration: Swee Leong Sing
Resources: Swee Leong Sing
Supervision: Swee Leong Sing
Visualization: Yanting Liu
Writing–original draft: Yanting Liu
Writing–review and editing: Swee Leong Sing, Yanting Liu

Ethics approval and consent to participate

Not applicable.

Consent for publication

Not applicable.

Availability of data

Not applicable.

References

1. Gao W, Zhang Y, Ramanujan D, *et al.*, 2015, The status, challenges, and future of additive manufacturing in engineering. *Comput Aided Des*, 69: 65–89.

   https://doi.org/10.1016/j.cad.2015.04.001

2. Herzog D, Seyda V, Wycisk E, *et al.*, 2016, Additive manufacturing of metals. *Acta Mater*, 117: 371–392.

   https://doi.org/10.1016/j.actamat.2016.07.019

3. Yeong WY, Goh GL, Goh GD, *et al.*, 2022, 3D printing of soft grippers with multimaterial design: Towards shape conformance and tunable rigidity. *Mater Today Proc*, 70: 525–530.

   https://doi.org/10.1016/j.matpr.2022.09.552

4. ISO/TC 261 and ASTM Committee F42, 2021, ISO/ASTM 52900:2021 Additive Manufacturing - General Principles - Fundamentals and Vocabulary. United Kingdom: ISO.

5. Lores A, Azurmendi N, Agote I, *et al.*, 2019, A review on recent developments in binder jetting metal additive manufacturing: Materials and process characteristics. *Powder Metall*, 62: 267–296.

   https://doi.org/10.1080/00325899.2019.1669299

6. Li M, Du W, Elwany A, *et al.*, 2020, Metal binder jetting additive manufacturing: A literature review. *J Manuf Sci Eng*, 142: 090801.

   https://doi.org/10.1115/1.4047430

7. Gaytan SM, Cadena MA, Karim H, *et al.*, 2015, Fabrication of barium titanate by binder jetting additive manufacturing technology. *Ceram Int*, 41: 6610–6619.

   https://doi.org/10.1016/j.ceramint.2015.01.108

8. Oropeza D, Roberts R, Hart AJ, 2022, A rapid development workflow for binder inks for additive manufacturing with application to polymer and reactive binder ink formulation. *J Manuf Process*, 73: 471–482.

   https://doi.org/10.1016/j.jmapro.2021.10.068

9. Do T, Kwon P, Shin CS, 2017, Process development toward full-density stainless steel parts with binder jetting printing. *Int J Mach Tools Manuf*, 121: 50–60.

   https://doi.org/10.1016/j.ijmachtools.2017.04.006

10. Wu S, Yang Y, Huang Y, *et al.*, 2023, Study on powder particle behavior in powder spreading with discrete element method and its critical implications for binder jetting additive manufacturing processes. *Virtual Phys Prototyp*, 18: e2158877.

    https://doi.org/10.1080/17452759.2022.2158877

11. Grant LO, Higgs CF 3rd, Cordero ZC, 2023, Sintering mechanics of binder jet 3D printed ceramics treated with a reactive binder. *J Eur Ceram Soc*, 43: 2601–2613.

    https://doi.org/10.1016/j.jeurceramsoc.2022.12.017

12. Oropeza D, Hart AJ, 2021, Reactive binder jet additive manufacturing for microstructural control and dimensional stability of ceramic materials. *Addit Manuf*, 48: 102448.

    https://doi.org/10.1016/j.addma.2021.102448

13. Bai Y, Williams CB, 2018, Binder jetting additive manufacturing with a particle-free metal ink as a binder precursor. *Mater Des*, 147: 146–156.

    https://doi.org/10.1016/j.matdes.2018.03.027

14. Du W, Ren X, Ma C, *et al.*, 2019, Ceramic binder jetting additive manufacturing: Particle coating for increasing powder sinterability and part strength. *Mater Lett*, 234: 327–330.

    https://doi.org/10.1016/j.matlet.2018.09.118

15. Saboori A, Gallo D, Biamino S, *et al.*, 2017, An overview of additive manufacturing of titanium components by directed energy deposition: Microstructure and mechanical properties. *Appl Sci*, 7: 883.

    https://doi.org/10.3390/app7090883

16. Dass A, Moridi A, 2019, State of the art in directed energy deposition: From additive manufacturing to materials design. *Coatings*, 9: 418.

    https://doi.org/10.3390/coatings9070418

17. Piscopo G, Iuliano L, 2022, Current research and industrial application of laser powder directed energy deposition. *Int J Adv Manuf Technol*, 119: 6893–6917.

    https://doi.org/10.1007/s00170-021-08596-w

18. Svetlizky D, Das M, Zheng B, *et al.*, 2021, Directed energy deposition (DED) additive manufacturing: Physical characteristics, defects, challenges and applications. *Mater Today*, 49: 271–295.

    https://doi.org/10.1016/j.mattod.2021.03.020

19. Kim MJ, Saldana C, 2020, Thin wall deposition of IN625 using directed energy deposition. *J Manuf Process*, 56: 1366–1373.

    https://doi.org/10.1016/j.jmapro.2020.04.032

20. Aversa A, Saboori A, Marchese G, *et al.*, 2019, Application of directed energy deposition-based additive manufacturing in repair. *Appl Sci*, 9: 3316.

    https://doi.org/10.3390/app9163316

21. Zhang Y, Jing H, Xu L, *et al.*, 2021, Effects of different scanning patterns on nickel alloy-directed energy deposition based on thermal analysis. *Virtual Phys Prototyp*, 16: S98–S115.

https://doi.org/10.1080/17452759.2021.1896173

22. Feenstra DR, Banerjee R, Fraser HL, *et al.*, 2021, Critical review of the state of the art in multi-material fabrication via directed energy deposition. *Curr Opin Solid State Mater Sci*, 25: 100924.

https://doi.org/10.1016/j.cossms.2021.100924

23. Li C, Hodgson P, Preuss M, *et al.*, 2023, Rolling-assisted direct energy deposited Inconel 718: Microstructural evolution and mechanical properties after optimized heat treatment. *J Mater Sci Technol*, 144: 118–127.

https://doi.org/10.1016/j.jmst.2022.10.021

24. Loh GH, Pei E, Gonzalez-Gutierrez J, *et al.*, 2020, An overview of material extrusion troubleshooting. *Appl Sci*, 10: 4776.

https://doi.org/10.3390/app10144776

25. 3D Bioprinting Processes: A Perspective on Classification and Terminology-publicly Available Content Database-ProQuest. Available from: https://www.proquest.com/publiccontent/docview/2667821253?parentsessionid=g5su4k00jcjidvwri1of%2fvos6r6xqgutqyvil8iniw4%3d&pq-origsite=360link&accountid=13876 [Last accessed on 2022 Dec 20].

26. Spoerk M, Arbeiter F, Koutsamanis I, *et al.*, 2021, Personalised urethra pessaries prepared by material extrusion-based additive manufacturing. *Int J Pharm*, 608: 121112.

https://doi.org/10.1016/j.ijpharm.2021.121112

27. Davis AY, Zhang Q, Wong JP, *et al.*, 2019, Characterization of volatile organic compound emissions from consumer level material extrusion 3D printers. *Build Environ*, 160: 106209.

https://doi.org/10.1016/j.buildenv.2019.106209

28. Vidakis N, Petousis M, Michailidis N, *et al.*, 2023, Polyethylene glycol and polyvinylpyrrolidone reduction agents for medical grade polyamide 12/silver nanocomposites development for material extrusion 3D printing: Rheological, thermomechanical, and biocidal performance. *React Funct Polym*, 190: 105623.

https://doi.org/10.1016/j.reactfunctpolym.2023.105623

29. Yang H, Lim JC, Liu Y, *et al.*, 2017, Performance evaluation of ProJet multi-material jetting 3D printer. *Virtual Phys Prototyp*, 12: 95–103.

https://doi.org/10.1080/17452759.2016.1242915

30. Mora S, Pugno NM, Misseroni D, 2022, 3D printed architected lattice structures by material jetting. *Mater Today*, 59: 107–132.

https://doi.org/10.1016/j.mattod.2022.05.008

31. Gülcan O, Günaydın K, Tamer A, 2021, The state of the art of material jetting-a critical review. *Polymers* (*Basel*), 13: 2829.

https://doi.org/10.3390/polym13162829

32. Moore JP, Williams CB, 2015, Fatigue properties of parts printed by PolyJet material jetting. *Rapid Prototyp J*, 21: 675–685.

https://doi.org/10.1108/RPJ-03-2014-0031

33. Milovanović A, Sedmak A, Golubović Z, *et al.*, 2021, The effect of time on mechanical properties of biocompatible photopolymer resins used for fabrication of clear dental aligners. *J Mech Behav Biomed Mater*, 119: 104494.

https://doi.org/10.1016/j.jmbbm.2021.104494

34. Golhin AP, Srivastava C, Strandlie A, *et al.*, 2023, Effects of accelerated aging on the appearance and mechanical performance of materials jetting products. *Mater Des*, 228: 111863.

https://doi.org/10.1016/j.matdes.2023.111863

35. Sing SL, Yeong WY, 2020, Laser powder bed fusion for metal additive manufacturing: Perspectives on recent developments. *Virtual Phys Prototyp*, 15: 359–370.

https://doi.org/10.1080/17452759.2020.1779999

36. Sing SL, An J, Yeong WY, *et al.*, 2016, Laser and electron-beam powder-bed additive manufacturing of metallic implants: A review on processes, materials and designs. *J Orthop Res*, 34: 369–385.

https://doi.org/10.1002/jor.23075

37. Awad A, Fina F, Goyanes A, *et al.*, 2021, Advances in powder bed fusion 3D printing in drug delivery and healthcare. *Adv Drug Deliv Rev*, 174: 406–424.

https://doi.org/10.1016/j.addr.2021.04.025

38. Goodridge RD, Ziegelmeier S, 2017, Powder bed fusion of polymers. In: Laser Additive Manufacturing. United Kingdom: Woodhead Publishing. p. 181–204.

https://doi.org/10.1016/B978-0-08-100433-3.00007-5

39. Grasso ML, Colosimo BM, 2017, Process defects and *in situ* monitoring methods in metal powder bed fusion: A review. *Meas Sci Technol*, 28: 044005.

https://doi.org/10.1088/1361-6501/aa5c4f

40. Liverani E, Toschi S, Ceschini L, *et al.*, 2017, Effect of selective laser melting (SLM) process parameters on microstructure and mechanical properties of 316L austenitic stainless steel. *J Mater Process Technol*, 249: 255–263.

https://doi.org/10.1016/j.jmatprotec.2017.05.042

41. Zhong Y, Rännar LE, Wikman S, *et al.*, 2017, Additive manufacturing of ITER first wall panel parts by two approaches: Selective laser melting and electron beam melting. *Fusion Eng Des*, 116: 24–33.

https://doi.org/10.1016/j.fusengdes.2017.01.032

42. Romedenne M, Pillai R, Kirka M, *et al.*, 2020, High temperature air oxidation behavior of Hastelloy X processed by electron beam melting (EBM) and selective laser melting (SLM). *Corros Sci*, 171: 108647.

https://doi.org/10.1016/j.corsci.2020.108647

43. Bhavar V, Kattire P, Patil V, *et al.*, 2014, A Review on Powder Bed Fusion Technology of Metal Additive Manufacturing. Boca Raton: CRC Press.

44. Zhao X, Li S, Zhang M, *et al.*, 2016, Comparison of the microstructures and mechanical properties of Ti-6Al-4V fabricated by selective laser melting and electron beam melting. *Mater Des*, 95: 21–31.

https://doi.org/10.1016/j.matdes.2015.12.135

45. Monti C, Turani M, Papis K, *et al.*, 2023, A new Al-Cu alloy for LPBF developed via ultrasonic atomization. *Mater Des*, 229: 111907.

https://doi.org/10.1016/j.matdes.2023.111907

46. Xiao F, Shu D, Wang D, *et al.*, 2023, Effect of Zn content on the formability and aging precipitation of Al-Zn-Mg-Cu-Nb alloys prepared by LPBF. *J Mater Res Technol*, 25: 6338–6355.

https://doi.org/10.1016/j.jmrt.2023.07.057

47. Pilipović A, 2022, Chapter 11-sheet lamination. In: Izdebska-Podsiadły J, editor. Polymers for 3D Printing, Plastics Design Library. Norwich, NY: William Andrew Publishing. p. 127–136.

https://doi.org/10.1016/B978-0-12-818311-3.00008-2

48. Gibson I, Rosen DW, Stucker B, 2010, Sheet lamination processes. In: Additive Manufacturing Technologies: Rapid Prototyping to Direct Digital Manufacturing. Boston, MA: Springer US. p. 223–252.

https://doi.org/10.1007/978-1-4419-1120-9_8

49. Gibson I, Rosen D, Stucker B, *et al.*, 2021, Sheet lamination. In: Khorasani M, editor. Additive Manufacturing Technologies. Cham: Springer International Publishing. p. 253–283.

https://doi.org/10.1007/978-3-030-56127-7_9

50. You X, Tan Y, Takeyama M, *et al.*, 2023, Fabrication of a turbine disk alloy by electron beam sheet lamination and investigation on the improved high temperature creep performance. *J Mater Sci Technol*, 143: 216–233.

https://doi.org/10.1016/j.jmst.2022.10.013

51. Piedra-Cascón W, Krishnamurthy VR, Att W, *et al.*, 2021, 3D printing parameters, supporting structures, slicing, and post-processing procedures of vat-polymerization additive manufacturing technologies: A narrative review. *J Dent*, 109: 103630.

https://doi.org/10.1016/j.jdent.2021.103630

52. Pagac M, Hajnys J, Ma QP, *et al.*, 2021, A review of vat photopolymerization technology: Materials, applications, challenges, and future trends of 3D printing. *Polymers (Basel)*, 13: 598.

https://doi.org/10.3390/polym13040598

53. Maines EM, Porwal MK, Ellison CJ, *et al.*, 2021, Sustainable advances in SLA/DLP 3D printing materials and processes. *Green Chem*, 23: 6863–6897.

https://doi.org/10.1039/D1GC01489G

54. Tai XY, Zhakeyev A, Wang H, *et al.*, 2019, Accelerating fuel cell development with additive manufacturing technologies: State of the art, opportunities and challenges. *Fuel Cells*, 19: 636–650.

https://doi.org/10.1002/fuce.201900164

55. Sampson KL, Deore B, Go A, *et al.*, 2021, Multimaterial vat polymerization additive manufacturing. *ACS Appl Polym Mater*, 3: 4304–4324.

https://doi.org/10.1021/acsapm.1c00262

56. Zhang F, Zhu L, Li Z, *et al.*, 2021, The recent development of vat photopolymerization: A review. *Addit Manuf*, 48: 102423.

https://doi.org/10.1016/j.addma.2021.102423

57. Ng WL, Lee JM, Zhou M, *et al.*, 2020, Vat polymerization-based bioprinting-process, materials, applications and regulatory challenges. *Biofabrication*, 12: 022001.

https://doi.org/10.1088/1758-5090/ab6034

58. Milton LA, Viglione MS, Ong LJ, *et al.*, 2023, Vat photopolymerization 3D printed microfluidic devices for organ-on-a-chip applications. *Lab Chip*, 23: 3537–3560.

https://doi.org/10.1039/D3LC00094J

59. Bucciarelli A, Paolelli X, De Vitis E, *et al.*, 2022, VAT photopolymerization 3D printing optimization of high aspect ratio structures for additive manufacturing of chips towards biomedical applications. *Addit Manuf*, 60: 103200.

https://doi.org/10.1016/j.addma.2022.103200

60. Najeeb S, Zafar MS, Khurshid Z, *et al.*, 2016, Applications of polyetheretherketone (PEEK) in oral implantology and prosthodontics. *J Prosthodont Res*, 60: 12–19.

https://doi.org/10.1016/j.jpor.2015.10.001

61. Zhang Z, Breidt C, Chang L, *et al.*, 2004, Wear of PEEK composites related to their mechanical performances. *Tribol Int*, 37: 271–277.

https://doi.org/10.1016/j.triboint.2003.09.005

62. Tariverdian T, Navaei T, Milan PB, *et al.*, 2019, Chapter 16-functionalized polymers for tissue engineering and regenerative medicines. In: Mozafari M, Chauhan NP, editors. Advanced Functional Polymers for Biomedical Applications. Netherlands: Elsevier. p. 323–357.

https://doi.org/10.1016/B978-0-12-816349-8.00016-3

63. McKeen LW, 2009, Chapter 10-high-temperature polymers. In: The Effect of Creep and Other Time Related Factors on Plastics and Elastomers, in Plastics Design Library. 2nd ed. Boston: William Andrew Publishing. p. 337–372.

https://doi.org/10.1016/B978-0-8155-1585-2.50012-1

64. Siewert B, Plaza-Castro M, Sereno N, *et al.*, 2019, Chapter 20-applications of PEEK in the dental field. In: Kurtz SM, editor. PEEK Biomaterials Handbook, in Plastics Design Library. 2nd ed. Norwich, NY: William Andrew Publishing, p. 333–342.

https://doi.org/10.1016/B978-0-12-812524-3.00020-X

65. Katzer A, Marquardt H, Westendorf J, *et al.*, 2002, Polyetheretherketone--cytotoxicity and mutagenicity *in vitro*. *Biomaterials*, 23: 1749–1759.

https://doi.org/10.1016/S0142-9612(01)00300-3

66. Kurtz SM, 2019, Chapter 1-an overview of PEEK biomaterials. In: PEEK Biomaterials Handbook, in Plastics Design Library. 2nd ed. Norwich, NY: William Andrew Publishing. p. 3–9.

https://doi.org/10.1016/B978-0-12-812524-3.00001-6

67. Monich PR, Henriques B, de Oliveira AP, *et al.*, 2016, Mechanical and biological behavior of biomedical PEEK matrix composites: A focused review. *Mater Lett*, 185: 593–597.

https://doi.org/10.1016/j.matlet.2016.09.005

68. Verma S, Sharma N, Kango S, 2021, Developments of PEEK (polyetheretherketone) as a biomedical material: A focused review. *Eur Polym J*, 147: 110295.

https://doi.org/10.1016/j.eurpolymj.2021.110295

69. Singh R, Singh G, Singh J, *et al.*, 2020, 3D Printing of polyether-ether-ketone functional prototypes for engineering applications. In: Hashmi S, Choudhury IA, editors. Encyclopedia of Renewable and Sustainable Materials. Oxford: Elsevier. p. 207–214.

https://doi.org/10.1016/B978-0-12-803581-8.11543-7

70. Haleem A, Javaid M, 2019, Polyether ether ketone (PEEK) and its manufacturing of customised 3D printed dentistry parts using additive manufacturing. *Clin Epidemiol Glob Health*, 7: 654–660.

https://doi.org/10.1016/j.cegh.2019.03.001

71. Cicala G, Latteri A, Del Curto B, *et al.*, 2017, Engineering thermoplastics for additive manufacturing: A critical perspective with experimental evidence to support functional applications. *J Appl Biomater Funct Mater*, 15: 10–18.

https://doi.org/10.5301/jabfm.5000343

72. Manzoor F, Golbang A, Jindal S, *et al.*, 2021, 3D printed PEEK/HA composites for bone tissue engineering applications: Effect of material formulation on mechanical performance and bioactive potential. *J Mech Behav Biomed Mater*, 121: 104601.

https://doi.org/10.1016/j.jmbbm.2021.104601

73. Stepashkin AA, Chukov DI, Senatov FS, *et al.*, 2018, 3D-printed PEEK-carbon fiber (CF) composites: Structure and thermal properties. *Compos Sci Technol*, 164: 319–326.

https://doi.org/10.1016/j.compscitech.2018.05.032

74. Arif MF, Alhashmi H, Varadarajan KM, *et al.*, 2020, Multifunctional performance of carbon nanotubes and graphene nanoplatelets reinforced PEEK composites enabled via FFF additive manufacturing. *Compos B Eng*, 184: 107625.

https://doi.org/10.1016/j.compositesb.2019.107625

75. Zhang J, Su Y, Rao X, *et al.*, 2022, Additively manufactured polyether ether ketone (PEEK) skull implant as an alternative to titanium mesh in cranioplasty. *Int J Bioprint*, 9: 634.

https://doi.org/10.18063/ijb.v9i1.634

76. Zhang W, Liu L, Zhou H, *et al.*, 2023, Surface bisphosphonation of polyetheretherketone to manipulate immune response for advanced osseointegration. *Mater. Des*, 232: 112151.

https://doi.org/10.1016/j.matdes.2023.112151

77. Gao W, Han X, Sun D, *et al.*, 2023, Antibacterial properties of antimicrobial peptide HHC36 modified polyetheretherketone. *Front Microbiol*, 14: 1103956.

https://doi.org/10.3389/fmicb.2023.1103956

78. Liaw DJ, Wang KL, Huang YC, *et al.*, 2012, Advanced polyimide materials: Syntheses, physical properties and applications. *Prog Polym Sci*, 37: 907–974.

https://doi.org/10.1016/j.progpolymsci.2012.02.005

79. Polyimides. Available from: https://books.google.com/books/about/polyimides.html?hl=zh-cn&id=n7eigaukutic [Last accessed on 2022 Dec 07].

80. Weyhrich CW, Long TE, 2022, Additive manufacturing of high-performance engineering polymers: Present and future. *Polym Int*, 71: 532–536.

https://doi.org/10.1002/pi.6343

81. Guo Y, Ji Z, Zhang Y, *et al.*, 2017, Solvent-free and photocurable polyimide inks for 3D printing. *J Mater Chem A*, 5: 16307–16314.

https://doi.org/10.1039/C7TA01952A

82. Hegde M, Meenakshisundaram V, Chartrain N, *et al.*, 2017, 3D Printing all-aromatic polyimides using mask-projection stereolithography: Processing the nonprocessable. *Adv Mater*, 29: 1701240.

https://doi.org/10.1002/adma.201701240

83. Qin S, Jiang Y, Yang C, *et al.*, 2021, Three-dimensional printing of high-performance polyimide by direct ink writing of hydrogel precursor. *J Appl Polym Sci*, 138: 50636.

https://doi.org/10.1002/app.50636

84. Liu Z, Cai Y, Song F, *et al.*, 2022, Study on chemical graft structure modification and mechanical properties of photocured polyimide. *ACS Omega*, 7: 9582–9593.

    https://doi.org/10.1021/acsomega.1c06933

85. Gouzman I, Grossman E, Verker R, *et al.*, 2019, Advances in polyimide-based materials for space applications. *Adv Mater*, 31: 1807738.

    https://doi.org/10.1002/adma.201807738

86. Ye W, Wu W, Hu X, *et al.*, 2019, 3D printing of carbon nanotubes reinforced thermoplastic polyimide composites with controllable mechanical and electrical performance. *Compos Sci Technol*, 182: 107671.

    https://doi.org/10.1016/j.compscitech.2019.05.028

87. Yeh JW, Chen SK, Lin SJ, *et al.*, 2004, Nanostructured high-entropy alloys with multiple principal elements: Novel alloy design concepts and outcomes. *Adv Eng Mater*, 6: 299–303.

    https://doi.org/10.1002/adem.200300567

88. Wu Z, Bei H, Pharr GM, *et al.*, 2014, Temperature dependence of the mechanical properties of equiatomic solid solution alloys with face-centered cubic crystal structures. *Acta Mater*, 81: 428–441.

    https://doi.org/10.1016/j.actamat.2014.08.026

89. Dewangan SK, Mangish A, Kumar S, *et al.*, 2022, A review on High-Temperature Applicability: A milestone for high entropy alloys. *Eng Sci Technol Int J*, 35: 101211.

    https://doi.org/10.1016/j.jestch.2022.101211

90. Rong Z, Wang C, Wang Y, *et al.*, 2022, Microstructure and properties of FeCoNiCrX (X=Mn, Al) high-entropy alloy coatings. *J Alloys Compd*, 921: 166061.

    https://doi.org/10.1016/j.jallcom.2022.166061

91. Yeh JW, 2016, Overview of high-entropy alloys. In: Gao MC, Liaw PK, Zhang Y, *et al.*, editors. High-entropy Alloys: Fundamentals and Applications. Cham: Springer International Publishing. p. 1–19.

    https://doi.org/10.1007/978-3-319-27013-5_1

92. Senkov ON, Miracle DB, Chaput KJ, *et al.*, 2018, Development and exploration of refractory high entropy alloys-a review. *J Mater Res*, 33: 3092–3128.

    https://doi.org/10.1557/jmr.2018.153

93. Iroc LK, Tukac OU, Tanrisevdi BB, *et al.*, 2022, Design of oxygen-doped TiZrHfNbTa refractory high entropy alloys with enhanced strength and ductility. *Mater Des*, 223: 111239.

    https://doi.org/10.1016/j.matdes.2022.111239

94. Senkov ON, Wilks GB, Scott JM, *et al.*, 2011, Mechanical properties of $Nb_{25}Mo_{25}Ta_{25}W_{25}$ and $V_{20}Nb_{20}Mo_{20}Ta_{20}W_{20}$ refractory high entropy alloys. *Intermetallics*, 19: 698–706.

    https://doi.org/10.1016/j.intermet.2011.01.004

95. Senkov ON, Senkova SV, Woodward C, 2014, Effect of aluminum on the microstructure and properties of two refractory high-entropy alloys. *Acta Mater*, 68: 214–228.

    https://doi.org/10.1016/j.actamat.2014.01.029

96. Senkov ON, Woodward CF, 2011, Microstructure and properties of a refractory $NbCrMo_{0.5}Ta_{0.5}TiZr$ alloy. *Mater Sci Eng A*, 529: 311–320.

    https://doi.org/10.1016/j.msea.2011.09.033

97. Liu D, Yu Q, Kabra S, *et al.*, 2022, Exceptional fracture toughness of CrCoNi-based medium- and high-entropy alloys at 20 kelvin. *Science*, 378: 978–983.

    https://doi.org/10.1126/science.abp8070

98. Chen S, Tong Y, Liaw PK, 2018, Additive manufacturing of high-entropy alloys: A review. *Entropy*, 20: 937.

    https://doi.org/10.3390/e20120937

99. Chen Y, Zhou Q, 2022, Directed energy deposition additive manufacturing of CoCrFeMnNi high-entropy alloy towards densification, grain structure control and improved tensile properties. *Mater Sci Eng A*, 860: 144272.

    https://doi.org/10.1016/j.msea.2022.144272

100. Zhou R, Liu Y, Zhou C, *et al.*, 2018, Microstructures and mechanical properties of C-containing FeCoCrNi high-entropy alloy fabricated by selective laser melting. *Intermetallics*, 94: 165–171.

     https://doi.org/10.1016/j.intermet.2018.01.002

101. Ren J, Zhang Y, Zhao D, *et al.*, 2022, Strong yet ductile nanolamellar high-entropy alloys by additive manufacturing. *Nature*, 608: 62–68.

     https://doi.org/10.1038/s41586-022-04914-8

102. Lin D, Xu L, Li X, *et al.*, 2020, A Si-containing FeCoCrNi high-entropy alloy with high strength and ductility synthesized *in situ* via selective laser melting. *Addit Manuf*, 35: 101340.

     https://doi.org/10.1016/j.addma.2020.101340

103. Gao X, Yu Z, Hu W, *et al.*, 2020, *In situ* strengthening of CrMnFeCoNi high-entropy alloy with Al realized by laser additive manufacturing. *J. Alloys Compd*, 847: 156563.

     https://doi.org/10.1016/j.jallcom.2020.156563

104. Zhang M, Zhou X, Wang D, *et al.*, 2022, Additive manufacturing of *in-situ* strengthened dual-phase AlCoCuFeNi high-entropy alloy by selective electron beam melting. *J. Alloys Compd*, 893: 162259.

     https://doi.org/10.1016/j.jallcom.2021.162259

105. Karthik GM, Panikar S, Ram GD, *et al.*, 2017, Additive manufacturing of an aluminum matrix composite reinforced with nanocrystalline high-entropy alloy particles. *Mater Sci Eng A*, 679: 193–203.

     https://doi.org/10.1016/j.msea.2016.10.038

106. Li J, Xiang S, Luan H, *et al.*, 2019, Additive manufacturing of high-strength CrMnFeCoNi high-entropy alloys-based composites with WC addition. *J Mater Sci Technol*, 35: 2430–2434.

https://doi.org/10.1016/j.jmst.2019.05.062

107. Amar A, Li J, Xiang S, *et al.*, 2019, Additive manufacturing of high-strength CrMnFeCoNi-based high entropy alloys with TiC addition. *Intermetallics*, 109: 162–166.

https://doi.org/10.1016/j.intermet.2019.04.005

108. AMS4999: Titanium Alloy Laser Deposited Products-6al-4v-Annealed-SAE International. Available from: https://www.sae.org/standards/content/ams4999 [Last accessed on 2022 Dec 10].

109. AMS4999A: Titanium Alloy Direct Deposited Products 6Al-4V Annealed-SAE International. Available from: https://www.sae.org/standards/content/ams4999a [Last accessed on 2022 Dec 10].

110. Committee F42 on Additive Manufacturing Technologies. Available from: https://www.astm.org/committee-f42 [Last accessed on 2022 Dec 10].

111. Committee F42 Subcommittees. Available from: https://www.astm.org/get-involved/technical-committees/committee-f42/subcommittee-f42 [Last accessed on 2022 Dec 10].

112. ASTM Committee F42, 2021, ASTM F3049-14 (2021) Standard Guide for Characterizing Properties of Metal Powders Used for Additive Manufacturing Processes. United States: ASTM.

https://doi.org/10.1520/F3049-14R21

113. ASTM Committee F42, 2021, ASTM F3091/F3091M-14(2021) Standard Specification for Powder Bed Fusion of Plastic Materials. United States: ASTM.

https://doi.org/10.1520/F3091_F3091M-14R21

114. ASTM Committee F42, 2021, ASTM F3055-14a(2021) Standard Specification for Additive Manufacturing Nickel Alloy (UNS N07718) with Powder Bed Fusion. United States: ASTM.

https://doi.org/10.1520/F3055-14AR21

115. ASTM Committee F42, 2021, ASTM F3056-14(2021) Standard Specification for Additive Manufacturing Nickel Alloy (UNS N06625) with Powder Bed Fusion. United States: ASTM.

https://doi.org/10.1520/F3056-14R21

116. ASTM Committee F42, 2021, ASTM F2924-14(2021) Standard Specification for Additive Manufacturing Titanium-6 Aluminum-4 Vanadium with Powder Bed Fusion. United States: ASTM.

https://doi.org/10.1520/F2924-14R21

117. ASTM Committee F42, 2021, ASTM F3001-14(2021) Standard Specification for Additive Manufacturing Titanium-6 Aluminum-4 Vanadium ELI (Extra Low Interstitial) with Powder Bed Fusion. United States: ASTM.

https://doi.org/10.1520/F3001-14R21

118. ASTM Committee F42, 2016, ASTM F3187-16 Standard Guide for Directed Energy Deposition of Metals. United States: ASTM.

https://doi.org/10.1520/F3187-16

119. ISO/TC 261-Additive Manufacturing. ISO. Available from: https://www.iso.org/committee/629086.html [Last accessed on 2022 Dec 10].

120. Additive manufacturing-material Extrusion-based Additive Manufacturing of Plastic Materials-part 1: Feedstock Materials. Available from: https://www.astm.org/f3241-20.html [Last accessed on 2022 Dec 10].

121. CORDIS European Commission. Available from: https://cordis.europa.eu/project/id/319167/reporting [Last accessed on 2022 Dec 10].

122. TC562 National Additive Manufacturing Standardization Technical Committee. Available from: https://std.samr.gov.cn/search/orgdetailviewcnf?data_id=da4c780fa8756d08e05397be0a0a6dff [Last accessed on 2022 Dec 10].

123. Dubov A, Ruben S, 2022, Material development standards and methods for additive manufacturing in construction to meet building code requirements for certification. In: Progress in Additive Manufacturing 2020. United States: ASTM International. p. 375–385.

https://doi.org/10.1520/STP163720200103

124. Erps T, Foshey M, Luković MK, *et al.*, 2021, Accelerated discovery of 3D printing materials using data-driven multiobjective optimization. *Sci Adv*, 7: eabf7435.

https://doi.org/10.1126/sciadv.abf7435

125. Goh GD, Huang X, Huang S, *et al.*, 2023, Data imputation strategies for process optimization of laser powder bed fusion of Ti6Al4V using machine learning. *Mater Sci Addit Manuf*, 2: 50.

https://doi.org/10.36922/msam.50

126. Bagheri A, Cremona C, 2020, Formulation of mix design for 3D printing of geopolymers: A machine learning approach. *Mater Adv*, 1: 720–727.

https://doi.org/10.1039/D0MA00036A

127. Analytical Investigation of Aerosol Jet Printing. Available from: https://www-tandfonline-com.libproxy1.nus.edu.sg/doi/full/10.1080/02786826.2014.940439 [Last accessed on 2023 Sep 04].

128. Goh GL, Zhang H, Goh GD, *et al.*, 2022, Multi-objective optimization of intense pulsed light sintering process for aerosol jet printed thin film. *Mater Sci Addit Manuf*, 1: 10.

https://doi.org/10.36922/msam.26

129. Jiang P, Ji Z, Zhang X, *et al.*, 2018, Recent advances in direct ink writing of electronic components and functional devices. *Prog Addit Manuf*, 3: 65–86.

https://doi.org/10.1007/s40964-017-0035-x

ACCSCIENCE PUBLISHING

Materials Science in Additive Manufacturing

ORIGINAL RESEARCH ARTICLE

Modeling and experimental investigation of fiber orientation in cast and 3D-printed cementitious composites

Mingyang Li[1], Dong Zhang[2], Teck Neng Wong[1], Ming Jen Tan[1], and Yiwei Weng[3]*

[1]Singapore Centre for 3D Printing, Nanyang Technological University, Singapore

[2]Sustainable and Innovation Bridge Engineering Research Centre, College of Civil Engineering, Fuzhou University, China

[3]Department of Building and Real Estate, The Hong Kong Polytechnic University, Hong Kong, China

Abstract

Fiber orientation is process-related and has significant impacts on material performance. However, existing studies only consider the impact of individual factors on the fiber orientation, either boundary impacts or flow field impacts. This work aims to study fiber orientation by considering the combined impact of these two factors. Analytical models were first constructed, which revealed that when the flow of material is negligible, fiber orientation is impacted by the boundary conditions. When the flow field is non-negligible, fiber orientation is affected by the direction of flow streamlines. Specimens were then prepared using fluorescence image processing and μ-computed tomography scanning for fiber orientation analysis. The results indicate that fiber orientation could be controlled by varying boundary constraints and flow fields. Mechanical results reveal that when the designed condition achieves directional-orientated fibers, the mechanical property of specimens could be enhanced with the applied stress direction being the same as the fiber orientation. This work provides a novel insight to tailor fiber-reinforced cementitious material properties by designing the boundary constraints and flow fields in the cast and printing processes.

Keywords: Additive manufacturing; Fiber orientation; Flow field; Boundary constraint; Mechanical property

1. Introduction

Fiber orientation plays a key role in the mechanical performance of fiber-reinforced composites (FRCs). The addition of short fibers in brittle concrete matrix contributes to the fiber bridging effect, which could improve the energy absorption capacity and crack resistance of plain concrete[1]. Wu and Li's[2] work reveals that material mechanical property is affected by the fiber orientation. With an increasing inclination angle, which represents the angle between the fiber orientation and the loading force in the tensile test, the *in situ* fiber strength decreases, leading to a deterioration of the fiber-bridging effect[3].

Fiber orientation is process-related in the material. In sprayable FRCs, fibers are distributed in a two-dimensional plane[4,5]. In extrudable FRCs, on the other hand,

***Corresponding author:**
Yiwei Weng
(yiwei.weng@polyu.edu.hk)

Citation: Li M, Zhang D, Wong TN, *et al.*, 2023, Modeling and experimental investigation of fiber orientation in cast and 3D-printed cementitious composites. *Mater Sci Add Manuf*, 2(3): 1603.
https://doi.org/10.36922/msam.1603

Received: August 15, 2023

Accepted: September 9, 2023

fibers are distributed along the extrusion direction due to the impact of flow profile development[6-8]. In cast FRCs, the boundary constraint of molds determines the fiber orientation. Theoretical models, as presented by Lu and Leung[9], address the 1D boundary constraint of molds. In 3D printable concrete, Hamhach and Volkmer[10] proposed that fiber orientation exhibits a directional distribution, which aligns with the printing direction. Figueiredo *et al.*[11] suggested that fibers mainly orientate themselves diagonally within the cross-section plane of printed filaments rather than parallel to the print path.

However, as discussed in detail in Section 2, the limitations of previous works lie in the insufficient exploration and investigation of the impacts of boundary constraints of molds and material flow field conditions on fiber orientation. Lu and Leung[9] studied the influence of boundary constraints of molds on fiber orientation in a 1D case; however, they did not obtain an analytical solution, and thus, they could not extend their findings to more practical 2D and 3D cases. Stahli *et al.*[7] noted the impact of flow profile on fiber orientation; however, they considered fiber orientation in the plug flow region to remain unchanged, and the connection between fiber orientation and flow field cannot be well established.

This work was motivated by the abovementioned research gap. The impacts of boundary constraints and flow field on the fiber orientation and their corresponding impacts on mechanical properties were investigated. Analytical models were constructed to analyze and predict fiber orientation with respect to the boundary constraint and flow field, respectively. In the experimental part, the cast and printed specimens were prepared for validation. Directional casting (DC) and random casting (RC) processes were adopted to fabricate casting specimens, obtaining different types of flow fields while considering boundary constraints. Printed specimens were fabricated using different printing configurations to achieve various conditions of boundary constraints and flow fields. Fiber orientation was then analyzed through fluorescence image processing and μ-computed tomography (μ-CT) scanning. Finally, the impacts of fiber orientation on the mechanical properties were evaluated.

The remainder of the article is organized as follows. In Section 2, analytical models of the impacts of 1D, 2D, and 3D boundary constraints on the fiber orientation are constructed, and the impacts of the boundary constraint and the flow field on fiber orientation are discussed and elaborated upon. In Section 3, the experimental design for casting, 3D printing process, and characterization methods is presented. In Section 4, the results of the tests are reported for cast and 3D-printed specimens. In Section 5, the results are discussed on the impact of printing parameters on the boundary constraints, flow fields, and fiber orientations. The mechanical performance of the specimens has also been investigated, and the results are reported here. In Section 6, a summary of this work is provided, and the future work is sketched.

2. Theory and modeling

2.1. Impacts of boundary constraints on fiber orientation

Theoretically, with no flow in materials, the fiber dispersion should follow the idealized random distribution, in which fibers have an equal probability of pointing to any direction in three-dimensional space. However, this theoretical randomness is often not achieved in practice. This is due to:

(i) The casting process, which induces preferential flow of the paste in the horizontal direction, causing the fibers to follow a distribution between 2D and 3D.

(ii) The limited freedom of fibers near the surfaces to rotate in their corresponding dimension within the specimen.

Lu and Leung[9] have stated three different scenarios based on 1D boundary constraints without providing analytical solutions for fiber orientation. In the following sections, these three scenarios will be briefly reviewed, the analytical solutions for fiber orientation will be derived, and the same approach will be extended to 2D and 3D cases.

2.1.1. One-dimensional boundary constraint

As shown in Figure 1, a 1D boundary constraint indicates that a restriction exists on one pair of opposite surfaces, such as the top and bottom surfaces. z is defined as the distance between the center of the fiber and the restricted surface of the member, θ is the inclination angle, and l_f is the fiber length. When the fiber is too close to the restricted surface, it may intersect with the surface, and thus, the orientation direction is limited depending on its distance from the surface. Otherwise, if the fiber is not in close proximity to the restricted surface, it is free in the matrix. Hence, to differentiate whether the fibers intersect with the surface, two cases are discussed here.

The first case ($z < l_f/2$) is schematically shown in Region 1 (Figure 2). Two different scenarios are discussed. When the fibers are at a small inclination angle θ, there is no intersection between the fiber and the boundary. As shown by the bold dashed line in Figure 2A**,** a circular locus is

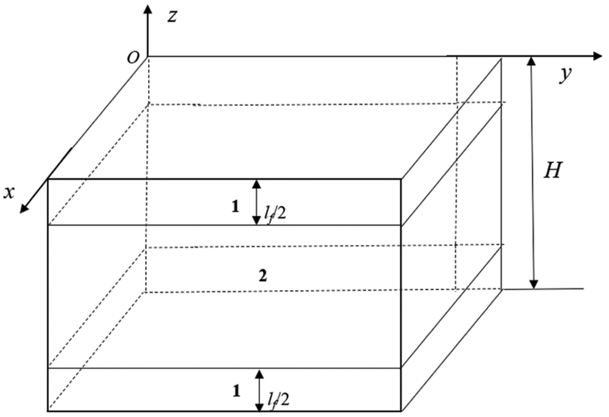

Figure 1. Divided regions of 1D boundary constraint.

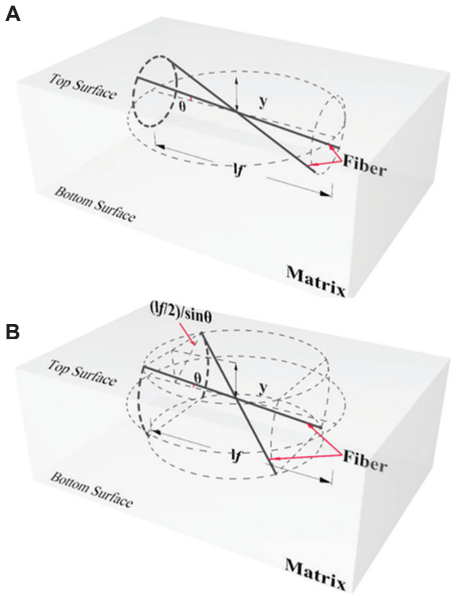

Figure 2. (A and B) Schematic of fiber orientation in 1D boundary constraint[9]. Image reprinted with permission, Copyright © 2017, Elsevier Ltd.

formed through the left endpoints of fibers. In this case, the circumference of the locus is given by Equation I[9]:

$$P(z,\theta)=\left(\frac{l_f}{2}\right)\sin\theta\cdot 2\pi \quad \text{when } \theta \le \arcsin\left(\frac{z}{l_f/2}\right) \tag{I}$$

Otherwise, as shown in Figure 2B, fibers are restrained by the boundary when the fiber inclination angle θ is larger than a critical angle. As can be seen from the bold dashed line in Figure 2B, the left endpoints of such fibers form a locus composed of two arcs, as shown by the bold dashed line. The total length of the two arcs is given by Equation II[9]:

$$P(z,\theta)=\left\{\begin{aligned}&\left(\frac{l_f}{2}\right)\sin\theta\cdot\\&2\pi-4\arccos\left[\frac{z}{\left(l_f/2\right)\sin\theta}\right]\end{aligned}\right\} \quad \text{when } \theta \le \arcsin\left(\frac{z}{l_f/2}\right) \tag{II}$$

Afterward, the second region is illustrated in Figure 1 (region 2). Under this condition, the fiber is free within the matrix, and the length of the arc formed by the end of the fiber can be expressed as follows[9]:

$$P(z,\theta)=\left(\frac{l_f}{2}\right)\sin\theta\cdot 2\pi \tag{III}$$

Let $w=z/(l_f/2)$ be the dimensionless coordinate; Equations I–III can be combined as

$$P(w,\theta)=\begin{cases}\sin\theta\cdot 2\pi & w>1 \text{ or } w\ge\sin\theta\\ \sin\theta\cdot\left[2\pi-4\arccos\left(\dfrac{w}{\sin\theta}\right)\right] & w<1 \text{ and } w<\sin\theta\end{cases} \tag{IV}$$

Then, the number of fibers can be calculated through the arc circumference[12]. When the fiber intersects with the boundary, fiber numbers can be quantified as follows:

$$\begin{aligned}&\text{Num}\left(z,\left[\theta,\theta+d\theta\right]\right)\\&=N\cdot 2\cdot\frac{l_f\cos\theta}{2}\cdot\frac{P(z,\theta)d\theta}{\int_0^{\pi/2}P(z,\theta)d\theta}=\frac{ZV_f\cos\theta}{\pi r_f^2}\cdot\\&\frac{P(w,\theta)d\theta}{\int_0^{\pi/2}P(w,\theta)d\theta}\end{aligned} \tag{V}$$

Where N is the number of fibers per unit volume, which can be computed by $N=ZV_f/\pi l_f r_f^2$. Here, V_f and r_f represent the volume fraction and radius of the fiber, respectively. The total number of fibers crossing this plane at a given angle can be integrated through the thickness:

$$\begin{aligned}&\text{Num}\left(\left[0,Z\right],\left[\theta,\theta+d\theta\right]\right)\\&=2\int_0^{Z/2}\text{Num}\left(z,\left[\theta,\theta+d\theta\right]\right)dz=\frac{2ZV_f\cos\theta}{\pi r_f^2}\\&\int_0^{Z/l_f}\left[\frac{P(w,\theta)d\theta}{\int_0^{\pi/2}P(w,\theta)d\theta}\right]dw\end{aligned} \tag{VI}$$

Depending on the member's dimensions, Equation VI has three different conditions:

(iii). When $Z/l_f \leq \sin\theta$

$$\text{Num}\left(\left[0,Z\right],\left[\theta,\theta+d\theta\right]\right)$$

$$=\frac{2ZV_f\sin\theta\cos\theta d\theta}{\pi^2 r_f^2}i\left\{\begin{array}{l}\text{Li}_2\left(1-\exp\left[2i\arcsin\left(\frac{Z}{l_f\sin\theta}\right)\right]\right)\Big)\\ -\arcsin^2\left(\frac{Z}{l_f\sin\theta}\right)\end{array}\right\} \tag{VII}$$

(iv). When $Z/l_f > \sin\theta$ and $Z/l_f \leq 1$

$$\text{Num}\left(\left[0,Z\right],\left[\theta,\theta+d\theta\right]\right)$$

$$=\frac{2ZV_f\sin\theta\cos\theta d\theta}{\pi^2 r_f^2}\left\{\begin{array}{l}i\left[\text{Li}_2\left(1-\exp\left(i\pi\right)\right)-\left(\frac{\pi}{2}\right)^2\right]\\ +\pi\ln\left(\frac{Z}{l_f\sin\theta}\right)\end{array}\right\} \tag{VIII}$$

(v). When $Z/l_f > 1$

$$\text{Num}\left(\left[0,Z\right],\left[\theta,\theta+d\theta\right]\right)$$

$$=\frac{2ZV_f\sin\theta\cos\theta d\theta}{\pi^2 r_f^2}\left\{\begin{array}{l}i\left[\text{Li}_2\left(1-\exp\left(i\pi\right)\right)-\left(\frac{\pi}{2}\right)^2\right]\\ +\pi\left[\ln\left(\frac{1}{\sin\theta}\right)+\frac{Z}{l_f}-1\right]\end{array}\right\} \tag{IX}$$

Where $\text{Li}_2(t)$ is the polylogarithm with order 2 and argument t. Although Equations VII–IX have complex formations, their values are real numbers. The detailed integration for the 1D case is provided in Appendix A.

2.1.2. Two-dimensional and three-dimensional boundary constraints

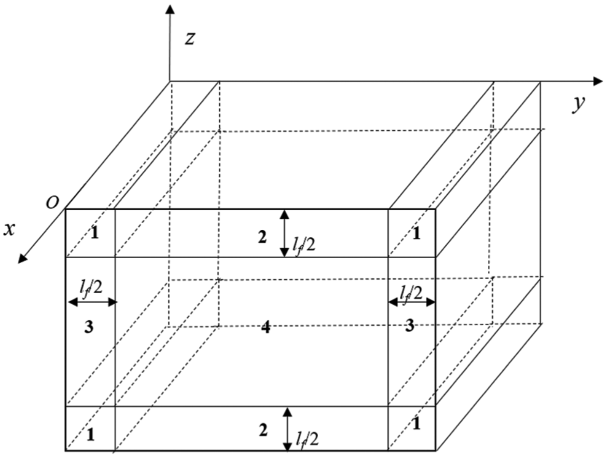

Figure 3. Divided regions for the 2D boundary constraint.

The 2D boundary constraint is shown in Figure 3. Similar to the 1D case, the coordinates can be non-dimensionalized by letting $v=y/(l_f/2)$ and $w=z/(l_f/2)$, where y and z represent the distance between the center of the fiber and the boundary in the width and thickness directions, respectively. Four different cases are discussed in this section, that is, Region 1 (v<1 and w<1), Region 2 (v<1 and w≥1), Region 3 (v≥1 and w<1), and Region 4 (v≥1 and w≥1). Note that for different cases, Regions 2, 3, and 4 may not exist. For Region 1, the total length of the distribution arc is given by:

$$P\left(v,w,\theta\right)=$$

$$\begin{cases}\sin\theta\cdot 2\pi & \theta\leq a\\ \sin\theta\cdot\left\{2\pi-4\arccos\left[\frac{\min\left(v,w\right)}{\sin\theta}\right]\right\} & a<\theta\leq b\\ \sin\theta\cdot\left[\begin{array}{l}2\pi-4\arccos\left(\frac{v}{\sin\theta}\right)\\ -4\arccos\left(\frac{w}{\sin\theta}\right)\end{array}\right] & b<\theta \text{ and } \sin\theta\leq c\\ 0 & \sin\theta>c\end{cases} \tag{X}$$

Where $a=\arcsin\left[\min\left(v,w\right)\right]$, $b=\arcsin\left[\max\left(v,w\right)\right]$, $c=\sqrt{v^2+w^2}$.

For Regions 2 and 3, the entire lengths of the distribution arc are:

$$P\left(v,w,\theta\right)=\begin{cases}\sin\theta\cdot 2\pi\\ \theta\leq\arcsin\left[\min\left(v,w\right)\right]\\ \sin\theta\cdot\left\{2\pi-4\arccos\left[\frac{\min\left(v,w\right)}{\sin\theta}\right]\right\}\\ \theta>\arcsin\left[\min\left(v,w\right)\right]\end{cases} \tag{XI}$$

For Region 4, the total length of the distribution arc is expressed as Equation III. Similar to the 1D case, the total number of fibers crossing a specific cross-section plane at a given angle can be integrated through the cross-section:

$$
\begin{aligned}
&\mathrm{Num}\left(\left[0,Y\right],\left[0,Z\right],\left[\theta,\theta+d\theta\right]\right)\\
&=4\int_0^{Z/l_f}\int_0^{Y/l_f}\mathrm{Num}\left(v,w,\left[\theta,\theta+d\theta\right]\right)dvdw=\frac{4YZV_f\cos\theta d\theta}{\pi r_f^2}\cdot\\
&\int_0^{Z/l_f}\int_0^{Y/l_f}\left[\frac{P\left(v,w,\theta\right)d\theta}{\int_0^{\pi/2}P\left(v,w,\theta\right)d\theta}\right]dvdw \qquad \text{(XII)}
\end{aligned}
$$

The detailed integration for the 2D case is provided in Appendix B, and for the 3D case in Appendix C. The completeness of conditions of the 3D case is demonstrated in Appendix D. To best estimation of the authors, 2D and 3D cases are unlikely to have analytical solutions due to the arctan terms in the denominator of the Region 1 integrations, and a numerical method would be required to compute the fiber orientation distribution for 2D and 3D cases.

2.2. Effects of flow field on fiber orientation

Streamlines in a flow field are curves tangent to the velocity vector[13]. In a steady-state flow field, a small motion path line of particles is identical to the streamline passing through its start point. When considering a piece of fiber within such a flow field, its different sections move at different velocities described by different streamlines. In most cases, these streamlines exhibit different velocity magnitudes, causing the fiber to rotate in response to the applied torque, as shown in Figure 4. Consequently, the entire fiber flows following one streamline when it reaches a steady state.

Since cementitious materials used in 3D printing typically exhibit high viscosity, the flow conditions are usually considered laminar[14]. In addition, the fiber content used in cementitious material is relatively small, typically ranging from 0.5% to 2% by volume[15,16]. Therefore, it is reasonable to assume that all fibers eventually follow the streamlines of cementitious materials in a flow field, resulting in the same fiber orientation as the streamline orientation. However, given that the velocity differences between streamlines can be small, the transient fiber orientation is influenced by the initial state and the development of the flow field.

3. Materials and methods

3.1. Materials and mixing process

The mixture proportions used in this study are listed in Table 1. The mortar mixture consists of Ordinary Portland Cement (OPC, ASTM Type I, Grade 42.5, Singapore), silica fume (SF, undensified, Grade 940), fine sand, fly ash (FA, Class F), water, superplasticizer, and polyvinyl alcohol (PVA) fibers. The PVA fibers have a length of 8 mm and a diameter of 40 μm, with detailed mechanical performance information available in Weng *et al.*[17]. Particle size distribution and chemical composition data for cement, SF, and FA can be found in other previous studies[18,19]. The gradation curve of fine sand used in this study is depicted in Figure 5.

Hobart mixer X200L with a 20 L capacity was utilized for the mixing process. The powders were dry mixed for 1 min with speed I (33 rpm). Subsequently, the superplasticizer was added to the water, and the resulting liquid mixture was added to the dry powders. Afterward, the mixing process continued for 1 min at speed I (33 rpm), followed by 1 min at speed II (61 rpm). Finally, speed III (113 rpm) was applied for 2 min.

3.2. Preparation of cast specimens

Cast specimens were prepared using different casting approaches to explore the impacts of flow field conditions

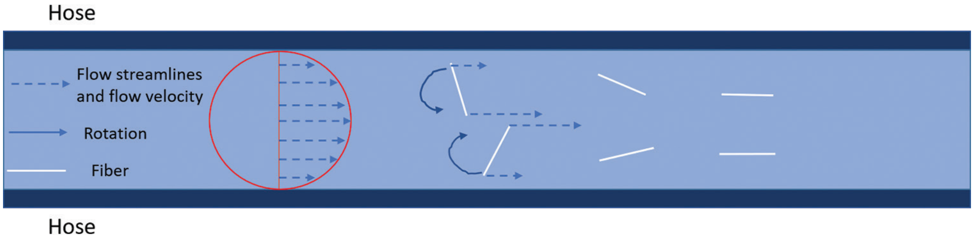

Figure 4. Fiber in a flow field eventually flows along a streamline.

Table 1. Mixture proportion

Ordinary Portland Cement	Fly ash	Sand	Water	Silica fume	Fiber[1]	Superplasticizer
1.0	1.0	0.8	1.1	0.2	1.0	0.2

Notes: The values of the ingredients are expressed as a weight proportion of cement content.
[1] Fiber content is expressed as the volume fraction of the mix, while all the other ingredients are expressed as the weight proportion.

and boundary constraints on fiber orientation and mechanical properties. The first approach, known as the DC process, involved filling the casting mold with materials from one end to the other through the flow of material, as shown in Figure 6A. The dog-bone mold has dimensions of 150 mm×35 mm×15 mm in the gauge length area, with an overall length of 350 mm. The second approach, referred to as the RC process, involved manually filling the mold with materials in a random manner. The specimen's surface was then flattened using a scraper, followed by applying vibration to consolidate the material, as illustrated in Figure 6B. The rectangular mold measures 400 mm × 100 mm × 10 mm (L × W × D). Finally, specimens were moisture-cured in a climate chamber at 95 ± 5% relative humidity and 26 ± 2°C for 28 days.

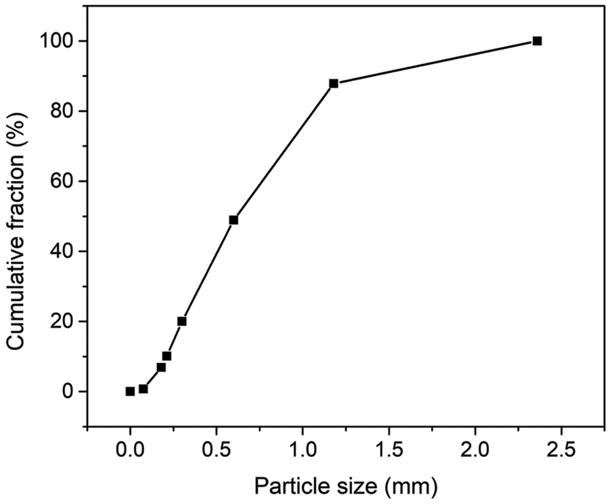

Figure 5. Gradation curve of fine sand.

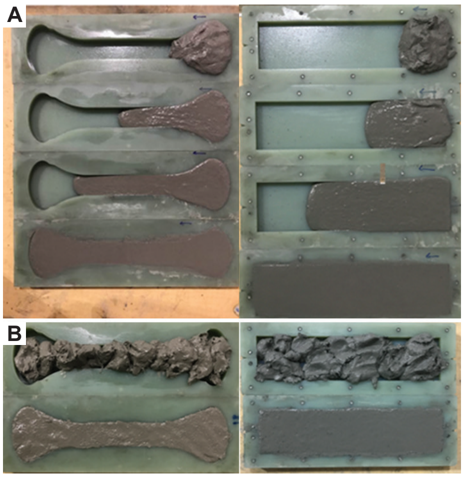

Figure 6. (A) Directional casting process, dog-bone specimens for the tensile test, and rectangular specimens for the flexural test. (B) Random casting process.

3.3. Preparation of printing specimens

3.3.1. Relation between printing parameters, filament dimension, and flow field

Extrusion-based 3D concrete printing (3DCP) is another novel technology in the construction sector, which can achieve more precise control of the flow field compared to the DC and RC processes, as discussed in Section 3.2. The material flow field in 3DCP is significantly impacted by two parameters: nozzle travel speed and pump rotational speed. It is commonly understood that pump rotational speed is considered proportional to material bulk velocity. Specifically, during the extrusion phase, materials are delivered to the nozzle head through a pumping system with a certain pump rotational speed (material bulk velocity). Then, during the deposition phase, a nozzle travels at a particular speed to deposit materials and build a structure based on a computer-aided design model. Therefore, both of these processes may affect the material flow field and, thus, the fiber orientation. While several studies have explored fiber orientation in 3DCP[10,11], as discussed in Section 1, previous research has primarily focused on the impact of the pumping process on fiber orientation, neglecting an investigation into the effect of printing parameters. Furthermore, one of the unique characteristics of 3DCP is the printing of a structure by stacking extruded filaments layer-atop-layer, and the boundaries of these printed filaments may also affect fiber orientation. However, the impact of the printed filament boundaries on fiber orientation has been insufficiently studied in previous research works.

In summary, this section is motivated by the abovementioned research gaps. Fiber orientation in 3DCP is explored by considering the impacts of the flow field controlled by pumping and nozzle travel processes, as well as the boundary constraints of printed filament.

In 3DCP, the relationship between various printing parameters can be obtained using the material volume conservation principle, assuming that the printed filament is continuous and that the cementitious material is considered incompressible[20-22]:

$$\frac{10^6}{60}\dot{V} = W_f H_f v = W_n H_n u \tag{XIII}$$

$$\dot{V} = c\omega_p \tag{XIV}$$

Where $\dot{V}$ (L/min) is the volumetric flow rate of material in a hose, v (mm/s) and u (mm/s) are the nozzle travel speed and material bulk velocity, respectively; W (mm) and H (mm) are the width and height of a printed filament (subscript f) or the nozzle opening (subscript n), respectively. The relationship between material volumetric flow rate, $\dot{V}$, and pump rotational speed is expressed by Equation XIV, where ω_p (rpm) is the pump rotational speed. c is the calibration coefficient, which is calibrated as 2.61×10^{-3} L/(min·rpm) for the pump and material used in this study. The schematic of Equation XIII is shown in Figure 7, in which a printed filament dimension is the same as the dimension of a printing nozzle.

The printing configurations in 3DCP could be classified into two configurations. In the first configuration, the printing parameters are determined by matching standoff distance with the nozzle opening height as well as matching nozzle travel speed with the material bulk velocity at the nozzle tip, essentially setting $v = u$ and $H_f = H_n$ in Equation XIII. As a result, the printed filament should have the same width as the nozzle. In this configuration, flow streamlines are expected to be well-aligned. In other words, the flow field and flow streamlines can maintain a steady state within the printed filament, and consequently, the fibers are directionally distributed. The pair of printing parameters that achieves directional flow streamlines is defined as satisfying the matching criteria, as shown in Figure 8A.

In the second configuration, when the nozzle travel speed is not equal to the material bulk velocity at the nozzle tip (typically with $v < u$), the streamlines are affected by the substrate and the previously deposited materials, as shown in Figure 8B. Consequently, the orientation of flow streamlines can become widely distributed. In other words, under such conditions, pairs of printing parameters cannot achieve a steady-state flow and directional flow streamlines in the printed filament, and the fibers' distribution is impacted by other factors, such as boundary conditions.

3.3.2. Experimental design

Various pairs of printing parameters were determined to achieve different printing configurations to explore the impacts of flow fields and boundary constraints of printed filament on the fiber orientation in printed specimens. The first configuration is characterized by pairs of printing parameters that satisfy matching criteria, such as having the nozzle travel speed equal to the material bulk velocity at the nozzle tip ($v = u$ and $H_f = H_n$ in Equation XIII). A simple method to achieve the matching criteria is to set every pair of parameters equal in Equation XIII. Specifically, by letting $H_f = H_n$ and $W_f = W_n$, the values of v, u, $\dot{V}$ and ω_p in Equations XIII and XIV can be calculated.

The second configuration involves pairs of printing parameters that do not follow the matching criteria, such as having the nozzle movement velocity unequal to the material bulk velocity at the nozzle tip ($v \neq u$). This second configuration is achieved by changing the nozzle movement speed while maintaining the pump rotational speed (material bulk velocity) constant. The printing parameters for different configurations adopted in this study are listed in Table 2.

The materials were printed using a gantry printer, as shown in Figure 9[23,24]. The nozzle dimensions were 12.98 mm × 28.62 mm (W × H), and the standoff distance of 20 mm was maintained for each layer. According to Table 2, printing parameters for Groups 1–3 were designed

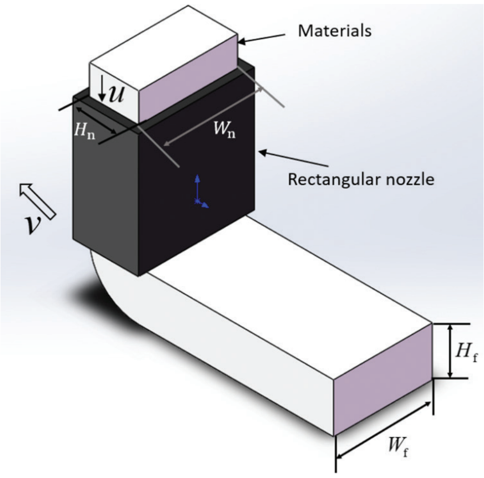

Figure 7. Dimensions and velocities in the 3D concrete printing process.

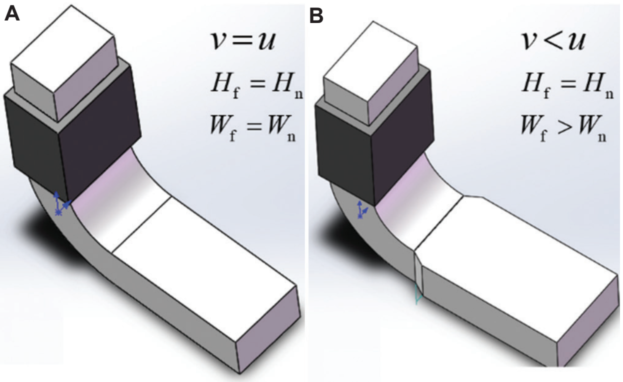

Figure 8. Different streamline orientation distributions under different printing parameter setups in 3D concrete printing (A) satisfying the matching criteria; (B) that do not satisfy the matching criteria.

Table 2. Printing parameters

Mix	1[a]	2[a]	3[a]	4[b]	5[b]	6[b]	7[b]
Pumping speed (L/min)	2.57	3.09	3.6	1.5	1.5	1.5	1.5
Nozzle movement speed (mm/s)	100	120	140	40	60	80	100

[a] The pairs of printing parameters follow the matching criteria.

[b] The pairs of printing parameters that do not follow the matching criteria. When the pumping speed is 1.5 L/min, the nozzle movement velocity should be 58.5 mm/s in the matching criteria.

to meet the matching criteria as per Equation XIII, while printing parameters for Groups 4 – 7 were intentionally set to deviate from the matching criteria.

3.4. Fiber orientation analysis and mechanical property testing

The fluorescence image processing method was adopted to quantify the PVA fiber orientation. PVA fibers possess unique fluorescence properties: When exposed to UV light within the wavelength ranging from 370 nm to 390 nm, they emit green light in the wavelength range of 440 nm to 460 nm[25]. As a result, under a fluorescence microscope, PVA fibers appear bright green color, while the surrounding cementitious matrix appears black[26]. Specifically, PVA fibers appear as circles, and the inclination angle between the fiber and specimen surface is defined as zero degrees, as it is perpendicular to the observed plane[27]. In contrast, when the fiber appears as a line, the inclination angle is defined as 90 degrees, indicating that the fiber is parallel to the analyzed surface in the fluorescence image[28].

After curing, three small specimens were cut from the dog-bone specimen in three different sections to be used as DC and RC specimens. In the case of DC specimens, the flow direction is from the right side to the left side, as plotted in Figure 10A. Specimens 1 and 3 correspond to the beginning and ending points of the rectangular area, respectively. Specimen 2 is located in the middle section of the dog-bone specimen. Each of these specimens measures 20 mm in length. The right surface of each cut piece was selected for analysis, and each cutting surface was divided into 14 areas for capturing fluorescence images (Figure 10B). The fluorescence image processing method was then adopted to analyze fiber orientation[25], with the imaging processing software IMARIS used to analyze the fluorescence image and obtain the probability distribution of fiber orientation.

The printing path to fabricate specimens for fiber orientation analysis is shown in Figure 11A, and the printing parameters for this part are listed in Table 2. After curing, five 20 mm long specimens were cut from printed filaments (Figure 11B). The right surface of each cut specimen was selected for analysis, and each cutting surface was divided into 14 areas for capturing fluorescence images (Figure 10B). The fluorescence image processing method was then adopted to analyze fiber orientation[25] and obtain the probability distribution of fiber orientation using the software IMARIS.

μ-CT scanning is a widely adopted non-destructive technology[29]. In this part, the fiber orientation is also quantitively analyzed using a μ-CT scanner in a 3D space. A small cylinder with a diameter of 10 mm and a length of 50 mm, as shown in Figure 12, was employed for analysis with SkyScan 1173. The pixel size for each scan is 6.8 μm. The detailed analysis procedures are the same as in the authors' previous work[29].

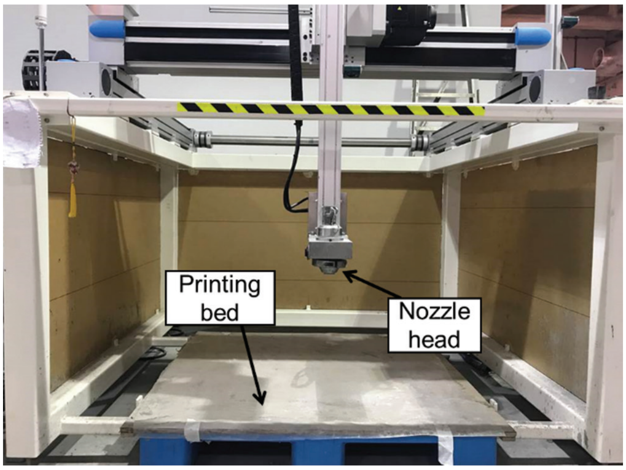

Figure 9. Gantry printer.

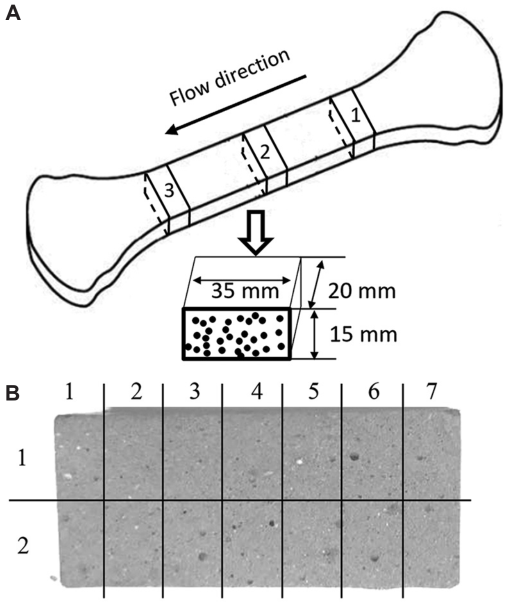

Figure 10. Preparation of specimens for fiber orientation analysis: (A) Cast specimen for fiber analysis. (B) Grid notation of the cutting plane and area of each captured image compared with the whole cross-section.

4. Results

4.1. Fiber orientation analysis: cast specimens

The relationship between the fluorescence image pattern and fiber orientation angle can be observed in Figure 13. The differences in the 2D fluorescence image pattern between "green-color dots" and "green-color lines" can be distinguished by examining the area and shape of the green color patterns in the fluorescence images. For example, in Figure 13, the 0-degree pattern exhibits a significantly smaller area in the 2D fluorescence image pattern compared to the 90-degree pattern. As a result, the computation process can be achieved by several steps: (i) Convert the RGB image to a grayscale image; (ii) convert the grayscale image to a binary image using a thresholding algorithm through IMARIS[30]; and (iii) perform statistical analysis on the angle of fiber orientation based on the binary image. A similar method has been described in a previous study[30].

Figure 14 shows representative fluorescence images of specimens fabricated by different casting approaches in Figure 6. The green color represents the fluorescence emission of fibers. The size of each image represents 3.55 mm × 2.44 mm in Figure 10B. Figure 14A is a typical fluorescence image obtained from DC specimens. As seen from the figure, almost all cross-sections of fibers appear as round dots when the DC approach was adopted, and this phenomenon indicates that a large portion of fibers possesses a small inclination angle. In contrast, fibers appear in various shapes, such as lines, dots, and ellipses, as shown in Figure 6B when the RC approach was used. The result suggests that fiber orientation has a wider range in RC specimens compared to DC specimens.

Figure 15 presents the probability analysis results of fiber orientation on different surfaces of specimens prepared using different casting approaches. The fiber orientation of DC specimens is more directional compared to that of RC specimens. When the DC approach was adopted, approximately 70% of fibers exhibited an inclination angle between 0 and 15°. In contrast, when the RC is adopted, <50% of fibers exhibited an inclination angle between 0 and 15°. Fibers with small inclination angles indicate alignment with the material flow direction during the casting process.

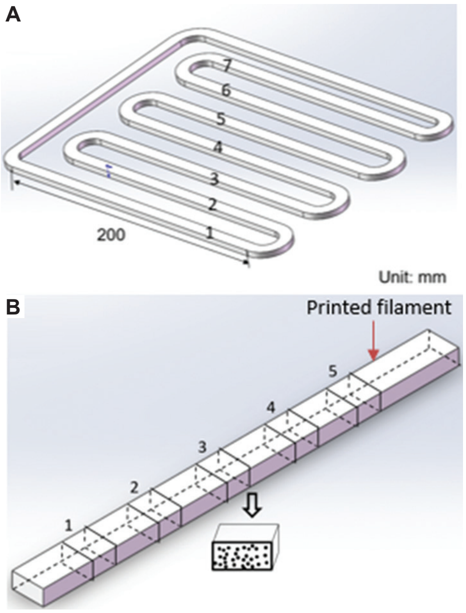

Figure 11. Printing path for specimens of μ-computed tomography analysis: (A) The printing path consists of single-layer filaments. (B) Cut specimens obtained from a printed filament.

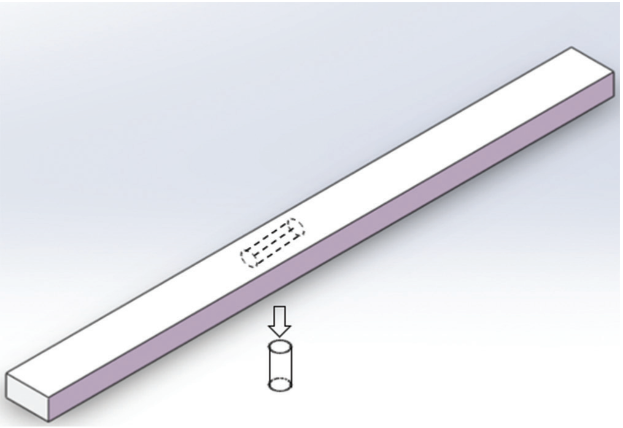

Figure 12. Specimen preparation for μ-computed tomography scanning.

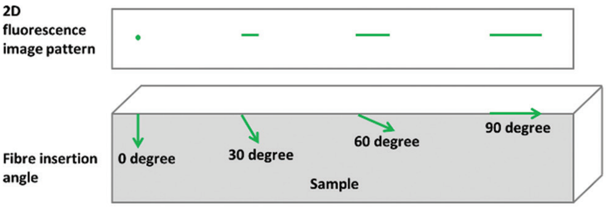

Figure 13. The relationship between fluorescence image pattern and the fiber insertion angle.

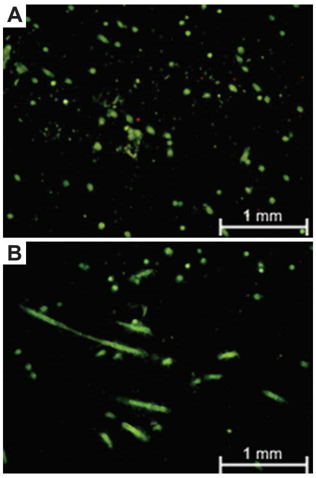

Figure 14. Typical fluorescence result of eight specimens. (A) The specimen obtained from directional casting specimens. (B) The specimen obtained from RC specimens. Scale bar: 1 mm.

Furthermore, as the material flows from specimen 1 to specimen 3 (Figure 10A), the percentage of fibers with small inclination angles (0–15°) increases slightly. This indicates that the flow profile can influence fiber orientation, causing it to align with the flow field direction. The flow field can reach a steady state within a short flow distance due to high viscosity, while the fibers need time to rotate and change their orientation. In general, fibers with longer rotational time can achieve better directional orientation. However, the differences in fiber orientation among the three different surfaces are small because the time difference between the three locations is insufficient to induce a significant change in the direction of a substantial portion of fibers.

In addition, compared to the fiber orientation of DC specimens, the fiber orientation of RC specimens exhibits a lower degree of directional orientation (Figure 15). A large portion of the fiber (approximately 40%) still shows small inclination angles (0 – 15°). This may be attributed to the strong impact of vibration applied during the RC process for consolidation, especially given the material's high viscosity.

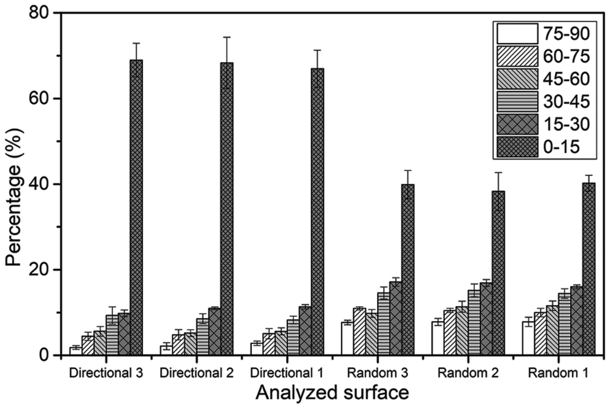

Figure 15. The result of fiber distribution of directional casting (DC) and random casting specimens from the fluorescence microscope. The flow direction in DC is from Surface 1 to Surface 3.

4.2. Fiber orientation analysis: Printing specimens

When the fluid reaches a steady state, the streamlines of the flow field are stable, and consequently, the fibers tend to distribute along the flow streamlines (Section 2.2). According to the discussion in Section 3.3, when the printing parameters follow the matching criteria, fibers in the steady-state fluid should be in directional orientation, which is along the printing direction. In contrast, the fiber should be less directional due to fluid disturbance at the nozzle tip when the pair of printing parameters does not follow the matching criteria.

Figure 16 shows the typical fluorescence images of specimens printed by different parameters. As shown in Figure 16 (A–C), almost all fibers appear as round dots when the first printing configuration is satisfied, and this phenomenon indicates that a large portion of fiber possesses a small inclination angle. In contrast, fibers appear in different shapes, such as lines, dots, and ellipses, as shown in Figure 16 (D–G), when the printing parameters do not follow the matching criteria. The result suggests that fibers are dispersed more randomly, similar to the fiber orientation in random cast specimens, as shown in Figure 16H.

IMARIS was adopted to process fluorescence images to obtain the probability distribution of fiber orientation of 3D printed specimens, and the result is plotted in Figure 17. As shown in the figure, more than 70% of fibers exhibit an inclination angle between 0 and 15 degrees

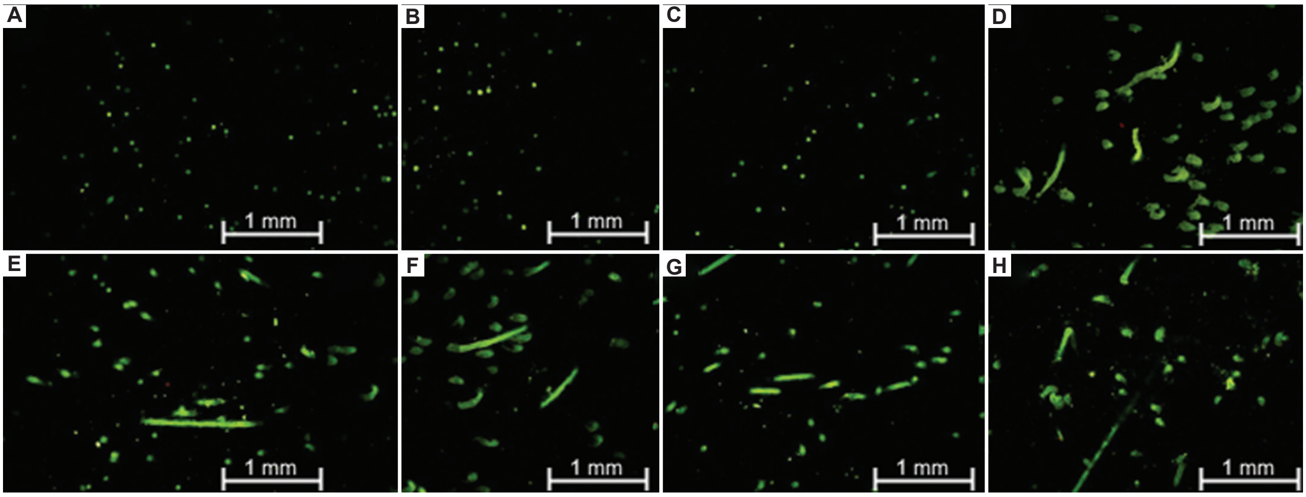

Figure 16. Fluorescence result of eight specimens: (A–C) specimens printed following matching criteria; (D–G) specimens printed not following matching criteria; (H) random cast specimen. Scale bar: 1 mm.

when the first printing configuration was satisfied during the printing process. Otherwise, <50% of fibers exhibit an inclination angle between 0 and 15°. Fibers exhibiting a small inclination angle indicate that they are aligned with the printing direction.

Figure 18 shows the 3D fiber distribution in the specimen obtained from the μ-CT scan. As seen in the figure, when the specimen is fabricated using the printing parameters that adhere to the matching criteria, fibers (white lines in Figure 18A) exhibit a high degree of directional orientation, aligning with the printing direction. However, in Figure 18B, with specimens fabricated using parameters that do not follow the matching criteria, fibers tend to have a more random orientation. The results from μ-CT scanning are in line with the results from the image analysis shown in Figure 17.

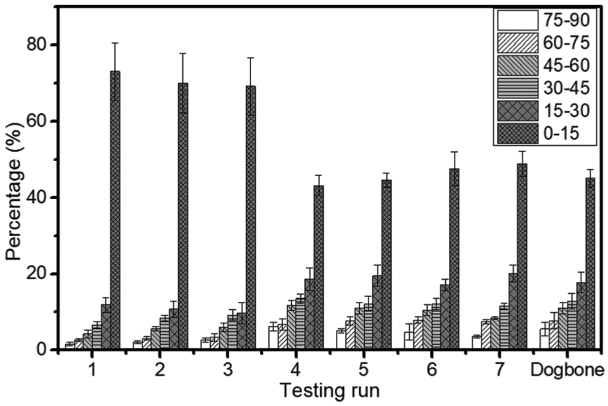

Figure 17. The result of fiber distribution in printed specimens from the fluorescence microscope.

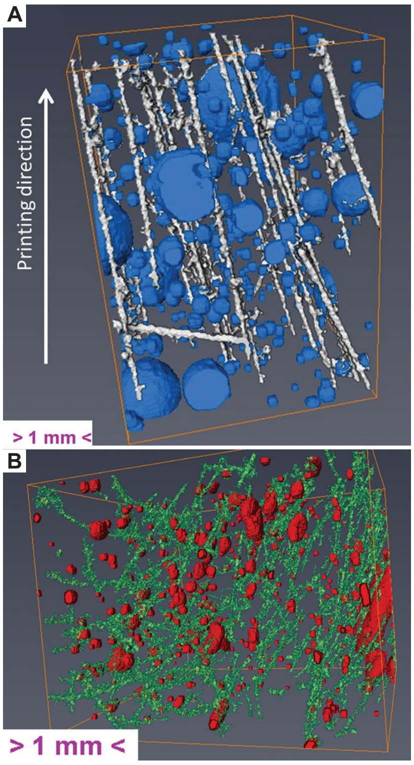

Figure 18. Micro-computed tomography scan analysis result of specimens fabricated by: (a) the printing parameters following the matching criteria, where the cross-section of printed filaments has the same dimension as that of nozzle opening and the flow streamlines are well aligned; (b) the printing parameters that do not follow the matching criteria.

5. Discussion

5.1. Effects of printing parameters on filament dimensions

The dimensions of printed filaments are affected by printing parameters due to the material volumetric conservation principle in the printing process. As discussed in Section 3.3, when the printing parameters adhere to the matching criteria, the dimensions of the printed filament should match those of the nozzle opening. Conversely, when the printing parameters do not meet the matching criteria, the dimensions should differ.

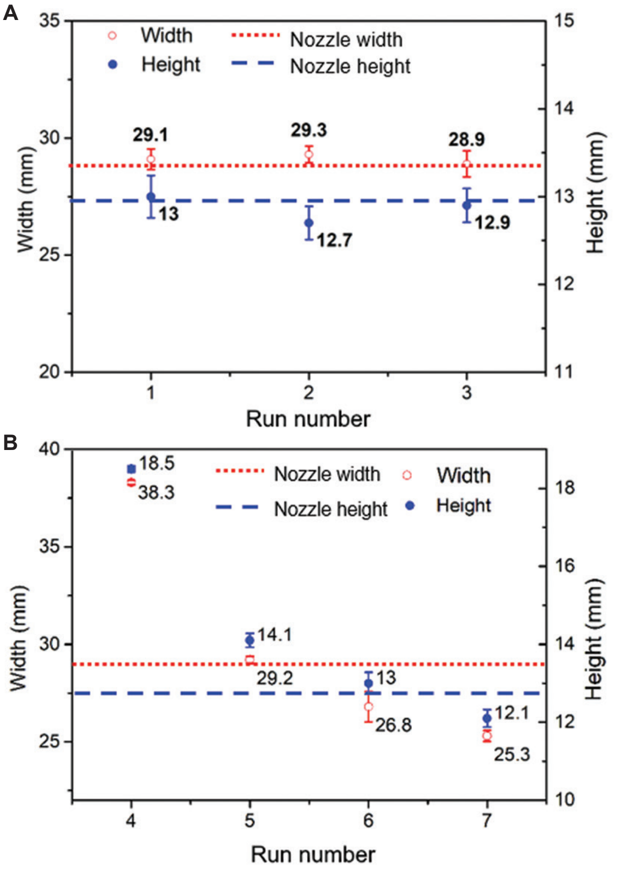

Figure 19. The height and width of the printed filament: (A) Printing parameters follow the matching criteria; (B) printing parameters do not follow the matching criteria.

The relationship between the printing parameters and the dimension of printed filaments is shown in Figure 19. The pair of printing parameters of test runs 1, 2, and 3 follows the matching criteria. The dimensions of each printed filament are plotted in Figure 19A. The nozzle adopted for printing is 12.98 mm × 28.62 mm (H × W). As shown in Figure 19A, with printing parameters following the matching criteria, printed filaments have almost the same dimensions as the size of the nozzle opening. The slight difference between the dimensions of printed filament and nozzle head opening is possible due to the material slump, resulting in decreased filament height and width.

The pair of printing parameters of test runs 4, 5, 6, and 7 does not follow the matching criteria. Figure 19B shows the dimensions of printed filaments. As shown in Figure 19B, with the increase of nozzle movement speed from 40 mm/s to 100 mm/s while material bulk velocity maintains a constant, both the width and height of printed filaments decrease due to the volumetric conservation principle.

5.2. Comparison between theoretical and experimental results

Figure 20A presents a comparison between the results of the 1D and 2D boundary models with experimental results. As shown in figure, the 2D boundary constraints model provides better prediction accuracy than the 1D model. However, it is also evident that prediction results based on 2D boundary constraints exhibit a large variance from the experimental value. This variation might be attributed to the non-ideal random conditions in the RC process, where vibrations during the casting process could induce material flow, generate flow streamlines, and change fiber orientation. As a consequence, the fibers of RC specimens exhibit higher directional orientation than that calculated by the theoretical models.

Figure 21 presents a comparison between the computational fluid dynamics (CFD) simulation results and experimental results regarding fiber orientation in specimens fabricated using the DC process. As shown in figure, while the CFD simulation results show a good fit with the experimental results, there is also a discrepancy between the two. This disparity may be attributed to the fact that in the CFD simulation, the streamlines become well-aligned with the boundary after a short distance. However, in practical DC processes, the flow duration and distance are limited, which may not provide sufficient time for the fibers to rotate. Consequently, the CFD simulation results suggest that the fibers have a higher degree of directional orientation than the experimental results.

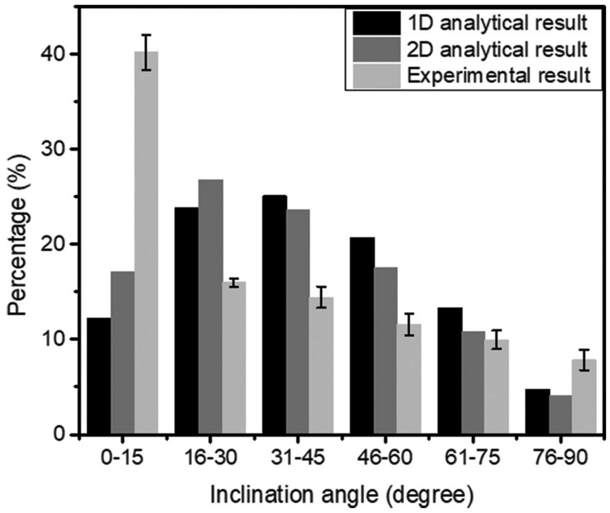

Figure 20. Comparison among the 1D prediction, 2D prediction, and experimental values of the random casting process.

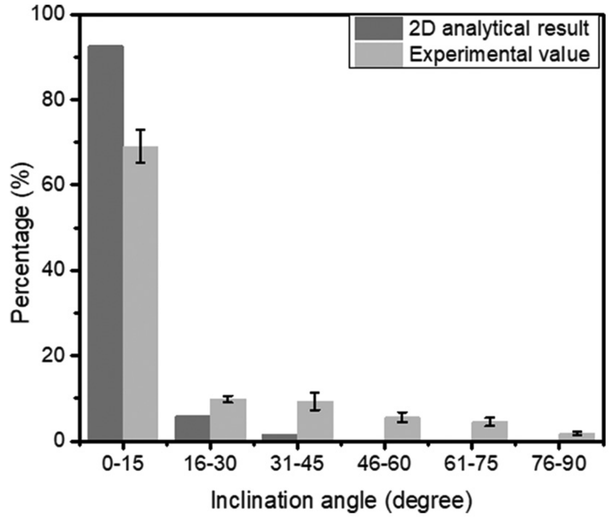

Figure 21. Comparison between the computational fluid dynamics simulation results and the experimental results of the directional casting process.

Furthermore, when the pair of printing parameters does not follow the matching criteria, the comparison between the results of the 2D model predictions and the experimental tests is presented in Figure 22. As shown in figure, variations in the printed filament dimensions lead to changes in fiber orientation. With an increase in nozzle travel speed and a decrease in printed filament dimensions, the material tends to flow in the printing direction, and the decreased filament dimensions impose tighter boundary constraints on the fibers. As a result, the percentage of fiber with a small inclination angle increases.

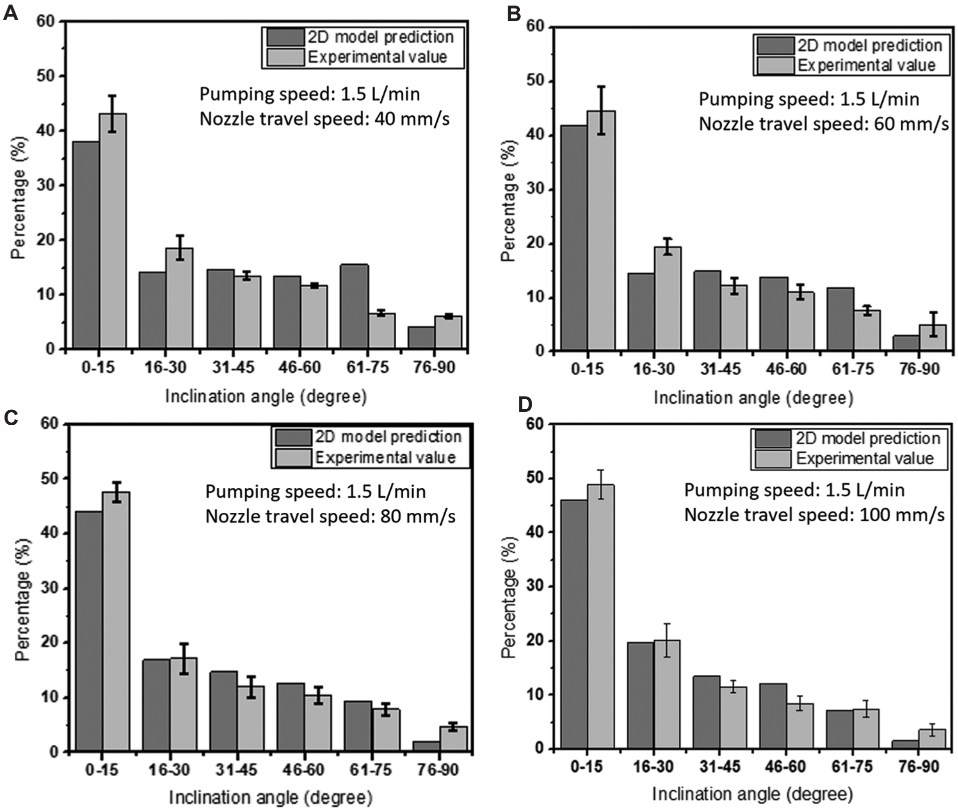

Figure 22. Comparison between the prediction value and experimental value of specimens printed with parameters that do not follow matching criteria: (A) 1.5, 40; (B) 1.5, 60; (C) 1.5, 80; and (d)1.5, 100

The simulation and experimental results show some deviations. For instance, in the experimental test results, the percentage of fibers with a large inclination angle is much lower than in the simulation, especially in cases with low nozzle travel speeds. This discrepancy arises because the simulation considers only the streamlines of the material flow and does not consider the constraints imposed by the geometry and the time required for the fibers to rotate. Therefore, the percentage of fibers with a 0 – 15° inclination angle in the simulation results is lower than in the experimental results, while the percentage of fibers with a high inclination angle in the simulation results is higher than in the experimental results. Interestingly, due to the relatively long time required for fibers to rotate, there are still some fibers oriented in the transverse direction, with inclination angles between 76 – 90° in the experimental results. However, in the simulation, the influence of nozzle movement makes it difficult for the streamlines to exhibit such large inclination angles. These factors contribute to the lower simulated percentage of fibers with a 76 – 90° inclination angle compared to the experimental results.

5.3. Mechanical characterization: cast specimens

Figure 23 shows the tensile and flexural behavior of specimens fabricated using the DC and the RC processes. As shown in Figure 23A and B, specimens fabricated using the DC process exhibit both strain-hardening and deflection-hardening behavior. In contrast, RC specimens exhibit a strain-softening phenomenon. Furthermore, the ultimate tensile strength of specimens fabricated using the DC process is approximately 3 times higher than that of specimens fabricated using the RC process. Similarly, the ultimate flexural strength of specimens fabricated using the DC process is also approximately 3 times higher than that of specimens fabricated using the RC process. In addition to these strength differences, both the tensile and flexural strains of specimens fabricated using the DC process exhibit superior behavior compared to RC process specimens.

The difference in mechanical performance between RC specimens and DC specimens can be attributed to differences in fiber orientation, as discussed in Section 4.1. The load direction of the tensile test is

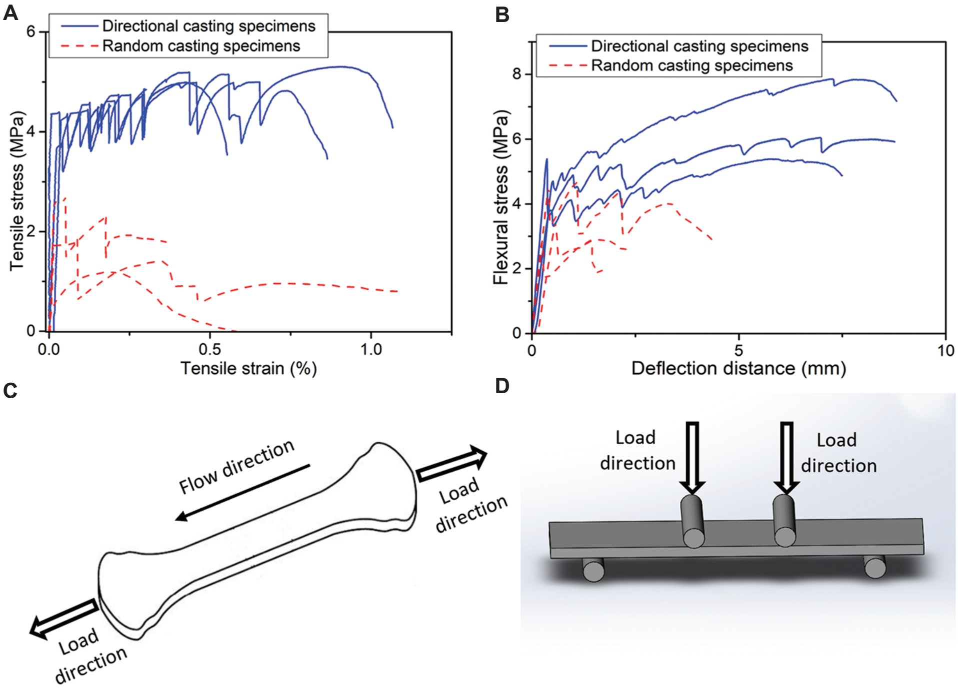

Figure 23. Results of mechanical property: (A) Tensile stress versus tensile strain of specimens through the different casting approaches; (B) flexural stress versus deflection distance of specimens through different casting methods; (C) schematically shows the load direction of tensile test; and (D) schematically shows the load direction of flexural test.

shown in Figure 23C and D. When the specimens are fabricated using the DC process, a high percentage of fibers have a small inclination angle (0 – 15°), indicating that a significant number of fibers are oriented in the load direction. In contrast, when the RC process is adopted, fewer fibers are oriented in the load direction compared to DC specimens. Therefore, better tensile performance is achieved when using the DC approach for specimen preparation compared to specimens fabricated using the RC process.

Furthermore, the load direction for the flexural test is shown in Figure 23D. Although the load direction is perpendicular to the specimen, the stress generated during the bending test acts perpendicular to the cross-section of specimens. When the DC process is adopted, a significant number of fibers are oriented in the stress direction during the flexural test. Consequently, better flexural performance is achieved.

5.4. Mechanical characterization: Printing specimens

The gantry printer was employed to fabricate 3D-printed specimens for the flexural test. A printing nozzle with approximately 30 mm in length and 15 mm in width was used. The standoff distance was 15 mm for each layer, and the printed path is shown in Figure 24. The mechanical testing method has been stated in a previous study[31]. The printing parameters adopted for fabricating specimens are listed in Table 3. Test run 1 follows the matching criteria, while the others do not follow the matching criteria, as discussed in Section 3.3.

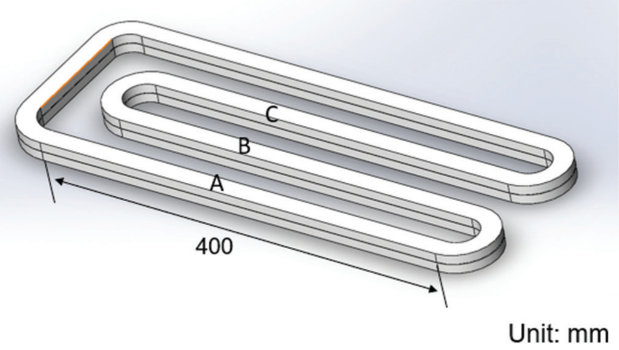

Figure 24. Printing path for specimens of the mechanical test.

As discussed in Section 3.3, the dimensions of printed filaments differ in the second configuration. To address this, a new experimental setup was designed aimed at diminishing the size effect of printed filaments on the mechanical properties of printed specimens, as shown in Figure 25. For each pair of printing parameters listed in Table 3, two batches of materials with the same mixture were printed. One batch included fibers, while the other batch did not. Both flexural properties of the printed fiber mixture and the non-fiber mixture were tested (Figure 25), and improvement ratios of flexural stress (σ) and deflection distance (δ) were adopted to characterize the impact of fiber orientation on the mechanical performance, as expressed by Equation XV.

$$\text{Increment ratio of flexural stress} = \frac{\sigma'}{\sigma}$$

$$\text{Increment ratio of deflection distance} = \frac{\varepsilon'}{\varepsilon} \qquad \text{(XV)}$$

Figure 26 presents the relative improvement ratios of mechanical performance. As shown in Figure 26, when the printing parameters follow the matching criteria and the fibers exhibit a high degree of directional distribution, the flexural strength and deflection distance of the printed fiber mixture can increase by up to 180% and 380%, respectively, compared to the printed non-fiber mixture.

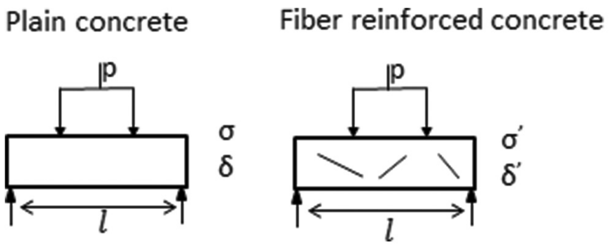

Figure 25. Experimental setups for mechanical performance test of printed specimens.

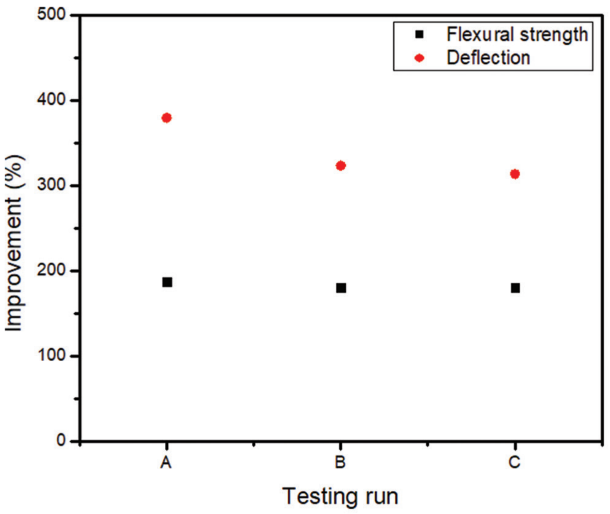

Figure 26. The improvement in the mechanical performance of printed specimens with various printing configurations.

Table 3. Testing run for the 3D-printed specimens

Run No.	A	B	C
Pumping speed (mm/s)	650[1]	650[2]	650[2]
Nozzle movement speed (mm/s)	66.7[1]	53.3[2]	40[2]

[1] The pairs of printing parameters follow the matching criteria.

[2] The pairs of printing parameters that do not follow the matching criteria.

In the case of printing Parameter A that follows the matching criteria, the fibers align well within the printed filament, as discussed in Sections 3.3 and 4. However, for printing Parameters B and C, which do not follow the matching criteria, the fibers tend to exhibit a lower degree of directional distribution within the printed filaments, as discussed in Section 4. Consequently, the flexural properties of the specimens printed using printing Parameter A surpass those of Parameters B and C.

6. Conclusions

In this work, a comprehensive investigation was conducted to assess the impacts of boundary constraints and flow fields on fiber orientation. First, analytical models and CFD simulations were developed to predict fiber orientation based on boundary constraints and flow fields. Subsequently, both cast and printed specimens were prepared to investigate the impacts of boundary constraints and flow fields on fiber orientation and mechanical performance. The analysis of fiber orientation relied on the fluorescence image processing method and μ-CT scan, while mechanical performance was evaluated through tensile and flexural properties assessment.

The results reveal that the fibers of cast specimens prepared using the DC process exhibit a higher degree of directional fiber orientation, attributed to the well-aligned flow field generated by the DC process. In addition, the mechanical performance of DC specimens is superior to that of specimens prepared through the RC process.

In the case of printed specimens, when they are fabricated with printing parameters following the matching criteria, the cross-section of printed filaments matches the dimensions of the nozzle opening, resulting in well-aligned flow streamlines. Consequently, fibers exhibit a higher degree of directional orientation, aligning with the printing direction. However, when specimens are fabricated with printing parameters that do not follow the matching criteria, fibers tend to have a random orientation, which is limited by the boundary constraints of printed filaments.

The findings in this work have practical significance for both cast and printed FRCs. By controlling the fiber orientation through adjustments in the printing parameters, it becomes possible to enhance the mechanical performance of components, enabling them to withstand greater loads. Furthermore, structures requiring specific directional performance, such as those needing directional thermoconductivity or directional electrical-conductivity, can be realized by designing the printing parameters to control fiber orientation.

Acknowledgments

None.

Funding

The authors would like to acknowledge the Hong Kong Polytechnic University (P0044561), the National Research Foundation, Prime Minister's Office, Singapore, under its Medium-Sized Centre funding scheme, CES_SDC Pte Ltd, and Chip Eng Seng Corporation Ltd. for their funding and support in this research project.

Conflict of interest

The authors declare no conflicts of interest.

Author contributions

Conceptualization: Mingyang Li and Yiwei Weng
Data curation: Mingyang Li and Yiwei Weng
Formal analysis: Mingyang Li and Yiwei Weng
Funding acquisition: Teck Neng Wong and Ming Jen Tan
Investigation: Mingyang Li, Yiwei Weng, and Dong Zhang
Methodology: Mingyang Li, Yiwei Weng, and Dong Zhang
Supervision: Yiwei Weng
Validation: Mingyang Li and Yiwei Weng
Writing – original draft: Mingyang Li and Yiwei Weng
Writing – review & editing: Mingyang Li, Yiwei Weng, Teck Neng Wong, and Ming Jen Tan

Ethics approval and consent to participate

Not applicable.

Consent for publication

Not applicable.

Availability of data

Some or all data, models, or codes that support the findings of this study are available from the corresponding author on reasonable request.

References

1. Weng Y, Li M, Tan MJ, *et al.*, 2018, 3D Printable High Performance Fiber Reinforced Cementitious Composites for Large-scale Printing. In: Proceedings of the 3rd International Conference on Progress in Additive Manufacturing (Pro-AM 2018). p. 19–24.

   https://doi.org/10.25341/D4B591

2. Wu HC, Li VC, 1992, Snubbing and bundling effects on multiple crack spacing of discontinuous random fiber-reinforced brittle matrix composites. *J Am Ceram Soc*, 75: 3487–3489.

   https://doi.org/10.1111/j.1151-2916.1992.tb04457.x

3. Kanda T, Li VC, 1998, Interface property and apparent strength of high-strength hydrophilic fiber in cement matrix. *J Mater Civ Eng*, 10: 5–13.

   https://doi.org/10.1061/(ASCE)0899-1561(1998)10:1(5)

4. Kaufmann J, Frech K, Schuetz P, *et al.*, 2013, Rebound and orientation of fibers in wet sprayed concrete applications. *Constr Build Mater*, 49: 15–22.

   https://doi.org/10.1016/j.conbuildmat.2013.07.051

5. Segura-Castillo L, Cavalaro SH, Goodier C, *et al.*, 2018, Fibre distribution and tensile response anisotropy in sprayed fibre reinforced concrete. *Mater Struct*, 51: 29.

   https://doi.org/10.1617/s11527-018-1156-5

6. Shao Y, Qiu J, Shah SP, 2001, Microstructure of extruded cement-bonded fiberboard. *Cem Concr Res*, 31: 1153–1161.

   https://doi.org/10.1016/S0008-8846(01)00535-X

7. Stähli P, Custer R, van Mier JG, 2008, On flow properties, fibre distribution, fibre orientation and flexural behaviour of FRC. *Mater Struct*, 41: 189–196.

   https://doi.org/10.1617/s11527-007-9229-x

8. Peled A, Shah SP, 2003, Processing effects in cementitious composites: Extrusion and casting. *J Mater Civ Eng*, 15: 192–199.

   https://doi.org/10.1061/(ASCE)0899-1561(2003)15:2(192)

9. Lu C, Leung CK, 2017, Theoretical evaluation of fiber orientation and its effects on mechanical properties in engineered cementitious composites (ECC) with various thicknesses. *Cem Concr Res*, 95: 240–246.

   https://doi.org/10.1016/j.cemconres.2017.02.024

10. Hambach M, Volkmer D, 2017, Properties of 3D-printed fiber-reinforced Portland cement paste. *Cem Concr Compos*, 79: 62–70.

    https://doi.org/10.1016/j.cemconcomp.2017.02.001

11. Figueiredo SC, Rodriguez CR, Ahmed ZY, *et al.*, 2020, Mechanical behavior of printed strain hardening cementitious composites. *Materials* (*Basel*), 13: 2253.

    https://doi.org/10.3390/ma13102253

12. Aveston J, Kelly A, 1973, Theory of multiple fracture of fibrous composites. *J Mater Sci*, 8: 352–362.

    https://doi.org/10.1007/BF00550155

13. Panton RL, 2006, Incompressible Flow. Hoboken: John Wiley and Sons.

14. Lao W, Li M, Wong TN, *et al.*, 2020, Improving surface finish quality in extrusion-based 3D concrete printing using

machine learning-based extrudate geometry control. *Virtual Phys Prototyp*, 15: 178–193.

https://doi.org/10.1080/17452759.2020.1713580

15. Weng Y, Li M, Liu Z, *et al.*, 2019, Printability and fire performance of a developed 3D printable fibre reinforced cementitious composites under elevated temperatures. *Virtual Phys Prototyp*, 14: 284–292.

    https://doi.org/10.1080/17452759.2018.1555046

16. Li VC, Bos FP, Yu K, *et al.*, 2020, On the emergence of 3D printable engineered, strain hardening cementitious composites (ECC/SHCC). *Cem Concr Res*, 132: 106038.

    https://doi.org/10.1016/j.cemconres.2020.106038

17. Weng Y, Lu B, Li M, *et al.*, 2018, Empirical models to predict rheological properties of fiber reinforced cementitious composites for 3D printing. *Constr Build Mater*, 189: 676–685.

    https://doi.org/10.1016/j.conbuildmat.2018.09.039

18. Weng Y, Li M, Tan MJ, *et al.*, 2018, Design 3D printing cementitious materials via Fuller Thompson theory and Marson-Percy model. *Constr Build Mater*, 163: 600–610.

    https://doi.org/10.1016/j.conbuildmat.2017.12.112

19. Weng Y, Ruan S, Li M, *et al.*, 2019, Feasibility study on sustainable magnesium potassium phosphate cement paste for 3D printing. *Constr Build Mater*, 221: 595–603.

    https://doi.org/10.1016/j.conbuildmat.2019.05.053

20. Li M, Weng Y, Liu Z, *et al.*, 2022, Optimizing of chemical admixtures for 3D printable cementitious materials by central composite design. *Mater Sci Addit Manuf*, 1: 16.

    https://doi.org/10.18063/msam.v1i3.16

21. Weng Y, Li M, Zhang D, *et al.*, 2021, Investigation of interlayer adhesion of 3D printable cementitious material from the aspect of printing process. *Cem Concr Res*, 143: 106386.

    https://doi.org/10.1016/j.cemconres.2021.106386

22. Weng Y, Li M, Ruan S, *et al.*, 2020, Comparative economic, environmental and productivity assessment of a concrete bathroom unit fabricated through 3D printing and a precast approach. *J Clean Prod*, 261: 121245.

    https://doi.org/10.1016/j.jclepro.2020.121245

23. Weng Y, Li M, Wong TN, *et al.*, 2021, Synchronized concrete and bonding agent deposition system for interlayer bond strength enhancement in 3D concrete printing. *Autom Constr*, 123: 103546.

    https://doi.org/10.1016/j.autcon.2020.103546

24. Weng Y, Ahamed NA, Lee BJ, *et al.*, 2021, Extracting BIM information for lattice Toolpath planning in digital concrete printing with developed dynamo script: A case study. *J Comput Civ Eng*, 35: 05021001.

    https://doi.org/10.1061/(ASCE)CP.1943-5487.0000964

25. Ranade R, Stults MD, Lee B, *et al.*, 2012, Effects of fiber dispersion and flaw size distribution on the composite properties of PVA-ECC. In: High Performance Fiber Reinforced Cement Composites. Dordrecht: Springer. p. 107–114.

26. Torigoe S, Horikoshi T, Ogawa A, *et al.*, 2003, Study on evaluation method for PVA fiber distribution in engineered cementitious composite. *J Adv Concr Technol*, 1: 265–268.

    https://doi.org/10.3151/jact.1.265

27. Suuronen JP, Kallonen A, Eik M, *et al.*, 2013, Analysis of short fibres orientation in steel fibre-reinforced concrete (SFRC) by X-ray tomography. *J Mater Sci*, 48: 1358–1367.

    https://doi.org/10.1007/s10853-012-6882-4

28. Tosun-Felekoğlu K, Felekoğlu B, Ranade R, *et al.*, 2014, The role of flaw size and fiber distribution on tensile ductility of PVA-ECC. *Compos B Eng*, 56: 536–545.

    https://doi.org/10.1016/j.compositesb.2013.08.089

29. Ruan S, Qiu J, Weng Y, *et al.*, 2019, The use of microbial induced carbonate precipitation in healing cracks within reactive magnesia cement-based blends. *Cem Concr Res*, 115: 176–188.

    https://doi.org/10.1016/j.cemconres.2018.10.018

30. Lee BY, Kim JK, Kim JS, *et al.*, 2009, Quantitative evaluation technique of polyvinyl alcohol (PVA) fiber dispersion in engineered cementitious composites. *Cem Concr Compos*, 31: 408–417.

    https://doi.org/10.1016/j.cemconcomp.2009.04.002

31. Weng Y, Lu B, Tan MJ, *et al.*, 2016, Rheology and Printability of Engineered Cementitious Composites-a Literature Review. In: Proceedings of the 2nd International Conference on Progress in Additive Manufacturing (Pro-AM 2016). p. 427–432.

Appendices

Appendix A: Analytical result of one-dimensional boundary constraints

For a 1D case with thickness Z, the amount of fiber per unit length and width can be computed by:

$$N=\frac{ZV_f}{\pi l_f r_f^2} \quad \text{(AI)}$$

This volume can be divided into two regions, that us, Region 1 ($z < l_f/2$and Region 2 ($z\geq l_f/2$), as shown in Figure A1, where z is the distance from the boundary. For different cases, Region 2 may not exist. For Region 1, the total length of the distribution arc is:

$$P(z,\theta)=\begin{cases}\left(\frac{l_f}{2}\right)\sin\theta\cdot 2\pi & \theta\leq\arcsin\left(\frac{z}{l_f/2}\right)\\ \left(\frac{l_f}{2}\right)\sin\theta\cdot\left[2\pi-4\arccos\left(\frac{z}{l_f\sin\theta/2}\right)\right] & \theta>\arcsin\left(\frac{z}{l_f/2}\right)\end{cases} \quad \text{(AII)}$$

For Region 2, the total length of the distribution arc is:

$$P(z,\theta)=\left(\frac{l_f}{2}\right)\sin\theta\cdot 2\pi \quad \text{(AIII)}$$

If the distance between the fiber center and one specific cross-section plane is more than $\pm l_f\cos\theta/2$, the fiber cannot pass through the plane. Thus, the number of fibers crossing this plane at a given angle can be computed for any distance z from the boundary:

$$\text{Num}\left(z,\left[\theta,\theta+d\theta\right]\right)=N\cdot 2\cdot\frac{l_f\cos\theta}{2}\cdot\frac{P(z,\theta)d\theta}{\int_0^{\pi/2}P(z,\theta)d\theta} \quad \text{(AIV)}$$

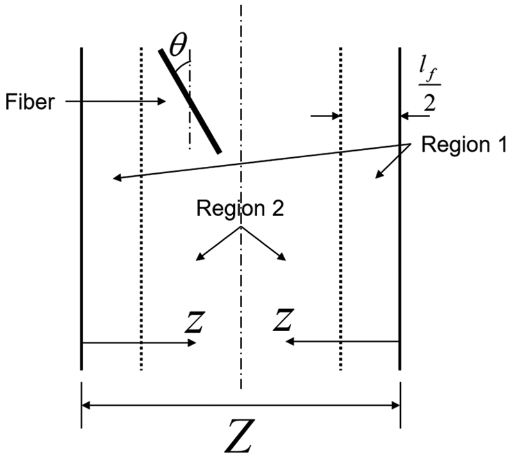

Figure A1. The schematic of 1D case with two different regions.

Substituting Equation AI into Equation AIV:

$$\text{Num}\left(z,\left[\theta,\theta+d\theta\right]\right)=\frac{ZV_f\cos\theta}{\pi r_f^2}\cdot\frac{P(z,\theta)d\theta}{\int_0^{\pi/2}P(z,\theta)d\theta} \quad \text{(AV)}$$

Then, the total number of fibers crossing this plane at a given angle can be integrated through the thickness:

$$\text{Num}\left(\left[0,Z\right],\left[\theta,\theta+d\theta\right]\right)=2\int_0^{Z/2}\text{Num}\left(z,\left[\theta,\theta+d\theta\right]\right)dz \quad \text{(AVI)}$$

Substituting Equation AV into Equation AVI:

$$\text{Num}\left(\left[0,Z\right],\left[\theta,\theta+d\theta\right]\right)=\frac{2ZV_f\cos\theta}{\pi r_f^2}$$

$$\int_0^{Z/2}\left[\frac{P(z,\theta)d\theta}{\int_0^{\pi/2}P(z,\theta)d\theta}\right]dz \quad \text{(AVII)}$$

Let $w=z/(l_f/2)$ be the dimensionless coordinate, Equations AII and AIII can be combined as:

$$P(w,\theta)=\begin{cases}\sin\theta\cdot 2\pi & w>1 \text{ or } w\geq\sin\theta\\ \sin\theta\cdot\left[2\pi-4\arccos\left(\frac{w}{\sin\theta}\right)\right] & w<1 \text{ and } w<\sin\theta\end{cases} \quad \text{(AVIII)}$$

and Equation (AVII) can be rewritten as:

$$\text{Num}\left(\left[0,Z\right],\left[\theta,\theta+d\theta\right]\right)=\frac{2ZV_f\cos\theta}{\pi r_f^2}$$

$$\int_0^{Z/l_f}\left[\frac{P(w,\theta)d\theta}{\int_0^{\pi/2}P(w,\theta)d\theta}\right]dw \quad \text{(AIX)}$$

For a specific position in region 1, where $u<1$:

$$\begin{aligned}\int_0^{\pi/2}P(w,\theta)d\theta&=\int_0^{\arcsin w}P(w,\theta)d\theta+\int_{\arcsin w}^{\pi/2}P(w,\theta)d\theta\\ &=\int_0^{\arcsin w}2\pi\sin\theta d\theta+\\ &\quad\int_{\arcsin w}^{\pi/2}\left\{\left[2\pi-4\arccos\left(\frac{w}{\sin\theta}\right)\right]\sin\theta\right\}d\theta\end{aligned} \quad \text{(AX)}$$

Let θ_w=arcsin$w$ and integrate into Equation AX:

$$\begin{aligned}\int_0^{\pi/2}P(w,\theta)d\theta&=\int_0^{\theta_u}2\pi\sin\theta d\theta+\\ &\quad\int_{\theta_u}^{\pi/2}\left\{\left[2\pi-4\arccos\left(\frac{w}{\sin\theta}\right)\right]\sin\theta\right\}d\theta\\ &=2\pi-4\int_{\theta_u}^{\pi/2}\left[\sin\theta\arccos\left(\frac{w}{\sin\theta}\right)\right]d\theta\end{aligned} \quad \text{(AXI)}$$

where,

$$\int_{\theta_w}^{\pi/2}\left[\sin\theta\arccos\left(\frac{w}{\sin\theta}\right)\right]d\theta$$

$$=-\int_{\theta_w}^{\pi/2}\arccos\left(\frac{w}{\sin\theta}\right)d\cos\theta$$

$$=-\cos\theta\arccos\left(\frac{w}{\sin\theta}\right)\Bigg|_{\theta_w}^{\pi/2}+\int_{\theta_w}^{\pi/2}\cos\theta d\arccos\left(\frac{w}{\sin\theta}\right)$$

$$=0+\int_{\theta_w}^{\pi/2}\frac{w\cos^2\theta}{\sin\theta\sqrt{\sin^2\theta-w^2}}d\theta$$

$$=w\int_{\theta_w}^{\pi/2}\frac{1}{\sqrt{1-\cos^2\theta-w^2}}d\cos\theta-w\int_{\theta_w}^{\pi/2}\frac{1}{\left(1-\cos^2\theta\right)\sqrt{1-\cos^2\theta-w^2}}d\cos\theta \quad \text{(AXII)}$$

and,

$$\int_{\theta_w}^{\pi/2}\frac{w\cos^2\theta}{\sin\theta\sqrt{\sin^2\theta-w^2}}d\theta$$

$$=w\int_{\theta_w}^{\pi/2}\frac{\sin\theta\cos^2\theta}{\sin^2\theta\sqrt{\sin^2\theta-w^2}}d\theta$$

$$=-w\int_{\theta_w}^{\pi/2}\frac{\cos^2\theta}{\left(1-\cos^2\theta\right)\sqrt{1-\cos^2\theta-w^2}}d\cos\theta$$

$$=w\int_{\theta_u}^{\pi/2}\frac{1}{\sqrt{1-\cos^2\theta-w^2}}d\cos\theta$$

$$-w\int_{\theta_u}^{\pi/2}\frac{1}{\left(1-\cos^2\theta\right)\sqrt{1-\cos^2\theta-w^2}}d\cos\theta \quad \text{(AXIII)}$$

As $\sin\theta_w=w$, let $\cos\theta=\cos\theta_w\sin\omega$, then $\omega=\arcsin(\cos\theta/\cos\theta_w)$ and $d\cos\theta=\cos\theta_w\cos\omega d\omega$. Therefore, Equation AXIII can be integrated as:

$$w\int_{\theta_w}^{\pi/2}\frac{1}{\sqrt{1-\cos^2\theta-w^2}}d\cos\theta-$$

$$w\int_{\theta_w}^{\pi/2}\frac{1}{\left(1-\cos^2\theta\right)\sqrt{1-\cos^2\theta-w^2}}d\cos\theta$$

$$=w\int_{\pi/2}^{0}\frac{\cos\omega}{\sqrt{1-\sin^2\omega}}d\omega-w\int_{\pi/2}^{0}\frac{1}{1-\cos^2\theta_w\sin^2\omega}d\omega \quad \text{(AXIV)}$$

$$=w\int_{\pi/2}^{0}1d\omega+w\int_{\pi/2}^{0}\frac{1}{1+\sin^2\theta_w\tan^2\omega}d\tan\omega$$

$$=-\frac{\pi w}{2}+\frac{\pi}{2}$$

Substituting Eq. into Eq. :

$$\int_{0}^{\pi/2}P\left(w,\theta\right)d\theta$$

$$=2\pi-4\left(-\frac{\pi w}{2}+\frac{\pi}{2}\right) \quad \text{(AXV)}$$

$$=2\pi w$$

Substituting Equation AXV into Equation AVII:

$$\mathrm{Num}\left(\left[0,Z\right],\left[\theta,\theta+d\theta\right]\right)=\frac{2ZV_f\cos\theta d\theta}{\pi r_f^2}$$

$$\int_{0}^{Z/l_f}\frac{P\left(w,\theta\right)}{2\pi w}dw \quad \text{(AXVI)}$$

According to Equation AII, when $Z/l_f\leq\sin\theta$:

$$Num\left(\left[0,Z\right],\left[\theta,\theta+d\theta\right]\right)$$

$$=\frac{2ZV_f\cos\theta d\theta}{\pi r_f^2}\int_{0}^{Z/l_f}\frac{\sin\theta\left[2\pi-4\arccos\left(\frac{w}{\sin\theta}\right)\right]}{2\pi w}dw$$

$$=\frac{2ZV_f\sin\theta\cos\theta d\theta}{\pi^2r_f^2}\int_{0}^{Z/l_f}\frac{\pi-2\arccos\left(\frac{w}{\sin\theta}\right)}{w}dw$$

$$=\frac{2ZV_f\sin\theta\cos\theta d\theta}{\pi^2r_f^2}$$

$$i\left\{\begin{array}{l}Li_2\left(1-\exp\left[2i\arcsin\left(\frac{Z}{l_f\sin\theta}\right)\right]\right)\\-\arcsin^2\left(\frac{Z}{l_f\sin\theta}\right)\end{array}\right\} \quad \text{(AXVII)}$$

where $\mathrm{Li}_2(t)$ is the polylogarithm with order 2 and argument t. Although Equation AVII has a complex formation, its value is a real number.

When $Z/l_f>\sin\theta$ and $Z/l_f\leq 1$,

$$\mathrm{Num}\left(\left[0,Z\right],\left[\theta,\theta+d\theta\right]\right)$$

$$=\frac{2ZV_f\cos\theta d\theta}{\pi r_f^2}\left\{\begin{array}{l}\int_{0}^{\sin\theta}\frac{\sin\theta\left[2\pi-4\arccos\left(\frac{w}{\sin\theta}\right)\right]}{2\pi w}du\\+\int_{\sin\theta}^{Z/l_f}\frac{\sin\theta\cdot 2\pi}{2\pi w}dw\end{array}\right\}$$

$$=\frac{2ZV_f\sin\theta\cos\theta d\theta}{\pi^2r_f^2}\left[\begin{array}{l}\int_{0}^{\sin\theta}\frac{\pi-2\arccos\left(\frac{w}{\sin\theta}\right)}{w}du\\+\int_{\sin\theta}^{Z/l_f}\frac{\pi}{w}dw\end{array}\right]$$

$$=\frac{2ZV_f\sin\theta\cos\theta d\theta}{\pi^2r_f^2}\left\{\begin{array}{l}i\left[\mathrm{Li}_2\left(1-\exp\left(i\pi\right)\right)-\left(\frac{\pi}{2}\right)^2\right]\\+\pi\ln\left(\frac{Z}{l_f\sin\theta}\right)\end{array}\right\} \quad \text{(AXVIII)}$$

and when $Z/l_f > 1$,

$$\begin{aligned}
&\mathrm{Num}\left(\left[0,Z\right],\left[\theta,\theta+d\theta\right]\right)\\
&=\frac{2ZV_f\cos\theta d\theta}{\pi r_f^2}\left\{\int_0^1\left[\frac{P\left(w,\theta\right)d\theta}{\int_0^{\pi/2}P\left(w,\theta\right)d\theta}\right]dw+\int_1^{Z/l_f}\sin\theta dw\right\}\\
&=\frac{2ZV_f\sin\theta\cos\theta d\theta}{\pi^2 r_f^2}\left\{\begin{aligned}&i\left[\mathrm{Li}_2\left(1-\exp\left(i\pi\right)\right)-\left(\frac{\pi}{2}\right)^2\right]\\&+\pi\left[\ln\left(\frac{1}{\sin\theta}\right)+\frac{Z}{l_f}-1\right]\end{aligned}\right\}
\end{aligned}\tag{AXIX}$$

Appendix B: Two-dimensional boundary constraints

For a 2D case with width Y and thickness Z, the amount of fiber per unit length can be computed by:

$$N=\frac{YZV_f}{\pi l_f r_f^2}\tag{BI}$$

Similar to the 1D case, the coordinates can be non-dimensionalized by letting $v=y/(l_f/2)$ and $w=z/(l_f/2)$, where y and z are the distances from the boundary in width and thickness directions, respectively. Therefore, the body can be divided into four regions, that is, Region 1 ($v<1$ and $w<1$), Region 2 ($v<1$ and $w\geq 1$), Region 3 ($v\geq 1$ and $w<1$), and Region 4 ($v\geq 1$ and $w\geq 1$), as shown in Figure B1. For different cases, Regions 2, 3, and 4 may not exist.

If the distance between the fiber center and a specific cross-section plane is more than $\pm l_f\cos\theta/2$, the fiber cannot pass through the plane. Thus, the number of fibers crossing this specific cross-section plane at a given angle can be computed for any dimensionless coordinates (v, w) from the boundaries:

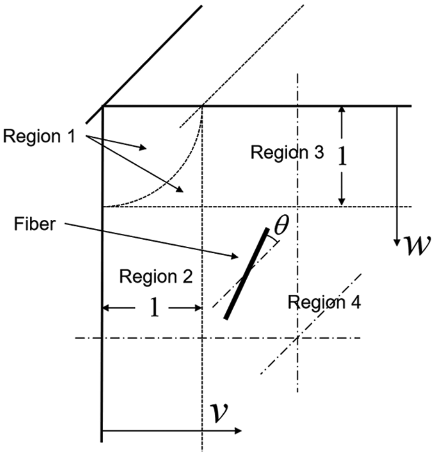

Figure B1. The schematic of a non-dimensionalized 2D case with four different regions.

$$\begin{aligned}
&\mathrm{Num}\left(v,w,\left[\theta,\theta+d\theta\right]\right)\\
&=N\cdot 2\cdot\frac{l_f\cos\theta}{2}\cdot\frac{P\left(v,w,\theta\right)d\theta}{\int_0^{\pi/2}P\left(v,w,\theta\right)d\theta}\\
&=\frac{YZV_f\cos\theta}{\pi r_f^2}\cdot\frac{P\left(v,w,\theta\right)d\theta}{\int_0^{\pi/2}P\left(v,w,\theta\right)d\theta}
\end{aligned}\tag{BII}$$

and the total number of fibers crossing this plane at a given angle can be integrated through the cross-section:

$$\begin{aligned}
&\mathrm{Num}\left(\left[0,Y\right],\left[0,Z\right],\left[\theta,\theta+d\theta\right]\right)\\
&=4\int_0^{Z/l_f}\int_0^{Y/l_f}\mathrm{Num}\left(v,w,\left[\theta,\theta+d\theta\right]\right)dvdw\\
&=\frac{4YZV_f\cos\theta d\theta}{\pi r_f^2}\cdot\int_0^{Z/l_f}\int_0^{Y/l_f}\left[\frac{P\left(v,w,\theta\right)d\theta}{\int_0^{\pi/2}P\left(v,w,\theta\right)d\theta}\right]dvdw
\end{aligned}\tag{BIII}$$

where for Region 1:

$$P\left(v,w,\theta\right)=\begin{cases}\sin\theta\cdot 2\pi & \theta\leq\arcsin\left[\min\left(v,w\right)\right]\\ \sin\theta\cdot\left\{\begin{aligned}&2\pi-\\&4\arccos\left[\frac{\min\left(v,w\right)}{\sin\theta}\right]\end{aligned}\right\} & \begin{aligned}&\arcsin\left[\min\left(v,w\right)\right]\\&<\theta\leq\arcsin\\&\left[\max\left(v,w\right)\right]\end{aligned}\\ \sin\theta\cdot\left[\begin{aligned}&2\pi-\\&4\arccos\left(\frac{v}{\sin\theta}\right)-\\&4\arccos\left(\frac{w}{\sin\theta}\right)\end{aligned}\right] & \begin{aligned}&\arcsin\left[\max\left(v,w\right)\right]\\&<\theta\text{ and }\sin\theta\leq\sqrt{v^2+w^2}\end{aligned}\\ 0 & \sin\theta>\sqrt{v^2+w^2}\end{cases}\tag{BIV}$$

for Region 2:

$$P\left(v,w,\theta\right)=\begin{cases}\sin\theta\cdot 2\pi & \theta\leq\arcsin v\\ \sin\theta\cdot\left[2\pi-4\arccos\left(\frac{v}{\sin\theta}\right)\right] & \theta>\arcsin v\end{cases}\tag{BV}$$

for Region 3:

$$P\left(v,w,\theta\right)=\begin{cases}\sin\theta\cdot 2\pi & \theta\leq\arcsin w\\ \sin\theta\cdot\left[2\pi-4\arccos\left(\frac{w}{\sin\theta}\right)\right] & \theta>\arcsin w\end{cases}\tag{BVI}$$

for Region 4:

$$P\left(v,w,\theta\right)=\sin\theta\cdot 2\pi\tag{BVII}$$

Consider a specific position (v, w) in Region 1 where v ≤w <1 and $\sqrt{v^2+w^2}<1$, similar to the 1D case shown in Equation A10:

$$\begin{aligned}&\int_0^{\pi/2} P(v,w,\theta)d\theta\\&=\int_0^{\arcsin v} P(v,w,\theta)d\theta+\int_{\arcsin v}^{\arcsin w} P(v,vw,\theta)d\theta\\&+\int_{\arcsin w}^{\arcsin\sqrt{v^2+w^2}} P(v,w,\theta)d\theta+\int_{\arcsin\sqrt{v^2+w^2}}^{\pi/2} P(v,w,\theta)d\theta\end{aligned}\tag{BVIII}$$

Substituting Equation B4 into Equation B8 and rearranging:

$$\begin{aligned}&\int_0^{\pi/2} P(v,w,\theta)d\theta\\&=2\pi\int_0^{\arcsin\sqrt{v^2+w^2}}\sin\theta d\theta-4\int_{\arcsin v}^{\arcsin\sqrt{v^2+w^2}}\sin\theta\arccos\left(\frac{v}{\sin\theta}\right)d\theta\\&-4\int_{\arcsin w}^{\arcsin\sqrt{v^2+w^2}}\sin\theta\arccos\left(\frac{w}{\sin\theta}\right)d\theta\end{aligned}\tag{BIX}$$

Let θ_v=arcsin$v$, θ_w=arcsin$w$, and $\theta_r=\arcsin\left(\sqrt{v^2+w^2}\right)$, Equation BXIX can be rewritten as:

$$\begin{aligned}&\int_0^{\pi/2} P(v,w,\theta)d\theta\\&=2\pi\int_0^{\theta_r}\sin\theta d\theta-4\int_{\theta_v}^{\theta_r}\sin\theta\arccos\left(\frac{v}{\sin\theta}\right)d\theta\\&-4\int_{\theta_w}^{\theta_r}\sin\theta\arccos\left(\frac{w}{\sin\theta}\right)d\theta\end{aligned}\tag{BXIX}$$

where

$$\int_0^{\theta_r}\sin\theta d\theta=1-\cos\theta_r=1-\sqrt{1-v^2-w^2}\tag{BXI}$$

Similar to Equation AXIV, it can be computed that:

$$\begin{aligned}&\int_{\theta_v}^{\theta_r}\sin\theta\arccos\left(\frac{v}{\sin\theta}\right)d\theta\\&=-\sqrt{1-v^2-w^2}\arctan\left(\frac{w}{v}\right)-\\&v\left[\frac{\pi}{2}-\arcsin\left(\frac{\sqrt{1-v^2-w^2}}{\sqrt{1-v^2}}\right)\right]\\&+\left[\frac{\pi}{2}-\arctan\left(\frac{v\sqrt{1-v^2-w^2}}{w}\right)\right]\end{aligned}\tag{BXII}$$

and

$$\begin{aligned}&\int_{\theta w}^{\theta_r}\sin\theta\arccos\left(\frac{w}{\sin\theta}\right)d\theta\\&=-\sqrt{1-v^2-w^2}\arctan\left(\frac{v}{w}\right)-\\&w\left[\frac{\pi}{2}-\arcsin\left(\frac{\sqrt{1-v^2-w^2}}{\sqrt{1-w^2}}\right)\right]\\&+\left[\frac{\pi}{2}-\arctan\left(\frac{w\sqrt{1-v^2-w^2}}{v}\right)\right]\end{aligned}\tag{BXIII}$$

Substituting Equations BXI–BXIII into Equation BX and rearranging:

$$\begin{aligned}&\int_0^{\pi/2} P(v,w,\theta)d\theta\\&=2\pi(v+w-1)-4\left[\begin{matrix}v\arctan\left(\dfrac{\sqrt{1-v^2-w^2}}{w}\right)\\+w\arctan\left(\dfrac{\sqrt{1-v^2-w^2}}{v}\right)\end{matrix}\right]\\&+4\left[\arctan\left(\frac{v\sqrt{1-v^2-w^2}}{w}\right)+\arctan\left(\frac{w\sqrt{1-v^2-w^2}}{v}\right)\right]\end{aligned}\tag{BXIV}$$

Similarly, when $\sqrt{v^2+w^2}\geq 1$, Equation BVIII becomes:

$$\begin{aligned}&\int_0^{\pi/2} P(v,w,\theta)d\theta\\&=\int_0^{\arcsin v} P(v,w,\theta)d\theta+\int_{\arcsin v}^{\arcsin w} P(v,w,\theta)d\theta\\&+\int_{\arcsin w}^{\pi/2} P(v,w,\theta)d\theta\\&=2\pi-4\left(-\frac{\pi v}{2}+\frac{\pi}{2}\right)-4\left(-\frac{\pi w}{2}+\frac{\pi}{2}\right)\\&=2\pi(v+w-1)\end{aligned}\tag{BXV}$$

Apparently, Equations BXIV and BXV can also be applied for conditions where $v<w<1$.

Comparing Equations BV–BVII with Equation AVIII, it can be concluded that for Region 2:

$$P(v,w,\theta)=P(v,\theta)\tag{BXVI}$$

for Region 3:

$$P(v,w,\theta)=P(w,\theta)\tag{BXVII}$$

and for Region 4:

$$\int_0^{\pi/2} P\left(v,w,\theta\right)d\theta = 2\pi \tag{BXVIII}$$

Therefore, when $Y/l_f \le Z/l_f < 1$ and $\sqrt{Y^2+Z^2}\big/l_f \le 1$, Equation BIII can be written as:

$$\begin{aligned}&\mathrm{Num}\left(\left[0,Y\right],\left[0,Z\right],\left[\theta,\theta+d\theta\right]\right)\\ &= \frac{4YZV_f\cos\theta d\theta}{\pi r_f^2}\cdot\int_0^{Z/l_f}\int_0^{Y/l_f}\left[\frac{P\left(v,w,\theta\right)d\theta}{\int_0^{\pi/2}P\left(v,w,\theta\right)d\theta}\right]dvdw\end{aligned} \tag{BXIX}$$

where $P(v,w,\theta)$ is given by Equation BVI and $\int_0^{\pi/2}P\left(v,w,\theta\right)d\theta$ is computed by Equation BXIV. When $Y/l_f \le Z/l_f < 1$ and $\sqrt{Y^2+Z^2}\big/l_f > 1$, Equation BIII can be written as:

$$\begin{aligned}&\mathrm{Num}\left(\left[0,Y\right],\left[0,Z\right],\left[\theta,\theta+d\theta\right]\right)\\ &= \frac{4YZV_f\cos\theta d\theta}{\pi r_f^2}\Bigg\{\int_0^{\sqrt{1-Y^2/l_f^2}}\int_0^{Y/l_f}\left[\frac{P\left(v,w,\theta\right)d\theta}{\int_0^{\pi/2}P\left(v,w,\theta\right)d\theta}\right]dvdw\\ &+\int_{\sqrt{1-Y^2/l_f^2}}^{Z/l_f}\int_0^{\sqrt{1-w^2}}\left[\frac{P\left(v,w,\theta\right)d\theta}{\int_0^{\pi/2}P\left(v,w,\theta\right)d\theta}\right]dvdw\\ &+\int_{\sqrt{1-Y^2/l_f^2}}^{Z/l_f}\int_{\sqrt{1-w^2}}^{Y/l_f}\left[\frac{P\left(v,w,\theta\right)d\theta}{\int_0^{\pi/2}P\left(v,w,\theta\right)d\theta}\right]dvdw\Bigg\}\end{aligned} \tag{BXX}$$

Where $P(v,w,\theta)$ is given by Equation BIV. $\int_0^{\pi/2}P\left(v,w,\theta\right)d\theta$ is computed by Equation BXIV in the first two terms and is computed by Equation BXV in the third term. When $Y/l_f < 1$ and $Z/l_f \ge 1$, Equation BIII can be written as:

$$\begin{aligned}&\mathrm{Num}\left(\left[0,Y\right],\left[0,Z\right],\left[\theta,\theta+d\theta\right]\right)\\ &= \frac{4YZV_f\cos\theta d\theta}{\pi r_f^2}\Bigg\{\int_0^{\sqrt{1-Y^2/l_f^2}}\int_0^{Y/l_f}\left[\frac{P\left(v,w,\theta\right)d\theta}{\int_0^{\pi/2}P\left(v,w,\theta\right)d\theta}\right]dvdw\\ &+\int_{\sqrt{1-Y^2/l_f^2}}^{1}\int_0^{\sqrt{1-w^2}}\left[\frac{P\left(v,w,\theta\right)d\theta}{\int_0^{\pi/2}P\left(v,w,\theta\right)d\theta}\right]dvdw+\\ &\int_{\sqrt{1-Y^2/l_f^2}}^{1}\int_{\sqrt{1-w^2}}^{X/l_f}\left[\frac{P\left(v,w,\theta\right)d\theta}{\int_0^{\pi/2}P\left(v,w,\theta\right)d\theta}\right]dvdw\\ &+\int_1^{Z/l_f}\int_0^{Y/l_f}\left[\frac{P\left(v,w,\theta\right)d\theta}{\int_0^{\pi/2}P\left(v,w,\theta\right)d\theta}\right]dvdw\Bigg\}\end{aligned} \tag{BXXI}$$

where $P(v,w,\theta)$ is given by Equation BIV. $\int_0^{\pi/2}P\left(v,w,\theta\right)d\theta$ is computed by Equation BXVI in the first two terms and is computed by Equation BXV in the third term. According to Equation BXVI:

$$\begin{aligned}&\int_1^{Z/l_f}\int_0^{Y/l_f}\left[\frac{P\left(v,w,\theta\right)d\theta}{\int_0^{\pi/2}P\left(v,w,\theta\right)d\theta}\right]dvdw\\ &= \int_1^{Z/l_f}\int_0^{Y/l_f}\left[\frac{P\left(v,\theta\right)d\theta}{2\pi v}\right]dvdw\\ &= \begin{cases} i\left\{\begin{aligned}&\mathrm{Li}_2\left(1-\exp\left[2i\arcsin\left(\frac{Y}{l_f\sin\theta}\right)\right]\right)\\ &-\arcsin^2\left(\frac{Y}{l_f\sin\theta}\right)\end{aligned}\right\} & Y/l_f \le \sin\theta\\ \left(\frac{Z}{l_f}-1\right)\frac{\sin\theta}{\pi} & \\ i\left\{\begin{aligned}&\left[\mathrm{Li}_2\left(1-\exp\left(i\pi\right)\right)-\left(\frac{\pi}{2}\right)^2\right]+\\ &\pi\ln\left(\frac{Y}{l_f\sin\theta}\right)\end{aligned}\right\}\left(\frac{Z}{l_f}-1\right)\frac{\sin\theta}{\pi} & Y/l_f > \sin\theta\end{cases}\end{aligned} \tag{BXXII}$$

When $Y/l_f \ge 1$ and $Z/l_f \ge 1$, Equation BIII can be written as:

$$\begin{aligned}&\mathrm{Num}\left(\left[0,Y\right],\left[0,Z\right],\left[\theta,\theta+d\theta\right]\right)\\ &= \frac{4YZV_f\cos\theta d\theta}{\pi r_f^2}\Bigg\{\int_0^1\int_0^{\sqrt{1-w^2}}\left[\frac{P\left(v,w,\theta\right)d\theta}{\int_0^{\pi/2}P\left(v,w,\theta\right)d\theta}\right]dvdw\\ &+\int_0^1\int_{\sqrt{1-w^2}}^{Y/l_f}\left[\frac{P\left(v,w,\theta\right)d\theta}{\int_0^{\pi/2}P\left(v,w,\theta\right)d\theta}\right]dvdw+\\ &\int_1^{Z/l_f}\int_0^1\left[\frac{P\left(v,w,\theta\right)d\theta}{\int_0^{\pi/2}P\left(v,w,\theta\right)d\theta}\right]dvdw\\ &+\int_0^1\int_1^{Y/l_f}\left[\frac{P\left(v,w,\theta\right)d\theta}{\int_0^{\pi/2}P\left(v,w,\theta\right)d\theta}\right]dvdw+\\ &\int_1^{Z/l_f}\int_1^{Y/l_f}\left[\frac{P\left(v,w,\theta\right)d\theta}{\int_0^{\pi/2}P\left(v,w,\theta\right)d\theta}\right]dvdw\Bigg\}\end{aligned} \tag{BXXIII}$$

where $P(v,w,\theta)$ is given by Equation BIV. $\int_0^{\pi/2}P\left(v,w,\theta\right)d\theta$ is computed by Equation BXIV in the first term and is computed by Equation BXV in the second term. Similar to Equation BXXII:

$$\int_1^{Z/l_f}\int_0^1\left[\frac{P(v,w,\theta)d\theta}{\int_0^{\pi/2}P(v,w,\theta)d\theta}\right]dvdw$$

$$=\int_1^{Z/l_f}\int_0^{Y/l_f}\left[\frac{P(v,\theta)d\theta}{2\pi u}\right]dvdw$$

$$=i\left\{\begin{matrix}\left[\mathrm{Li}_2\left(1-\exp(i\pi)\right)-\left(\frac{\pi}{2}\right)^2\right]+\\ \pi\ln\left(\frac{Y}{l_f\sin\theta}\right)\end{matrix}\right\}\left(\frac{Z}{l_f}-1\right)\frac{\sin\theta}{\pi} \tag{BXXIV}$$

and

$$\int_0^1\int_1^{Y/l_f}\left[\frac{P(v,w,\theta)d\theta}{\int_0^{\pi/2}P(v,w,\theta)d\theta}\right]dvdw$$

$$=\int_1^{Y/l_f}\int_0^1\left[\frac{P(w,\theta)d\theta}{2\pi w}\right]dwdv$$

$$=i\left\{\begin{matrix}\left[\mathrm{Li}_2\left(1-\exp(i\pi)\right)-\left(\frac{\pi}{2}\right)^2\right]+\\ \pi\ln\left(\frac{Z}{l_f\sin\theta}\right)\end{matrix}\right\}\left(\frac{Y}{l_f}-1\right)\frac{\sin\theta}{\pi} \tag{BXXV}$$

According to Equations BVII and BXVIII:

$$\int_1^{Z/l_f}\int_1^{Y/l_f}\left[\frac{P(v,w,\theta)d\theta}{\int_0^{\pi/2}P(v,w,\theta)d\theta}\right]dvdw=\left(\frac{Y}{l_f}-1\right)\left(\frac{Z}{l_f}-1\right)\sin\theta \tag{BXXVI}$$

To the authors' best estimation, Equations BXIX, BXX, BXXI, and BXXIII are unlikely to have an analytical solution due to the arctan terms in the denominator of region 1, and numerical method would be required to compute the fiber orientation distribution for 2D cases.

Appendix C: Three-dimensional boundary constraints

Similar to the 2D case, for a 3D case with length *X*, width *Y*, and thickness *Z*, the amount of fiber can be computed by:

$$N=\frac{XYZV_f}{\pi l_f r_f^2} \tag{CI}$$

Let $u=x/(l_f/2)$, $v=y/(l_f/2)$, and $w=z/(l_f/2)$, where *x*, *y*, and *z* are the distance from the boundary in length, width, and thickness directions, respectively. Therefore, the body can be divided into eight regions, that is, Region 1 ($u<1$, $v<1$, and $w<1$), Region 2 ($u<1$, $v<1$, and $w\geq1$), Region 3 ($u<1$, $v\geq1$, and $w<1$), Region 4 ($u<1$, $v\geq1$, and $w\geq1$), Region 5 ($u\geq1$, $v<1$, and $w<1$), Region 6 ($u\geq1$, $v<1$, and $w\geq1$), Region 7 ($u\geq1$, $v\geq1$, and $w<1$), and Region 8 ($u\geq1$, $v\geq1$, and $w\geq1$). For different cases, Regions 2–8 may not exist.

If the distance between the fiber center and a specific cross-section plane is more than $\pm l_f\cos\theta/2$, the fiber cannot pass through the plane. Thus, the number of fibers crossing this specific cross-section plane at a given angle can be computed for any dimensionless coordinates (*u*, *v*, *w*) from the boundaries:

$$\mathrm{Num}\left(u,v,w,[\theta,\theta+d\theta]\right)$$

$$=N\cdot2\cdot\frac{l_f\cos\theta}{2}\cdot\frac{P(u,v,w,\theta)d\theta}{\int_0^{\pi/2}P(u,v,w,\theta)d\theta} \tag{CII}$$

$$=\frac{XYZV_f\cos\theta}{\pi r_f^2}\cdot\frac{P(u,v,w,\theta)d\theta}{\int_0^{\pi/2}P(u,v,w,\theta)d\theta}$$

Moreover, the total number of fibers crossing this plane at a given angle can be integrated through the cross-section:

$$\mathrm{Num}\left([0,X],[0,Y],[0,Z],[\theta,\theta+d\theta]\right)$$

$$=8\int_0^{Z/l_f}\int_0^{Y/l_f}\int_0^{X/l_f}\mathrm{Num}\left(u,v,w,[\theta,\theta+d\theta]\right)dudvdw$$

$$=\frac{8XYZV_f\cos\theta d\theta}{\pi r_f^2} \tag{CIII}$$

$$\int_0^{Z/l_f}\int_0^{Y/l_f}\int_0^{X/l_f}\left[\frac{P(u,v,w,\theta)d\theta}{\int_0^{\pi/2}P(u,v,w,\theta)d\theta}\right]dudvdw$$

where for Region 1:

$$P(u,v,w,\theta)=$$

$$\begin{cases}0 & \theta<\arccos u\\ \sin\theta\cdot2\pi & \theta\geq\arccos u\text{ and }\theta\leq\arcsin\left[\min(v,w)\right]\\ \sin\theta\cdot\left\{\begin{matrix}2\pi-\\ 4\arccos\left[\frac{\min(v,w)}{\sin\theta}\right]\end{matrix}\right\} & \theta\geq\arccos u\text{ and }\arcsin\left[\min(v,w)\right]<\theta\leq\arcsin\left[\max(v,w)\right]\\ \sin\theta\cdot\left[\begin{matrix}2\pi-\\ 4\arccos\left(\frac{v}{\sin\theta}\right)-\\ 4\arccos\left(\frac{w}{\sin\theta}\right)\end{matrix}\right] & \theta\geq\arccos u\text{ and }\arcsin\left[\max(v,w)\right]<\theta\text{ and }\sin\theta\leq\sqrt{v^2+w^2}\\ 0 & \theta\geq\arccos u\text{ and }\sin\theta>\sqrt{v^2+w^2}\end{cases} \tag{CIV}$$

for Region 2:

$$P(u,v,w,\theta)=\begin{cases} 0 & \theta<\arccos u \\ \sin\theta\cdot 2\pi & \theta\geq\arccos u \text{ and } \theta\leq\arcsin v \\ \sin\theta\cdot\left[2\pi-4\arccos\left(\dfrac{v}{\sin\theta}\right)\right] & \theta\geq\arccos u \text{ and } \theta>\arcsin v \end{cases} \quad \text{(CV)}$$

for Region 3:

$$P(u,v,w,\theta)=\begin{cases} 0 & \theta<\arccos u \\ \sin\theta\cdot 2\pi & \theta\geq\arccos u \text{ and } \theta\leq\arcsin w \\ \sin\theta\cdot\left[2\pi-4\arccos\left(\dfrac{w}{\sin\theta}\right)\right] & \theta\geq\arccos u \text{ and } \theta>\arcsin w \end{cases} \quad \text{(CVI)}$$

for Region 4:

$$P(u,v,w,\theta)=\begin{cases} 0 & \theta<\arccos u \\ \sin\theta\cdot 2\pi & \theta\geq\arccos u \end{cases} \quad \text{(CVII)}$$

For Regions 5 – 8, the functions are described by Equations BIV–BVII, respectively. Comparing Equations CIV–CVII with Equations BIV–BVII, respectively, it can be concluded that:

$$P(u,v,w,\theta)=\begin{cases} 0 & \theta<\arccos u \\ P(v,w,\theta) & \theta\geq\arccos u \end{cases} \quad \text{(CVIII)}$$

and, thus, Equation CIII becomes:

$$\begin{aligned} &\mathrm{Num}([0,X],[0,Y],[0,Z],[\theta,\theta+d\theta]) \\ &=\frac{8XYZV_f\cos\theta d\theta}{\pi r_f^2}\left\{\begin{array}{c}\displaystyle\int_0^{\cos\theta}\int_0^{Y/l_f}\int_0^{Z/l_f}0dwdvdu+ \\ \displaystyle\int_{\cos\theta}^{X/l_f}\int_0^{Y/l_f}\int_0^{Z/l_f}\left[\frac{P(v,w,\theta)d\theta}{\int_0^{\pi/2}P(v,w,\theta)d\theta}\right] \\ dwdvdu\end{array}\right\} \\ &=2X\left(\frac{X}{l_f}-\cos\theta\right)\mathrm{Num}([0,Y],[0,Z],[\theta,\theta+d\theta]) \end{aligned} \quad \text{(CIX)}$$

Appendix D: Region 1 in three-dimensional boundary constraints

For Region 1 in the 3D case, an apparent restriction is that the fiber cannot exist in the area where $x^2+y^2+z^2<l_f^2/4$. This restriction can be fully covered by conditions $\theta<\arccos\left(\frac{x}{l_f/2}\right)$ and $\theta>\arcsin\left(\frac{\sqrt{y^2+z^2}}{l_f/2}\right)$. This conclusion can be derived from this proposition: Given $x^2+y^2+z^2<l_f^2/4$, it can be proven that $\arcsin\left(\frac{\sqrt{y^2+z^2}}{l_f/2}\right)<\arccos\left(\frac{x}{l_f/2}\right)$

Proof:

Let $\alpha=\arccos\left(\frac{x}{l_f/2}\right)$, $\beta=\arcsin\left(\frac{\sqrt{y^2+z^2}}{l_f/2}\right)$, then $\cos\alpha=\frac{x}{l_f/2}$, $\sin\beta=\frac{\sqrt{y^2+z^2}}{l_f/2}$.

Therefore,

$$\begin{aligned} \sin\alpha&=\sqrt{1-\cos^2\alpha}=\sqrt{\frac{l_f^2/4-x^2}{l_f^2/4}} \\ &>\sqrt{\frac{x^2+y^2+z^2-x^2}{l_f^2/4}}=\frac{\sqrt{y^2+z^2}}{l_f/2}=\sin\beta \end{aligned} \quad \text{(DI)}$$

which means $\alpha>\beta$ since $\alpha<\varpi/2$ and $\beta<\varpi/2$. Thus, $\arcsin\left(\frac{\sqrt{y^2+z^2}}{l_f/2}\right)<\arccos\left(\frac{x}{l_f/2}\right)$. Therefore, given a specific θ in the area where $x^2+y^2+z^2<l_f^2/4$, it can be found that either $\theta<\arccos\left(\frac{x}{l_f/2}\right)$ or $\theta>\arcsin\left(\frac{\sqrt{y^2+z^2}}{l_f/2}\right)$, where both conditions would give $P(u,v,w,\theta)=0$ in Equation CIV.

ACCSCIENCE PUBLISHING

Materials Science in Additive Manufacturing

ORIGINAL RESEARCH ARTICLE

Fatigue behavior of additively manufactured Ti3Al2V alloy

Amit Bandyopadhyay*, Sushant Ciliveri, Stefano Guariento, Nathan Zuckschwerdt, William W. Hogg

W. M. Keck Biomedical Materials Research Laboratory, School of Mechanical and Materials Engineering, Washington State University, Pullman, Washington 99164, USA

Abstract

In this study, we measured the tensile, compression, and fatigue behavior of additively manufactured Ti3Al2V as a function of build orientation. Ti3Al2V alloy was prepared by mixing commercially pure titanium and Ti6Al4V in 1:1 wt. ratio. Laser powder bed fusion-based additive manufacturing technique was used to fabricate the samples. Tensile tests resulted in an ultimate strength of 989 ± 8 MPa for Ti3Al2V. Ti6Al4V 90° orientation samples showed a compressive yield strength of 1178 ± 33 MPa and that for Ti3Al2V 90° orientation samples were 968 ± 24 MPa. By varying the build orientation to account for anisotropy, Ti32 45° and Ti32 0° samples displayed almost similar compressive yield strength values of 1071 ± 16 and 1051 ± 18 MPa, respectively, which were higher than that of Ti32 90° sample. Fatigue loading revealed an endurance limit (10 million cycles) of 250 MPa for Ti6Al4V and of 219 MPa for Ti3Al2V built at 90° orientation. The effect of the build orientation was significant under fatigue loading; Ti3Al2V built at 45° and 0° orientations displayed endurance limits of 387.5 MPa and 512 MPa, respectively; more than two-fold increment in endurance limit was observed. In conclusion, the superior attributes of Ti3Al2V alloy over Ti6Al4V alloy, as demonstrated in this study, justify its potential in load-bearing applications, particularly for use in orthopedic devices.

Keywords: Additive manufacturing; Titanium alloys; Alloy design; Load-bearing implants; Fatigue behavior

***Corresponding authors:**
Amit Bandyopadhyay
(amitband@wsu.edu)

Citation: Bandyopadhyay A, Ciliveri S, Guariento S, *et al*., 2023, Fatigue behavior of additively manufactured Ti3Al2V alloy. *Mater Sci Addi Manuf*, 2(3): 1705. https://doi.org/10.36922/msam.1705

Received: August 29, 2023

Accepted: September 12, 2023

1. Introduction

The selection of metallic biomaterial for creating load-bearing implants depends on several critical factors, including mechanical properties, cytotoxicity, corrosion resistance, and biocompatibility of the material. Titanium (Ti) alloys are the most popular choice among the metallic biomaterials for load-bearing implant applications[1,2]. Specifically, commercially pure titanium (CpTi) has been popularized for over six decades as a first-generation Ti-based biomaterial as it is not cytotoxic and shows excellent corrosion resistance[3]. Possessing high strength and excellent fatigue resistance is an essential requirement of implant devices for hard tissue replacement at load-bearing sites. However, CpTi exhibits poor fatigue performance, and this has prompted a search for alternative materials to fill the application gap. An alloy Ti6Al4V originally designed as an aerospace material by the Army Research Laboratory in the 1950s, which is resistant to high-temperature oxidation, was found to be an ideal material to replace CpTi[4-6]. Ti6Al4V shows high strength and excellent fatigue resistance compared to CpTi. Despite having a lower biocompatibility compared with CpTi[7,8], Ti6Al4V alloy has been employed as the ultimate orthopedic implant material of choice over the past six decades[5,9-12].

Along with promising mechanical performance, biocompatibility plays a key role in the implant's stability and lifespan[13]. Aside from that, improper implant fixation is one of the major issues necessitating revision surgery procedures. Delayed tissue growth, implant surface integration, and host bone attachment are signs of poor biocompatibility with the material[14]. Since Ti6Al4V does not aid in accelerated bone healing[13], implant loosening becomes a common nuisance among the elderly patients with compromised bone, necessitating revision surgery procedures on such patients, which severely affect their health and ultimately reduce their life expectancy. To account for the poor biocompatibility of α+β phase Ti6Al4V, various high-strength-low-modulus β-Ti alloys with a relatively higher fraction of a variety of biocompatible β stabilizers, such as Mo, Nb, Ta, Fe, Cr, and Zr, have been designed and developed[3,15,16]. Despite possessing superior biological performance, these β-Ti alloys lacked fatigue strength compared to Ti6Al4V, making them less than ideal for most load-bearing applications[17-19]. Lin *et al.* found that the fatigue strength of commercial Ti-13Nb-13Zr[20] and Ti-7.5Mo[21] β-Ti alloys was lower than both Ti6Al4V and CpTi[17]. In face of the absence of an ideal material, the search for a suitable Ti-alloy with enhanced biocompatibility and adequate mechanical performance, especially fatigue strength, has never stopped.

An implant surgically placed *in vivo* at a load-bearing site is constantly under cyclic loading conditions. Fatigue is a principal factor of mechanical failure[22], and thus, fatigue resistance is one of the critical determinants of an implant's longevity[23]. Since β-Ti alloys manifest poorer fatigue performance[3], a different approach to designing the alloy must be implemented. Instead of introducing modifications to β-Ti alloy, we decided to develop Ti6Al4V alloy with better performance, focusing on the α+β-Ti phase domain. Knowing that the alloying elements, Al and V, confer high strength and excellent fatigue resistance on the resultant Ti6Al4V, we postulate that modifying their compositions would engender better performance of the alloy. Thus, we ponder whether adjusting the composition of Al and V to 6 wt.% and 4 wt.%, respectively, could create a Ti3Al2V alloy that boast higher biocompatibility compared with Ti6Al4V and is suitable for orthopedic applications.

This study employed a novel approach to alloy design: An alloy Ti3Al2V with reduced Al and V contents. An intermediate alloy between CpTi and Ti6Al4V is expected to possess enhanced biocompatibility without a significant degradation in strength. This study is focused on exploring the mechanical performance of this Ti3Al2V alloy, especially the fatigue behavior. This alloy was designed by mixing CpTi and Ti6Al4V in 1:1 weight ratio. This composition was processed through laser powder bed fusion (L-PBF)-based additive manufacturing (AM) technique. AM offers higher degrees of processing freedom over conventional methods and the flexibility of designing novel alloys in complex shapes and sizes[24-26]. AM aids in mimicking the patient's bone into the implant to be surgically placed, significantly reducing post-operative complications[27,28]. Since AM is a layer-wise process, the anisotropy parameter is crucial for the mechanical performance of AM parts under fatigue loading[10]. In this study, Ti3Al2V was fabricated in three orientations, 0°, 45°, and 90° to the build surface for compressive and fatigue characterization.

2. Materials and methods

2.1. Fabrication through L-PBF

Samples were designed on 3DXpert CAD Software (3D Systems, Rock Hill, SC). Compression and fatigue samples were designed and processed with 0°, 45°, and 90° orientations to the build direction, as shown in Figure 1. Fabrication was carried out using L-PBF-based AM technique on a PBF system (3D Systems ProX® DMP 200, Rock Hill, SC) consisting of a fiber laser (300 W) and applying wavelength (λ) = 1070 nm. Commercially pure Ti (CpTi) and Ti6Al4V (Ti64) powders were procured from AP&C (GE Additive, Cincinnati, Ohio, USA) and GKN Hoeganaes (Cinnaminson, NJ), respectively. Ti3Al2V (Ti32) composition was prepared by mixing CpTi and Ti64 in 1:1 weight ratio. All powders were spherically shaped and sieved to obtain a particle size <63 µm. The powders were loaded in the PBF system supply chamber and purged under an argon atmosphere to obtain an O_2 <500 ppm. A CpTi build plate of 2.5 cm thickness was secured on the build platform. The printing operation was carried out with a layer thickness of 30 µm, a laser power of 180 W, and a scan speed of 1600 mm/s.

2.2. Post-processing of fatigue specimens

Fatigue samples were subjected to post-processing steps to ensure consistent and reproducible results during subsequent analyses. These steps included turning, heat treatment, and sanding the samples before fatigue testing. Ti32 0° and 45° orientation samples or samples processed via PBF were printed with support layers

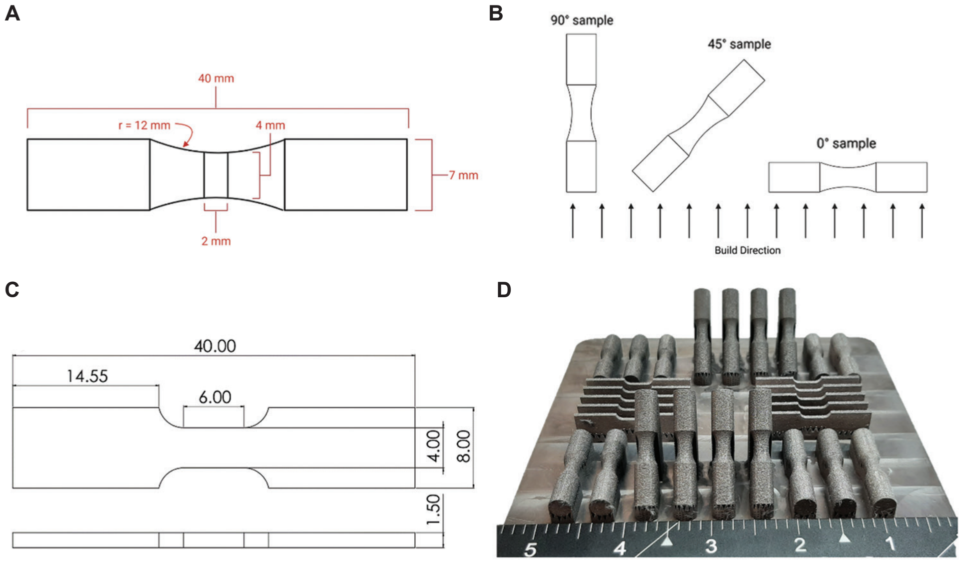

Figure 1. (A) Dimensions of the fatigue samples designed and printed by laser powder bed fusion (L-PBF)-based additive manufacturing technique. (B) A schematic of different orientations at 0°, 45°, and 90° to the build plate used for printing and testing the fatigue samples. (C) Dimensions of the tensile test coupons designed and printed via L-PBF. (D) Fatigue specimen at 0° and 45° orientations to the build plate and tensile specimens on completion of the build plate post-printing process.

positioned beneath the cylindrical surfaces, unlike their 90° counterparts. Before performing surface smoothing, it was necessary to eliminate the support structures. This task was accomplished using pliers and a vice grip to pry the supports off. This procedure and the prints themselves gave rise to minor deformation in the samples, which resulted in non-concentric samples. To address this issue, Tormach 770MX (Tormach Inc., Monona, WI) CNC machine with a rapid turn feature was utilized to remove sufficient material from the samples until they were concentric and free of any deformations. A pilot hole was drilled in the other end of the sample and fit with a live center to improve rigidity when turning.

The initial steps, which were meant for achieving a smooth surface finish on the 0° and 45° samples, involved Autodesk Fusion 360 and the Tormach 770MX. Each of the sample was then gripped by one end in the chuck, while the other was supported concentrically using a center point tool in the tailstock. This step was necessary for all 0° and 45° samples to ensure concentric rotation. Using the CNC machine with carbide insert tool, machining was performed only to create a smooth surface. Multiple passes were made gradually until the surface of the fatigue sample was visually smooth. The same Tormach surface smoothing process was performed on all Ti32 0°, 45°, and 90° samples. Once the samples were turned and processed, the next step was to remove the overhanging metal initially secured in the chuck of the CNC machine. When the fatigue samples were turned, part of the metal was secured in the chuck to ensure that a strong grip was held on the part. This extra piece of metal was removed using a bandsaw. Once removed, the sample was placed in a Thermolyne 48000 (Waltham, MA) furnace at 400°C for 1 h. The sample would then be furnace-cooled for 12 h. Finally, after being heat-treated, the sample was placed in a drill press, and the gauge and stems were sanded down using 400–600 grit emery cloth until all visual defects were removed.

2.3. Microstructural characterization

The top surface of the fatigue specimens was cut and mounted in a phenolic resin. The samples were ground with 80–1200 SiC grit-size grinding papers and polished using alumina dispersed in deionized water, with particle size gradually reducing from 1 to 0.05 µm. The samples were etched in Kroll's reagent, and the microstructure was imaged using a Keyance digital microscope (Model VHX-7000, Itasca, IL).

2.4. Tensile and compression tests

Dog-bone-shaped samples were mounted using manual non-shift wedge grips in a Shimadzu AG-1S Precision Universal Tensile Tester (Shimadzu, Columbia, MD). The samples were tested till failure using a constant crosshead displacement rate of 0.75 mm/min, and the raw load versus displacement data was recorded. All samples used, which were produced in adherence to the ASTM 52909 guidelines[29], p. 52 concerning sample sizing, had a designed size of a gauge length of 6 mm and a cross-sectional area of 4 mm × 1.5 mm. The samples were put in a furnace at 400°C for 1 h for heat treatment, and then furnace-cooled. The fracture surface of the tensile specimens was observed under a field emission scanning electron microscope (FESEM, FRI-SIRION, Portland, OR). Dense samples fabricated through L-PBF with a diameter of 7 mm and height of ~15 mm were used for compression tests. Ti64 samples used were built at a 90° orientation. For Ti32, the samples tested were built in 0°, 45°, and 90° orientations to the build plate. The samples were tested on an Instron servohydraulic system (600DXS, Grove City, Pennsylvania) in accordance with the ASTM E9-19 guidelines[30]. A 1.3 mm/min crosshead displacement rate was used, and the raw load versus displacement data was recorded. Compressive yield strength was evaluated from the raw data using the 0.2% strain offset method. Each composition and orientation were tested for at least 3 times.

2.5. Fatigue test

The post-processed samples were subjected to cyclic loading on an ADMET (Norwood, MA) Rotating Beam Fatigue Test System (4-point loading) fitted with Tormach (Madison, Wisconsin) 6 mm ER32 collets, in accordance with ISO 1143[31]. The gauge length of the test specimens was cleaned with ethanol. The system applies a load calculated from the stress amplitude and measured gauge diameter. The stress amplitude used was calculated as:

$$S = F\frac{32L}{\pi d^3} \tag{I}$$

Where F is the bending force applied, L is the force arm length, and d is the gauge diameter. Table 1 shows the loads selected expressed as the ratios of the applied bending loads to their respective compressive yield strength. Once the set load was applied, the sample was rotated at 3000 rpm until fracture or reached 10 million cycles without fracture at a stress amplitude of S and a stress ratio of R = −1 for pure reverse stress-controlled loading. The endurance limit was the lowest bending stress at which samples reached 10 million cycles without fracture. Following fracture, the fracture surfaces were observed under a Keyance digital microscope (Model VHX-7000, Itasca, IL).

3. Results

Ti6Al4V alloy is widely used in the manufacture of orthopedic implants owing to its excellent strength and fatigue performance. Compared with CpTi, Ti6Al4V alloy exhibits poorer biological performance but higher strength. The enhanced strength of Ti6Al4V alloy is attributed to the alloying elements, Al and V, whose primary function is to resist high-temperature oxidation, a common defect in aerospace applications. Since high-temperature oxidation resistance is not required in orthopedic implants, a novel

Table 1. Fatigue results for Ti64 and Ti32 compositions built at different orientations

Composition	Orientation	Nomenclature	Compressive yield stress (MPa)	Stress amplitude (MPa)	Stress ratio (stress amplitude/ compressive yield strength)	Cycles
Ti64	90°	Ti64-90	1178	387.5	0.33	19,275
				300	0.25	25,039
						87,147
				250	0.21	10 million*
Ti32	90°	Ti32-90	968	387.5	0.40	2385
						1930
				339.94	0.35	10,355
						1352
				219.318	0.23	10 million*
	45°	Ti32-45	1071	512.5	0.48	3,993,108
						4,907,598
				450	0.42	10 million*
						6,263,225
				387.5	0.36	10 million*
	0°	Ti32-0	1051	512.5	0.49	10 million*
						10 million*
				450	0.43	10 million*
				387.5	0.37	10 million*

alloy, Ti3Al2V, with reduced Al and V composition in Ti6Al4V, was designed and developed in this study specifically for orthopedic applications. We hypothesize that the fatigue resistance and strength performance of Ti32 alloy are comparable to those of Ti64.

3.1. Microstructure and build orientation

Figure 2 shows the microstructures of Ti64-90 and Ti32 at 0-45-90° build orientations. All samples showed typical metastable α’ martensitic needle-like morphology on the surface, typically observed in additively manufactured Ti64. Ti32-90 displayed residual pores on the surface, indicating interlayer lack of fusion; the top surface where the microstructure was observed was perpendicular to the build direction. The Ti32-45 and Ti32-0 had minimal residual pores since the top surface lies at an angle to the build direction. The effect of this interlayer lack of fusion pores was also observed in their respective fatigue performance.

3.2. Static mechanical performance: Tensile and compression behavior

Fatigue deformation primarily consists of alternating tensile and compression loading. It is essential to understand the behavior of Ti32 under static tensile and compression loading before fatigue tests. Extensive studies

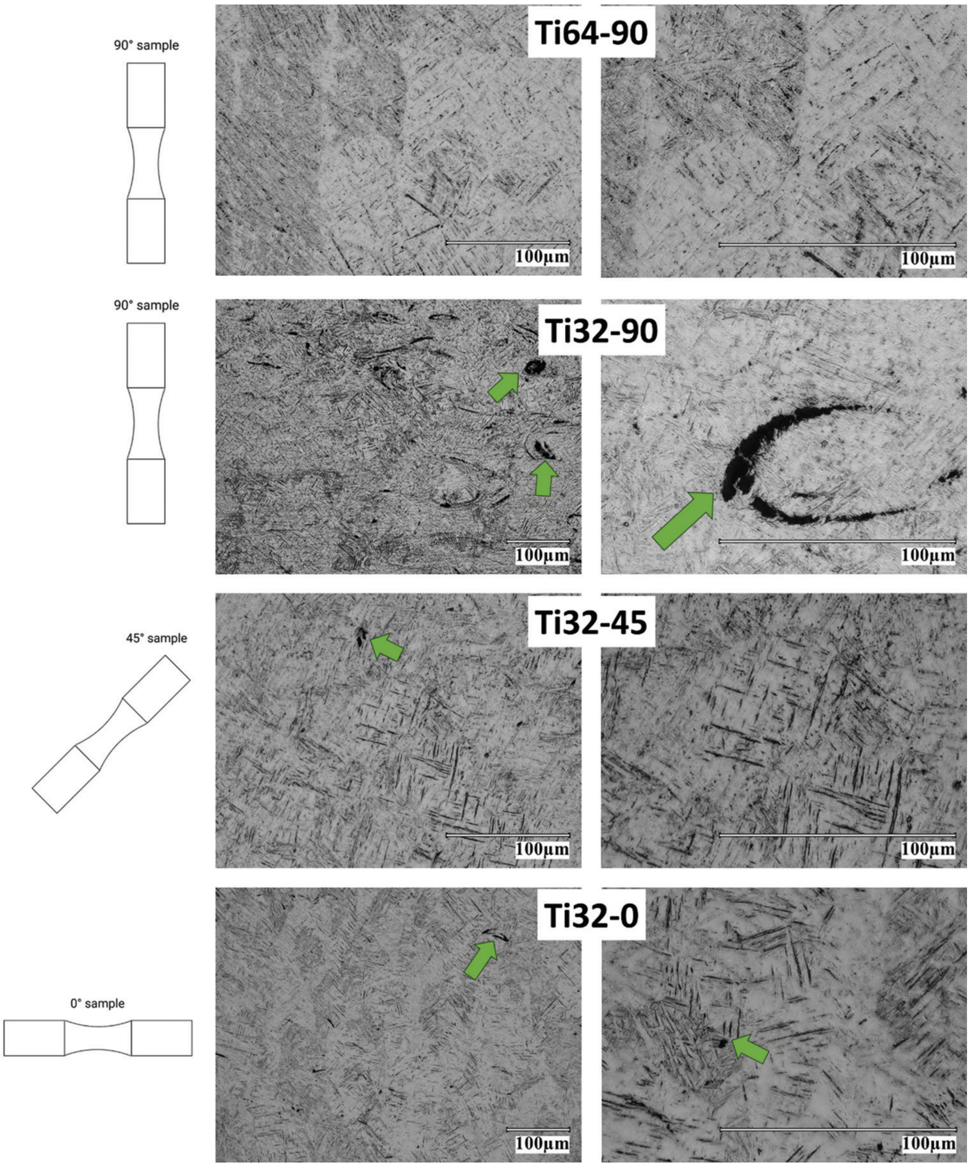

Figure 2. Top surfaces of the microstructures of Ti64-90 and Ti32-90, Ti32-45, and Ti32-0 samples. α’ martensitic needle-like morphology is observed in all specimens. The top surface of Ti32-90 perpendicular to the build direction displays large residual pores. The top surface of Ti32-45 and Ti32-0 show comparatively lesser residual pores.

have been carried out to evaluate the tensile performance of Ti64 alloy (Table 2). In this study, Ti32 alloy was subjected to tensile tests to evaluate the stress at failure (Table 3). As-printed non-heat-treated tensile specimens displayed a tensile elastic modulus of 106.8 ± 4.8 GPa, close to that of Ti6Al4V. Since Ti32 was designed with CpTi and Ti64 concoction in 1:1 weight ratio, and both CpTi and Ti64 displayed an elastic modulus ranging from 110 to 114 GPa, the tensile modulus of Ti32 was observed within a similar range. The ultimate tensile strength of non-heat treated Ti32 test specimens was 989 ± 8 MPa, which is quite similar to that of Ti64, ranging from 900 to 1200 MPa as reported in various studies (Table 2). AM-processed structures show high strengths due to their fast heating and cooling nature. Heat treatment was carried out to relieve the AM process-induced residual stresses.

The tensile elastic modulus of the heat-treated Ti32 specimens was 107.6 8 ± 5.8 GPa, similar to that of non-heat-treated specimens. The ultimate tensile strength was found to be 989 ± 4 MPa, similar to that of the non-heat-treated specimens, suggesting the heat treatment did not impact the tensile behavior. ISO 5823-3 (implants for surgery metallic materials) dictates that the Ti64 should have a tensile strength of at least 860 MPa[32]. The tensile strength of Ti32 specimens, however, exceeds this minimum strength requirement. Figure 3 shows the microstructure of the fracture surfaces from tensile tests for Ti32. The micrographs revealed dimple ridges, indicating the ductile behavior of Ti32 in conjunction with the specimen elongation of 8 ± 2% after failure. All samples fractured at 45° to the loading direction. No effect of heat treatment was observed.

It is essential to consider anisotropy while evaluating the mechanical properties of AM-processed structures. Compression tests were carried out for Ti64 built at 90° to the build plate and Ti32 built at three orientations (0, 45, and 90°), and the respective compressive yield strengths are presented in Table 3. Compositional variation from Ti64 to Ti32 was accompanied by a reduction in compressive yield strength due to lower content of Al and V alloying elements in Ti32. Ti64-90 showed a compressive yield strength of 1178 ± 33 MPa, and that for Ti32-90 was 968 ± 24 MPa. An effect of the build orientation was observed in the compressive yield strength; compressive yield strength was found to increase with the reduction in built angle. The Ti32-45 and Ti32-0 displayed almost similar compressive yield strength values of 1071 ± 16 and 1051 ± 18 MPa, respectively, which were higher than that of Ti32-90.

3.3. Dynamic mechanical loading: Rotating-bending fatigue

The fatigue performance of Ti32 is expected to deteriorate after the Al and V contents of Ti64 are reduced in the process of making Ti32. The standard, ASTM F1800, dictates that only composition achieving at least 10 million cycles before failure is qualified as an orthopedic device material. In this study, the endurance limit was considered the bending stress at which the fatigue specimens reached 10 million cycles without failure. Table 1 presents the cycles till failure for Ti64 and Ti32, which are visualized

Table 2. Reported tensile modulus and ultimate tensile strength of Ti6Al4V processed via directed energy deposition, electron beam melting, and laser powder bed fusion-based AM techniques

AM technique	Post-processing	Tensile modulus (GPa)	Ultimate tensile strength (MPa)	References
Directed energy deposition	Machined	-	1041 – 1087	[33]
	Annealed at 600°C for 2 h	95.1	907	[34]
	As-printed	-	761 – 821	[35]
	Machined	-	1163	[36]
Electron beam melting	Machined	-	1073	[37]
	Machined	-	972	[38]
	As-printed	-	851	[39]
	Machined	119	1045	[40]
Laser powder bed fusion	Annealed at 950° C for 30 min, machined	118	1042	[41]
	Machined	110	1095	[42]
	Machined	-	1246	[38]
	Annealed at 730°C for 2 h, machined	101	1046	[43]
	Annealed at 640°C for 4 h, machined	127	1032	[40]

AM: Additive manufacturing

Table 3. Tensile test results for heat-treated and non-heat-treated specimens, and compressive yield strength for Ti64 and Ti32 with different build orientations

Tensile test results		
Sample	**Elastic modulus (GPa)**	**Ultimate tensile strength (MPa)**
Non-heat-treated Ti32	106.8±4.8	989±8
Heat-treated Ti32	107.6±5.8	989±4
Compression test results		
Sample	**Build orientation**	**Compressive yield strength (MPa)**
Ti6Al4V		
Ti64-90	90°	1178±33
Ti3Al2V		
Ti32-90	90°	968±24
Ti32-45	45°	1071±16
Ti32-0	0°	1051±18

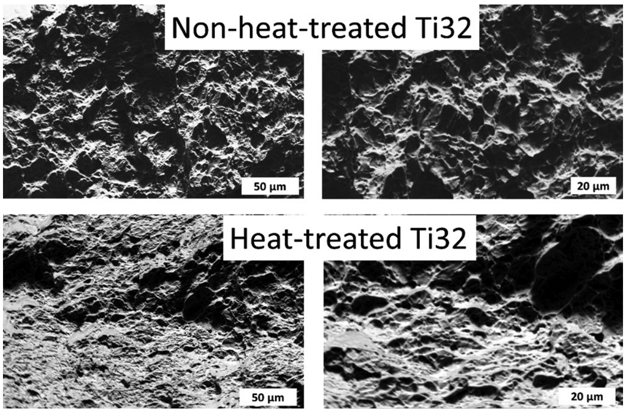

Figure 3. Fracture surfaces of Ti32 tensile test specimens for non-heat-treated and heat-treated conditions.

as plots in Figure 4A, along with pictures of the fracture surface morphology in Figure 4B. With a compressive yield strength of 1178 MPa for Ti64, its high cycle fatigue reached 10 million cycles at 250 MPa at a stress ratio of 0.21 for additively manufactured Ti64-90 specimens. Comparatively, for Ti32-90 with lower Al and V contents, the 10 million cycle mark was achieved at a lower stress of 219 MPa; however, it should be noted that the stress ratio was 0.22, close to the stress ratio of 0.21 for Ti64-90.

AM is a layer-wise process that produces structures with anisotropic behavior, which contributes to variations in the mechanical performance depending on the build orientation. Along with the compressive strength, the fatigue performance is affected by the build orientation. For Ti32-45, 10 million cycles were reached at a stress ratio of 0.36 (bending stress 387.5), higher than that for both Ti64-90 and Ti32-90 test specimens. With a further decrease in the build orientation, Ti32-0 reached 10 million cycles at an even higher stress ratio of 0.48 (bending stress 512.5 MPa). Thus, with a change in build orientation from 90° to 0°, Ti32 would show better fatigue performance than Ti64, compensating for the reduced amounts of Al and V in the former. Figure 4B shows the fracture surface morphologies for Ti64-90 and Ti32-90/45 specimens. The fracture started at the surface of the specimens under fatigue loading and propagated throughout the specimen, ultimately leading to failure. This suggests that the surface properties greatly influence their fatigue performance.

4. Discussion

In this study, we implemented a novel alloy design based on Ti6Al4V to enhance biocompatibility for orthopedic implants. The newly designed alloy, Ti3Al2V, with reduced Al and V contents in Ti6Al4V, is expected to demonstrate good mechanical performance without significant reduction from Ti6Al4V. Since implants at load-bearing sites are performed under a multiaxial loading condition *in vivo*, it is essential to improve the mechanical strength of such alloys, particularly under cyclic fatigue loading, to avoid fractures and implant failures *in vivo*.

Fracture of specimens under cyclic loading starts at the surface of the gauge length, suggesting that higher surface roughness of the test specimens leads to early fractures. Another critical parameter is the presence of residual pores, which contributes to faster crack propagation and early failure[40]. AM-processed parts are known to possess rough surface and residual pores in each layer due to the layer-wise nature of the process[44-46]. Of note, machining is often implemented to reduce surface roughness introduced by the L-PBF process. Fatigue life and endurance limit of AM-processed Ti6Al4V have been studied extensively (Table 4), and as shown in various studies, L-PBF-processed Ti6Al4V has low endurance limit. In this study, L-PBF-manufactured and machined Ti6Al4V built at 90° orientations displayed an endurance limit of 250 MPa, similar to that observed in various studies (Table 4).

Surface roughness plays a crucial role in preventing crack propagation and enhancing fatigue life[51,52]. After investigating the fatigue performance of as-printed and machined L-PBF-built Ti6Al4V, Vayssette *et al.* found that the strength to reach 0.2 million cycles was 223 MPa for as-printed specimens and 513 MPa for machined samples[53]. High cycle fatigue values for Ti6Al4V presented in Table 1 were evaluated for test specimens machined at 1200 rpm on a CNC machine. To observe if machining parameters had any significant effect on the surface roughness and subsequently on the fatigue performance,

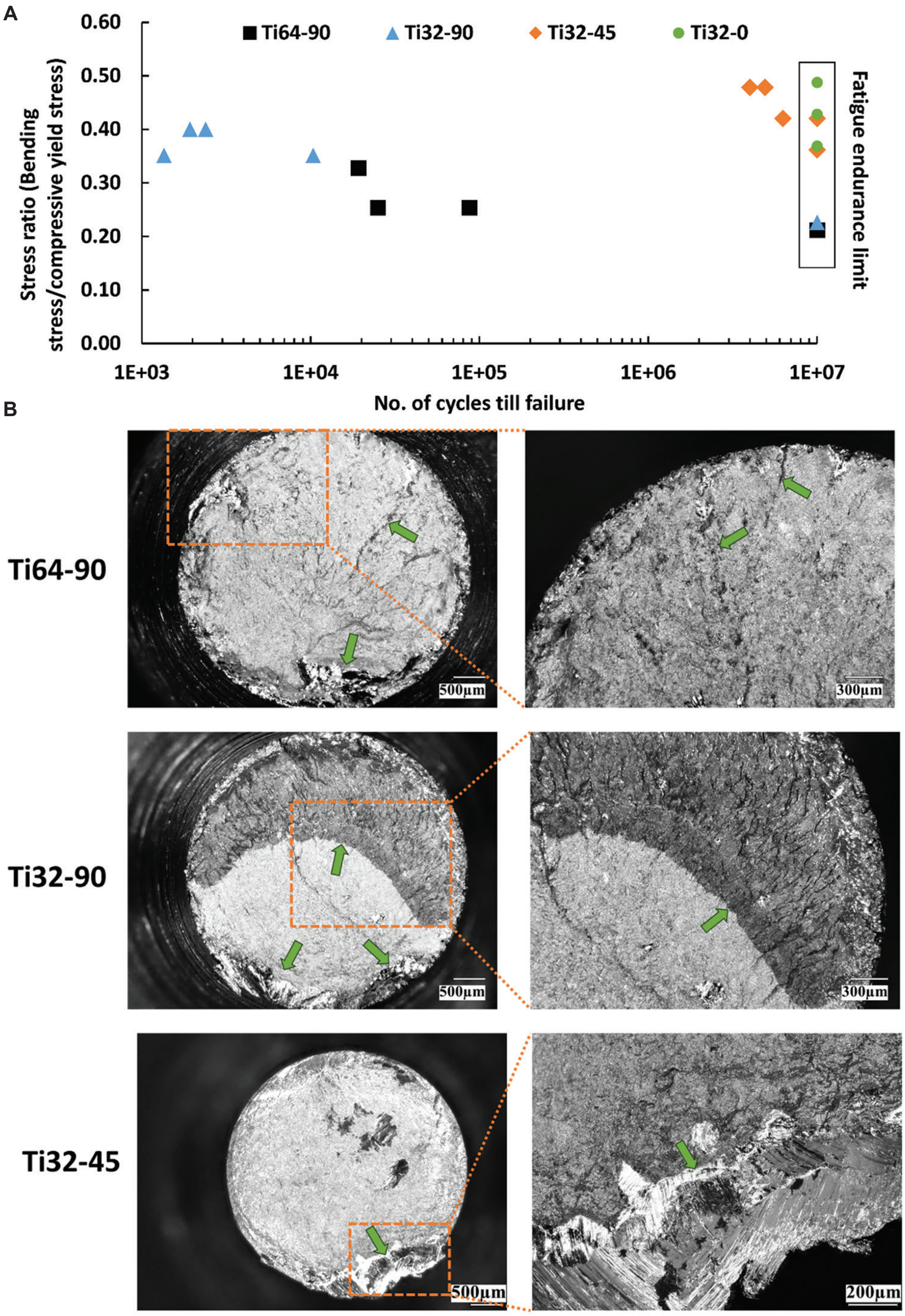

Figure 4. (A) High cycle fatigue plot for Ti64-90 and Ti32-90/45/0 specimens at various loads. The Y-axis represents the ratio of the applied bending stress to their respective compressive yield strengths. The endurance limit was marked and considered as the loads for which 10 million cycles were achieved before failure. (B) Optical images of the fracture surfaces for Ti64-90, Ti32-90, and Ti32-45 specimens. The arrows indicate the onset of failure and crack propagation through the specimens at failure.

Ti64-90 specimens were also machined at 600 rpm and tested for fatigue failure. A lower machining revolutions per minute (RPM) had a significant effect on the fatigue life. The endurance limit for Ti64-90 increased from 250 MPa (1200 rpm) to 300 MPa (600 rpm), with 4 million cycles observed at 500 MPa for Ti64-90 (600 rpm). Figure 5 shows the microscopic features on the periphery of the specimens machined at 1200 and 600 rpm. Figure 5A presents high-

Table 4. Endurance limit for L-PBF processed Ti6Al4V with post-processing treatments from various studies

AM technique	Post-processing	Stress amplitude ratio (R)	Endurance limit (MPa)	References
Laser powder bed fusion	As-printed, machined	−1	220	[47]
	As-printed	0.1	350	[48]
	Heat-treated, machined	0.1	400	[49]
	As-printed	−0.2	210	[50]
	As-printed, polished	−1	250	[40]

AM: Additive manufacturing; L-PBF: Laser powder bed fusion

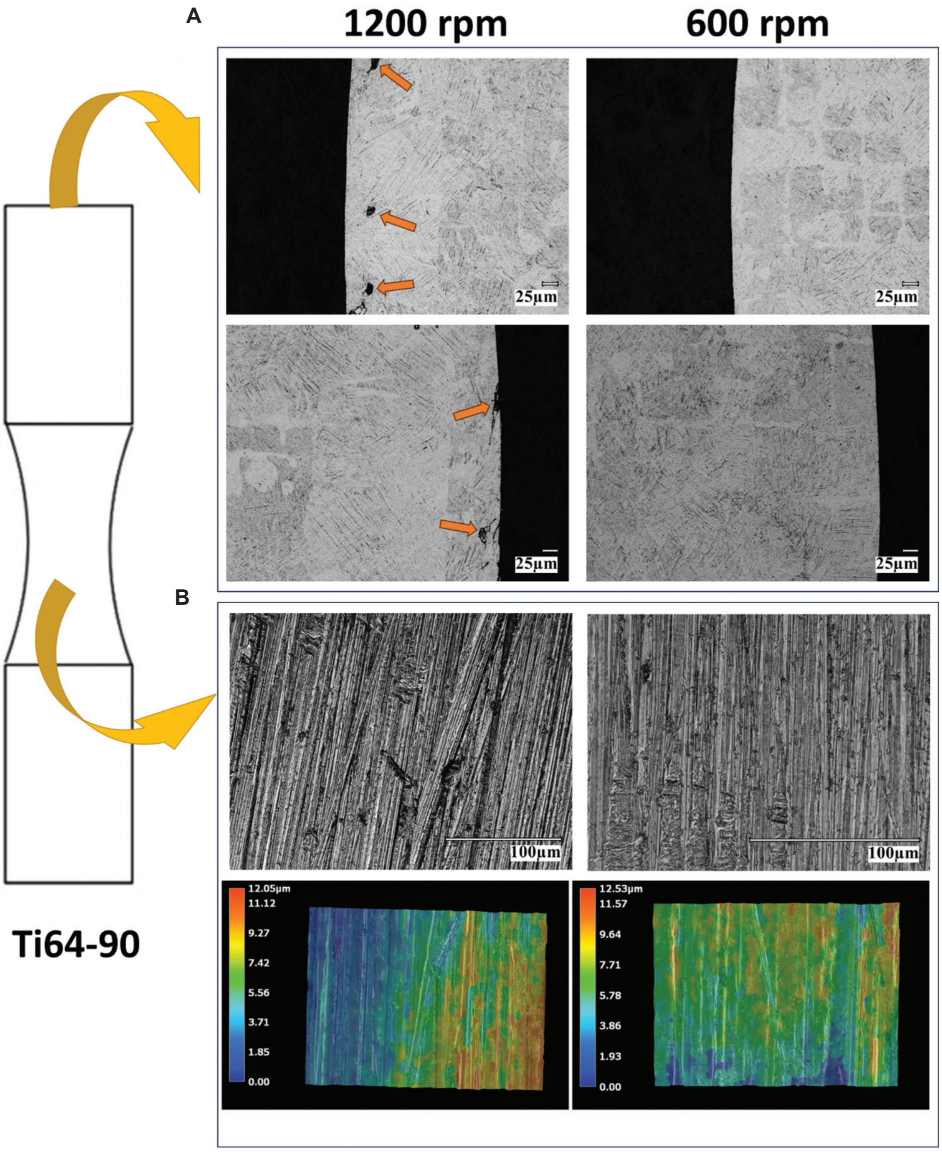

Figure 5. Effect of machining revolutions per minute on the surface of Ti46-90 fatigue specimens. (A) High-magnification images of the top surface of the fatigue specimens with machined surfaces at 1200 and 600 rpm. Defects are observed on the periphery of the surface of samples machined at 1200 rpm, while those machined at 600 rpm show a clean outer surface. (B) High-magnification images of the gauge region of the fatigue specimens post-machining, and depth profiling representing the surface roughness. Fatigue specimens machined at 1200 rpm display rugged surfaces with depth profiling indicating large variation in depths at the gauge region, signifying higher surface roughness. Specimens machined at a lower speed at 600 rpm display lower ruggedness at the gauge area, with surface depth profiling indicating a more uniform pattern and a lower surface roughness than that for 1200 rpm specimens.

magnification images that highlight the defects observed at the periphery of the top surface of the fatigue specimen, which contributed to its early failure under fatigue loading. However, the specimen machined at 600 rpm had a clean surface with minimal to no defects. Figure 5B presents high-magnification images and surface depth profiling at the gauge region. A lower degree of roughness can be observed for the specimen machined at 600 rpm, with surface depth profiling showing a more homogeneous depth distribution than at 1200 rpm. As discussed, a lower surface roughness for the 600 rpm machined Ti64-90 specimen resulted in a higher endurance limit. This indicates that machining parameters can affect surface defects and roughness, thereby influencing fatigue performance.

The excellent fatigue resistance of Ti6Al4V is due to the presence of the alloying elements Al and V. The endurance limit is expected to reduce with a decrease of alloying elements content. The fatigue limit was observed to be lowered to 219 MPa for Ti3Al2V specimens built at 90° orientation. It should be noted that the ratios of endurance limit to compressive yield strength of these compositions are almost the same (0.21 for Ti64-90 vs. 0.23 for Ti32-90), suggesting the only factor contributing to reduced endurance limit is the reduction in the alloying elements. A reduction of the build orientation lessens the number of layers required for specimen processing, thereby reducing the residual porosities between consecutive layers as can be seen from the microstructural images (Figure 2); Ti32-90 possesses interlayer lack of fusion pores, which contribute to an endurance limit lower than those of Ti32-45 and Ti32-0. For Ti32-45, the endurance limit was 387.5 MPa, which exceeds that of Ti64-90. With further reduction in build orientation, Ti32-0 displayed the highest endurance limit of 512.5 MPa, more than twice that for Ti64-90, which was similar to that of wrought-heat-treated Ti6Al4V (~500 MPa), as reported by Janeček *et al.*[54]. The heat treatment at 400°C conducted in this study was to relieve stresses with retainment of fine α' grains. Heat treatments of Ti6Al4V above its β transus temperature (995°C) have been shown to further enhance the fatigue performance due to the transformation of martensitic α' to homogeneously distributed α+β microstructure[37]. Although the build orientation for Ti3Al2V alloy did not significantly influence the compressive yield strength, its impact on the fatigue performance was apparent. The reduced Al and V contents in Ti3Al2V did not significantly alter the alloy's fatigue behavior, and thus, it holds potential in orthopedic implant applications.

5. Conclusion

CpTi exhibits better biocompatibility compared with Ti6Al4V but lacks strength and fatigue resistance. A novel alloy design is implemented in this study by reducing the Al and V contents in Ti6Al4V to design Ti3Al2V, an intermediate alloy between CpTi and Ti6Al4V. This alloy was designed specifically for orthopedic applications and is expected to exhibit no significant reduction in mechanical performance when compared to Ti6Al4V. AM was implemented to process Ti6Al4V and Ti3Al2V compositions. The main findings of this study are summarized as follows:

(i) Tensile tests revealed an ultimate tensile strength of 989 MPa for Ti3Al2V, which is close to the range of strength values for Ti6Al4V (1000–1100 MPa) reported in various studies
(ii) Compressive yield strength reduction of 18% was observed in Ti3Al2V (968 ± 24 MPa) compared to Ti6Al4V (1178 ± 33 MPa) built at 90° orientation to the build plate
(iii) After exploring the effects of build direction accounting for anisotropy, we found that the Ti3Al2V specimens built at 45° and 0° displayed an increase in compressive yield strength; however, no significant difference was observed between the Ti3Al2V 45° (1071 ± 16 MPa) and 0° (1051 ± 18 MPa) specimens
(iv) Fatigue specimens built at 90° orientation exhibited an endurance limit of 250 MPa for Ti6Al4V and 219 MPa for Ti3Al2V upon reaching 10 million cycles without failure, and had almost similar ratios of applied bending stress to their respective compressive yield strengths (0.21 vs. 0.23, respectively)
(v) The effect of build orientation for Ti3Al2V specimens on the fatigue behavior was significant, and the endurance limit increased more than two-fold for Ti3Al2V specimens built at 0° (512 MPa).

Our results showed that despite having reduced contents of Al and V than in Ti6Al4V, the Ti3Al2V alloy holds a huge potential in orthopedic device applications, given its high strength and excellent fatigue performance.

Acknowledgments

The authors would like to acknowledge initial experimental support from Mr. Lile Squires, and Dr. Jose Avila.

Funding

The authors would like to acknowledge financial support from the National Science Foundation under Grant Number CMMI 1934230. The research results reported in this publication are supported by the National Institute of Arthritis and Musculoskeletal and Skin Diseases of the National Institutes of Health under Award Numbers R01 AR067306 and R01 AR078241. The content is solely the responsibility of the authors and does not necessarily

represent the official views of the National Institutes of Health.

Conflict of interest

The authors declare no conflict of interest.

Author contributions

Conceptualization: Amit Bandyopadhyay
Formal analysis: Sushant Ciliveri, Nathan Zuckschwerdt
Funding acquisition: Amit Bandyopadhyay
Investigation: Sushant Ciliveri, Stefano Guariento, Nathan Zuckschwerdt, William W. Hogg
Methodology: Stefano Guariento, William W. Hogg
Project administration: Amit Bandyopadhyay
Supervision: Amit Bandyopadhyay
Writing–original draft: Sushant Ciliveri, Nathan Zuckschwerdt
Writing–review & editing: Amit Bandyopadhyay.

Ethics approval and consent to participate

Not applicable.

Consent for publication

Not applicable.

Availability of data

Data will be available from the corresponding author on reasonable request.

References

1. Bose S, Ke D, Sahasrabudhe H, *et al.*, 2018, Additive manufacturing of biomaterials. *Prog Mater Sci*, 93: 45–11.

   https://doi.org/10.1016/j.pmatsci.2017.08.003

2. Bandyopadhyay A, Mitra I, Avila JD, *et al.*, 2023, Porous metal implants: Processing, properties, and challenges. *Int J Extrem Manuf*, 5: 032014.

   https://doi.org/10.1088/2631-7990/acdd35

3. Chen LY, Cui YW, Zhang LC, 2020, Recent development in beta titanium alloys for biomedical applications. *Metals*, 10: 1139.

   https://doi.org/10.3390/met10091139

4. Bandyopadhyay A, Traxel KD, Lang M, *et al.*, 2022, Alloy design via additive manufacturing: Advantages, challenges, applications and perspectives. *Mater Today*, 52: 207–224.

   https://doi.org/10.1016/j.mattod.2021.11.026

5. Liu S, Shin YC, 2019, Additive manufacturing of Ti6Al4V alloy: A review. *Mater Des*, 164: 107552.

   https://doi.org/10.1016/j.matdes.2018.107552

6. Ciliveri S, Bandyopadhyay A, 2023, Understanding the influence of alloying elements on the print quality of powder bed fusion-based metal additive manufacturing: Ta and Cu addition to Ti alloy. *Virtual Phys Prototyp*, 18: e2248464.

   https://doi.org/10.1080/17452759.2023.2248464

7. Han CH, Johansson CB, Wennerberg A, *et al.*, 1998, Quantitative and qualitative investigations of surface enlarged titanium and titanium alloy implants. *Clin Oral Implants Res*, 9: 1–10.

   https://doi.org/10.1034/j.1600-0501.1998.090101.x

8. Johansson CB, Lausmaa J, Röstlund T, *et al.*, 1993, Commercially pure titanium and Ti6AI4V implants with and without nitrogen-ion implantation: Surface characterization and quantitative studies in rabbit cortical bone. *J Mater Sci Mater Med*, 4: 132–141.

   https://doi.org/10.1007/BF00120382

9. Yavari SA, Wauthle R, van der Stok J, *et al.*, 2013, Fatigue behavior of porous biomaterials manufactured using selective laser melting. *Mater Sci Eng C*, 33: 4849–4858.

   https://doi.org/10.1016/j.msec.2013.08.006

10. Bandyopadhyay A, Upadhyayula M, Traxel KD, *et al.*, 2019, Influence of deposition orientation on fatigue response of LENS™ processed Ti6Al4V. *Mater Lett*, 255: 126541.

    https://doi.org/10.1016/j.matlet.2019.126541

11. Benedetti M, Cazzolli M, Fontanari V, *et al.*, 2016, Fatigue limit of Ti6Al4V alloy produced by selective laser sintering. *Proc Struct Integr*, 2: 3158–3167.

    https://doi.org/10.1016/j.prostr.2016.06.394

12. Mitra I, Bose S, Dernell WS, *et al.*, 2021, 3D printing in alloy design to improve biocompatibility in metallic implants. *Mater Today*, 45: 20–34.

    https://doi.org/10.1016/j.mattod.2020.11.021

13. Bandyopadhyay A, Espana F, Balla VK, *et al.*, 2010, Influence of porosity on mechanical properties and *in vivo* response of Ti6Al4V implants. *Acta Biomater*, 6: 1640–1648.

    https://doi.org/10.1016/j.actbio.2009.11.011

14. Bandyopadhyay A, Mitra I, Goodman SB, *et al.*, 2023, Improving biocompatibility for next generation of metallic implants. *Prog Mater Sci*, 133: 101053.

    https://doi.org/10.1016/j.pmatsci.2022.101053

15. Sing SL, 2022, Perspectives on additive manufacturing enabled beta-titanium alloys for biomedical applications. *Int J Bioprint*, 8: 478.

    https://doi.org/10.18063/ijb.v8i1.478

16. Zhang T, Liu CT, 2022, Design of titanium alloys by additive manufacturing: A critical review. *Adv Powder Mater*, 1: 100014.

    https://doi.org/10.1016/j.apmate.2021.11.001

17. Lin CW, Ju CP, Lin JH, 2005, A comparison of the fatigue behavior of cast Ti-7.5Mo with c.p. titanium, Ti-6Al-4V and Ti-13Nb-13Zr alloys. *Biomaterials*, 26: 2899–2907.

https://doi.org/10.1016/j.biomaterials.2004.09.007

18. Akahori T, Niinomi M, Fukui H, *et al.*, 2005, Improvement in fatigue characteristics of newly developed beta type titanium alloy for biomedical applications by thermo-mechanical treatments. *Mater Sci Eng C*, 25: 248–254.

https://doi.org/10.1016/j.msec.2004.12.007

19. Niinomi M, 2008, Mechanical biocompatibilities of titanium alloys for biomedical applications. *J Mech Behav Biomed Mater*, 1: 30–42.

https://doi.org/10.1016/j.jmbbm.2007.07.001

20. Standard Specification for Wrought Titanium-13 Niobium-13 Zirconium Alloy for Surgical Implant Applications (UNS R58130). Available from: https://www.astm.org/f1713-08r21e01.html [Last accessed on 2022 May 06].

21. Ho WF, Ju CP, Lin JH, 1999, Structure and properties of cast binary Ti-Mo alloys. *Biomaterials*, 20: 2115–2122.

https://doi.org/10.1016/S0142-9612(99)00114-3

22. Ciliveri S, Bandyopadhyay A, 2021, Influence of strut-size and cell-size variations on porous Ti6Al4V structures for load-bearing implants. *J Mech Behav Biomed Mater*, 126: 105023.

https://doi.org/10.1016/j.jmbbm.2021.105023

23. Sterling AJ, Torries B, Shamsaei N, *et al.*, 2016, Fatigue behavior and failure mechanisms of direct laser deposited Ti–6Al–4V. *Mater Sci Eng A*, 655: 100–112.

https://doi.org/10.1016/j.msea.2015.12.026

24. Bandyopadhyay A, Zhang Y, Bose S, 2020, Recent developments in metal additive manufacturing. *Curr Opin Chem Eng*, 28: 96–104.

https://doi.org/10.1016/j.coche.2020.03.001

25. Chua C, Sing SL, Chua CK, 2023, Characterisation of *in-situ* alloyed titanium-tantalum lattice structures by laser powder bed fusion using finite element analysis. *Virtual Phys Prototyp*, 18: e2138463.

https://doi.org/10.1080/17452759.2022.2138463

26. Yang J Gao H, Zhang D, *et al.*, 2021, Static compressive behavior and material failure mechanism of trabecular tantalum scaffolds fabricated by laser powder bed fusion-based additive manufacturing. *Int J Bioprint*, 8: 438.

https://doi.org/10.18063/ijb.v8i1.438

27. Bandyopadhyay A, Ciliveri S, Bose S, 2022, Metal additive manufacturing for load-bearing implants. *J Indian Inst Sci*, 102: 561–584.

https://doi.org/10.1007/s41745-021-00281-x

28. Haleem A, Javaid M, 2019, 3D scanning applications in medical field: A literature-based review. *Clin Epidemiol Glob Health*, 7: 199–210.

https://doi.org/10.1016/j.cegh.2018.05.006

29. ISO. 14:00-17:00, ISO/ASTM 52909:2022. Available from: https://www.iso.org/standard/74639.html [Last accessed on 2023 Aug 16].

30. Standard Test Methods of Compression Testing of Metallic Materials at Room Temperature. Available from: https://www.astm.org/e0009-19.html [Last accessed on 2023 Jan 20].

31. ISO. 14:00-17:00, ISO 1143:2021. Available from: https://www.iso.org/standard/79575.html [Last accessed on 2023 Sep 10].

32. ISO. 14:00-17:00, ISO 5832-3:2021. Available from: https://www.iso.org/standard/79626.html [Last accessed on 2023 Jul 23].

33. Carroll BE, Palmer TA, Beese AM, 2015, Anisotropic tensile behavior of Ti-6Al-4V components fabricated with directed energy deposition additive manufacturing. *Acta Mater*, 87: 309–320.

https://doi.org/10.1016/j.actamat.2014.12.054

34. Wang F, Mei J, Jiang H, *et al.*, 2007, Laser fabrication of Ti6Al4V/TiC composites using simultaneous powder and wire feed. *Mater Sci Eng A*, 445–446: 461–466.

https://doi.org/10.1016/j.msea.2006.09.093

35. Alcisto J, Enriquez A, Garcia H, *et al.*, 2011, Tensile properties and microstructures of laser-formed Ti-6Al-4V. *J Materi Eng Perform*, 20: 203–212.

https://doi.org/10.1007/s11665-010-9670-9

36. Dinda GP, Song L, Mazumder J, 2008, Fabrication of Ti-6Al-4V scaffolds by direct metal deposition. *Metall Mater Trans A*, 39: 2914–2922.

https://doi.org/10.1007/s11661-008-9634-y

37. Galarraga H, Warren RJ, Lados DA, *et al.*, 2017, Effects of heat treatments on microstructure and properties of Ti-6Al-4V ELI alloy fabricated by electron beam melting (EBM). *Mater Sci Eng A*, 685: 417–428.

https://doi.org/10.1016/j.msea.2017.01.019

38. Wysocki B, Maj P, Sitek R, *et al.*, 2017, Laser and electron beam additive manufacturing methods of fabricating titanium bone implants. *Appl Sci*, 7: 657.

https://doi.org/10.3390/app7070657

39. Edwards P, O'Conner A, Ramulu M, 2013, Electron beam additive manufacturing of titanium components: Properties and performance. *J Manuf Sci Eng*, 135: 061016.

https://doi.org/10.1115/1.4025773

40. Chastand V, Quaegebeur P, Maia W, *et al.*, 2018, Comparative

study of fatigue properties of Ti-6Al-4V specimens built by electron beam melting (EBM) and selective laser melting (SLM). *Mater Charact*, 143: 76–81.

https://doi.org/10.1016/j.matchar.2018.03.028

41. Hollander DA, von Walter M, Wirtz T, *et al.*, 2006, Structural, mechanical and *in vitro* characterization of individually structured Ti-6Al-4V produced by direct laser forming. *Biomaterials*, 27: 955–963.

    https://doi.org/10.1016/j.biomaterials.2005.07.041

42. Facchini L, Magalini E, Robotti P, *et al.*, 2010, Ductility of a Ti-6Al-4V alloy produced by selective laser melting of prealloyed powders. *Rapid Prototyp J*, 16: 450–459.

    https://doi.org/10.1108/13552541011083371

43. Vilaro T, Colin C, Bartout JD, 2011, As-fabricated and heat-treated microstructures of the Ti-6Al-4V alloy processed by selective laser melting. *Metall Mater Trans A*, 42: 3190–3199.

    https://doi.org/10.1007/s11661-011-0731-y

44. Yu W, Xiao Z, Zhang X, *et al.*, 2022, Processing and characterization of crack-free 7075 aluminum alloys with elemental Zr modification by laser powder bed fusion. *Mater Sci Addit Manuf*, 1: 4.

    https://doi.org/10.18063/msam.v1i1.4

45. Zhang X, Xiao Z, Yu W, *et al.*, 2022, Influence of erbium addition on the defects of selective laser-melted 7075 aluminium alloy. *Virtual Phys Prototyp*, 17: 406–418.

    https://doi.org/10.1080/17452759.2021.1990358

46. Sing SL, Huang S, Goh GD, *et al.*, 2021, Emerging metallic systems for additive manufacturing: *In-situ* alloying and multi-metal processing in laser powder bed fusion. *Prog Mater Sci*, 119: 100795.

    https://doi.org/10.1016/j.pmatsci.2021.100795

47. Mertova K, Dzugan J, Roudnicka M, 2018, Fatigue properties of SLM-produced Ti6Al4V with various post-processing processes. *IOP Conf Ser Mater Sci Eng*, 461: 012052.

    https://doi.org/10.1088/1757-899X/461/1/012052

48. Gong H, Rafi K, Gu H, *et al.*, 2015, Influence of defects on mechanical properties of Ti-6Al-4V components produced by selective laser melting and electron beam melting. *Mater Des*, 86: 545–554.

    https://doi.org/10.1016/j.matdes.2015.07.147

49. Xu W, Sun S, Elambasseril J, *et al.*, 2015, Ti-6Al-4V additively manufactured by selective laser melting with superior mechanical properties. *JOM*, 67: 668–673.

    https://doi.org/10.1007/s11837-015-1297-8

50. Edwards P, Ramulu M, 2014, Fatigue performance evaluation of selective laser melted Ti-6Al-4V. *Mater Sci Eng A*, 598: 327–337.

    https://doi.org/10.1016/j.msea.2014.01.041

51. Fatemi A, Molaei R, Sharifimehr S, *et al.*, 2017, Multiaxial fatigue behavior of wrought and additive manufactured Ti-6Al-4V including surface finish effect. *Int J Fatigue*, 100: 347–366.

    https://doi.org/10.1016/j.ijfatigue.2017.03.044

52. Pegues J, Roach M, Williamson RS, *et al.*, 2018, Surface roughness effects on the fatigue strength of additively manufactured Ti-6Al-4V. *Int J Fatigue*, 116: 543–552.

    https://doi.org/10.1016/j.ijfatigue.2018.07.013

53. Vayssette B, Saintier N, Brugger C, *et al.*, 2018, Surface roughness of Ti-6Al-4V parts obtained by SLM and EBM: Effect on the high cycle fatigue life. *Proc Eng*, 213: 89–97.

    https://doi.org/10.1016/j.proeng.2018.02.010

54. Janeček M, Novy F, Harcuba P, *et al.*, 2015, The very high cycle fatigue behaviour of Ti-6Al-4V alloy. *Acta Phys Pol Ser A*, 128: 497–503.

    https://doi.org/10.12693/aphyspola.128.497

ACCSCIENCE PUBLISHING

Materials Science in Additive Manufacturing

ORIGINAL RESEARCH ARTICLE

Additive manufacturing of continuous carbon fiber-reinforced silicon carbide composite by fused filament fabrication and precursor infiltration pyrolysis

Xiang Nie[1], Siqi Wu[1], Lei Yang[1,2]*, Chunze Yan[1]*, and Yusheng Shi[1]

[1]State Key Laboratory of Materials Processing and Die and Mould Technology, School of Materials Science and Engineering, Huazhong University of Science and Technology, 430074, China

[2]Department of Mechanical Design and Manufacturing, School of Transportation and Logistics Engineering, Wuhan University of Technology, Wuhan, 430070, China

Abstract

Continuous fiber reinforced silicon carbide composites (C_f/SiC) are known for their advantages such as high strength, high modulus, high thermal conductivity, and low density. In this paper, we propose an integrated C_f/SiC preparation and processing process. The continuous carbon fiber-reinforced resin matrix composite green parts were processed by fused filament fabrication, and then ceramicized by precursor infiltration pyrolysis process. The processing parameters of the green parts, the performance of the green-part specimens, the phase evolution in the post treatment, and the performance of C_f/SiC samples were investigated. The infill line distance (ILD) had a huge influence on the mechanical properties of green parts and C_f/SiC. The bending strength of the green parts and the C_f/SiC specimens increased with the decrease in ILD. The maximum bending strength of 169.48 MPa and 155.83 MPa was achieved for the carbon fiber/polyethylene terephthalate glycol (C_f/PETG) and polylactic acid (C_f/PLA) green parts, respectively. The highest bending strength of 47.73 MPa of the C_f/SiC material was obtained with the C_f/PLA green parts, while the bending strength of 93.79 MPa was obtained for the C_f/SiC with C_f/PETG green parts. The increase in mechanical properties was believed to result from the pyrolyzed carbon brought by PETG and the increase of the equivalent fiber density within the single layer after a larger nozzle size was used.

Keywords: Additive manufacturing; Continuous fiber; Resin composites; Precursor infiltration pyrolysis; Silicon carbide composites

***Corresponding authors:**
Lei Yang
(lei.yang@whut.edu.cn)
Chunze Yan
(c_yan@hust.edu.cn)

Citation: Nie X, Wu S, Yang L, *et al.*, 2023, Additive manufacturing of continuous carbon fiber-reinforced silicon carbide composite by fused filament fabrication and precursor infiltration pyrolysis. *Mater Sci Add Manuf*, 2(3): 1604. https://doi.org/10.36922/msam.1604

Received: August 15, 2023

Accepted: September 8, 2023

1. Introduction

Silicon carbide (SiC) ceramic is known for its high strength, high modulus, heat resistance, anti-corrosion, abrasion resistance, and low density[1-3], for which it is widely applied in the aerospace and automobile industries, as well as energy sector[4-6]. With the continuous development of these fields, SiC ceramics with higher requirements are urgently needed. However, monophase SiC is highly brittle and can result in catastrophic damage under extreme working conditions[7].

To overcome the shortcomings of monophase SiC, scholars all over the world have been researching about adding reinforcing phases such as particles[8], whiskers[9-11], and fibers[12-14] into the SiC ceramic to improve strength and toughness. Among the reinforcing methods, carbon and SiC fibers are the best reinforcements to reduce brittle fracture by mechanisms of crack deflection, as well as fiber debonding and pull-out[15].

Fiber-reinforced SiC composites come in two different forms: short fiber-reinforced and continuous fiber-reinforced. The former has been studied for decades and shows better performance than monophase SiC ceramics[16-19]. In contrast, the strength and toughness of SiC composites are more effectively enhanced following the reinforcement with continuous fibers. Sun *et al.*[20] obtained SiC fiber-reinforced SiC composites (SiC_f/SiC) composites prepared by chemical vapor deposition (CVD) and the flexural strength and fracture toughness can reach 534.20 MPa and 38.84 MPa $m^{1/2}$, respectively. Zhang *et al.*[21] investigated the interfacial layers in the process of preparing fiber-reinforced SiC composites using the chemical vapor infiltration (CVI) method. It revealed that due to the supersaturation of the carbon-hydrogen intermediate, the formation of isotropic multi-layer amorphous carbon interfacial phases was prone to occur. This type of interfacial phase could lead to a strength reduction of 28 – 40% in the composite material. However, employing the low-pressure CVI process could prevent the occurrence of this phenomenon. Zhou *et al.*[22] successfully fabricated three-dimensional carbon fiber-reinforced SiC-based composites using the vapor silicon infiltration method. The specimens exhibited non-destructive fracture behavior, and the ultimate flexural stress of the samples reached 238.9 ± 41.2 MPa at 1973 K.

Conventional procedures for fabricating continuous fiber-reinforced SiC composites include pre-pregnant tape preparation, fiber placement, compression molding forming, and chemical vapor infiltration or precursor infiltration pyrolysis (PIP), which are complex and cannot yield parts with complex shaped[23]. Additive manufacturing adopts the principle of layer-by-layer manufacturing and superposition and can integrally form components with complex structures[24-26]. The outstanding advantages of additive manufacturing include short manufacturing process, high material utilization rate, and flexibility in structure shaping[27-30]. The fabrication of short fiber-reinforced SiC composites using additive manufacturing processes, such as vat photopolymerization[5,31-33] and laser powder bed fusion[4,34,35], has been reported. However, these additive manufacturing techniques, which exclusively employ powders or pastes as feedstock[36,37], are unable to produce continuous fiber-reinforced SiC composites. Fused filament fabrication (FFF) is the most commonly used additive manufacturing technique, which is known for stability, simplicity, and low cost[38-40]. FFF technology, utilizing filament-like materials as feedstock, enables the incorporation of continuous fibers mixed with various resin filament materials, either supplied directly or pre-prepared as composite pre-impregnated filaments. The FFF technique has been used to fabricate continuous fiber-reinforced polymers to produce lightweight structures[41-43]. Thus, the combination of FFF additive manufacturing and SiC ceramic post-processing techniques allows the fabrication of continuous fiber-reinforced SiC composite materials.

Mei *et al.*[44] employed an FFF *in situ* impregnation process to investigate two methods for combining ceramic precursors and continuous carbon fibers using thermoplastic resin as the matrix material. The first method involved feeding both ceramic precursors and continuous carbon fibers into a heated nozzle, while the second method directly extruded a mixture of ceramic precursors and carbon fibers, followed by SiC ceramic deposition and densification through CVI. The former yielded stable continuous fiber-reinforced SiOC composites at 1100°C, and the latter, after CVI processing, produced SiOC/SiC composites with a bending strength 7.6 times that of monolithic SiOC ceramics. In summary, whether fabricated through conventional or additive manufacturing methods, continuous fiber-reinforced SiC composites have reduced fracture toughness and the fabrication process is complex and less precise. Therefore, it is essential to investigate a novel process for fabricating continuous fiber-reinforced SiC composites to enhance the performance of the composites.

In this work, an additive manufacturing method for fabricating continuous carbon fiber-reinforced SiC (C_f/SiC) composites is proposed. A modified FFF device was used as the printing platform, and a pre-pregnant continuous carbon fiber/polylactic acid (C_f/PLA) and polyethylene terephthalate glycol ($C_f/PETG$) resin composite feedstock was used as the filaments. The porous continuous fiber-reinforced resin green part was additively manufactured. PIP process was used to transform green parts into C_f/SiC composite parts. The purpose of this study was to seek the feasibility of additive manufacturing C_f/SiC composite parts with complex geometries. Furthermore, the study attempted to establish correlations between the processing parameters, resultant microstructures, and the mechanical performance of the C_f/resin green parts and C_f/SiC composite parts.

2. Materials and methods

2.1. Raw materials

The PLA/PETG resin filament (eSUN, Shenzhen, China) and continuous carbon fiber (T300-1K; Jilin Carbon

Valley Co., Ltd., Jilin, China) were used as the matrix and reinforcing phase of the pre-pregnant feedstock, respectively. Polycarbosilane (PCS; KH-VHPCS-1S, Institute of Chemistry Chinese Academy of Sciences) was used as the precursor of the PIP process.

2.2. Pre-pregnant feedstock preparation

The resin filament and continuous carbon fiber bundle went through a screw extruder, in which the matrix resin and the reinforcement phase of carbon fiber were combined into one pre-pregnant feedstock. The pre-pregnant feedstock consists of an outer matrix layer of the resin and an inner core of the fiber-reinforced phase that is homo-dispersed into the outer layer. The volume fraction of C_f in the feedstock is about 34%. The diameter of the feedstock is 0.4 mm. The procedure for fabricating pre-pregnant feedstock is shown in Figure 1D.

2.3. Additive manufacturing of continuous fiber-reinforced resin composites

A modified FFF printer was used as the additive manufacturing device and the pre-pregnant feedstock consisting of both the resin and continuous carbon fibers was used as the printing filament. The schematic diagram of the procedure for fabricating continuous fiber-reinforced resin composites is shown in Figure 1. The feedstock was directly supplied into the printing head. As the printing began, the resin was melted in the heater, and the fibers coated with melted resin adhered to the workbench. As the workbench was moved by the designed toolpath, the resin and fibers were pulled out and the corresponding trail was formed. After printing few layers, the green parts specimens were fabricated. The diameters of nozzle and the feedstock are 0.8 mm and 0.4 mm, respectively. The printing temperature is 210°C. The printing speed is 3 mm/s. The procedure for fabricating C_f/SiC composite parts is shown in Figure 2.

2.4. Preparation of C_f/SiC composites

After the green parts specimens were prepared by additive manufacturing, they were vacuum-impregnated with PCS. Then, the specimens were cured for the solidification of PCS to obtain the impregnated parts at 140°C for 2 h. As the decomposition temperature of the PLA and PETG resin is about 400°C and 500°C, respectively (Figure 3), lower than that of the PIP process, and when the carbonization and PIP process of impregnated parts were conducted at 1100°C for 2 h with a heating rate of 2 K/min under the

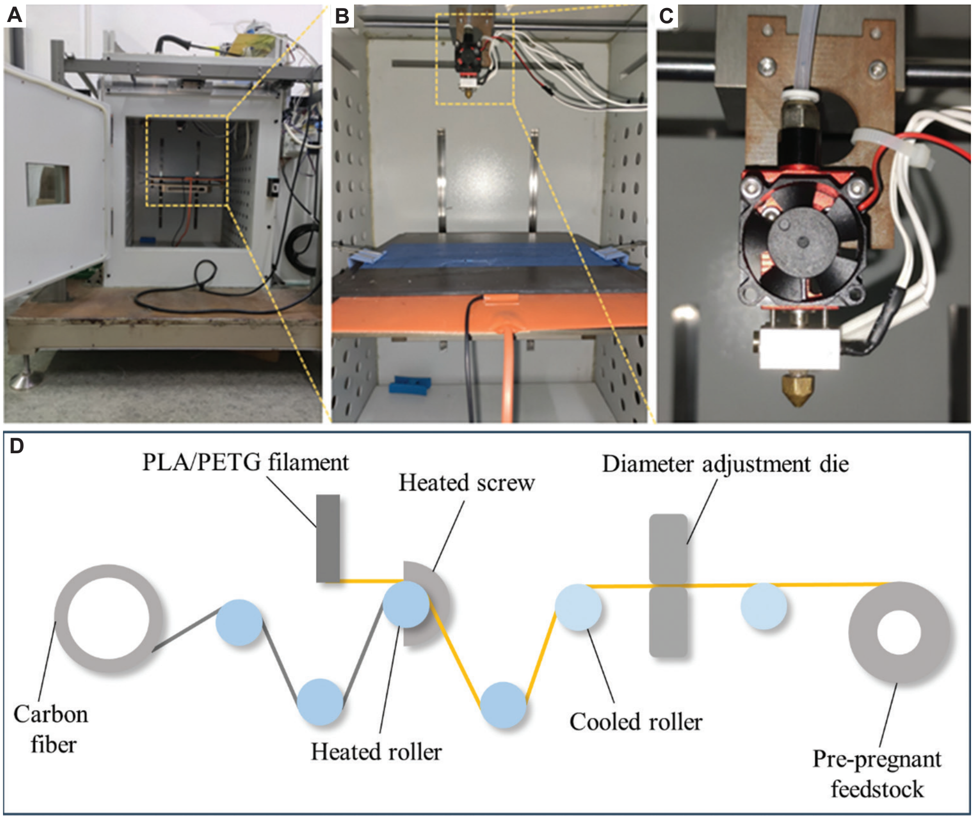

Figure 1. Modified fused filament fabrication printer equipment for additive manufacturing green parts. (A) The overall structure of the equipment. (B) Printing platform and print head. (C) Print head details. (D) Schematic diagram of the procedure for fabricating pre-pregnant feedstock.

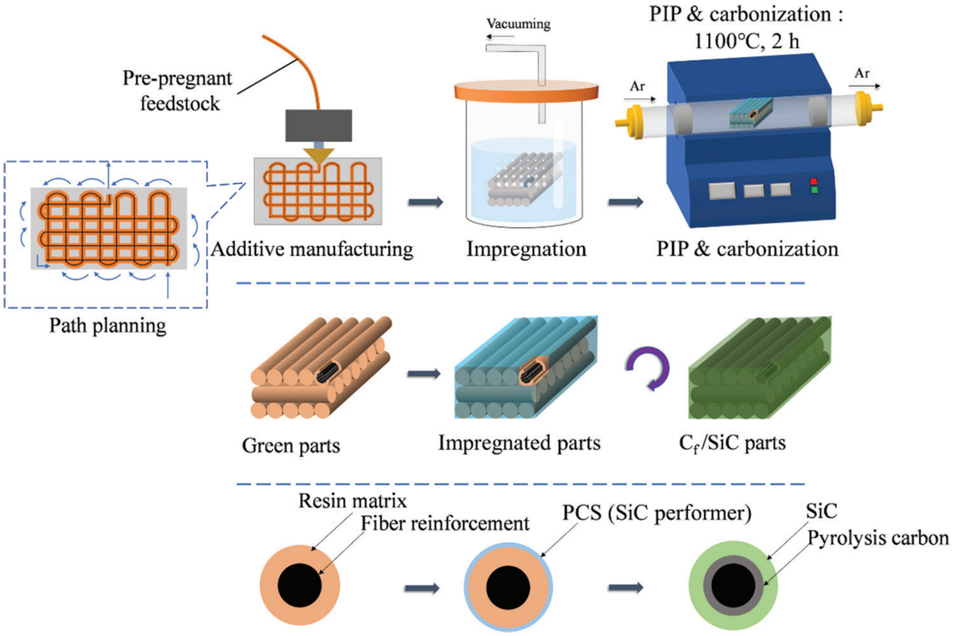

Figure 2. The schematic diagram of the procedure for fabricating carbon fiber/silicon carbide composite parts.

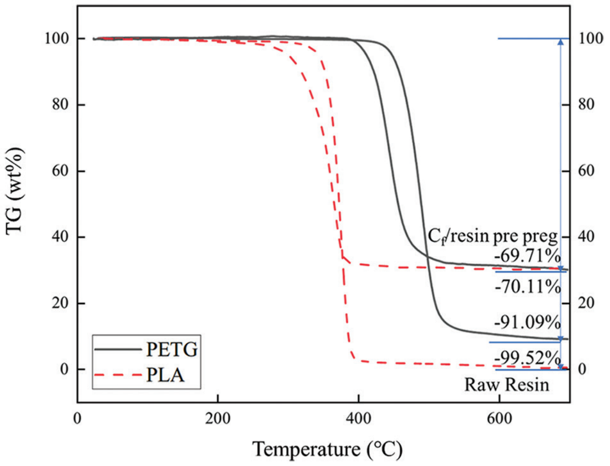

Figure 3. Thermogravimetric test results of polylactic acid and polyethylene terephthalate glycol resin and pre-pregnant.

protection of a 99.99% argon atmosphere in the tubular furnace, the PLA resin was first completely carbonized, and then the ceramic precursor was converted to SiC. The PIP process was conducted 9 times until the apparent porosity of all the specimens was above 90%.

2.5. Characterization and tests

The apparent porosity and bulk density of green parts and C_f/SiC specimens were measured by the Archimedes method. The microstructures of pre-pregnant filament, C_f/PLA green parts, and C_f/SiC specimens were observed by scanning electron microscope (SEM) (JSM-7600F, JEOL, Japan; Quanta 650, FEI, USA). The compositions of the C_f/SiC specimens were analyzed by X-ray diffractometer (XRD-7000, SHIMADZU Corporation, Japan), with Cu Kα radiation in the 2θ range between 10° and 80° with a scan speed of 10°/min. The flexural strength of the green parts and C_f/SiC specimens was measured by three-point bending tests using a universal testing machine (Zwick/Roell Z010, Ulm, Germany), and the green parts were cut into pieces, each with a dimension of 40 × 15 × 3 mm, by blade saw, and C_f/SiC specimens were cut into pieces, each with a dimension of 40 × 4 × 3 mm, by diamond wire saw. The fracture toughness was evaluated using the single-edge notched beam (SENB) method according to ASTM C1421-16 standard. Four notched samples with a dimension of 20 mm × 3 mm × 4 mm were prepared. The edge notch was introduced by a diamond wire saw with a width of 0.2 mm, and the ratio of the notch depth to specimen height (a/H) was in the range of 0.40–0.55. The notch depth was measured using a caliper. The fracture toughness, K_{IC} was calculated using the following equations:

$$K_{IC} = \frac{3P_{max}L}{2WH^{3/2}}\alpha^{1/2}Y \tag{I}$$

$$Y = \frac{1.99-\alpha(1-\alpha)(2.15-3.93\alpha+2.7\alpha^2)}{(1+2\alpha)(1-\alpha)^{3/2}} \tag{II}$$

where P_{max} is the maximum load during the three-point bending test; L is the support span; W is the specimen width; H is the specimen height; a is the notch depth; α is the ratio of a and H; and Y is the calibration factor.

2.6. Process parameters

An open-source slicing software Cura was first used to slice the computer-aided design (CAD) model into layers and make path planning according to process parameters. Then, the Gcode file generated by Cura was manually modified to fit the criteria of continuous fiber printing needs, such as no travel, no jump-point, and one-line moving. The infill line distance (ILD) is the most relevant process parameter in this work. The infill is the inner part of the continuous fiber-reinforced resin composite green part. Infill patterns can be lines, grids, hexagons, etc. In this work, orthogonal lines were selected as the infill pattern (shown in Figure 4). The printed blocks 100 × 100 × 3 mm are shown in Figure 5. The infill pattern of orthogonal lines provides voids for the filling of SiC or C source, thus featuring prominently in PCS or phenolic resin infiltration. As the infill pattern consists of multiple layers in space, there are straight lines in each infill layer. The amounts of these lines are decided by the parameter called ILD. This parameter also influences the size of voids created by intersectional vertical lines. As the distances of infill line increases, the size of voids increases, leading to higher level of PCS or phenolic resin infiltration and resulting in a higher proportion of SiC in final C_f/SiC specimens.

In this work, ILDs of 1.4, 1.6, 1.8, and 1.9 were selected, and specimens were named ILD-1.4, ILD-1.6, ILD-1.8, and ILD-1.9 (Figure 6), respectively. The mechanical properties of corresponding C_f/PLA green parts and C_f/SiC specimens were tested to delineate the mechanism of how the size of voids in C_f/PLA green parts influences the mechanical properties of C_f/PLA green parts and C_f/SiC specimens.

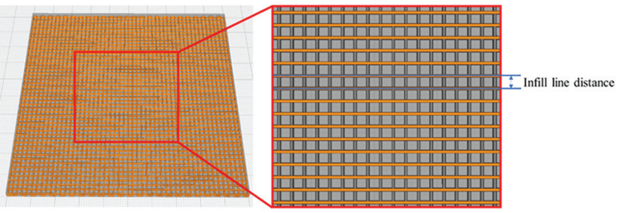

Figure 4. Slice of computer-aided design model and schematic diagram of infill pattern and infill line distance.

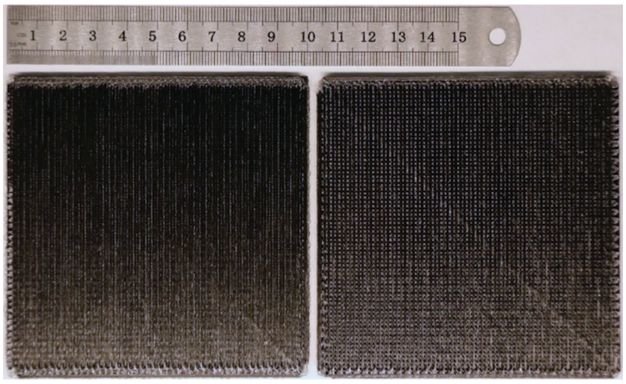

Figure 5. Printed blocks of green parts with the infill pattern of vertical lines fabricated by additive manufacturing: Infill line distance (ILD)-1.4 (left) and ILD-1.9 (right).

3. Result and discussion

3.1. Continuous fiber-reinforced resin composite green parts

3.1.1. Microstructure and morphology of the green parts

The size of the fiber-reinforced resin-based specimens prepared by additive manufacturing was 100 mm × 100 mm × 3 mm. Two smaller specimens with dimensions of 40 mm × 15 mm × 3 mm and 40 mm × 30 mm × 3 mm were obtained by blade sawing. Microscopic observation was performed using SEM, and the results are shown in Figure 7. Figure 7A shows that the cross-section of the blade-sawed specimen was smooth and flat, and the additive manufacturing forming layer could be clearly observed, which was composed of a multilayer structure such as resin-fiber-resin from the top to the bottom. Fiber bundles perpendicular to the cross-section in the axial direction were also observed. There was no interlayer porosity between the upper and lower forming layers, indicating that the additive manufacturing process had gone well and the layers with good interlayer bonding properties were obtained.

Figure 7B shows that the specimen surface consists of forming layers with orthogonal upper and lower printing directions. The filled part in each layer was not completely dense due to the setting of the ILD, and the unfilled part was macroscopically porous. The macroscopic pores provide channels as well as space for the impregnation of the ceramic precursor slurry into the interior of the specimen. From Figure 7C and 7D, it can be observed that the fiber bundles were closely interfaced with the resin matrix, forming a significant interfacial area, and the resin

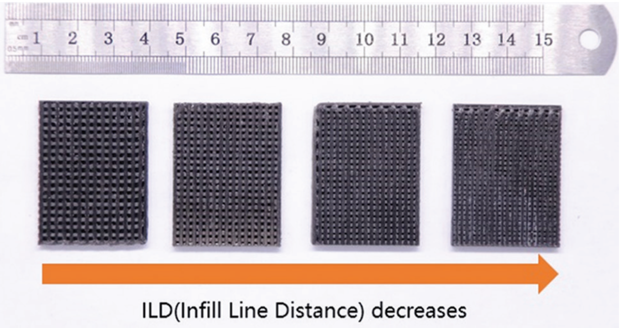

Figure 6. Continuous fiber-reinforced resin matrix composites fabricated by additive manufacturing: Infill line distance (ILD)-1.9 (first one from the left) to ILD-1.4 (first one from the right).

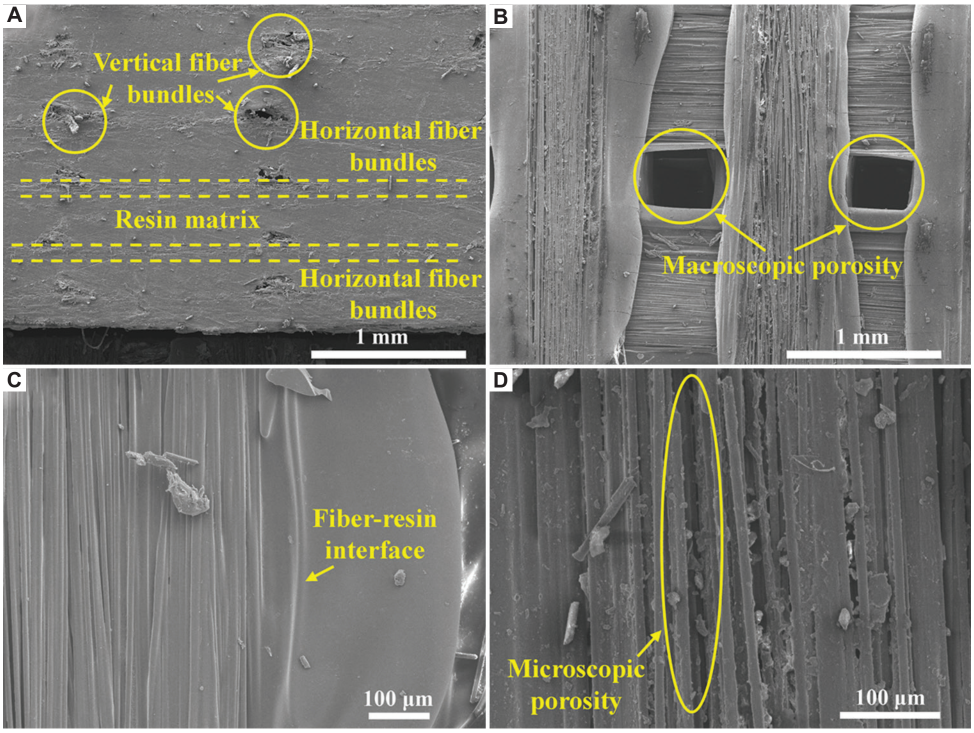

Figure 7. Scanning electron microscope observation of fiber-reinforced resin-based green parts specimens. (A) Cross-section, (B) surface, (C) fiber bundle-resin matrix large interface, and (D) fiber filaments and attached resin small interfaces.

adhered tightly to the fiber bundles without evident voids or pores. This enhanced the mechanical properties of the fiber-reinforced resin-based green parts, on the one hand, but also hinders the impregnation of the ceramic precursor slurry during the process, on the other hand, which is not conducive to a more adequate impregnation.

3.1.2. Mechanical properties of green parts

The specimen size of fiber-reinforced green parts evaluated in the three-point bending test was 40 mm × 15 mm × 3 mm (as shown in Figure 8). The test span was 30 mm, and the loading rate was 2 mm/min. The test was conducted according to the standard ISO 14125:1998. The test results are shown in Figure 9.

It can be found that as the ILD decreased, the percentage of fibers in the green parts specimens increased, the specimens became denser, and the bending strength became higher. The low flexural strength observed in the ILD-1.8 group may be due to the specimen selection position toward the edge, which resulted in an error in the test results. Table 1 shows the average bulk densities of the fiber-reinforced resin matrix composite green part specimens, where the bulk densities were determined by dividing the dry weight of the specimens by the apparent volume of the specimens. It can be seen that the bulk density of the specimens basically corresponds to the bending strength. The smaller the ILD, the larger the amount of fibers and resin in the specimens, and the higher the bulk density, resulting in the higher strength of the specimens.

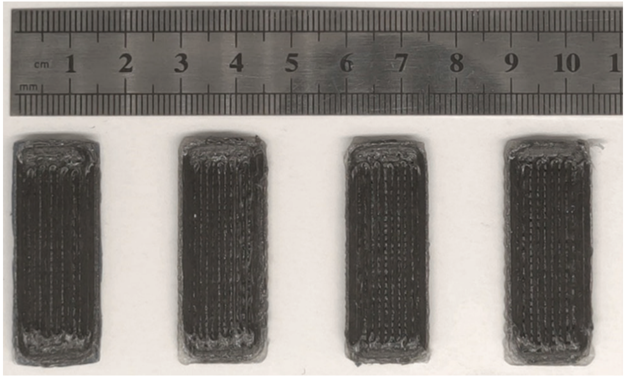

Figure 8. Three-point bending test specimens for continuous fiber-reinforced resin matrix composites.

Typical stress-displacement curves in each ILD group during the test are shown in Figure 9B. The curves are divided into four stages: a linear elastic stage from the beginning of the test to the yield point, in which the specimen has elastic properties; a yielding stage in which the slope of the curve decreases and fluctuates, but the stress is still rising; a sudden linear falling stage after rising to the maximum stress; and a falling stage in which the drop slows down and shows a ductile fracture after falling to a certain degree. The stress-displacement curve characteristics indicate that the continuous fiber-reinforced resin matrix composite printed by additive manufacturing has strong toughness. The cross-sectional SEM results in Figure 10 show that the resin matrix composites underwent different degrees of fiber pullout and matrix debonding at fracture, and the ILD-1.2 group with smaller ILD has longer fiber pullout length and more fiber pullout quantity compared to the ILD-1.4 group. Comparing the three-point bending test results, the cross-sectional properties also proved that the ILD directly affected the mechanical properties of the continuous fiber-reinforced resin matrix composites: as the ILD decreased, the bending properties of the continuous fiber-reinforced resin matrix composites became stronger.

3.2. Continuous fiber-reinforced SiC composites (C_f/SiC)

3.2.1. Densification and weight gain during PIP process

In this experiment, two continuous fiber-reinforced resin matrix composites with different resin matrix, namely, C_f/PETG and C_f/PLA, were used as green parts for the ceramicization treatment and the continuous fiber-reinforced SiC composites obtained from the post-

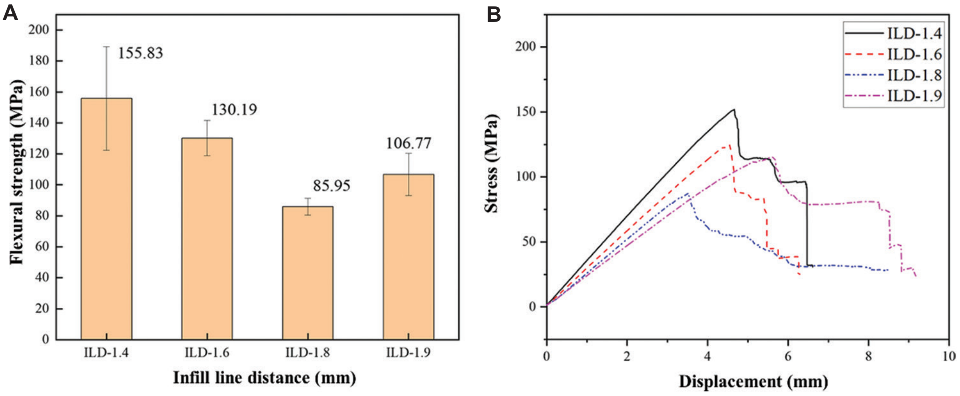

Figure 9. Results of three-point bending test of the continuous fiber-reinforced resin matrix composites. (A) Flexural strength and infill line distance. (B) Stress-displacement curves.

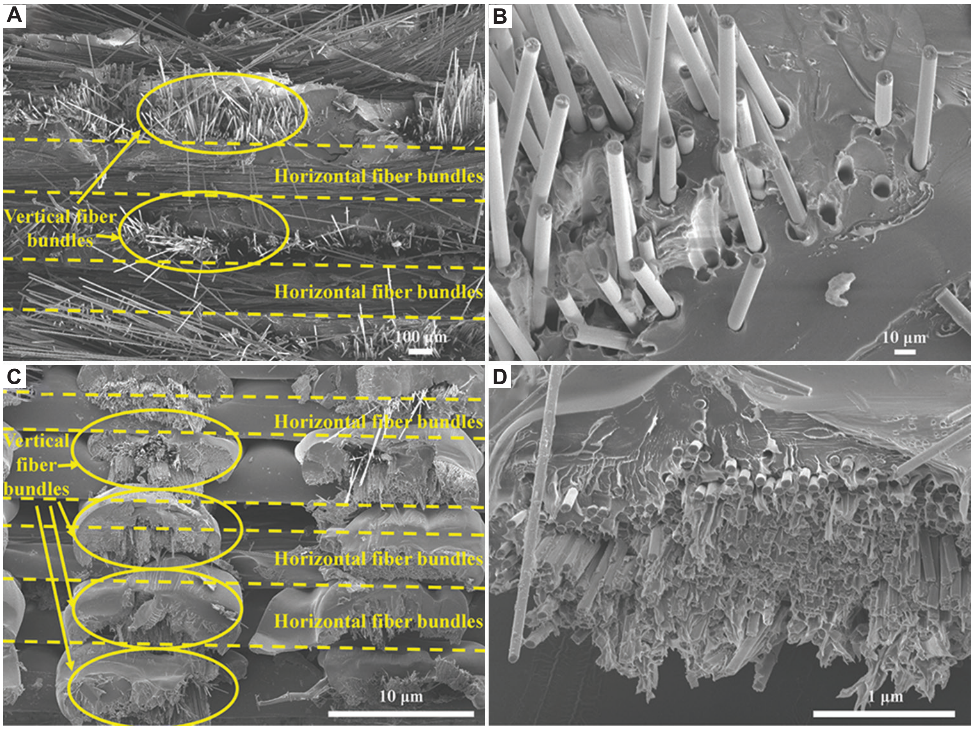

Figure 10. Fracture morphology of the cross-section of continuous fiber reinforced composites. (A and B) Infill line distance (ILD)-1.2. (C and D) ILD-1.4.

treatment of these two green parts are abbreviated as C$_f$/SiC (PETG) and C$_f$/SiC (PLA), respectively. Figures 11 and 12 show the average apparent porosity and average bulk density of the ILD-1.0 group of C$_f$/SiC (PETG) and ILD-1.4 group of C$_f$/SiC (PLA) specimens as the duration of PIP increases. A PIP cycle with a value of 0 indicates the green parts that have not yet undergone PIP treatment. As shown in Figure 12, after excluding the data of the green parts state, the apparent porosity decreased with the increase of the number of PIP cycles, the rate of decrease gradually slowed down and finally reached 7.2%, the bulk density increased with the increase of the number of PIP cycles, and the rate of increase gradually slowed down until it reaches 2.24 g/cm^3. The significant changes in the apparent porosity and bulk density were mainly caused by the high-temperature pyrolysis in the first PIP process, which caused the carbonization of the resin in green part specimens, resulting in a large number of pores between and within fiber bundles, and the decomposition of the resin also brought about a huge weight loss, thus leading to a significant increase in apparent porosity and a significant decrease in bulk density.

Table 1. Infill line distance and bulk density of continuous fiber-reinforced resin matrix green part specimens

Specimens	Infill line distance (mm)	Bulk density (g/cm³)
ILD-1.4 (PLA)	1.4	0.916
ILD-1.6 (PLA)	1.6	0.841
ILD-1.8 (PLA)	1.8	0.724
ILD-1.9 (PLA)	1.9	0.650

ILD: Infill line distance; PLA: Polylactic acid

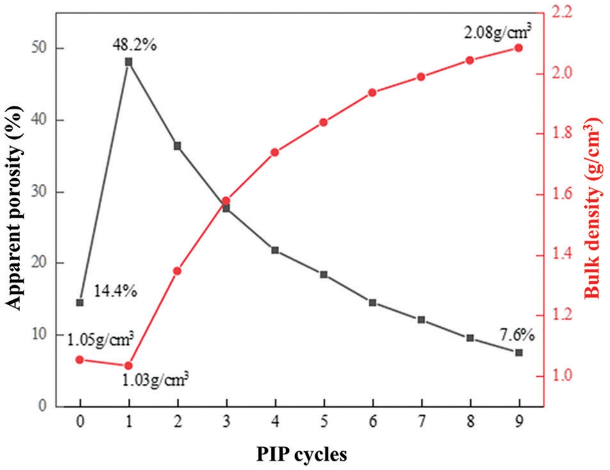

Figure 11. Relationship between apparent porosity/bulk density and precursor infiltration pyrolysis period for carbon fiber/polyethylene terephthalate glycol (C$_f$/PETG) green parts and C$_f$/SiC (PETG) specimens.

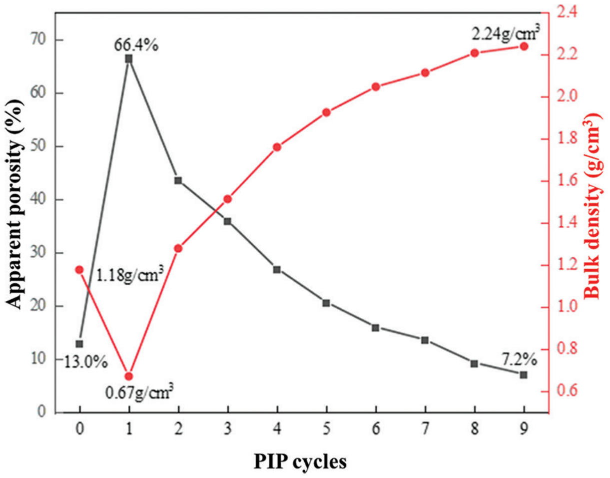

Figure 12. Relationship between apparent porosity/bulk density and precursor infiltration pyrolysis period for C$_f$/PLA green parts and C$_f$/SiC (PLA) specimens.

Figure 13 shows the gradual change of surface morphology of the C$_f$/SiC specimens with the change of PIP cycles. It can be seen that the surface morphology of the specimen became denser and the surface became flatter as the number of PIP cycles increased, indicating that the composite had undergone significant densification in multiple PIP cycles.

Tables 2-5 present the relationship between the variation of bulk density and porosity with PIP cycles for C$_f$/SiC (PETG) and C$_f$/SiC (PLA) specimens of different

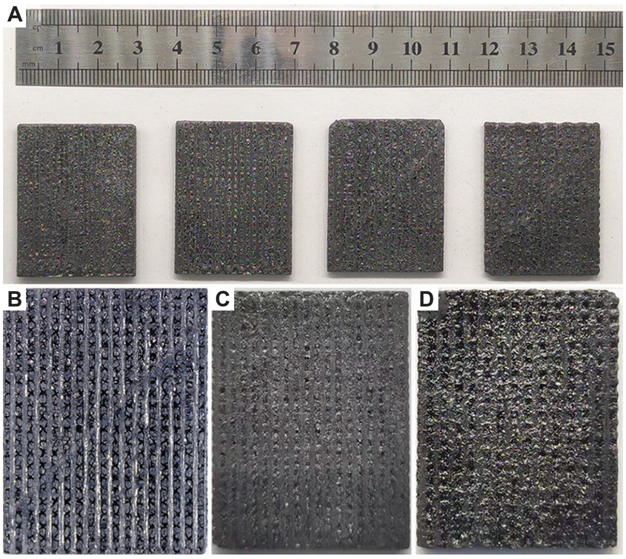

Figure 13. Morphology evolution of Cf/SiC specimens during precursor infiltration pyrolysis (PIP) process. (A) After nine cycles of PIP (from left to right: infill line distance [ILD]-1.4, ILD-1.6, ILD-1.8, ILD-1.9). (B) After the first PIP cycle. (C) After four cycles of PIP. (D) After seven cycles of PIP.

Table 2. Variation of bulk density (g/cm^3) of C$_f$/PETG green parts and C$_f$/SiC (PETG) specimens with PIP cycles

ILD	Green parts	1st cycle	2nd cycle	9th cycle
ILD-1.0	1.0542	1.0350	1.3477	2.0841
ILD-1.2	1.1092	1.0523	1.3547	2.1311
ILD-1.4	1.0823	1.0443	1.3495	2.1854

ILD: Infill line distance; C$_f$/PETG: Carbon fiber/polyethylene terephthalate glycol; C$_f$/SiC: Carbon fiber/silicon carbide; PIP: Precursor infiltration pyrolysis

Table 3. Variation of apparent porosity (%) of C$_f$/PETG green parts and C$_f$/SiC (PETG) specimens with PIP cycles

ILD	Green parts	1st cycle	2nd cycle	9th cycle
ILD-1.0	14.4301	48.1589	36.4084	7.5551
ILD-1.2	13.3717	47.7997	36.4869	6.4543
ILD-1.4	17.5792	49.0309	37.5655	5.5887

ILD: Infill line distance; C$_f$/PETG: Carbon fiber/polyethylene terephthalate glycol; C$_f$/SiC: Carbon fiber/silicon carbide; PIP: Precursor infiltration pyrolysis

Table 4. Variation of bulk density (g/cm^3) of C$_f$/PLA green parts and C$_f$/SiC (PLA) specimens with PIP cycles

ILD	Green parts	1st cycle	2nd cycle	9th cycle
ILD-1.4	1.1772	0.6714	1.2791	2.2391
ILD-1.6	1.1714	0.7570	1.3336	2.2509
ILD-1.8	1.0844	0.8597	1.4505	2.2331
ILD-1.9	1.0833	1.0139	1.5032	2.2264

ILD: Infill line distance; C$_f$/PLA: Carbon fiber/polylactic acid; C$_f$/SiC: Carbon fiber/silicon carbide; PIP: Precursor infiltration pyrolysis

Table 5. Variation of apparent porosity (%) of C$_f$/P PLA green parts and C$_f$/SiC (PLA) specimens with PIP cycles

ILD	Green parts	1st cycle	2nd cycle	9th cycle
ILD-1.4	12.9890	66.4412	43.5404	7.1637
ILD-1.6	13.1404	62.9703	41.4452	7.1693
ILD-1.8	20.0344	58.9546	35.7299	7.7472
ILD-1.9	20.2687	51.9076	33.3048	7.6816

ILD: Infill line distance; C$_f$/PLA: Carbon fiber/polylactic acid; C$_f$/SiC: Carbon fiber/silicon carbide; PIP: Precursor infiltration pyrolysis

ILD groups. From the C$_f$/SiC (PLA) specimens, it can be found that the bulk density of resin matrix composite specimens decreased with the increase of ILD and the porosity increased with the increase of ILD at the green parts state. With the increase of PIP cycles, the bulk density of SiC composite specimens increased with the increase of ILD, and the porosity decreased with the increase of ILD. A different trend was shown before and after the ceramicization treatment. This is due to the fact that in resin matrix composites, the ILD is directly related to the actual composite usage at the same volume. As the ILD increases, the resin and fiber dosage of the specimen at the same volume decreases, and the macroscopic pores between the fibers become larger, leading to a reduction in the bulk density of the resin matrix composite and an increase of porosity. After the PIP ceramicization treatment, the density of the generated SiC is greater than that of carbon fibers. Therefore, as the ILD increases, the number of macroscopic pores of the specimens increases, and the ceramic precursors are able to impregnate more into the porous green parts, thus generating more SiC during the pyrolysis process and increasing the bulk density. In contrast, the porosity of the SiC composites was negatively correlated with the ILD, which is attributed to the fact that the fiber content in the specimen decreased as the ILD increased, and the voids between the individual fibers within the fiber bundles were the main source of the apparent porosity of the specimens, so the porosity of the SiC composites decreased as the fiber content decreased. However, C$_f$/SiC (PETG) showed the opposite trend at nine cycles. The reason is that the density of pyrolytic carbon generated after carbonization of PETG is lower than that of SiC generated by PIP, and when the ILD increases, the percentage of pyrolyzed carbon decreases, resulting in a higher bulk density of the specimen instead. Similarly, when the ILD increases, the pyrolytic carbon decreases and the C$_f$/SiC specimens become less microporous and less likely to block the impregnation channels, so the porosity decreases instead. Both of these trends become more and more obvious with increasing PIP cycles.

3.2.2. Microstructure and phase evolution of the C$_f$/SiC composites during PIP process

3.2.2.1. C$_f$/SiC (PETG)

The C$_f$/PETG group has a shorter ILD, so the specimens were pre-carbonized before the first cycle cracking. The porous green part specimens were first impregnated in the ceramic precursor, cured, and then pre-carbonized at 400°C/1 h. At this time, the PETG matrix was partially decomposed, resulting in the formation of more pores, as shown in Figure 14A and 14B, where the pre-carbonization caused the resin to decompose, resulting in more voids inside the fiber bundle to facilitate the next precursor impregnation. The surface scan results showed that many protruding Si-rich materials were formed on the fiber surface, and the interior of the fiber bundle was infiltrated by SiC ceramic precursor (Figure 15A–C). In addition, a large amount of C element distribution was observed in the SEM surface scan of the pre-carbonized specimens, indicating that PETG, as the matrix of C$_f$/PETG green parts, has a high residual carbon composition, and after pre-carbonization, PETG underwent partial decomposition to generate more pyrolyzed carbon, which, on the one hand, helps to protect carbon fibers from corrosion in the subsequent PIP process, and, on the other hand, increases the content of impure C elements in the final C_f/SiC products.

After the completion of pre-carbonization, the porous green part specimens were impregnated with the precursor again, followed by curing and first-cycle pyrolysis, at which time the SiC phase was generated for the first time in the specimen. Based on Figure 14C and D as well as Figure 15D–F, a large amount of SiC phase was generated on the surface of the specimen compared to the specimen after the pre-carbonation treatment, and large portions of the SiC phase produced cracks perpendicular to the fiber axes due to the thermal mismatch phenomenon with the fibers[45].

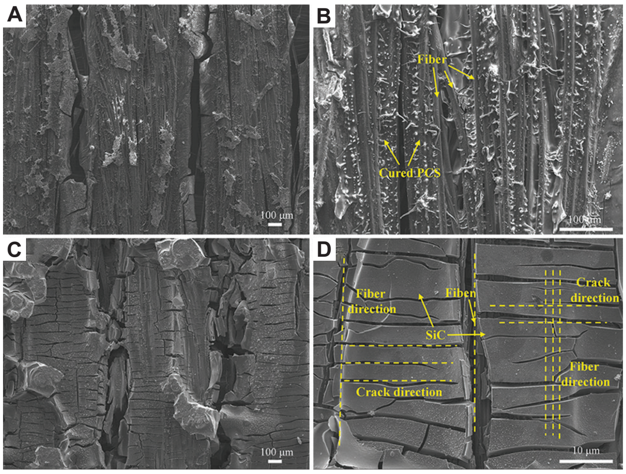

Figure 14. Scanning electron microscope observation of polyethylene terephthalate glycol (PETG)-based green parts. (A and B) Pre-carbonized PETG-based green parts. (C and D) PETG-based green parts in the first-cycle precursor infiltration pyrolysis.

3.2.2.2. C_f/SiC (PLA)

The first cycle of PIP is the point at which the green parts specimen is transformed from a resin-based composite to a ceramic-based composite. Figure 16 shows the micrographs of the specimen after undergoing the first-cycle PIP treatment. Compared with Figure 5, Figure 16A shows that the resin matrix in the specimen was almost completely decomposed, and the impregnated space left behind by the previous macroscopic hole became a large, collapsed SiC phase. Figure 16B shows the cross-section of the specimen, which was cut by scissors. It can be seen that the resin-fiber-resin multilayer structure in the green part specimens was left with only fiber layers parallel and perpendicular to the cross-section, thus leaving a large number of pores, which explains the significant increase in apparent porosity and the significant decrease in bulk density of the specimen after the first cycle of PIP treatment. Figure 16C shows the surface of the specimen, which shows that large thin planes of SiC phase was formed on the surface of the specimen, and the large SiC phase was divided into many small areas by many cracks along the direction perpendicular to the fiber axis. This is caused by several factors: (i) a large number of small molecules escape from the PCS during the pyrolysis process, resulting in a large volume shrinkage of the resulting ceramic product; (ii) the PIP process is accompanied by a large temperature difference between high and low temperatures; and (iii) the thermal expansion coefficient between the generated SiC phase and the carbon fiber does not match, resulting in cracking[45]. Figure 16D shows that the bond between the fibers and the matrix is very strong, forming a strong

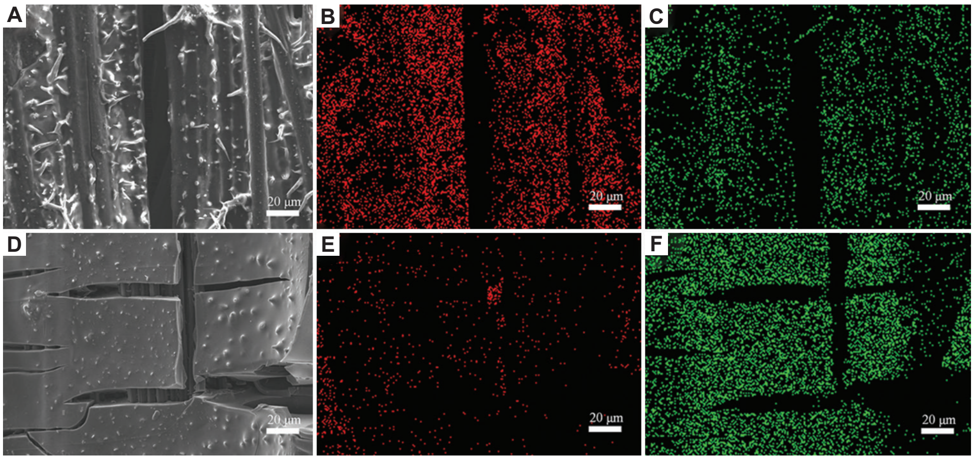

Figure 15. Energy dispersive spectroscopy surface scan results of polyethylene terephthalate glycol (PETG)-based green parts. (A) Pre-carbonized PETG-based green parts. (D) PETG-based green parts in the first-cycle precursor infiltration pyrolysis. (B and E) C element distribution. (C and F) Si element distribution.

interface. This does not facilitate the stress transfer during load bearing of the composite, thus weakening the mechanical properties of the composite.

Figure 17 illustrates the basic state of the specimen after the first cycle of PIP treatment: the carbon fiber skeleton is the main phase with large SiC phase covering the surface, while there is basically no SiC production inside the fiber bundle. This is due to the fact that the resin in the green parts prevents the infiltration of the ceramic precursor slurry, resulting in very little SiC production inside the fiber bundle, which is significantly different from the pre-carbonized C_f/SiC (PETG) composites as shown in Figure 14C and 14D.

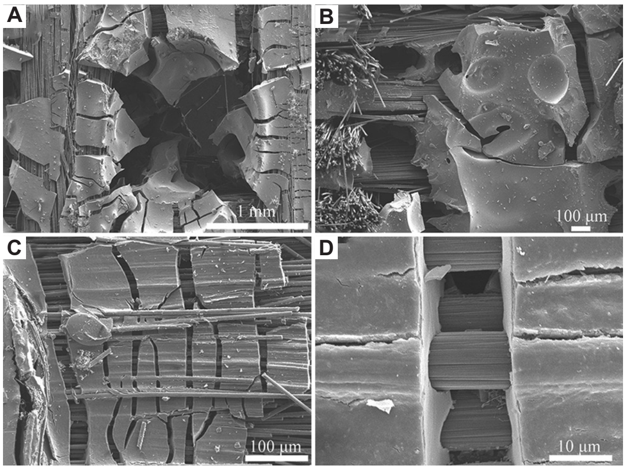

Figure 16. Scanning electron microscope results of polylactic acid-based green part first-cycle PIP-treated specimens. (A) The macroscopic hole. (B) The cross-section of the specimen. (C) The surface of the part. (D) The interface of the sample.

The second cycle of PIP is the onset of densification of the ceramic-based composite specimens, and the most significant weight gain of the composite is observed at this stage. Figure 18 shows the SEM and energy dispersive spectroscopy (EDS) results of the specimens after the second PIP treatment. As shown in Figure 17, the SiC phase also started to appear in the areas that were previously blocked by the resin. In addition to the large SiC generated in the first cycle, the specimen surface also displayed small and fine SiC. According to Figure 18F and 18H, the SiC had already started to be generated inside the fiber bundle.

Figure 19A shows the X-ray diffraction analysis (XRD) results of the specimens during the PIP process, and it can be seen that the XRD results of both the first-cycle and second-cycle PIPs did not clearly show the SiC characteristic peaks due to the low SiC content in the samples. However, the characteristic peak of β-SiC could be found in the XRD pattern of the ninth-cycle PIP, but the peak intensity was not high. It is presumed that this is due to the fact that the maximum temperature of the PIP process in this study was controlled at 1100°C, which is lower than the stable growth temperature of α-SiC and β-SiC, and most of the SiC phases with amorphous forms were obtained. In addition, Figure 19B shows the results of EDS elemental analysis of the C_f/SiC specimen after the nine-cycle PIP, which is dominated by C and Si elements and also contains a trace amount of O elements, which should be introduced during the PIP process or SEM testing, and the results confirmed the generation of SiC, which is consistent with the XRD results.

3.2.3. Mechanical properties of the C_f/SiC composites

The three-point bending test specimens were cut into a specimen size of 40 mm × 4 mm × 3 mm using a diamond

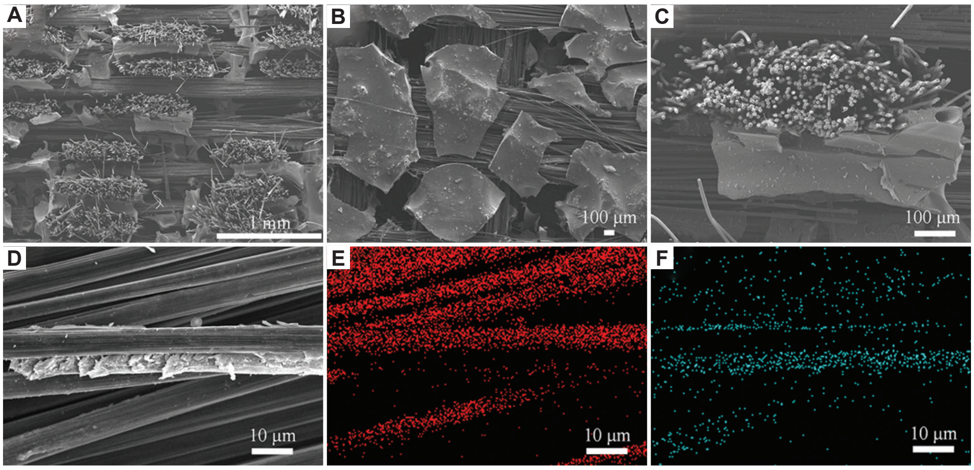

Figure 17. Scanning electron microscope and energy dispersive spectroscopy (EDS) results of polylactic acid-based green parts first-cycle precursor infiltration pyrolysis-treated specimens. (A–C) scanning electron microscope photos of specimen cross-section and surface. (D) Single fiber attached with a small amount of SiC. EDS surface scan results of (E) C element distribution and (F) Si element distribution for single fiber area.

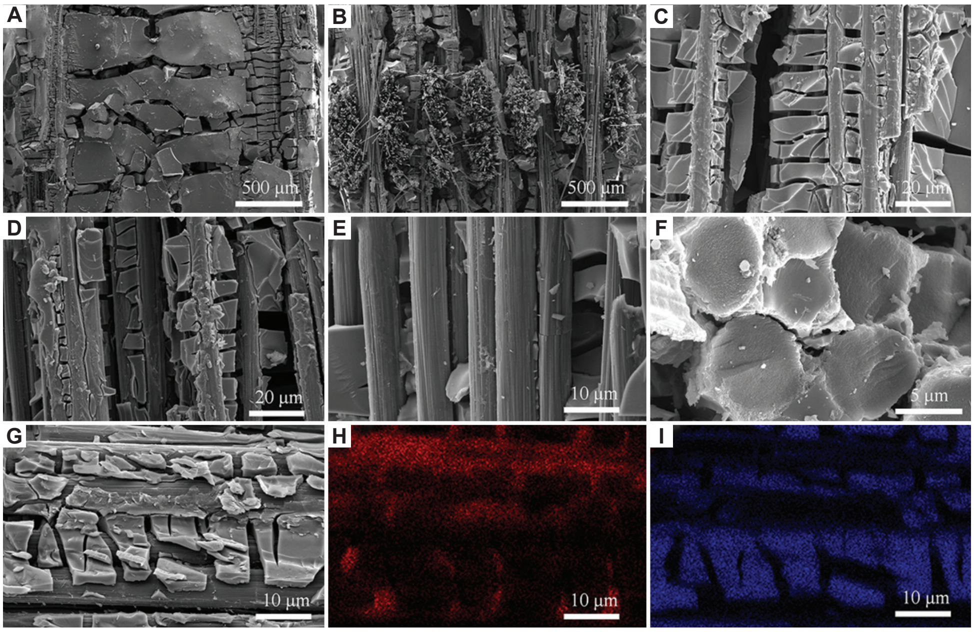

Figure 18. Scanning electron microscope (SEM) and energy dispersive spectroscopy (EDS) results of the second-cycle precursor infiltration pyrolysis -treated specimens of C_f/SiC (polylactic acid) composites. (A–G) SEM results. (H) EDS surface scan results of C elements. (I) Surface scan results of Si elements.

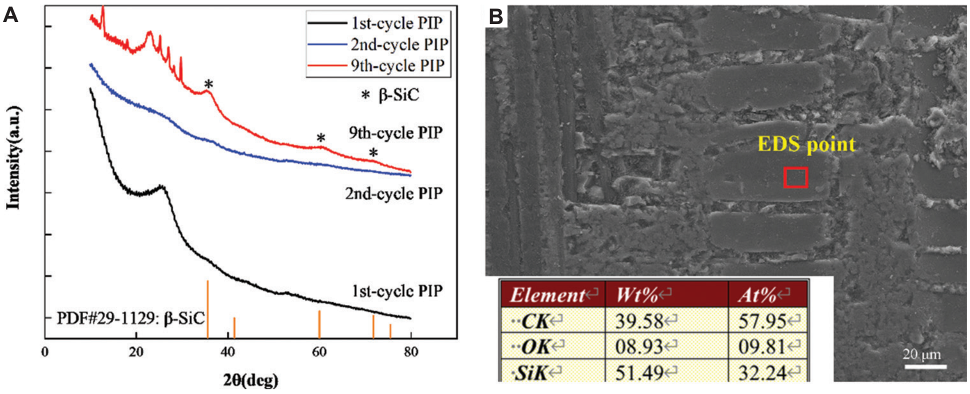

Element	Wt%	At%
CK	39.58	57.95
OK	08.93	09.81
SiK	51.49	32.24

Figure 19. Carbon fiber/silicon carbide (C_f/SiC) physical phase analysis. (A) X-ray diffraction results of C_f/SiC specimens during precursor infiltration pyrolysis (PIP). (B) energy dispersive spectroscopy point scanning results of ninth-cycle PIP.

wire cutter (as shown in Figure 20), with a span of 30 mm and a loading rate of 0.5 mm/min. The tests were conducted in accordance with the standard GBT6569 – 2006.

Figure 21 shows the mechanical properties of the two C_f/SiC composites with different ILDs. It can be seen that the bending strength of continuous fiber-reinforced SiC composites tends to decrease as the ILD increases because the percentage of carbon fibers in the specimens decreases and the SiC content rises as the ILD increases, and the reinforcing phase in the composite decreases, which leads to a decrease in the overall bending strength of the specimens. The error in the ILD-1.9 group was

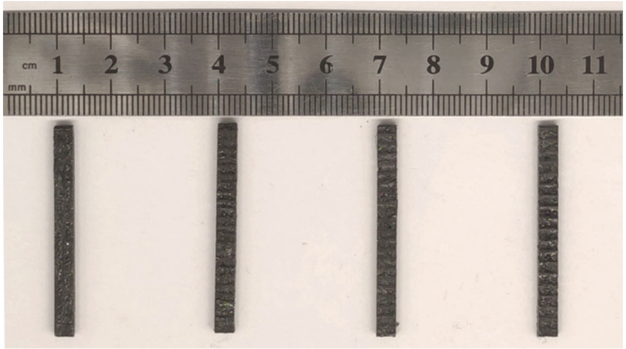

Figure 20. Standard specimens of carbon fiber/silicon carbide for three-point bending test.

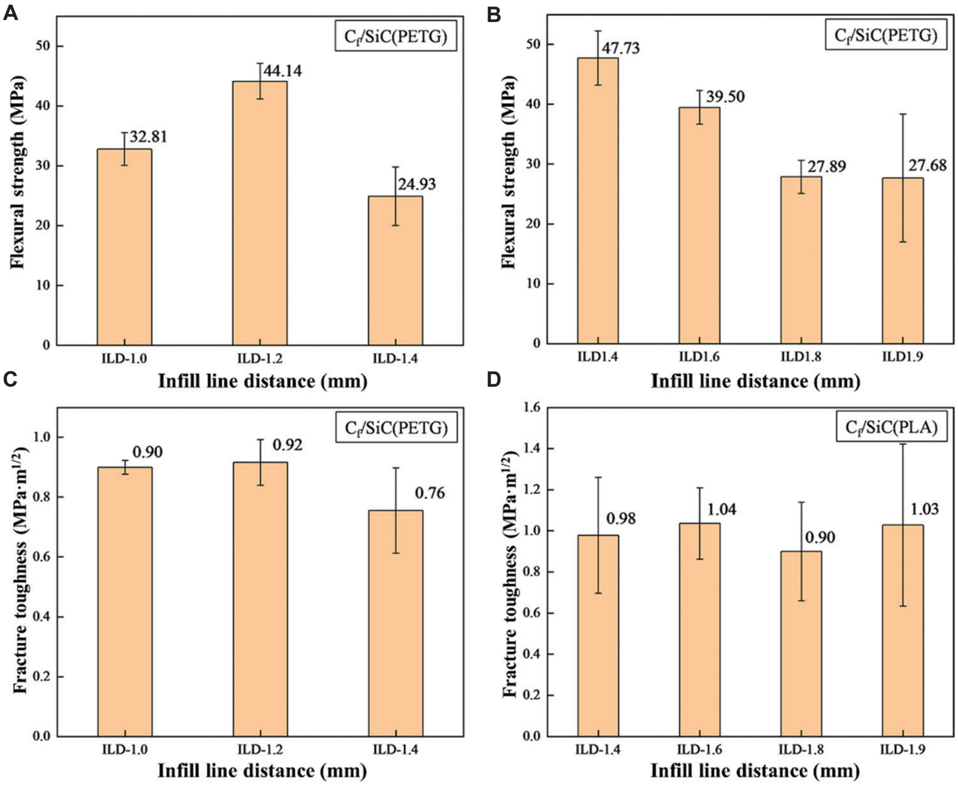

Figure 21. Carbon fiber/silicon carbide (C$_f$/SiC) composite mechanical properties tests. (A and C) Three-point bending and fracture toughness test results of C$_f$/SiC (polyethylene terephthalate glycol) composite. (B and D) Three-point bending and fracture toughness test results of C$_f$/SiC (polylactic acid) composite.

more prominent because the continuous fiber-reinforced SiC composites prepared by the PIP method had more internal closed pores and more defects. Especially when the density of the green parts was very low, the holes between the fiber skeletons became very large, resulting in plenty of macroscopic pores in the continuous fiber-reinforced SiC composites. As a result, more pores would be left behind inside the composites, essentially affecting the test results and resulting in errors of the bending strength. Moreover, when the ILD decreased, for instance, from 1.2 to 1.0 mm, the flexural strength declined from 44.14 MPa to 32.81 MPa. This is because the porosity of the green part specimens decreased by a large margin, and it was difficult for the green part specimens to impregnate PCS, thus resulting in the decrease of bending strength of the final C$_f$/SiC composite. An increase of the ILD, for example, from 1.8 to 1.9 mm, did not significantly reduce the bending strength; in fact, the bending strength of the specimens did not change much. This phenomenon is attributed to the fundamental inability of the ceramic precursors to completely fill the macroscopic pores due to the already large voids in the green part specimens. The incomplete filling of the pores leads to the fact that even an increase in the ILD cannot bring about a greater reduction in the impregnation volume and therefore cannot affect the bending strength of the final product.

Based on the comparison shown in Figure 21, it is known that the bending strength of C$_f$/SiC (PETG) composites was lower than that of C$_f$/SiC (PLA) composites for the same ILD (ILD-1.4). This is because the PETG-based green parts generate more pyrolyzed carbon during carbonization due to the high residual carbon composition in the PETG matrix material, generating many pyrolyzed carbon impurities in the final product and affecting the overall performance of the SiC composites. Similar to the bending strength, the fracture toughness showed a similar trend, but it was the ILD-1.6 group of C$_f$/SiC (PLA) that achieved a maximum fracture toughness of 1.04 MPa·m$^{1/2}$ due to the large fracture toughness test error caused by the uneven surface of continuous fiber-reinforced specimens, so the ILD-1.4 of C$_f$/SiC (PLA) and ILD-1.9 groups may have some deviations.

Figure 22 shows the stress-displacement curves of C$_f$/SiC (PETG) composites and C$_f$/SiC (PLA) composites in three-point bending with an ILD of 1.4. Among them, the stress-displacement curves of C$_f$/SiC (PETG) composites show the typical characteristics of fiber-reinforced ceramic

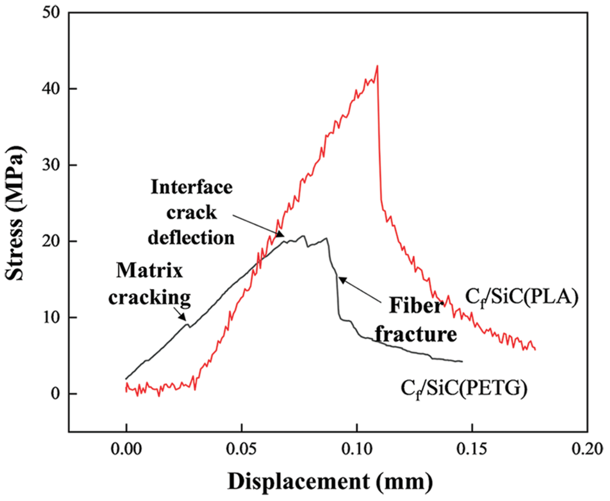

Figure 22. Three-point bending stress-displacement curves of carbon fiber/silicon carbide (C_f/SiC) (polyethylene terephthalate glycol) and C_f/SiC (polylactic acid) composites in infill line distance-1.4 group.

composites: When the stress of the specimen is lower than the cracking stress of the matrix, the curve presents linear elastic characteristics. When the stress exceeds the matrix cracking stress, the matrix cracks and expands, and the stress-displacement curve of the composite exhibits a nonlinear deformation characteristic. When the composite stress reaches its maximum value, the matrix-fiber interface starts to debond and fiber pullout occurs and the specimen eventually fractures[46].

The mechanical properties of continuous fiber-reinforced SiC composites could be obtained not only directly from the test, but also from the fracture morphology. Figure 23A–F show the SEM results captured from the cut surface of C_f/SiC (PETG) samples. Figure 23G–L show the SEM result of the three-point bending section of C_f/SiC (PETG) sample. As can be seen from Figure 23A–L, the fiber pull-out phenomenon was more obvious when ILD was shorter. With the increase of the ILD, the ductile fracture section manifesting obvious fiber pull-out phenomenon was transformed into a very flat brittle fracture. Based on Figure 24, C_f/SiC (PLA) composites showed more obvious fiber pull-out, matrix-fiber interface debonding and crack deflection, which are also consistent with the bending strength test results. In addition, EDS scan results of samples described in Figures 23 and 24 also indicate the presence of carbon fiber in the final product, and the carbon fiber did not suffer serious damage during multiple pyrolysis processes at high temperatures. Therefore, continuous fiber-reinforced SiC composite specimens with the maximum bending property of 47.73 MPa were obtained, which can achieve a certain degree of strengthening and toughening effect.

Although the carbon fibers suffered little corrosion during the PIP process, and a certain degree of toughening was achieved, the performance of the proposed continuous fiber-reinforced SiC composite for additive manufacturing was still lower than that of the continuous fiber-reinforced SiC composite prepared by the conventional process of two-dimensional woven carbon cloth laminated by puncture combined with PIP. The main reason is that for the ceramic precursor slurry to be impregnated into the porous fiber-reinforced green parts smoothly, a large pore space must be reserved in the design of green parts, which is reflected in the forming parameters of the green parts additive manufacturing process, where the ILD must be set to a larger value. Such forming parameters result in, first, a much lower percentage of the fiber-reinforced phase in the final product of C_f/SiC composites than that of C_f/SiC composites made by the conventional process. Second, the large ILD will eventually result in a large number of closed pores in the C_f/SiC compound during the first few PIP cycles, which are not connected to each other or to the outside world and cannot be filled by the ceramic precursor slurry impregnation during the subsequent PIP cycles to produce SiC. The combination of the two effects eventually reduces the mechanical properties of the C_f/SiC composites.

To overcome these problems, we first replaced PLA, a commonly used raw material in FFF additive technology, with PETG, a resin matrix material with higher residual carbon. Therefore, a pre-carbonization step was added before the carbonization step to partially carbonize and pyrolyze the PETG resin to create additional micropores, allowing the green parts to be impregnated with the ceramic precursor even at a shorter ILD. But the results showed little optimization. Taking the above into account, the bending strength of the C_f/SiC (PETG) composites (44.14 MPa) was nearly the same as that of the ILD-1.4 and even ILD-1.2 C_f/SiC (PLA) composites (47.73 MPa).

The reasons for this can be complex and multifaceted: Firstly, due to the mechanism of FFF additive devices, when the nozzle aperture of the heating head of the FFF device is fixed (0.8 mm in all cases used above), there is a lower limit to the setting of the ILD. When below this range, the distance between deposited lines is too small and the nozzle has a certain range of apertures, the molten prepreg filaments fed by the nozzle will undergo a lap behavior similar to that in the welding process to a larger extent, which will affect the forming quality of the green parts and the difficulty of impregnation of the precursor slurry. When the lap is too severe, it may even lead to the failure of the green parts forming. In this study, after several pre-experiments, the lower limit of this infill line distance

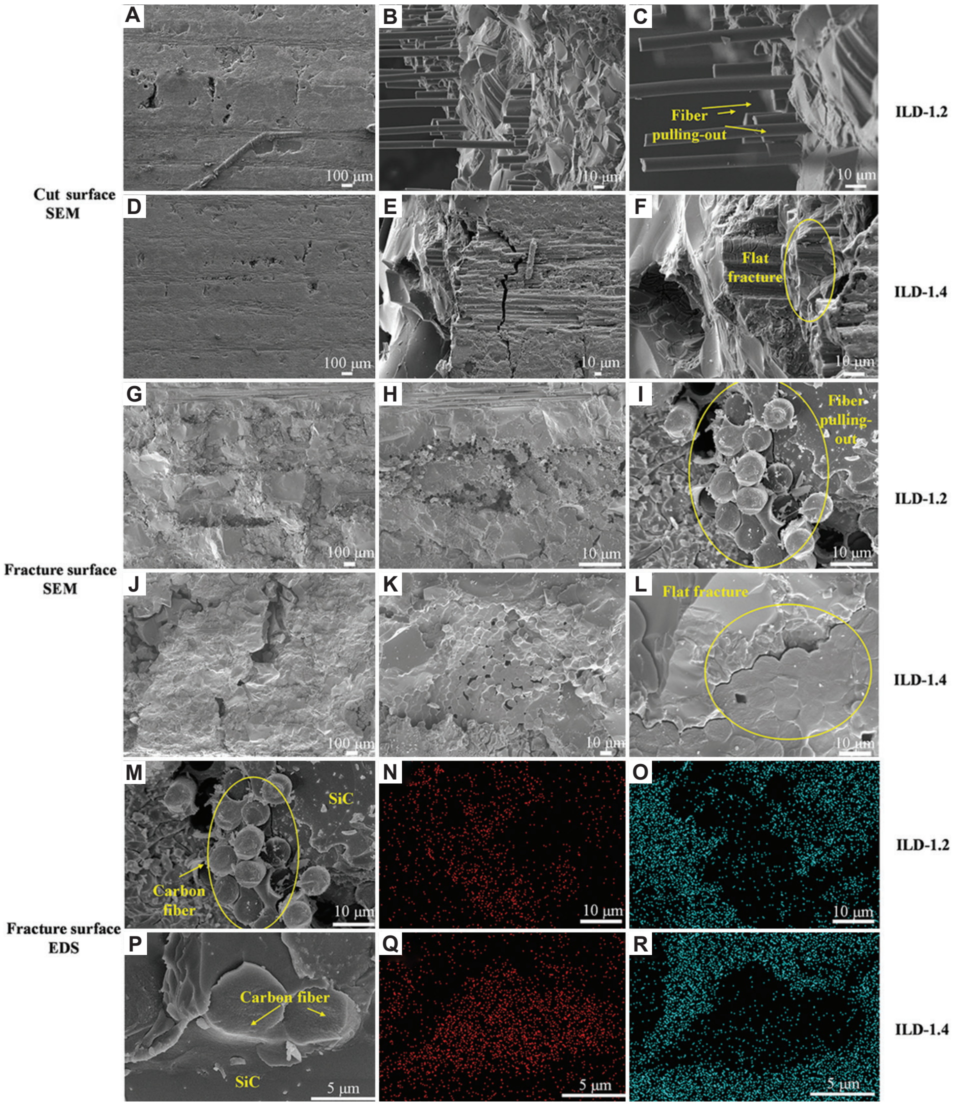

Figure 23. Scanning electron microscope (SEM) and energy dispersive spectroscopy scan results of carbon fiber/silicon carbide (PETG) composites. (A–C) SEM of cut surface of infill line distance (ILD)-1.2 specimens. (D–F) SEM of cut surface of ILD-1.4 specimens. (G–I) SEM of the cross-section of ILD-1.2 specimens. (J–L) SEM of the cross-section of ILD-1.2 specimens. (M–O) EDS results of ILD-1.2 specimens: (N) C element and (O) Si element. (P–R) EDS results of ILD-1.4 specimens: (Q) C element and (R) Si element.

is about 1.0 mm, which is why the infill line distance of PETG-based green parts is set to ILD-1.0, which is not much different from the ILD of PLA-based billets, that is, ILD-1.4, so the improvement effect is limited. However, according to the results, the reduction of the ILD to 1.0 mm did not enhance the bending strength of the C_f/SiC composite, but instead reduced it to a value lower than that of the ILD-1.2 group, and the overall bending strength of the C_f/SiC (PETG) composites was lower than that of the C_f/SiC (PLA) composites. This explains the mechanism underlying the effect of pyrolyzed carbon on the mechanical properties of C_f/SiC composites.

In the process of CVI-PIP preparation of C_f/SiC complexes, pyrolyzed carbon, as an interfacial layer between fibers/SiC, can protect carbon fibers, on the one hand, and reduce the fiber-substrate bond strength, on the other hand, facilitating the stress transfer between substrate-interface-fibers and thus enhancing the mechanical properties of C_f/SiC composites. However, the presence of excessive pyrolyzed carbon phase in the C_f/SiC composite also reduces the content of its main component, SiC matrix phase, which has a negative impact on the mechanical properties of the C_f/SiC composites. Therefore, replacing the resin matrix material with PETG introduces

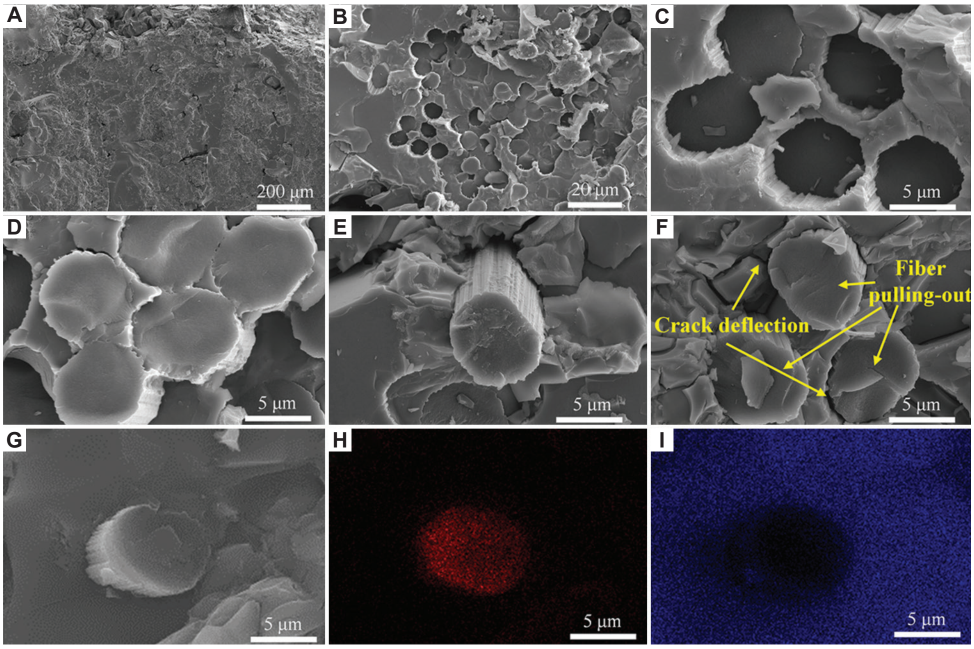

Figure 24. Scanning electron microscope (SEM) and energy dispersive spectroscopy (EDS) scanning results of carbon fiber/silicon carbide (polylactic acid) composite final product. (A–F) SEM scanning. (G–I) EDS scanning: (H) C element distribution and (I) Si element distribution.

a shorter ILD (a very short ILD affects the impregnation of the ceramic precursor), which enhances the proportion of the reinforcing phase and reduces the porosity, on the one hand, and introduces more pyrolyzed carbon, which causes both positive and negative effects, on the other hand. The combination of the two effects results in C_f/SiC (PETG) composites with a shorter ILD that has an overall performance inferior to that of C_f/SiC (PLA) composites with a longer ILD.

Therefore, this study proposes to optimize the nozzle aperture of the FFF additive equipment by replacing 0.8 mm aperture nozzle with 1.0 mm nozzle. Two sets of complementary experiments of C_f/SiC (PETG) composites utilized PETG-based prepreg with ILDs of 1.1 and 1.3 mm, respectively. A comparison of the specimens formed with 0.8 mm nozzle aperture and the supplementary experimental specimens formed with 1.0 mm nozzle is shown in Figure 25, where ILD-1.1 and ILD-1.3 are formed with 1.0 mm nozzle, and ILD-1.0, ILD-1.2, and ILD-1.4 are formed with 0.8 mm nozzle. It can be seen that the specimens in Figure 25C were more densely filled than the specimen in Figure 25B, although a larger ILD was used. This is due to the increased nozzle aperture and thicker filling line, which indirectly increased the filling density.

A comparison of the results of the three-point bending and fracture toughness tests of the C_f/SiC (PETG) specimens obtained from this experimental preparation and the C_f/SiC (PETG) and C_f/SiC (PLA) specimens using 0.8 mm aperture nozzles is shown in Figure 26, where the group using 0.8 mm aperture nozzles is referred to as 0.8-C_f/SiC (PETG) and 0.8-C_f/SiC (PLA), and the group using a 1.0 mm nozzle aperture is referred to as 1.0-C_f/SiC (PETG). The test results demonstrated that increasing the nozzle aperture diameter effectively improved the bending

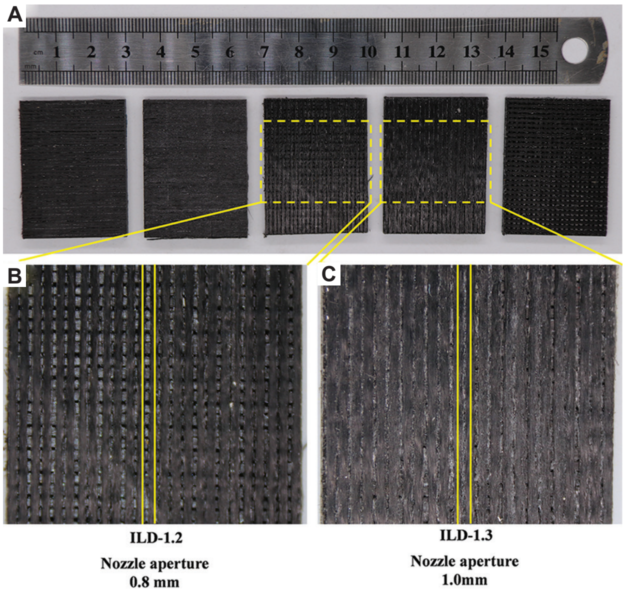

Figure 25. Photos of carbon fiber/polyethylene terephthalate glycol (C_f/PETG) green part samples. (A) Infill line distance (ILD)-1.0 to ILD-1.4 from the left to right. (B) 0.8-C_f/PETG with an ILD of 1.2 mm. (C) 1.0-C_f/PETG with an ILD of 1.0 mm.

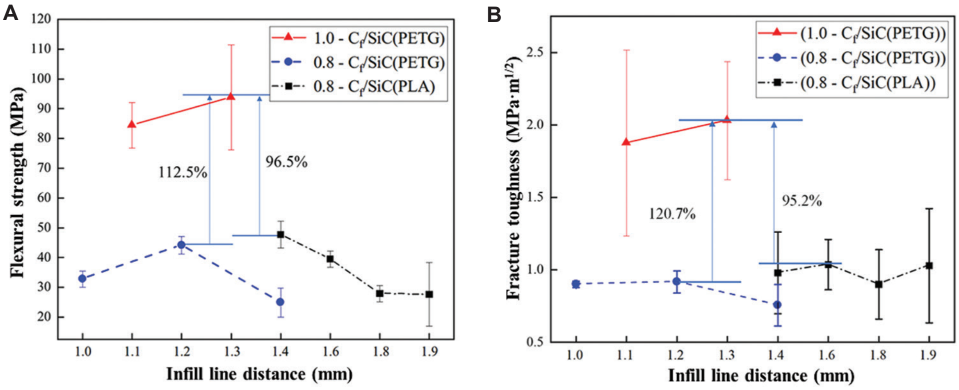

Figure 26. Comparison of three-point bending strength and fracture toughness test results for carbon fiber/silicon carbide (C$_f$/SiC) (polyethylene terephthalate glycol) with 0.8 mm nozzle aperture and C$_f$/SiC compound with 1.0 mm nozzle aperture. (A) Three-point bending. (B) Fracture toughness.

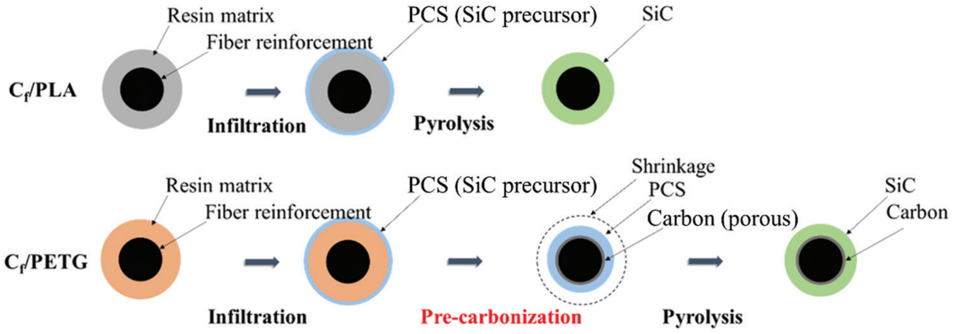

Figure 27. Schematic of phase evolution of carbon fiber/polylactic acid and carbon fiber/polyethylene terephthalate glycol during precursor infiltration pyrolysis process.

strength and fracture toughness of the C$_f$/SiC (PETG) composites, achieving an average bending strength of 93.79 MPa and a fracture toughness of 2.03 MPa·m$^{1/2}$. The bending strength and fracture toughness were significantly improved by 112.5% and 120.7%, respectively, compared to the largest group of 0.8-C$_f$/SiC (PETG), and by 96.5% and 95.2%, respectively, compared to the largest group of 0.8-C$_f$/SiC (PLA). The improvement in bending strength and fracture toughness due to the increase in nozzle aperture is perhaps caused by the increase in nozzle aperture and in the amount of prepreg delivered from the nozzle, resulting in an increase in the spreading width of the deposition line, more uniform spreading of fibers in the deposition line, a decrease in the fiber spacing between deposition lines in the deposition layer, which corresponds to an increase in the equivalent fiber density within a single layer, and a decrease in the fiber bundle-to-bundle spacing in green parts. The spacing will be reduced, so that the macroscopic pores of the green parts will be reduced, thus allowing more uniform impregnation of the ceramic precursor into the macroscopic pores between and within the fiber bundles, and eventually improving the mechanical properties of the C$_f$/SiC composites; the difference between C$_f$/PLA and C$_f$/PETG is shown in Figure 27. This is the reason why the final bending strength and fracture toughness of the 1.0-C$_f$/SiC (PETG) composites with an ILD of 1.3 mm were improved compared to the 0.8-C$_f$/SiC (PETG) with an ILD of 1.2 mm, even though the ILD was not reduced.

4. Conclusions

In this paper, the continuous carbon fiber-reinforced SiC was fabricated through green parts additive manufacturing and PIP post-ceramicization. The main conclusions are as follows:

(i) The bending strength of green part specimens increases with the decrease of ILD. The maximum bending strength for C$_f$/PETG composite of 169.48 MPa was achieved when the ILD was 1.0 mm, while that for C$_f$/PLA composite was 155.83 MPa when the ILD was 1.4 mm.

(ii) The apparent porosity and bulk density of the samples from the green parts to the first-cycle PIP change significantly, mainly because the high-temperature pyrolysis in the first PIP process carbonizes the resin in green part samples, thus producing a large number of pores between the fiber bundles and between the fiber filaments. Meanwhile, the decomposition of the resin also causes a huge weight loss. This results in a significant increase in apparent porosity and a significant decrease in bulk density.

(iii) The bending strength of continuous fiber-reinforced SiC composites decreases with the increase of ILD. This is because the percentage of carbon fiber in the sample decreases with the increase of ILD, and the content of SiC increases with the reduction of reinforcement phase in the composite, leading to a decrease in the overall bending strength.

(iv) Continuous carbon fiber-reinforced SiC composites with maximum bending strength and fracture toughness of 47.74 MPa and 1.04 MPa·m$^{1/2}$ were obtained. The bending strength of C_f/SiC (PETG) composite is lower than that of C_f/SiC (PLA) composite. A plausible reason is that PETG material has a high residual carbon composition, and more pyrolyzed carbon is generated during the carbonization process, resulting in excessive pyrolyzed carbon impurities in the final product, which affects the overall bending strength of the sample.

(v) After replacing the 0.8 mm aperture nozzle with 1.0 mm nozzle, the mechanical properties of C_f/SiC (PETG) composites are effectively improved, and the maximum average bending strength of 93.79 MPa and the fracture toughness of 2.03 MPa·m$^{1/2}$ can be obtained. The maximum average bending strength of C_f/SiC (PETG) composites produced with a 0.8 mm aperture nozzle is increased by 112.5 %.

The results obtained in this study revealed the correlations between the processing parameters, resultant microstructures, and mechanical performance of the C_f/resin green parts and C_f/SiC composite parts, which will contribute to the advancement and development of additive manufacturing of C_f/SiC composite parts with complex geometries.

Acknowledgments

None.

Funding

This work was supported by the Key Research and Development Plan of Hubei Province (2021BAA211 and 2022BAA030), and the National Natural Science Foundation of China (No. 52235008 and U203720003).

Conflict of interest

The authors declare that they have no known competing financial interests or personal relationships that could have appeared to influence the work reported in this paper.

Author contributions

Conceptualization: Xiang Nie, Lei Yang
Data curation: Xiang Nie, Siqi Wu
Formal analysis: Xiang Nie, Lei Yang
Investigation: Lei Yang, Chunze Yan, Yusheng Shi
Methodology: Xiang Nie
Supervision: Chunze Yan, Yusheng Shi
Visualization: Xiang Nie, Siqi Wu
Writing – original draft: Xiang Nie, Siqi Wu
Writing – review & editing: Lei Yang, Chunze Yan

Ethics approval and consent to participate

Not applicable.

Consent for publication

Not applicable.

Availability of data

Data related to this work can be acquired by contacting the corresponding author with a reasonable justification.

References

1. Yoon DH, Reimanis IE, 2020, A review on the joining of SiC for high-temperature applications. *J Korean Ceram Soc*, 57: 246–270.

   https://doi.org/10.1007/s43207-020-00021-4

2. Zhang NL, Yang JF, Deng YC, *et al.*, 2019, Preparation and properties of reaction bonded silicon carbide (RB-SiC) ceramics with high SiC percentage by two-step sintering using compound carbon sources. *Ceram Int*, 45: 15715–15719.

   https://doi.org/10.1016/j.ceramint.2019.04.224

3. Katoh Y, Ozawa K, Shih C, *et al.*, 2014, Continuous SiC fiber, CVI SiC matrix composites for nuclear applications: Properties and irradiation effects. *J Nucl Mater*, 448: 448–476.

   https://doi.org/10.1016/j.jnucmat.2013.06.040

4. Chen X, Yin J, Liu X, *et al.*, 2022, Effect of laser power on mechanical properties of SiC composites rapidly fabricated by selective laser sintering and direct liquid silicon infiltration. *Ceram Int*, 48: 19123–19131.

   https://doi.org/10.1016/j.ceramint.2022.03.203

5. Zhang H, Yang Y, Hu K, *et al.*, 2020, Stereolithography-based additive manufacturing of lightweight and high-strength Cf/SiC ceramics. *Addit Manuf*, 34: 101199.

   https://doi.org/10.1016/j.addma.2020.101199

6. Wu S, Yang L, Wang C, *et al.*, 2022, Si/SiC ceramic lattices with a triply periodic minimal surface structure prepared by laser powder bed fusion. *Addit Manuf*, 56: 102910.

https://doi.org/10.1016/j.addma.2022.102910

7. Idris MI, Konishi H, Imai M, *et al*., 2015, Neutron irradiation swelling of SiC and SiCf/SiC for advanced nuclear applications. *Energy Procedia*, 71: 328–336.

   https://doi.org/10.1016/j.egypro.2014.11.886

8. Zhao J, Shi L, Liu M, *et al*., 2022, Densification and enhancement of SiC particulate-reinforced fine-grain SiC ceramic. *Int J Appl Ceram Technol*, 19: 2514–2522.

   https://doi.org/10.1111/ijac.14112

9. Han F, Zhong Z, Zhang F, *et al*., 2014, Preparation and characterization of SiC Whisker-reinforced SiC porous ceramics for hot gas filtration. *Ind Eng Chem Res*, 54: 226–232.

   https://doi.org/10.1021/ie503626u

10. Lv X, Ye F, Cheng L, *et al*., 2019, Fabrication of SiC whisker-reinforced SiC ceramic matrix composites based on 3D printing and chemical vapor infiltration technology. *J Eur Ceram Soc*, 39: 3380–3386.

    https://doi.org/10.1016/j.jeurceramsoc.2019.04.043

11. Song N, Zhang HB, Liu H, *et al*., 2017, Effects of SiC Whiskers on the mechanical properties and microstructure of SiC ceramics by reactive sintering. *Ceram Int*, 43: 6786–6790.

    https://doi.org/10.1016/j.ceramint.2017.02.095

12. Han F, Zhong Z, Yang Y, *et al*., 2016, High gas permeability of SiC porous ceramics reinforced by mullite fibers. *J Eur Ceram Soc*, 36: 3909–3917.

    https://doi.org/10.1016/j.jeurceramsoc.2016.06.048

13. Chen R, Jin X, Hei D, *et al*., 2021, Enhanced mechanical strength of SiC reticulated porous ceramics via addition of *in-situ* chopped carbon fibers. *J Alloys Compd*, 888: 161638.

    https://doi.org/10.1016/j.jallcom.2021.161638

14. Li L, 2020, Temperature-dependent proportional limit stress of SiC/SiC fiber-reinforced ceramic-matrix composites. *High Temp Mater Processes*, 39: 209–218.

    https://doi.org/10.1515/htmp-2020-0052

15. Yin J, Lee SH, Feng L, *et al*., 2016, Fabrication of SiCf/SiC composites by hybrid techniques of electrophoretic deposition and polymer impregnation and pyrolysis. *Ceram Int*, 42: 16431–16435.

    https://doi.org/10.1016/j.ceramint.2016.07.177

16. Park JS, Nishimura H, Hayasaka D, *et al*., 2016, Fabrication of short SiC fiber reinforced SiC matrix composites with high fiber volume fraction. *Fusion Eng Des*, 109–111: 1174–1178.

    https://doi.org/10.1016/j.fusengdes.2015.12.060

17. Tang H, Zeng X, Xiong X, *et al*., 2009, Mechanical and tribological properties of short-fiber-reinforced SiC composites. *Tribol Int*, 42: 823–827.

    https://doi.org/10.1016/j.triboint.2008.10.017

18. Lu J, Ni D, Liao C, *et al*., 2021, Fabrication and microstructure evolution of C_{sf}/ZrB_2-SiC composites via direct ink writing and reactive melt infiltration. *J Adv Ceram*, 10: 1371–1380.

    https://doi.org/10.1007/s40145-021-0512-z

19. Zhou W, Meiser M, Wich F, *et al*., 2021, Fiber orientation dependence of tribological behavior of short carbon fiber reinforced ceramic matrix composites. *J Am Ceram Soc*, 105: 538–552.

    https://doi.org/10.1111/jace.18075

20. Sun G, Zhang C, Zhang Q, *et al*., 2022, Microstructure and mechanical properties of SiC_f/SiC composite prepared by chemical vapor infiltration. *Ceram Int*, 48: 36983–36991.

    https://doi.org/10.1016/j.ceramint.2022.08.267

21. Zhang J, Luo R, Zhang Y, *et al*., 2010, Effect of isotropic interlayers on the mechanical and thermal properties of carbon/carbon composites. *Mater Lett*, 64: 1536–1538.

    https://doi.org/10.1016/j.matlet.2010.04.013

22. Zhou Q, Dong S, Ding Y, *et al*., 2009, Three-dimensional carbon fiber-reinforced silicon carbide matrix composites by vapor silicon infiltration. *Ceram Int*, 35: 2161–2169.

    https://doi.org/10.1016/j.ceramint.2008.11.023

23. Chen Z, Sun X, Shang Y, *et al*., 2021, Dense ceramics with complex shape fabricated by 3D printing: A review. *J Adv Ceram*, 10: 195–218.

    https://doi.org/10.1007/s40145-020-0444-z

24. Zocca A, Lima P, Diener S, *et al*., 2019, Additive manufacturing of SiSiC by layerwise slurry deposition and binder jetting (LSD-print). *J Eur Ceram Soc*, 39: 3527–3533.

    https://doi.org/10.1016/j.jeurceramsoc.2019.05.009

25. Wu S, Yang L, Yang X, *et al*., 2022, Mechanical properties and energy absorption of AlSi10Mg Gyroid lattice structures fabricated by selective laser melting. *Smart Manuf*, 1: 2150001–2150002.

    https://doi.org/10.1142/S2737549821500010

26. Liu Z, Li Z, Wang Q, *et al*., 2022, Multimaterial additive manufacturing manipulator for fabricating magnetoelectric pressure sensors. *Sci China Technol Sci*, 65: 2542–2550.

    https://doi.org/10.1007/s11431-022-2154-9

27. Chen H, Wang X, Xue F, *et al*., 2018, 3D printing of SiC ceramic: Direct ink writing with a solution of preceramic polymers. *J Eur Ceram Soc*, 38: 5294–5300.

    https://doi.org/10.1016/j.jeurceramsoc.2018.08.009

28. Chen F, Liu K, Sun H, *et al*., 2018, Fabrication of complicated silicon carbide ceramic components using combined 3D printing with gelcasting. *Ceram Int*; 44: 254–260.

    https://doi.org/10.1016/j.ceramint.2017.09.166

29. Yang L, Wu S, Yan C, *et al*., 2021, Fatigue properties of Ti-6Al-4V Gyroid graded lattice structures fabricated by laser powder bed fusion with lateral loading. *Addit Manuf*, 46: 102214.

https://doi.org/10.1016/j.addma.2021.102214

30. Zhang K, Zeng T, Xu G, *et al*., 2020, Mechanical properties of SiC_p/SiC composite lattice core sandwich panels fabricated by 3D printing combined with precursor impregnation and pyrolysis. *Compos Struct*, 240: 112060.

https://doi.org/10.1016/j.compstruct.2020.112060

31. Lu ZL, Lu F, Cao JW, *et al*., 2014, Manufacturing properties of turbine blades of carbon fiber-reinforced SiC composite based on stereolithography. *Mater Manuf Process*, 29: 201–209.

https://doi.org/10.1080/10426914.2013.872269

32. Zheng W, Wu JM, Chen S, *et al*., 2022, Improved mechanical properties of SiC fiber reinforced silica-based ceramic cores fabricated by stereolithography. *J Mater Sci Technol*, 116: 161–168.

https://doi.org/10.1016/j.jmst.2021.12.012

33. Tang J, Chang H, Guo X, *et al*., 2022, Preparation of carbon fiber-reinforced SiC ceramics by stereolithography and secondary silicon infiltration. *Ceram Int*, 48: 25159–25167.

https://doi.org/10.1016/j.ceramint.2022.05.178

34. Zhu W, Fu H, Xu Z, *et al*., 2018, Fabrication and characterization of carbon fiber reinforced SiC ceramic matrix composites based on 3D printing technology. *J Eur Ceram Soc*; 38: 4604–4613.

https://doi.org/10.1016/j.jeurceramsoc.2018.06.022

35. Fu H, Zhu W, Xu Z, *et al*., 2019, Effect of silicon addition on the microstructure, mechanical and thermal properties of C_f/SiC composite prepared via selective laser sintering. *J Alloy Compd*, 792: 1045–1053.

https://doi.org/10.1016/j.jallcom.2019.04.129

36. Goh GD, Sing SL, Yeong WY, 2020, A review on machine learning in 3D printing: Applications, potential, and challenges. *Artif Intell Rev*, 54: 63–94.

https://doi.org/10.1007/s10462-020-09876-9

37. Gao H, An J, Chua CK, *et al*., 2023, 3D printed optics and photonics: Processes, materials and applications. *Mater Today*, 23.

https://doi.org/10.1016/j.mattod.2023.06.019

38. Hou Z, Tian X, Zhang J, *et al*., 2018, 3D printed continuous fibre reinforced composite corrugated structure. *Compos Struct*, 184: 1005–1010.

https://doi.org/10.1016/j.compstruct.2017.10.080

39. Chen P, Wang H, Su J, *et al*., 2022, Recent advances on high-performance polyaryletherketone materials for additive manufacturing. *Adv Mater*, 34: e2200750.

https://doi.org/10.1002/adma.202200750

40. Spece H, Yu T, Law AW, *et al*., 2020, 3D printed porous PEEK created via fused filament fabrication for osteoconductive orthopaedic surfaces. *J Mech Behav Biomed Mater*, 109: 103850.

https://doi.org/10.1016/j.jmbbm.2020.103850

41. Yu T, Zhang Z, Song S, *et al*., 2019, Tensile and flexural behaviors of additively manufactured continuous carbon fiber-reinforced polymer composites. *Compos Struct*, 225: 111147.

https://doi.org/10.1016/j.compstruct.2019.111147

42. Goh GD, Toh W, Yap YL, *et al*., 2021, Additively manufactured continuous carbon fiber-reinforced thermoplastic for topology optimized unmanned aerial vehicle structures. *Compos B Eng*, 216: 108840.

https://doi.org/10.1016/j.compositesb.2021.108840

43. Zhang J, Zhou Z, Zhang F, *et al*., 2020, Performance of 3D-printed continuous-carbon-fiber-reinforced plastics with pressure. *Materials*, 13: 471.

https://doi.org/10.3390/ma13020471

44. Mei H, Yan Y, Feng L, *et al*., 2018, First printing of continuous fibers into ceramics. *J Am Ceram Soc*, 102: 3244–3255.

https://doi.org/10.1111/jace.16234

45. Wang L, Hou F, Wang X, *et al*., 2015, Preparation and mechanical properties of continuous carbon nanotube networks modified C_f/SiC composite. *Adv Mater Sci Eng*, 2015: 465358.

https://doi.org/10.1155/2015/465358

46. Yin XW, Cheng LF, Zhang LT, *et al*., 2017, Fibre-reinforced multifunctional SiC matrix composite materials. *Int Mater Rev*, 62: 117–172.

https://doi.org/10.1080/09506608.2016.1213939

ACCSCIENCE PUBLISHING

Materials Science in Additive Manufacturing

ORIGINAL RESEARCH ARTICLE

Triply periodic minimal surfaces lattice structures: Functional graded and hybrid designs for engineering applications

Tian Lan[1], Chenxi Peng[1], Kate Fox[1], Truong Do[2]*, and Phuong Tran[1]*

[1]School of Engineering, RMIT University, Melbourne, VIC 3000, Australia

[2]College of Engineering and Computer Science, Vin University, Hanoi 14000, Vietnam

Abstract

In this work, we propose the strategies for designing radial graded sheet-based gyroid lattice and the approach to hybridizing solid-network-based gyroid lattice and primitive lattice. The elastic property of triply periodic minimal surfaces (TPMS) sheet-based gyroid lattice structures was explored. We also conducted numerical analysis to investigate the effect of functionally graded sheet-based gyroid lattices on the implant application, and explored the elastic properties of the uniform gyroid lattice parametrically with different relative densities based on the representative volume element model. Analytical equations based on the Gibson-Ashby model were generated to predict the elastic properties. Compressive tests on the samples fabricated by the Stratasys J750 were conducted to validate the feasibility of applying hybridization of different types of lattices. A comparison between radial hybrid primitive-gyroid and gyroid-primitive lattices revealed that the compressive behavior of gyroid-primitive was strengthened. We also found that the gyroid-primitive lattice could achieve auxetic compressive behavior. In conclusion, the numerical analysis illustrates that the application of the functional graded gyroid lattices can relieve the stress shielding effect as well as protects the bone from damage. The hybridization of different lattices can not only strengthen the mechanical properties of TPMS structures but also create a counter-intuitive deformation response.

Keywords: Gyroid lattice; Functional graded lattice; Hybrid lattice; Additive manufacturing; PolyJet printing

***Corresponding authors:**
Phuong Tran
(jonathan.tran@rmit.edu.au)
Truong Do
(truong.dt@vinuni.edu.vn)

Citation: Lan T, Peng C, Fox K, *et al*., 2023, Triply periodic minimal surfaces lattice structures: Functional graded and hybrid designs for engineering applications. *Mater Sci Add Manuf*, 2(3): 1753. https://doi.org/10.36922/msam.1753

Received: September 4, 2023

Accepted: September 11, 2023

1. Introduction

Cellular structures, which are vitalized by the continuous progress in additive manufacturing (AM) techniques, naturally have porous and lightweight characteristics, which explain their excellent performance in various applications, including aerospace components[1,2], energy absorption[3-6], heat sink[7-9], and biomedical implant applications[10,11]. Inspired by the principles observed in crystallographic and biological structures, lattice structures are characterized by architecturally designed unit cells and inherent periodicity, which significantly enhance manufacturability and allow for manipulation of their mechanical properties. To improve structural performance, large quantities of lattices have been developed based on their truss-based geometric features[12,13]. In addition, from the theoretical analysis, plate-based lattices, which have the potential to reach the Hashin-Shtrikman upper bounds, have been proposed as an excellent candidate for high-strength withstanding scenarios[14]. Unlike the truss-based or plate-based lattices that are constructed from explicit geometric primitives, triply periodic minimal surfaces (TPMS) surface-based lattices, which are generated based on the implicit TPMS functions, have attracted the attention of researchers due to their high specific strength and energy absorption capabilities[15].

TPMS can be characterized through the summation of a series of sinusoidal functions, resulting in a surface that has the capacity to minimize its surface area within a predefined boundary, while simultaneously maintaining a zero mean curvature and periodicity in 3D space. TPMS surface-based lattices can be categorized into sheet-based TPMS lattices and solid-network-based TPMS lattices. With the TPMS, the 3D space can be separated into two regions, the solid-network-based TPMS is generated by infilling the specific region separated by the surface. Instead of infilling regions, the sheet-based TPMS is generated by thickening the surface. The numerical and experimental analyses of the mechanical performance of both solid-network-based and sheet-based TPMS have been reported[15-18]. In addition, graded designs in the TPMS-based lattices have been developed and investigated[19]. Apart from the linear grading on the lattices' thickness, the graded TPMS in two and three dimensions has been manufactured and investigated, showing a great increase in energy absorption ability compared to the uniform TPMS lattices[18].

Classical TPMS lattices such as primitive, gyroid, and diamond with different materials have been widely investigated[20]. Among TPMS structures, the sheet-based gyroid structure has been proven to own a high strength-to-mass ratio as well as a low level of stress concentration when compared with other types of lattices[15,21]. In the context of orthopedic implant design, it becomes imperative to provide adequate physical stimulation to promote bone regeneration, while also ensuring compatibility with the mechanical attributes of the adjacent bone tissues. Stress shielding is a phenomenon that occurs when an implant, which is stiffer than the neighboring bone, cannot properly transfer forces to the nearby bone tissue. This can potentially hinder the regenerative process and increase the risk of implant failure[22]. One potential way to reduce the stress shielding effect is by intentionally making the implant less stiff near the area where it connects to the scaffold and tissue. Using functionally graded gyroid lattice designs in this context is a promising way to make this approach more effective.

The mechanical performance of TPMS lattices can be tuned with a combination of different unit cells instead of only adjusting specific topologies of a single type of unit cell. From the work proposed by Ren *et al.*[23], the hybridization of the I-graph-and-wrapped-package (IWP) and primitive TPMS lattices have shown their extraordinary stiffness under bending loading. To further modify the mechanical behavior of TPMS lattices, the hybridization of different TPMS lattices has been numerically analyzed and tested, illustrating their improvement in energy absorption and the modification of the deformation characteristics[18]. In the work proposed by Novak *et al.*[19], the plateau region with either hardening behavior or constant response can be obtained by the hybridization of gyroid and diamond lattices, which enables their potential applications in crashworthiness protection. The effects introduced by hybridization require more in-depth investigation due to the extensive design possibilities offered by the flexible hybridization approach. Nevertheless, the selection of an appropriate hybridization strategy, aimed at optimizing the structural performance of the system, remains undetermined.

In this work, popular TPMS design approaches, including graded design of sheet-based lattices and hybridization of solid-network-based lattices, along with their potential applications, were examined. In this paper, we present the methods of generating TPMS lattices, the strategies used to design uniform gyroid, graded gyroid, and hybrid design. Subsequently, we present our works in the numerical investigation of the graded gyroid lattices, which are regarded as an application to resolve the stress shielding effect. To explore the effectiveness of the selected hybridization strategies, several hybrid TPMS lattices were designed, fabricated, and tested. In the last section, the main findings of this work are summarized.

2. Design strategies of hybrid gyroid lattices

As illustrated in the previous work, TPMS can be obtained by utilizing different approaches, such as implicit, boundary, and parametric functions. In this work, the solid-network-based TPMS lattice, which was utilized to further generate hybrid lattices, as described in Section 4, was generated by applying the implicit function approach:

$$f(x,y,z) \leq c \tag{I}$$

where c is utilized to determine the isovalue offset from the zero level-set. For the sheet-based TPMS lattice investigated in Section 3, the solid region is calculated as:

$$f^2(x,y,z) \leq c^2 \tag{II}$$

where the thickness of the structure is controlled by intervals [-c,c], leading to the generation of the solid phase. The different mechanisms of generating TPMS lattices are clearly shown in Figure 1A, where the gyroid unit cell is regarded as an example.

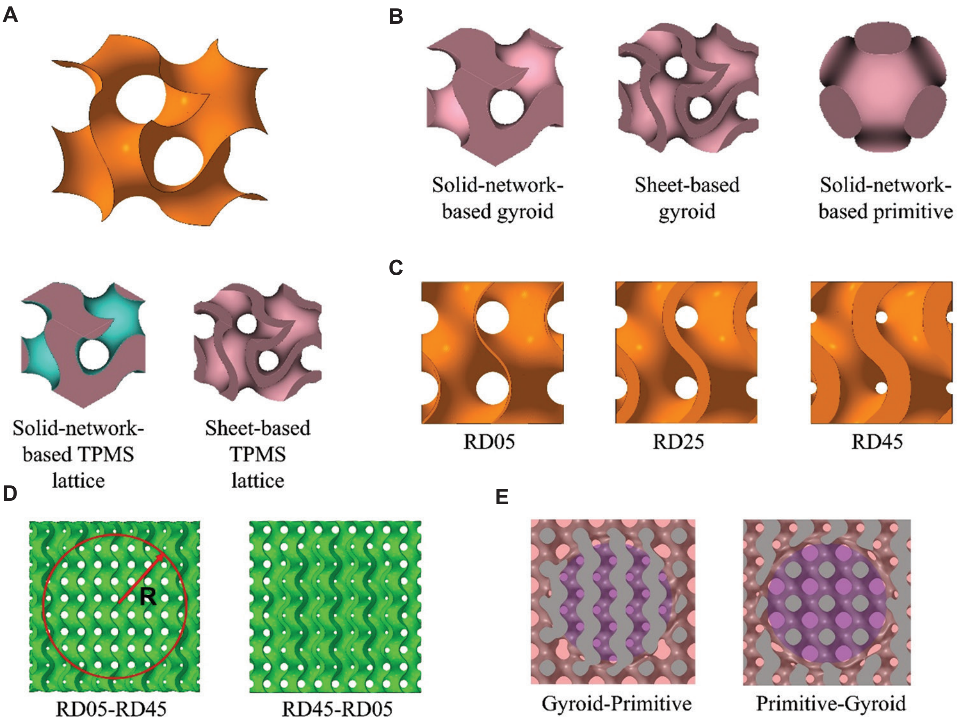

Figure 1. (A) Generation of sheet-based and solid-network-based triply periodic minimal surfaces (TPMS) lattice. (B) TPMS unit cell candidates. (C) Sheet-based gyroid lattices with different relative densities. (D) Graded sheet-based gyroid lattices. (E) Hybridization of solid-network-based TPMS lattices.

As shown in Figure 1B, the geometric features of gyroid and primitive TPMS lattices are described by the following functions:

$$f_{gyroid} = \cos(w_x x)\sin(w_y y) + \cos(w_y y)\sin(w_z z) + \cos(w_z z)\sin(w_x x), \quad \text{(III)}$$

$$f_{primitive} = \left[\cos(w_x x) + \cos(w_y y) + \cos(w_z z)\right] - 0.51\begin{bmatrix}\cos(w_x x)\cos(w_y y)\\ +\cos(w_y y)\cos(w_z z)\\ +\cos(w_x x)\cos(w_z z)\end{bmatrix}, \quad \text{(IV)}$$

where *x*, *y* and *z* are spatial Cartesian coordinates in the 3D space, *w* is the parameter to manipulate the periodicities of the TPMS function, which is defined by:

$$w_i = 2\pi \frac{n_i}{L_i} \; for \; i = x, y, z, \quad \text{(V)}$$

where n_i indicates the number of unit cells along x-, y-, and z-directions, and L_i controls the lattice size in the corresponding directions. As shown in Figure 1C, by manipulating the isovalue offset, the solid region can be tuned to control the relative density. Therefore, the graded TPMS lattices can be facilitated by assigning graded *c* values at the relevant regions. For hybridization, different types of solid-network-based TPMS lattices can be combined with the following function:

$$\phi = \mu\phi_{gyroid} + (1-\mu)\phi_{primitive}, \quad \text{(VI)}$$

where $\phi_{gyroid} = f_{gyroid} - c$ and $\phi_{primitive} = f_{primitive} - c$ are generated based on Equation I to represent solid-network-based TPMS lattices, and *μ* (*x*, *y*, *z*) is a spatial weighting function ranging from 0 to 1, where 0 indicates primitive and 1 indicates gyroid. According to the approach proposed by Yang *et al.*[23], the smooth connections between different TPMS lattices can be facilitated by applying the sigmoid function to the *μ* (*x*, *y*, *z*) function, which is expressed as follows:

$$\mu(x,y,z) = \frac{1}{1+\exp\left[-kG(x,y,z)\right]}, \quad \text{(VII)}$$

where *G* represents the connection region between gyroid and primitive lattices, and *k* is utilized to represent the transition width. For the radial hybridization as shown in Figure 1E, the boundary function can be expressed as follows:

$$G(x,y,z) = x^2 + y^2 - R^2. \quad \text{(VIII)}$$

where $G(x, y, z)$ represents the radius of the cylinder that is infilled with the first type of lattice. For the radial graded sheet-based gyroid lattices as shown in Figure 1D, the smooth grading can be implemented by controlling the c value with Equations VII and VIII.

3. Case study 1: Sheet-based graded gyroid lattices in orthopedic implant design

Simulation with the representative volume element (RVE) method was adopted to explore the elastic performance of the sheet-based gyroid structures with different relative densities. To implement the simulation, periodic boundary conditions were applied to unit cells, which can be expressed as follows:

$$u_i = (\mathbf{x}+\mathbf{L}) = u_i(\mathbf{x}) + \varepsilon^0 L_i,\ t_i(\mathbf{x}+\mathbf{L}) = -t_i(\mathbf{x})\ \forall x_i e_i \in \partial B, \tag{IX}$$

where u_i represents the displacement vector, x represents the point vector, and L is the characteristic length, ε^0 is the strain, and t_i represents the surface traction. The elastic constitutive behaviors of the sheet-based gyroid lattice structure, which has cubic symmetry, can be expressed as the following equation:

$$\begin{pmatrix}\sigma_{11}\\ \sigma_{22}\\ \sigma_{33}\\ \sigma_{12}\\ \sigma_{13}\\ \sigma_{23}\end{pmatrix} = \begin{bmatrix} C_{1111} & C_{1122} & C_{1122} & & \cdots & \\ C_{1122} & C_{1111} & C_{1122} & & & \\ C_{1122} & C_{1122} & C_{1111} & & & \\ & & & C_{1212} & & \\ & \vdots & & & C_{1212} & \\ & & & & & C_{1212} \end{bmatrix} \begin{pmatrix}\varepsilon_{11}\\ \varepsilon_{22}\\ \varepsilon_{33}\\ 2\varepsilon_{12}\\ 2\varepsilon_{13}\\ 2\varepsilon_{23}\end{pmatrix}. \tag{X}$$

According to the periodic boundary conditions proposed by Dong *et al.*[25], three independent components, namely, C_{1111}, C_{1122}, and C_{1212}, can effectively represent the constitutive matrix of the sheet-based gyroid lattice. For the base material, the properties of titanium alloy were applied. From the constitutive matrix, elastic properties including elastic modulus E, Poisson's ratio v, shear modulus G, and bulk modulus K can be calculated as:

$$E = \frac{(C_{1111} - C_{1122})(C_{1111} + 2C_{1122})}{C_{1111} + C_{1122}}. \tag{XI}$$

$$K = \frac{1}{3}(C_{1111} + 2C_{1122}). \tag{XII}$$

$$G = C_{1212}. \tag{XIII}$$

$$v = \frac{C_{1212}}{C_{1111} + C_{1122}}. \tag{XIV}$$

To illustrate the effect brought by applying the functional graded gyroid structures to mitigate the stress shielding, finite element analysis was conducted using commercial software ABAQUS/Explicit 2020. Based on the conceptual implant design illustrated in Figure 2A, the simulation focused on the exploration of the compressive behavior of the gyroid infillings with different density gradients. According to the simulation set-up shown in Figure 2B, two rigid plates were utilized as the simplified model in the simulation of the uniaxial compression test. The displacement, which is equal to the 0.05 strain of the gyroid lattice, was applied on the top rigid plate. The bottom plate was fixed. General contact was applied to simulate the contact behavior between the rigid plates and the sheet-based gyroid lattices. The friction coefficient for the tangential behavior was set to be 0.3. The normal behavior was set with the hard contact formulation. The material property of titanium alloy was modeled in accordance with the Johnson-Cook model[26].

The dimension of the gyroid lattice was set to be 10 mm in width and length; the height of the lattice was set to be 6 mm; and the size of the unit cell was set to be 2 mm. Three different sheet-based lattices were designed: (i) Uniform gyroid lattice RD25 with a relative density of 25%; (ii) radial graded gyroid lattices RD05-45 with the relative density 5% in the inner region and the relative density 45% in the outer region; and (iii) radial graded

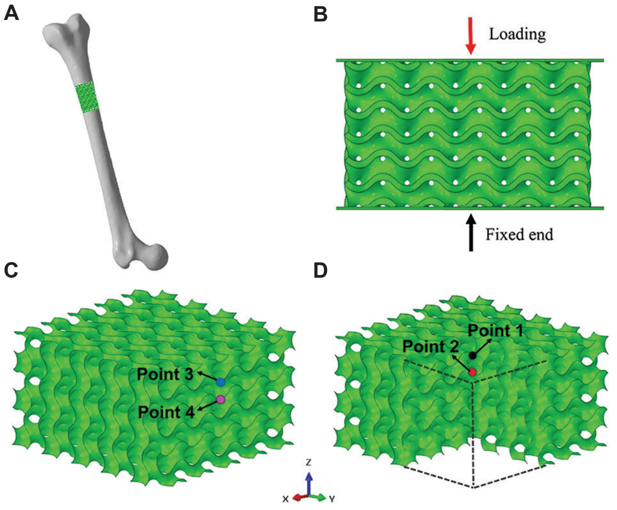

Figure 2. (A) Conceptual design of embedding sheet-based gyroid lattices in orthopedic implants. (B) Simulation set-up for the compression test. (C) Full model of the gyroid lattices. (D) Quarter model of the gyroid lattices.

gyroid lattices RD45-05 with the relative density 45% in the inner region and the relative density 5% in the outer region. All three lattices had the same overall 25% relative density. The 3-node triangular shell (S3R) element was utilized to mesh the gyroid lattice, where 195,900 elements were utilized to guarantee the model quality. To investigate the stress shielding reduction, the displacement of two points on the edge of the lattice (point 3 and point 4 as shown in Figure 2C) and two points in the core of the lattice (point 1 and point 2 as shown in Figure 2D) was extracted for comparison. The stress contour was obtained from the simulation to further assist the analysis of gyroid lattices as implant infillings.

The elastic modulus, shear modulus, bulk modulus, and Poisson's ratio of the sheet-based gyroid lattices under different relative densities are presented in Figure 3A-D, respectively. As shown in Figure 3A-D, the elastic modulus, bulk modulus, and shear modulus of the sheet-based gyroid lattice increase when the relative density increases, whereas the Poisson's ratio decreases when the relative density increases. The Gibson-Ashby model[27] was utilized to fit the simulation. The dashed lines in Figure 3A-C indicate that the elastic properties from the Gibson-Ashby model fit well with the simulation results. The relevant Gibson-Ashby model results are illustrated as follows:

$$E = 58.13\rho_{*}^{1.21} \tag{XV}$$

$$G = 26.93\rho_{*}^{1.27} \tag{XVI}$$

$$K = 48.08\rho_{*}^{1.11} \tag{XVII}$$

Equations XV and XVI show that both the exponent values of elastic modulus E, which is equal to 1.21, and shear modulus G, which is equal to 1.27, of the sheet-based gyroid lattices are between 1.0 and 2.0, indicating that the sheet-based gyroid lattice under uniaxial compression and shear loading has a combined stretching- and bending-dominated behavior. The exponent value for bulk modulus is closer to 1.0, suggesting that the sheet-based gyroid lattice under triaxial loads has a stretching-dominated behavior. As shown in Figure 3D, the relative density has a limited impact on the Poisson's ratio.

The stress contours of the uniform gyroid lattice with a relative density of 25%, the graded gyroid lattice with a relative density of inner 5% and outer 45%, and the graded gyroid lattice with a relative density of inner 45% and outer 5% under a 5% compressive strain are shown in Figure 4. As shown in Figure 4A, the outer region of the uniform sheet-based gyroid lattice has a higher level of stress, whereas the stress in the central region of the lattice is at a much lower level. Compared with the uniform case, the central part

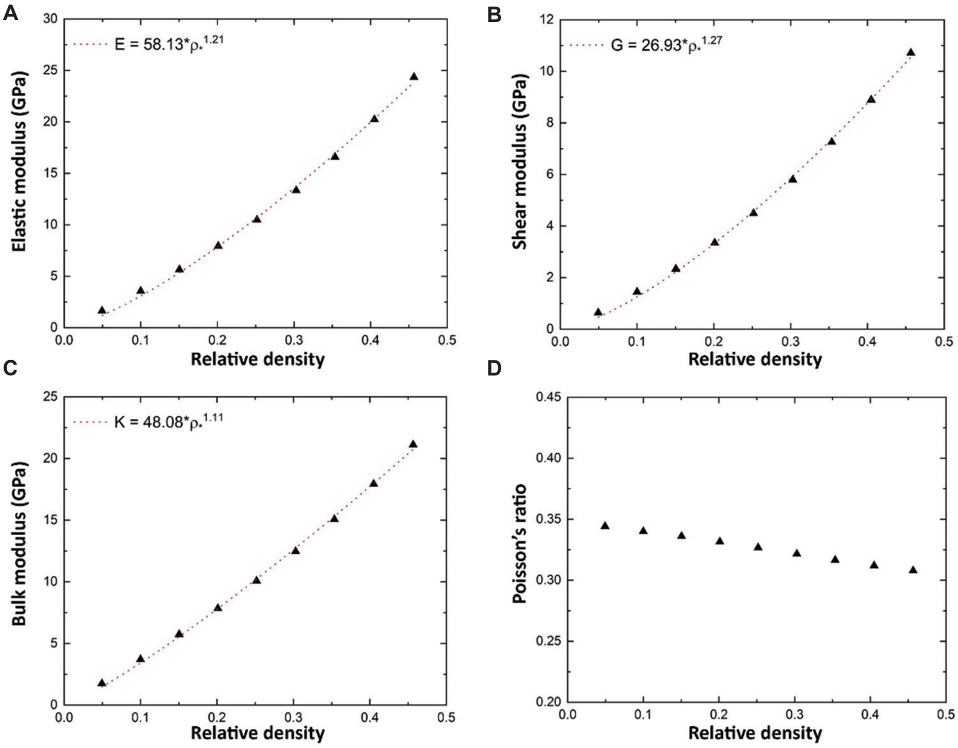

Figure 3. Elastic properties of the sheet-based gyroid lattice under different relative density: (A) Elastic modulus E, (B) Shear modulus G, (C) Bulk modulus K, and (D) Poisson's ratio ν.

illustrates a larger low-stress area for the graded lattice with a relative density of inner 5% and outer 45% (Figure 4B). As shown in Figure 4C, the central part illustrates a smaller low-stress area for the graded lattice with a relative density of inner 45% and outer 5% compared with the uniform case. In addition, a more uniform stress distribution was obtained on the graded lattice structure with a relative density of inner 45% and outer 5%. The stress on the external surfaces was found to be higher than the stress in the core region for both the uniform case and the graded lattice with a relative density of inner 5% and outer 45%. We also found no stress concentration in the transition region for both the graded cases, pointing to the excellence of the smooth grading with the sigmoid function. Taken together, the sheet-based gyroid lattices with graded relative density can match the flexible mechanical demand of the bone implant application.

The displacement histories recorded at four points, which are shown in Figure 2C and D, in the gyroid lattice at different compressive strains are shown in Figure 5. For two graded gyroid lattices, the displacements at point 2 decreased compared to that of the uniform gyroid lattice. The lowest displacement at point 2 was detected for the graded gyroid with a relative density of inner 5% and outer 45%. As a result, the stiffness at the top region increased, indicating that the introduction of graded gyroid lattice structure as infillings of implants can protect the bone from damage. Compared to the uniform case, the displacement at point 3 for two graded gyroid lattices also increased, whereas the displacement at point 4 reduced. As a result, the stiffness at the side region decreased, indicating that the introduction of graded gyroid lattice structure as infillings of implants can effectively relieve the stress shielding effect.

4. Case study 2: Solid-network-based hybrid TPMS lattices in tuning compliant response

For the hybridization of TMPS lattices, Stratasys J750 (Stratasys Ltd.), which is based on the material jetting technique, was utilized to manufacture all samples. Stratasys J750 fabricates objects by solidifying the droplets of photopolymers with ultraviolet light. A previous study has shown that Stratasys J750 is capable of accurately fabricating samples with sharp features (*e.g.*, cube) at 500 μm level and samples with round features (*e.g.*, cylinder)

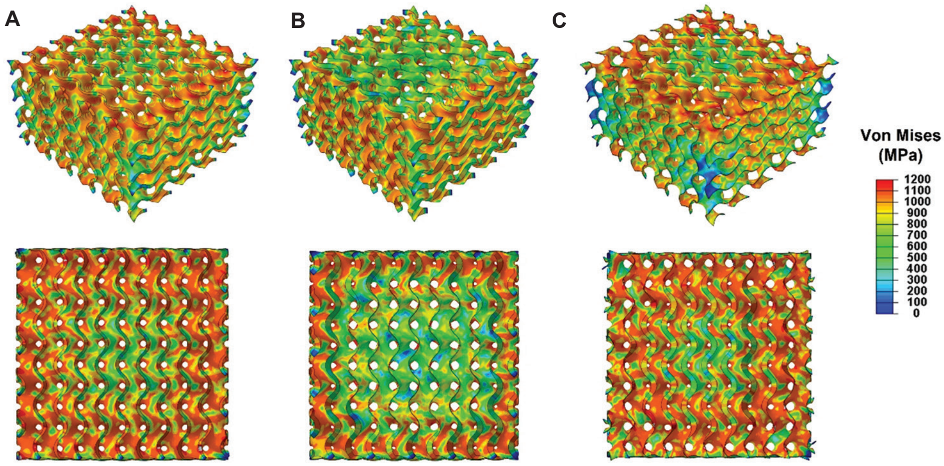

Figure 4. Stress contour of sheet-based gyroid lattices at 5% strain: (A) Uniform lattice with a relative density of 25%, (B) graded lattice with a relative density of inner 5% and outer 45%, and (C) graded lattice with a relative density of inner 45% and outer 5%.

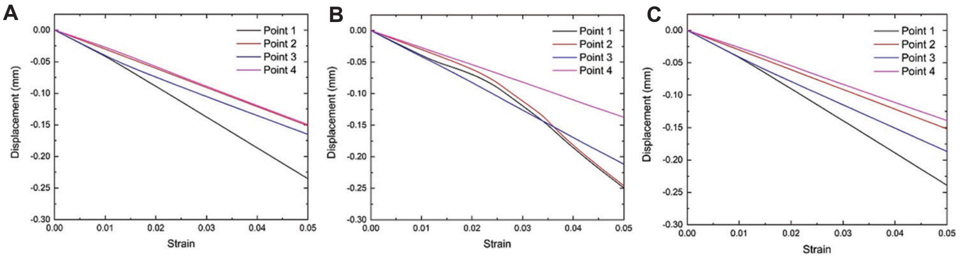

Figure 5. Displacement histories of the sheet-based gyroid lattices recorded at four points: (A) Uniform lattice with a relative density of 25%, (B) graded lattice with a relative density of inner 5% and outer 45%, and (C) graded lattice with a relative density of inner 45% and outer 5%.

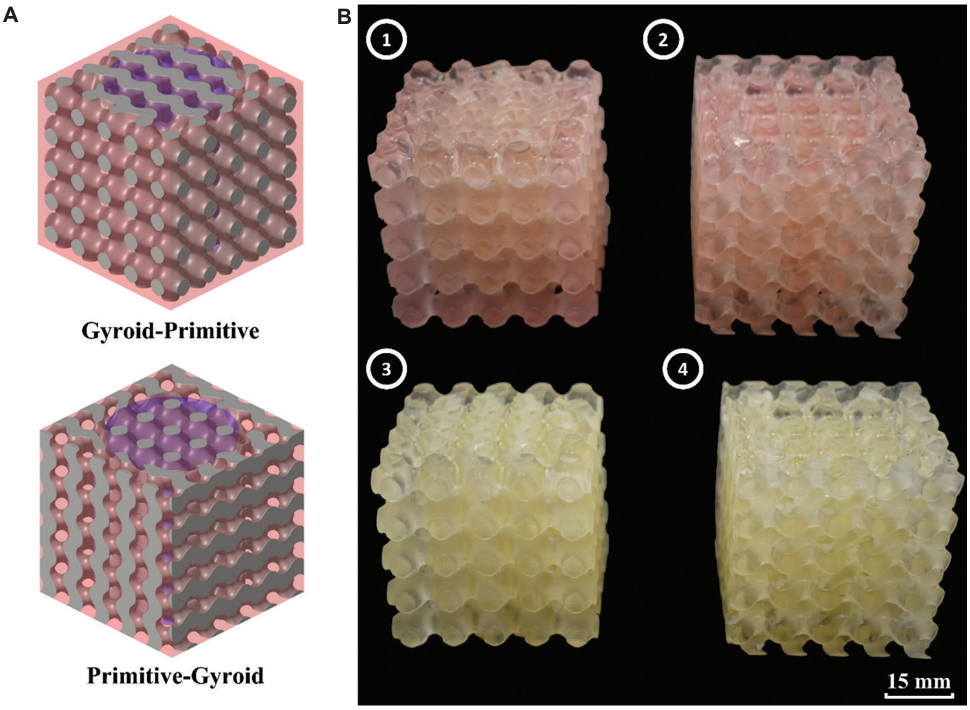

Figure 6. (A) As-designed hybrid triply periodic minimal surfaces lattices. (B) As-manufactured hybrid triply periodic minimal surfaces lattices.

at 250 μm[6]. With a very high accuracy of up to 14 μm layer thickness and the rubber-like nature of printed material, Stratasys J750 has been utilized to explore compliant design[28]. The printer is compatible with multiple types of polymer materials, including VeroMagentaV (VMV) and Agilus30. As a rigid material, VMV can be mixed with the softer Agilus30 so that a material with a different shore-hardness can be produced[29].

In this work, the A30, which has a shore hardness of 30, and A40, which has a shore hardness of 40, were utilized as the base materials. Two different unit cells, which are solid-network-based primitive and solid-network-based gyroid, are radially hybrid as illustrated in Figure 1E. The selection of unit cells is based on their deformation behavior, where the solid-network-based gyroid exhibits bending-dominated behavior and the solid-network-based primitive exhibits stretch-dominated behavior as reported in the literature[23]. The dimension of the hybrid lattice was set to be 50 mm in width, length, and height. The size of the unit cell was set to be 10 mm. Two different hybridization schemes with the same overall relative densities were adopted: (i) Radial hybrid lattice gyroid-primitive where gyroid unit cells located in the inner region and primitive located in the outer region; and (ii) radial hybrid lattices primitive-gyroid where primitive unit cells located in the inner region and gyroid located in the outer region. The as-manufactured gyroid-primitive A40, primitive-gyroid A40, gyroid-primitive A30, and primitive-gyroid A30 samples were labeled sequentially from 1 to 4, as shown in Figure 6B, where the as-designed models are illustrated in Figure 6A. To explore the influence by combining different types of TPMS lattices, uniaxial compression tests were conducted by utilizing the Shimadzu universal testing machine. The 2 mm/min load rate was adopted with a 50 kN load cell. Each design was tested with three samples to ensure the repeatability.

Figure 7 shows the compressive response for different hybrid lattice samples. According to the force-displacement curves, two slope changes, which indicate the beginning of post-yielding and the densification, were clearly observed for all cases. Thus, the deformation of both types of hybrid lattices was divided into three stages: (1) a nearly linear stage where the force increases with the increase of displacement under an approximately linear relation; (2) a continual deformation stage with a hardening under different degree; and (3) densification stage. As shown in Figure 7A and B, the gyroid-primitive design can increase the slope of the force-displacement curve when compared to the primitive-gyroid design. As a result, the higher strength at stage 2 can be achieved by the gyroid-primitive lattices, where the drop of force at the transition between stage 1 and stage 2 observed in primitive-gyroid can be mitigated. The strengthening effect obtained in primitive-gyroid lattices indicates that allocating the stretch-dominated lattices on the side of the structure to withstand higher stress and the bending-dominated lattices on the

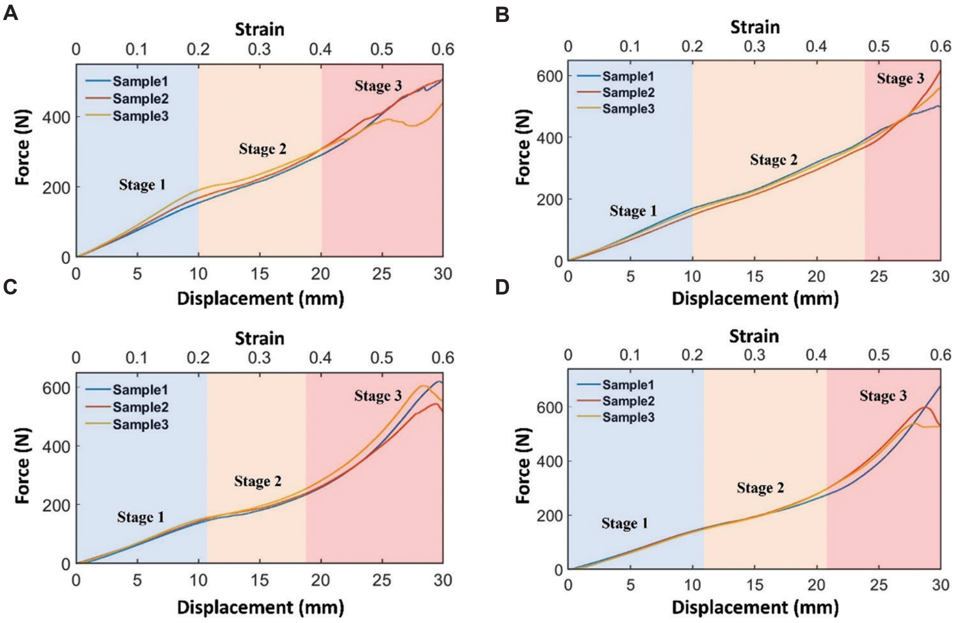

Figure 7. Compressive response of hybrid triply periodic minimal surfaces lattices under a load rate of 2 mm/min: (A) Gyroid-primitive A30, (B) gyroid-primitive A40, (C) primitive-gyroid A30, and (D) primitive-gyroid A40.

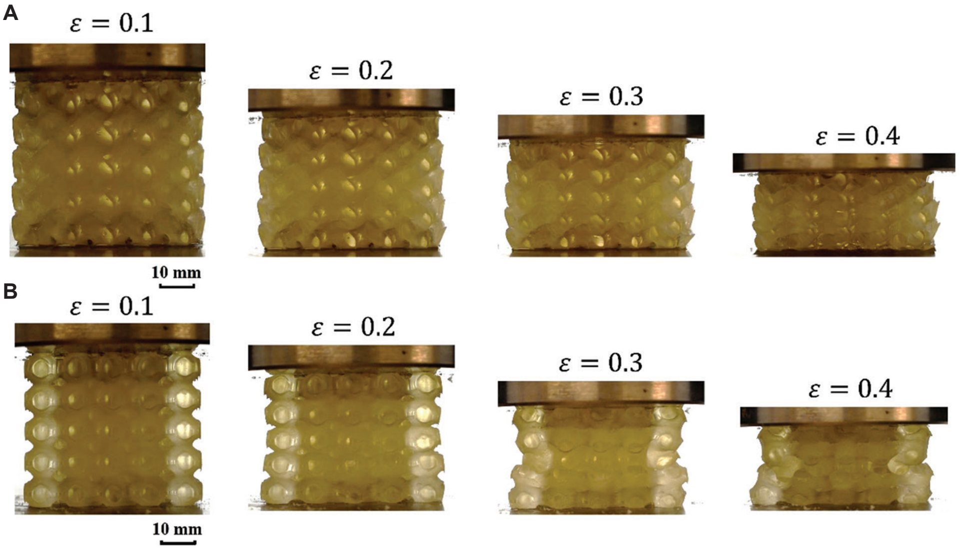

Figure 8. Deformation of hybrid lattices under compressive tests: (A) Primitive-gyroid lattice, and (B) gyroid-primitive lattice.

core of the structure to enlarge the ductility can improve the effectiveness of TPMS lattices.

Regarding the influence brought by the base material, compared with A30 samples are shown in Figure 7A and C, A40 samples (as shown in Figure 7B and D) have a more smooth transition between stage 1 and stage 2. In addition, the A40 can significantly increase the duration of stage 2 for both types of hybrid lattices, leading to a shorter densification stage. As a result, the energy absorption for both types of hybrid lattices can be increased with the base material that has a higher shore hardness.

Figure 8 illustrates the deformation history of both types of A30 hybrid lattices under compressive tests. Due to the similar compressive behavior shared by both A30 and A40 samples, only the deformation history of the A30 samples is illustrated here. As shown in Figure 8A, the primitive-gyroid lattices exhibit a transverse expansion during compression, indicating positive Poisson's ratio. As shown in Figure 8B, different deformation behavior can be achieved for the gyroid-primitive lattices where the transverse shrinkage can be observed during compression, indicating an auxetic compressive characteristic. In summary, the hybridization of different types of TPMS lattices can contribute to a counter-intuitive behavior, exhibiting auxetic behavior that has been proven to own superior properties and broad applications[30].

5. Conclusion

In this work, the elastic property of TPMS sheet-based gyroid lattice structures was explored. The design strategy of graded TPMS lattices and the hybridization of different types of lattices were illustrated, providing guidance for developing design strategies of novel TPMS-based lattice structures in future.

Numerical analysis was conducted to investigate the effect of applying functional graded sheet-based gyroid lattices to the implant application. The displacement at different positions and the stress contour was extracted based on the finite element modeling simulation. The results demonstrated that the functional graded gyroid lattice structures can effectively reduce the stress shielding effect. In addition, elastic properties of the uniform gyroid lattice with different relative densities were parametrically explored based on the RVE model. The analytical equation based on the Gibson-Ashby model was generated by fitting the simulation results, which can be utilized to predict the elastic properties to assist the future design of TPMS-based lattice structures. In conclusion, the numerical analysis illustrated that the application of the functional graded gyroid lattices can relieve the stress shielding effect as well as protects the bone from damage.

The feasibility of applying hybridization of different types of lattices was also validated by the compressive tests on the samples fabricated by the Stratasys J750. The study showcased the enhanced compressive behavior resulting from the comparison of radial hybrid primitive-gyroid and gyroid-primitive lattices. The deformation images provided a visual representation of the distinctive manifestation of auxetic compressive behavior resulting from the hybridization process. Consequently, the hybridization of distinct lattices not only enhances the mechanical characteristics of TPMS structures but also engenders a deformation response that defies conventional expectations.

Acknowledgment

The authors acknowledge the facilities, the scientific and technical assistance of the RMIT Centre of Additive Manufacturing (RCAM) and the RMIT Microscopy and Microanalysis Facilities (RMMF).

Funding

None.

Conflict of interest

The authors confirmed that there is no conflict of interest.

Author contributions

Conceptualization: Phuong Tran
Formal analysis: Tian Lan
Funding acquisition: Phuong Tran
Investigation: Tian Lan
Methodology: Chenxi Peng, Truong Do
Resources: Truong Do
Supervision: Kate Fox, Phuong Tran
Writing – original draft: Tian Lan
Writing – review & editing: Chenxi Peng, Kate Fox, Phuong Tran

All authors have read and agree to publish the final version of this paper.

Ethics approval and consent to participate

Not applicable.

Consent for publication

Not applicable.

Availability of data

Data are available from the corresponding author on reasonable request.

References

1. Pan C, Han Y, Lu J, 2020, Design and optimization of lattice structures: A review. *Appl Sci*, 10: 6374.

   https://doi.org/10.3390/app10186374

2. Nazir A, Abate KM, Kumar A, *et al.*, 2019, A state-of-the-art review on types, design, optimization, and additive manufacturing of cellular structures. *Int J Adv Manufact Technol*, 104: 3489–3510.

   https://doi.org/10.1007/s00170-019-04085-3

3. Xu F, Zhang X, Zhang H, 2018, A review on functionally graded structures and materials for energy absorption. *Eng Struct*, 171: 309–325.

   https://doi.org/10.1016/j.engstruct.2018.05.094

4. Wickramasinghe S, Do T, Tran P, 2020, FDM-based 3D printing of polymer and associated composite: A review on mechanical properties, defects and treatments. *Polymers*

(*Basel*), 12: 1529.

https://doi.org/10.3390/polym12071529

5. Tran P, Ngo TD, Ghazlan A, *et al.*, 2017, Bimaterial 3D printing and numerical analysis of bio-inspired composite structures under in-plane and transverse loadings. *Compos Part B Eng*, 108: 210–223.

   https:/doi.org//10.1016/j.compositesb.2016.09.083

6. Tee YL, Tran P, Leary M, *et al.*, 2020, 3D Printing of polymer composites with material jetting: Mechanical and fractographic analysis. *Addit Manuf*, 36: 101558.

   https://doi.org/10.1016/j.addma.2020.101558

7. Han XH, Wang Q, ParkYG, *et al.*, 2012, A review of metal foam and metal matrix composites for heat exchangers and heat sinks. *Heat Transfer Eng*, 33: 991–1009.

   https://doi.org/10.1080/01457632.2012.659613

8. Dixit T, Nithiarasu P, Kumar S, 2021, Numerical evaluation of additively manufactured lattice architectures for heat sink applications. *Int J Therm Sci*, 159: 106607.

   https://doi.org/10.1016/j.ijthermalsci.2020.106607

9. Samson S, Tran P, Marzocca, 2018, Design and modelling of porous gyroid heatsinks: Influences of cell size, porosity and material variation. Appl Therm Eng, 235: 121296.

   https://doi.org/10.1016/j.applthermaleng.2023.121296

10. Attarilar S, Ebrahimi M, Djavanroodi F, *et al.*, 2021, 3D printing technologies in metallic implants: A thematic review on the techniques and procedures. *Int J Bioprint*, 7: 306.

    https://doi.org/10.18063/ijb.v7i1.306

11. Depboylu FN, Yasa E, Poyraz Ö, *et al.*, 2022, Titanium based bone implants production using laser powder bed fusion technology. *J Mater Res Techn*, 17: 1408–1426.

    https://doi.org/10.1016/j.jmrt.2022.01.087

12. Yin H, Zhang W, Zhu L, *et al.*, 2022, Review on lattice structures for energy absorption properties. *Compos Struct*, 304: 16397.

    https://doi.org/10.1016/j.compstruct.2022.116397

13. Maconachie T, Leary M, Lozanovski B, *et al.*, 2019, SLM lattice structures: Properties, performance, applications and challenges. *Mater Des*, 183: 10813.

    https://doi.org/10.1016/j.matdes.2019.108137

14. Crook C, Bauer J, Izard AG, *et al.*, 2020, Plate-nanolattices at the theoretical limit of stiffness and strength. *Nat Commun*, 11: 1579.

    https://doi.org/10.1038/s41467-020-15434-2

15. Novak N, Al-Ketan O, Krstulović-Opara L, *et al.*, 2021, Quasi-static and dynamic compressive behaviour of sheet TPMS cellular structures. *Compos Struct*, 266: 113801.

    https://doi.org/10.1016/j.compstruct.2021.113801

16. Peng C, Tran P, 2020, Bioinspired functionally graded gyroid sandwich panel subjected to impulsive loadings. *Compos Part B Eng*, 188: 107773.

    https://doi.org/10.1016/j.compositesb.2020.107773

17. Peng C, Tran P, Mouritz AP, 2022, Compression and buckling analysis of 3D printed carbon fibre-reinforced polymer cellular composite structures. *Compos Struct*, 300: 116167.

    https://doi.org/10.1016/j.compstruct.2022.116167

18. Al-Ketan O, Lee DW, Rowshan R, *et al.*, 2020, Functionally graded and multi-morphology sheet TPMS lattices: Design, manufacturing, and mechanical properties. *J Mech Behav Biomed Mater*, 102: 103520.

    https://doi.org/10.1016/j.jmbbm.2019.103520

19. Novak N, Al-Ketan O, Borovinšek M, *et al.*, 2021, Development of novel hybrid TPMS cellular lattices and their mechanical characterisation. *J Mater Res Techn*, 15: 1318–1329.

    https://doi.org/10.1016/j.jmrt.2021.08.092

20. Al-Ketan O, Abu Al-Rub RK, 2019, Multifunctional mechanical-metamaterials based on triply periodic minimal surface lattices: A review. *Adv Eng Mater*, 21: 1900524.

    https://doi.org/10.1002/adem.201900524

21. Du Plessis A, Yadroitsava I, Yadroitsev I, *et al.*, 2018, Numerical comparison of lattice unit cell designs for medical implants by additive manufacturing. *Virtual Phys Prototyp*, 13: 266–281.

    https://doi.org/10.1080/17452759.2018.1491713

22. Han C, Li Y, Wang Q, *et al.*, 2018, Continuous functionally graded porous titanium scaffolds manufactured by selective laser melting for bone implants. *J Mech Behav Biomed Mater*, 80: 119–127.

    https://doi.org/10.1016/j.jmbbm.2018.01.013

23. Ren F, Zhang C, Liao W, *et al.*, 2021 Transition boundaries and stiffness optimal design for multi-TPMS lattices. *Mater Des*, 210: 110062.

    https://doi.org/10.1016/j.matdes.2021.110062a

24. Yang N, Quan Z, Zhang D, 2014, Multi-morphology transition hybridization CAD design of minimal surface porous structures for use in tissue engineering. *Comput Aided Des*, 56: 11–21.

    https://doi.org/10.1016/j.cad.2014.06.006

25. Dong G, Tang Y, Zhao YF, 2019, A 149 line homogenization code for three-dimensional cellular materials written in matlab. *J Eng Mater Technol*, 141: 011005.

    https://doi.org/10.1115/1.4040555

26. Peng C, Tran P, Nguyen-Xuan H, *et al.*, 2020, Mechanical performance and fatigue life prediction of lattice structures:

Parametric computational approach. *Compos Struct*, 235: 111821.

https://doi.org/10.1016/j.compstruct.2019.111821

27. Ashby MF, 2006, The properties of foams and lattices. *Philos Trans A Math Phys Eng Sci*, 364: 15–30.

    https://doi.org/10.1098/rsta.2005.1678

28. Wu C, Do TT, Tran P, 2021, Mechanical properties of polyjet 3d-printed composites inspired by space-filling peano curves. *Polymers*, 13: 3516.

    https://doi.org/10.3390/polym13203516

29. Tee YL, Peng C, Pille P, *et al.*, 2020, PolyJet 3D printing of composite materials: Experimental and modelling approach. *Jom*, 72: 1105–1117.

    https://doi.org/10.1007/s11837-020-04014-w

30. Ren X, Das R, Tran P, *et al.*, 2018, Auxetic metamaterials and structures: A review. *Smart Mater Struct*, 27: 23001.

    https://doi.org/10.1088/1361-665X/aaa61c

ACCSCIENCE PUBLISHING

Materials Science in Additive Manufacturing

ORIGINAL RESEARCH ARTICLE

Additive manufacturing: Application and validation of machine learning-based process-structure-property linkages in Ti-6Al-4V

Xi Gong, Willem Groeneveld-Meijer, and Guha Manogharan*

Department of Mechanical Engineering, Pennsylvania State University, PA, 16801, USA

Abstract

In the field of metal additive manufacturing (AM), various processes and heat treatments can yield unique grain morphologies, thereby influencing material properties and machining behavior. In this study, a novel workflow using a machine learning-based approach that combines statistical descriptors of textured AM-process induced microstructure, cutting force model (as a material response), and a data-mining method is established. It is proven to be a valid method for creating process-structure-property linkages for metal AM. This study focuses on two highly varied metal AM processes: Powder bed fusion (PBF, e.g., laser PBF and electron beam PBF) and directed energy deposition (DED, e.g., wire-fed plasma-directed energy deposition). The study also accounted for the effects of post-AM heat treatment and build orientation. It was found that the accuracy of material behavior predictions is highly correlated with AM processing conditions, building orientations, and machining conditions. Specifically, while initially applying PBF training data to DED samples resulted in a 15% root mean square prediction error, this error was subsequently reduced to <1% through cross-training using combined microstructure training data sets. This discrepancy could be attributed to the significantly different thermal cycling conditions in L-PBF and DED, which resulted in highly varied textured microstructures. Residual stresses generated during AM processing and the selection of machining parameters exert the highest impact on the machining behavior. The implications of these findings extend to the use of statistically descriptive microstructures for various AM processing conditions and build orientations in computational methods and other machining learning approaches.

Keywords: Additive manufacturing; Machine learning; Process-structure-property linkage; Ti-6Al-4V

***Corresponding author:**
Guha Manogharan
(gum53@psu.edu)

Citation: Gong X, Groeneveld-Meijer W, Manogharan G, 2023, Additive manufacturing: Application and validation of machine learning-based process-structure-property linkages in Ti-6Al-4V. *Mater Sci Add Manuf*, 2(3): 0999.
https://doi.org/10.36922/msam.0999

Received: May 25, 2023

Accepted: September 24, 2023

Published Online: September 29, 2023

1. Introduction

Metal additive manufacturing (AM) technologies offer an economical means of producing highly complex and customized parts with efficient material utilization, particularly suitable for low-volume production[1]. Two major classes of AM processes are employed for titanium alloys: powder bed fusion (PBF) and directed energy deposition (DED). Within a given part (based on build orientation), the microstructure and mechanical properties exhibit unique characteristics, strongly influenced by the chosen AM process, processing conditions, and subsequent post-AM treatments. In laser PBF, typical beam sizes range from 0.1 – 0.5 mm, with layer thicknesses between 20 and 75 μm when employing a laser source in an inert atmosphere, and 0.2 – 1 mm with layer thicknesses of approximately 75 – 125 μm for an electron beam source within a vacuum environment. In the DED process, the typical beam sizes range from 2 – 4 mm, with layer thicknesses between 500 and 1000 μm within a shielding gas or vacuum environment. The parameters employed in the DED process result in a coarse surface finish[2-6]. In recent years, several studies have explored the application of machining learning and deep learning methods to create the process-structure-property (PSP) linkages[7-11]. Figure 1 shows the workflow of the Ti-6Al-4V process-structure-property linkage study.

1.1. PBF AM methods for metals

The electron beam melting (EB-PBF) process is a PBF AM process known for its ability to produce full-density functional parts. This is achieved using a high-energy electron beam and "hot-bed" metal powder. Throughout the manufacturing process, the entire build tank is maintained at an elevated temperature under a vacuum environment. The electron beam is powered by a high-voltage electron beam (30 – 60 kV), as shown in Figure 2.

The EB-PBF can process multiple conductive material systems such as stainless steel (316), tool steel (H13), Ti-based superalloys (Ti-6Al-4V), Ni-based superalloys (Inconel 718), Co-based superalloys (Stellite 21), low-expansion alloys (Invar), hard metal, intermetallic compounds, aluminum, copper, niobium, and beryllium[4,12,13]. To eliminate the scattering and dissipation of electron beams that occur in the atmospheric environment, electron beaming systems are operated in a vacuum environment (10^{-3} Mbar in the chamber and 10^{-6} Mbar in the gun column). Compared to laser-based AM processes, the EB-PBF process is operated at higher working temperatures without the risk of oxygen uptake due to excellent thermal isolation and the desired vacuum environment. Higher chamber temperatures lead to lower residual stress compared to laser-based AM systems, and parts processed using EB-PBF can be used without secondary stress-relieving. Furthermore, the EB-PBF process involves a preheating step before melting, which partially sinters the powder layer to increase thermal conductivity during a melting pass, reducing the temperature gradient and preventing the formation of thermal cracks[4,13]. The preheating process also holds powder particles together, which can act as supports. Therefore, in the EB-PBF process, support structures are often employed for heat conduction. After the melting pass, the entire build plate is heated again with an electron beam (higher velocity and lower current) before the next power layer is spread. The EB-PBF process includes an "in-built" heat treatment step, where the machine is allowed to cool down to room temperature in an inert atmosphere before the build chamber is accessed.

Laser PBF (L-PBF) process, also known as selective laser sintering, selective laser melting (SLM), direct metal laser sintering, direct metal laser melting, uses a high-power laser beam to selectively fuse powder within an inert atmosphere, as shown in Figure 3. This process

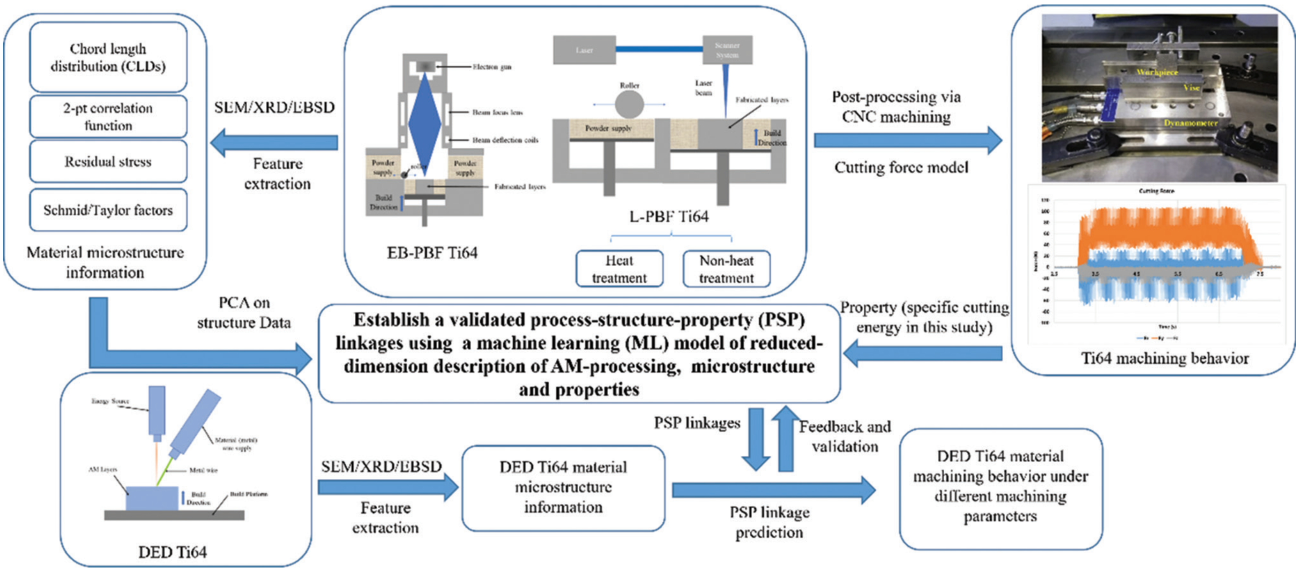

Figure 1. This research presents a validated machine learning model to predict process-structure-property linkage in additive manufacturing of Ti-6Al-4V. Abbreviations: CNC: Computer numerical control; DED: Directed energy deposition; EB-PBF: Electron beam-powder bed fusion; EBSD: Electron backscattered diffraction analysis; L-PBF: Laser powder bed fusion; PBF: Powder bed fusion; PCA: Principal component analysis; PSP: Process-structure-property; SEM: Scanning electron microscopy; XRD: X-ray diffraction analysis.

involves two pistons: one for supplying metal powder using a recoater to create the powder layer, and the other to hold the fabricated parts. The chamber is filled with inert gas, such as argon for reactive materials or nitrogen for non-reactive materials. In addition, a flow of inert gas passes over the powder layer to protect the part from oxidation, remove spatter, and clear metal fumes generated along the laser path.

The main process parameters are the power of the laser source, scan speed, focus offset, hatch distance, and layer thickness. At present, available L-PBF systems often use fiber lasers with 200 W to 1 kW peak power to selectively fuse the powder bed layer. The typical layer thickness value ranges between 20 and 100 μm depending on the material size distribution. Unlike the EB-PBF process, in "cold-bed" L-PBF processes, only the build platform is preheated (typically 75 – 200°C). Due to the rapid heating and high cooling rate, residual stresses are inherently developed. Stress relief heat treatment is often required before the final part is deployed in service. Table 1 shows the characteristic features of both PBF systems: L-PBF and EB-PBF processes.

When compared to the EB-PBF process, L-PBF processes have a lower build rate and scanning speed due to the electro-mechanical components involved in laser control. However, L-PBF offers better surface finish, higher accuracy, lower machine cost, and availability of larger build volumes.

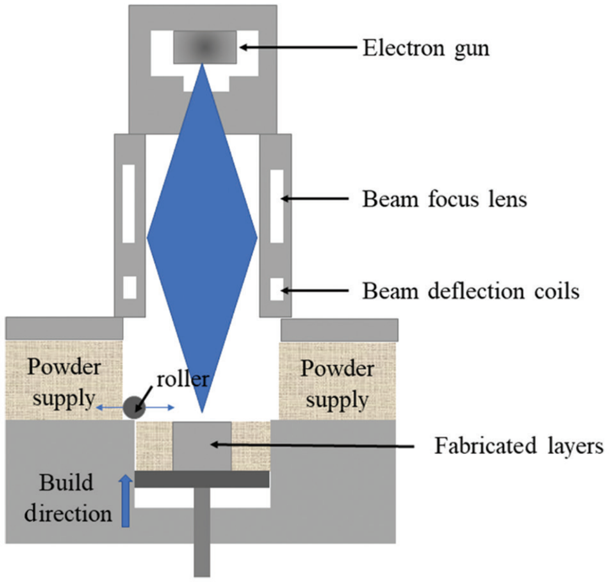

Figure 2. Electron beam-powder bed fusion.

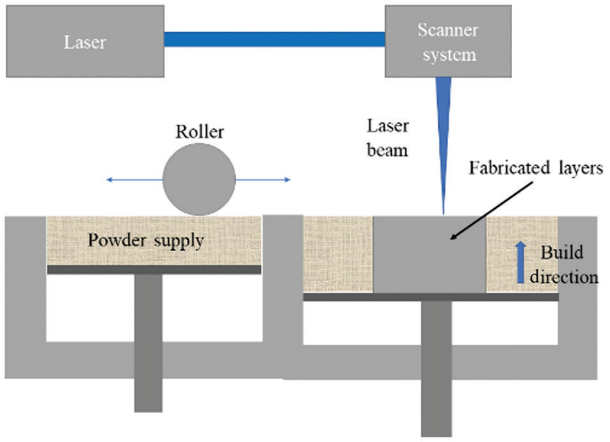

Figure 3. Laser powder bed fusion.

1.2. Directed energy deposition metal AM methods

Directed energy deposition (DED) is another layer-by-layer manufacturing technique to build metallic and functional components. In contrast to PBF processes, where a power source is used to melt a layer in the powder bed selectively, DED systems involve a powder or wire feeding system that delivers material to the melt pool created by the power source (like welding). In this process, a melt pool is formed on the surface of the substrate or previously deposited layer by using a high-energy power source such as a laser beam, electron beam, or plasma arc. Using numeric control (NC), the powder or wire is fed into the melt pool along with synchronized motion stage control. A single or multiple nozzle deposition heads can be used to deliver the powder or wire. Like other AM processes, the toolpath for each layer is generated by user-defined process parameters and a sliced 3D CAD model. Several equipment manufacturers also have their equipment labeled as DED processes, such as laser cladding (LC), direct metal deposition (DMD), direct light fabrication (DLF), laser direct casting (LDC), laser forming (Lasform), shape deposition manufacturing (SDM), laser

Table 1. Characteristic features of L-PBF and EB-PBF[14,15]

AM processing	L-PBF	EB-PBF
Power source	Fiber lasers	Tungsten cathode-based high-power electron beam
Build chamber environment	Argon or nitrogen	Vacuum
Preheating method	Platform heating	Preheat scanning
Powder preheating temperature (°C)	100 – 200	700 – 900
Maximum build rate (cm^3/h)	20 – 35	80
Layer thickness	20 – 100	50 – 200
Surface finish (Ra)	4 – 11	25 – 35
Minimum feature size (μm)	40 – 200	100
Geometric tolerance (mm)	± 0.05 – 0.1	± 0.2

Abbreviations: EB-PBF: Electron beam powder bed fusion; LPBF: Laser powder bed fusion.

engineer net shape (LENS), laser powder fusion (LPF), laser-aided direct-metal deposition (LADMD), laser-based multi-direction metal deposition (LBMDMD), and laser-aided manufacturing process (LAMP)[16].

Figures 4 and 5 show the typical powder DED machine and wire DED machine structure, respectively.

During the DED process, material feed rate and energy power can be adjusted to achieve the desired microstructural feature. In addition, variation to process parameters and multi-nozzle feedstock with different alloy systems can lead to a unique advantage for the DED process to fabricate functionally graded components. Due to the unique advantage of the material delivery system, the DED process can be used to repair and clad valuable parts that cannot be processed by other AM processes. Furthermore, the DED process provides a higher deposition rate and a wider process volume compared to other AM processes. During the DED process, different powders can be fed at the same time into the melt pool, which leads to in-situ alloying[16]. However, like PBF processes, secondary processes such as machining and heat treatment are required for DED parts.

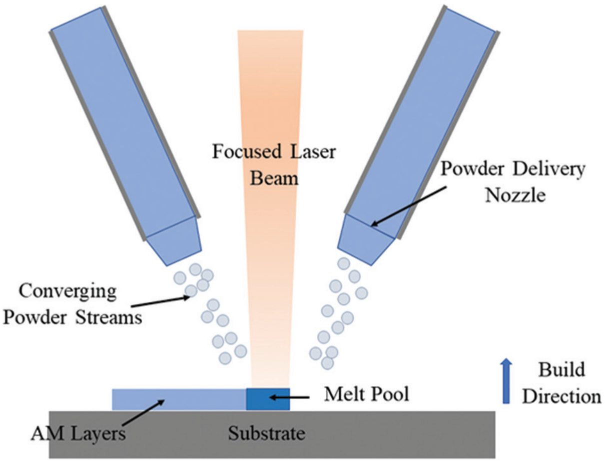

Figure 4. Powder-fed directed energy deposition.

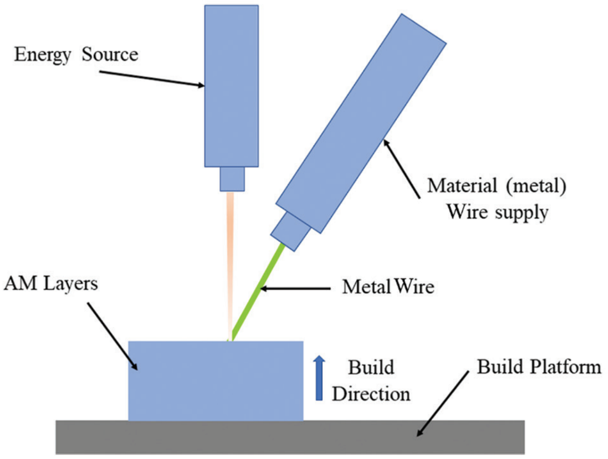

Figure 5. Wire-fed directed energy deposition.

A summary of comparisons between the different metal AM techniques is presented in Table 2 below:

1.3. Titanium metal AM processing

Metal AM processes have a significant impact on the microstructure and performance of the titanium alloys. In L-PBF and DED processes, elongated prior β grain boundaries grow in the same direction as the build orientation due to the cyclic thermal history[16,42,43]. However, microstructure and microhardness vary depending on build orientation and build height. The prior β grain size in DED parts is larger than in L-PBF, while the microhardness is higher in L-PBF parts[44]. In DED titanium, columnar, equiaxed, and a mix of columnar and equiaxed microstructure are observed, while in L-PBF, the lamellar colony, columnar, and Widmanstätten are usually observed[19,45-48].

Microstructural evolution in the AM processes and heat treatment could influence the machinability of titanium components. In general, finer microstructures lead to higher hardness and machining force. In L-PBF parts, heat treatment could lead to coarser microstructures, especially when the heat treatment temperature approaches or surpasses the β transus. This increases the average α laths size significantly and reduces yield stress and ultimate tensile stress[32]. In L-PBF parts, the near-surface microstructure is typically fine, and its grain orientation limits crystal dislocation, leading to higher slip resistance, and increased machining force[49]. In DED titanium components, subsurface deformation depth decreases with increasing machining speed. At a low cutting speed, the built-up edge phenomenon is observed at the cutting tooltip[50].

As AM-processed titanium alloys are known to have significant property differences, it is critical to build unique process-structure-property linkages (PSP) for a better understanding of the influence that varying grain morphology has on material performance. Previous research simulated grain structure evolution in the as-deposited state for L-PBF using computational fluid dynamics and phase-field framework[51]. Several researchers have developed analytical and finite-element models only to investigate residual stress and melt pool profiles without consideration for machining[52,53]. There is a growing number of reported efforts to develop PSP linkages to capture the underlying interactions between AM parameters and structure properties[54,55]. Machine learning (ML) models explore the relationship between structure and property based on existing data without constructing AM process-physics-based assumptions and numerical models[54,56,57]. Additional

Table 2. Process specific attributes of PBF and DED metal AM techniques

Process	Materials	Comments	References
Powder bed fusion			
EB-PBF	Titanium alloys (Ti-6Al-4V), nickel alloys (Inconel 625, 718, 740, Rene 142), steel alloys (SS 316), TiAl (γ-TiAl), high-entropy alloy (AlCoCrFeNi)	(i) Vacuum operation condition, which reduces thermal convection, thermal gradients, contamination, and oxidation (ii) High build but inferior dimensional and surface finish (iii) High build chamber temperature and preheating reduce the thermal gradient in the powder bed (iv) Preheating holds the powder together and acts as a support structure for the overhang structure	[17–26]
L-PBF	Titanium alloys (Ti-6Al-4V), nickel alloys (Inconel 625, 718, 738, 939), steel alloys (316 SS, 420 SS, 4340, M2 HSS, 17-4 SS), aluminum alloys (AlSi10Mg, AlSi12, Al-Sc), high-entropy alloys (FeCoCrNi)	(i) Protective gas operation environment (argon, nitrogen) (ii) Low build rate but high accuracy, larger build-up volumes compared with EB-PBF (iii) A fast cooling rate and a large thermal gradient leads to large residual stress (iv) Stress relief heat treatment and/or hot isotropic pressing (HIP) needed to achieve final mechanical properties	[27–34]
Directed energy deposition			
EB-PBF (wire)	Steel alloys (347 SS), titanium alloys (Ti-6Al-4V), aluminum alloys (2219 Al)	(i) Fabricate functionally graded and pure metal components (ii) Capability to repairing and cladding parts (iii) The high deposition rate and large volumes (iv) Limited by geometrical freedom due to lack of support (v) Inadequate geometrical accuracy and extremely pool surface finish.	[35,36]
Laser (wire) and LENS	Titanium alloys (Ti-6Al-4V), nickel alloys (Inconel 718), steel alloys (4340)		[37–39]
WAAM	Titanium alloys (Ti-6Al-4V), steel alloys (10V, 15-5 PH, 309), aluminum alloys (Al-Mg)		[40,41]

Abbreviations: EB-PBF: Electron beam powder bed fusion; LENS: Laser engineer net shape; L-PBF: Laser powder bed fusion; WAAM: Wire arc additive manufacturing.

studies have summarized different ML methods and their applications in AM manufacturing[58-60].

To achieve the designed geometric dimensioning and tolerancing (GD&T) and surface finish, post-processing, usually a subtractive machining process, is required for metal AM components. In a production cycle from design to manufacturing to inspection, GD&T is the common language to communicate the acceptable quality of geometric elements of the parts. GD&T standard is based on mathematical representations of an acceptable range of variation in geometry based on manufacturing process-specific knowledge bases to specify design intent and prevent misrepresentation during production processes. The tolerance specification is the specification of the type and value of tolerance based on the GD&T standard[61]. Compared to traditional processes, AM processes can produce complex geometries, which lead to potential tolerance and specification issues. In addition, since metal AM processes produce components with different microstructure and mechanical properties when compared to traditionally manufactured parts, there is a critical research potential to discover ideal post-process machining parameters for AM products.

Since AM technologies afford the creation of complex geometries, shorten fabrication time and material cost, and enable low-volume production and mass customization, they offer a new approach to fabricating Ti-6Al-4V alloys[62]. However, in most mechanical and aerospace Ti-6Al-4V applications, post-processing, such as stress relief heat treatment and computer numerical control (CNC) machining, are required to achieve the required mechanical properties, designed tolerance, and surface finish. Summarizing the prior work in the machining of AM Ti-6Al-4V, researchers found that when compared to conventionally manufactured Ti-6Al-4V products, the Ti-6Al-4V alloys fabricated using AM processes have highly different material characteristics such as microstructure, and different mechanical properties such as yield strength, hardness, tensile strength, and elongation. In addition, researchers have established that machining behavior, such as cutting force in turning and milling, finished surface roughness, and tool wear behavior, is quite different when machining AM Ti-6Al-4V parts compared with conventional wrought parts. However, a critical knowledge gap exists in understanding the fundamental relationship between AM Ti-6Al-4V material properties and their machining behavior, specifically across different AM processing techniques.

1.4. Strain hardening and temperature effects on Ti-6Al-4V AM parts

Strain hardening is one of the most important considerations in the evaluation of the machining of metallic materials. The strength, ductility, toughness, and deformability of materials are intimately related to strain-hardening characteristics[63-67]. For Ti-6Al-4V, the dominant HCP metals present a more complex case due to their low symmetry that restricts the number of slip systems, which leads to a strong plastic anisotropy. Different strain hardening behaviors have been reported in many Ti alloys, such as compression testing at high temperatures[64]; stage III strain hardening happens only at elevated temperatures on tensile flow behavior testing[65]. Hardening capacity and strain hardening exponent decreased with increasing strain rate or decreasing temperature on electron beam welding of Ti-6Al-4V. Stage III hardening happened after yielding in the heat affect zone (HAZ). Furthermore, the hardening rate was strongly dependent on the strain rate and temperature.

However, the heterogeneity in AM Ti-6Al-4V parts might lead to varied material properties. According to the previous research, the mechanical properties are more heterogeneous along the AM build direction than the parallel HAZ. Mechanical properties such as strength and microhardness are microstructure-dependent. The mechanical heterogeneity along the AM path is dependent on the changing trend of the size of β columnar grain and martensite. The strain and strain rate heterogeneity also depend on the microstructure heterogeneity[62].

According to the previous research, for Ti-6Al-4V alloys, the flow stress increases when the strain rate increases and temperature decreases. Furthermore, the fracture strain increases with an increasing strain rate at a certain temperature. For a certain strain rate, the smallest fracture strain was observed at 700°C. Furthermore, the strain rate sensitivity increases with increasing strain and strain rate. Moreover, a direct correlation is found between the depth and density of the dimples and the magnitude of the fracture strain[67]. To better understand the Ti-6Al-4V machinability, cryogenic machining was applied to titanium alloys, and people found that the cryogenic coolant extended the tool life. Moreover, titanium chips show less deformation and heat was generated during chip formation with low feed and high depth of cut combination. At present, the machinability of titanium alloys is focused on the wrought parts. However, AM titanium shows a dramatic difference among mechanical properties, such as heterogeneity, tensile stress, microhardness, and so on.

During the machining of titanium, the strain magnitude and strain rate involved directly affect the machinability of the alloys. The Taylor model has been used to represent the strain rate and strain information statistically.

1.5. Characterization and machinability of AM-processed titanium

Titanium alloys are widely used in aerospace, bio-medical, and defense applications. Titanium alloys are often fabricated by conventional costly forging and casting processes, which have a lower material utilization ratio and lower production rate. Ti-6Al-4V alloy is an α-β dual-phase moderate-strength alloy with high comprehensive mechanical and chemical properties. Due to its excellent strength-to-weight ratio, Ti-6Al-4V alloy is widely used in the aerospace industry for manufacturing blades, discs, and cooling parts in compressors, as well as biomedical implants.

In critical aircraft structures, Ti-6Al-4V has been processed through forging. Ti-6Al-4V accounts for half of the total titanium alloy application[68]. AM technologies provide a new opportunity to produce large and complex Ti-6Al-4V products. Since there is an ever-growing research interest and application of this alloy, this research will focus on Ti-6Al-4V alloys, which have been fabricated through PBF and DED AM technologies.

Several investigators have focused on the material and mechanical properties of different AM-processed Ti-6Al-4V alloys. Rafi *et al.* compared Ti-6Al-4V alloys fabricated through the SLM process and EB-PBF process and found that martensitic α' microstructure dominates the SLM parts while α phase with β separating the α lamellae structure observed in EB-PBF sample. SLM Ti-6Al-4V samples have higher tensile strength, lower ductility, and higher fatigue limits than EB-PBF-produced samples[69]. Liu *et al.* investigated the mechanical properties of Ti-6Al-4V fabricated using laser melting deposition-SLM (LMD-SLM) hybrid AM process and found that the density of hybrid-forming can reach 99.5% with the existence of pores with diameter <20 μm, and tensile strength and elongation of the hybrid AM process can reach 918 MPa and 11%, respectively[70]. Shi *et al.* investigated Ti-6Al-4V alloys fabricated through SLM and wire arc AM (WAAM) processes. They found that short β columnar grains consisting of primarily martensite α' in SLM parts. In contrast, coarse β columnar grains awash with α lamellae lead to epitaxial growth observed in WAAM parts. Compared to the WAAM sample, SLM parts showed higher tensile strength and lower elongation, especially in samples built in a vertical direction[71].

Due to inherently different thermal cycling conditions and process parameters across AM processes, this will lead to diverse microstructure representation and mechanical properties. Due to the layer-by-layer processing, microstructure and mechanical properties change due to different cooling rates and thermal gradients within a single AM part. The previous research observed that the grain size increases along the build direction in Ti-4Al-4V AM samples, and mechanical properties such as hardness, yield strength, and elongation gradient also vary along the build direction[24,72-74]. In L-PBF and DED metal parts, heat treatment is also necessary to achieve the final geometrical shape and desired mechanical properties. Heat treatment directly affects the microstructure of the final metal AM parts. The previous research observed that there exists a preferred grain growth orientation in the Ti-6Al-4V sample before and after heat treatment, and grain growth and transformation are evident after heat treatment[32,75,76]. Since post-processing is necessary for most metal AM parts to achieve desired tolerance and remove support structures, machining behavior such as tool wear, cutting force, and specific cutting energy should be investigated due to large variations in material properties among Ti-6Al-4V alloys fabricated through different AM processes.

To reduce tool wear and cutting force, cryogenic machining was used in machining Ti-6Al-4V alloys. Bordin *et al.* investigated the tool wear and surface finish on EB-PBF Ti-6Al-4V samples and found that adhesive wear was the primary tool wear mechanism in both dry and cryogenic turning. When compared with dry machining, cryogenic machining led to a decrease in adhered layer thickness on the rake face, while crater wear was eliminated by cryogenic cooling. Cryogenic cooling improves surface integrity and leads to a better surface finish[77]. Polishetty *et al.* compared the machining force and surface finish of SLM Ti-6Al-4V samples with conventional produced wrought Ti-6Al-4V samples and found that cutting forces in SLM samples were higher than the machining of wrought parts. Another significant finding was that when the cutting speed increased, cutting forces increased on machining SLM Ti-6Al-4V samples while cutting force decreased during machining of wrought Ti-6Al-4V samples. SLM samples had better surface roughness than wrought parts[78,79]. Wu *et al.* observed extra strain hardening caused by strain gradient near the grain boundaries in microstructure gradient material, which leads to different properties compared with homogeneous material[80]. The difference in mechanical properties between heterogeneous and homogenous materials affects the machining mechanisms and will result in a different machining behavior.

Based on prior research, it is evident that the machinability and machining behavior for AM Ti-6Al-4V parts are clearly different from traditionally produced Ti-6Al-4V parts due to their difference in material characterization and mechanical properties. In addition, different AM technologies such as EB-PBF, L-PBF, and DED fabricated Ti-6Al-4V will produce highly varied microstructure, which will also lead to different machining behavior.

In this study, L-PBF-, EB-PBF-, and DED-processed Ti-6Al-4V are studied due to their different AM processing conditions and resulting grain morphologies. The authors build on their previous work on PBF ML study for process-structure-property linkages in the machining behavior of Ti-6Al-4V[7]. In this study, scanning electron microscopy (SEM), electron backscatter diffraction (EBSD), and X-ray diffraction (XRD) analysis methods are applied. Machining behavior, that is, specific cutting energy, is computed from a cutting force model using recorded data through a Taguchi experiment. Gradient tree-based boosting machine learning models and benchmark linear regression models are developed for a thorough validation study.

2. Methodology

2.1. Sample preparation

In this study, EB-PBF Ti-6Al-4V specimens were fabricated using an Arcam A2 EB-PBFchine with 50 μm layer thickness. L-PBF specimens were manufactured using the EOSINT M280 system with 200W laser power, 80 μm spot size, and approximately 40 kW/mm^2 power density. Half of the L-PBF specimens were heat-treated to relieve residual stress. DED Ti-6Al-4V specimens were fabricated using a MERKE IV machine with rapid plasma deposition technology. The layer thickness in the Z direction is around 3 – 4 mm. All DED specimens were heat-treated to relieve residual stresses.

2.2. Material structure data extraction

2.2.1. SEM data extraction

According to our previous research[7], the 2-point correlation functions[81-83], chord length distributions (CLDs)[84], and principal component analysis (PCA) have been proven to be valid low-order SEM microstructure feature extraction tools.

The 2-point statistics denote the Ti-6Al-4V microstructure conditional probability of finding the same phase (α/β) in spatial bins whose centers are separated by a vector set.

The CLDs describe the probability of finding a specific length chord within the microstructure. Considering the anisotropy of AM materials, CLDs were resolved along and directions of the microstructure to keep function analyses consistent.

2.2.2. XRD data extraction

XRD was used to directly measure the strain resulting from the distortion of the crystalline lattice structure, along with the associated residual stresses[85]. According to the previous study, the presence of shear stresses is indicated by splitting in the d-spacing-sin$^2\Psi$ plot[86]. Therefore, a regression analysis was used to calculate the principal stresses of each specimen.

2.2.3. EBSD data extraction

For constructing the valid PSP linkages among AM Ti-6Al-4V, the Schmid and Taylor models were utilized in this study. For feature extraction from EBSD data, the Schmid Factors (SFs) were calculated from different specimens based on three main slip systems, and Taylor Factors (TFs) were calculated based on three different strain rate conditions.

2.3. Machining experiment and specific cutting energy

The machining experiment was performed on a Haas VF2SS vertical CNC center. The cutting tools selected for the experiments were 6.35 mm (1/4 inch) nominal diameter six flute carbide end mills with KC635M TiAlN coating (Model HPFT250S6075).

Three levels of machining parameters selected for the machining experiments are shown in Table 3. As described above, two feed directions, XY and XZ, which are vertical and parallel to the build orientation, were utilized in the experiment for EB-PBF, as-AM L-PBF, heat-treated L-PBF, and DED specimens.

Specific cutting energy for each path was calculated based on our cutting force model.

3. Results

3.1. Material microstructure representation

In this study, 200 microstructure statistical volume elements (SVEs) are used to represent each AM Ti-6Al-4V sample level (L-PBF XY HT, L-PBF XZ HT, L-PBF XY NHT, L-PBF XZ NHT, EB-PBF XY, EB-PBF, DED XY, and DED XZ), as shown in Figure 6. In SVEs, the influence coefficient decayed to around zero within a ~210 μm region[87]. After SEM feature extraction and PCA, the number of dimensions was reduced from over 3000 initially to 238 as the PCA cumulative variance approaches >99%. This is critical for developing an SP linkage model that is both computationally feasible and accurate in predicting material response.

Table 3. Machining parameters

Levels	1	2	3
Depth of cut (mm)	0.6350	1.270	1.905
Feed (mm per tooth)	0.0127	0.0254	0.0381
Speed (m per min)	24.384	36.576	48.768

The near-surface residual stress from eight materials is shown in Table 4. Along the build direction, the DED sample shows larger compressive and shear stresses in the Z direction. L-PBF-AM sample shows large compressive stress in the Y direction. On the top layers, both the EB-PBF and DED samples show large compressive stress in the Y direction but minimal stress in the Z direction. L-PBF heat-treated sample shows massive tensile stress on top layers in the Y direction and compressive stress in the Z direction, while the as-AM L-PBF sample shows a small stress value on the top region.

The ratio of critical resolved shear stress (CRSS) applied to the Schmid model on basal, prismatic, and first-order pyramidal slip systems is 1:0.7:3[88,89]. In the Taylor model, considering the milling process, the deformation strain (DS) was expressed as a pure shear strain component and a rotation component in Equation I:

$$DS = \begin{pmatrix} 0 & 0 & \frac{\varepsilon}{2} \\ 0 & 0 & 0 \\ \frac{\varepsilon}{2} & 0 & 0 \end{pmatrix} + \begin{pmatrix} 0 & 0 & \frac{\varepsilon}{2} \\ 0 & 0 & 0 \\ -\frac{\varepsilon}{2} & 0 & 0 \end{pmatrix} \qquad \text{(I)}$$

For milling machining conditions, a generalized deformation strain form was applied to the Taylor model. For each surface, three replicate EBSD samples were collected as the representative data, as shown in Table 5, which presents the average values of the SFs and TFs on each surface under different strain rates.

3.2. Ti-6Al-4V machining behavior

The results from the Taguchi experiment, the specific cutting energy analyses, are shown in Figures 7 and 8. The ANOVA results in Table 6 indicate the P-values for material, feed, and speed are <0.05, which shows a significant impact on specific cutting energy. The depth of cut and material interaction shows a significant effect on specific cutting energy. As previous research shows, the specific cutting energy has a significant difference among L-PBF Ti-6Al-4V, and the DED Ti-6Al-4V also proved that the AM processes significantly affect machining behavior.

From the interaction plot, the DED-specific cutting energy decreases as the depth of cut increases, which show that the thermal softening phenomenon dominates the machining response in DED parts, which has been observed in the machining of titanium with coarser grains[93-95].

3.3. Process-structure-property linkages testing and validation

For each data sample, features include 238 principal components, three residual stress, 9 SFs, 9 TFs, and three

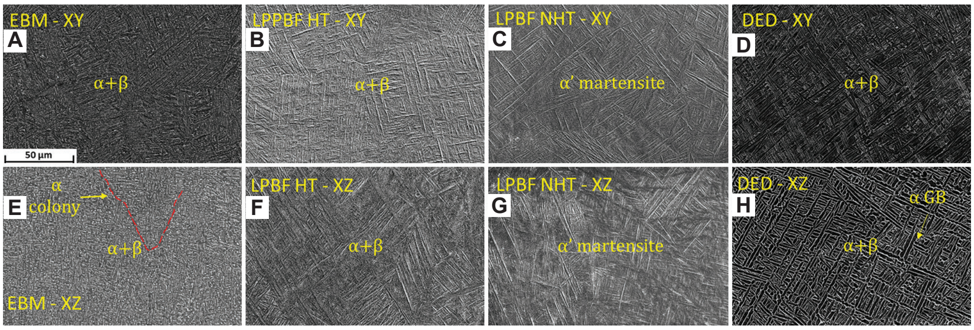

Figure 6. Representative SEM images of AM Ti-6Al-4V samples. (A) EB-PBF XY plane, (B) LPBFHT XY plane, (C) LPBFNHT XY plane, (D) DED XY plane, (E) EB-PBF XZ plane, (F) LPBFHT XZ plane, (G) LPBFNHT XZ plane, and (H) DED XZ plane.
Abbreviations: DED: Directed energy deposition; EB-PBF: Electron beam-powder bed fusion; SEM: Scanning electron microscopy.

Table 4. Crystal strain and residual stress

Material	ε22	ε23	E33	σ22 (MPa)	σ23 (MPa)	σ23 (MPa)
L-PBF XY HT	0.002297	−0.00062	−0.00246	273.343	−74.137	−292.612
L-PBF XZ HT	−0.00096	0.000059	−0.00189	−114.478	7.021	−224.865
L-PBF XY NHT	−0.00134	−0.00018	−0.00047	−159.341	−20.825	−55.981
L-PBF XZ NHT	−0.00179	0.000861	−0.00099	−213.367	102.459	−118.336
EB-PBF XY	−0.00411	0.000716	0.000364	−488.495	85.204	43.275
EB-PBF XZ	0.000951	−0.00105	−0.00083	113.169	−124.95	−99.31
DED XY	−0.0027	−0.00119	0.000658	−321.300	−141.610	78.264
DED XZ	0.00057	0.00364	−0.0055	67.830	433.160	−654.321

Abbreviations: DED: Directed energy deposition; EB-PBF: Electron beam powder bed fusion; LPBF: Laser powder bed fusion.

Table 5. Schmid factor and Taylor factor

Material	Basal (SD) (Schmid)	Prismatic (Schmid)	Pyramidal (Schmid)	ε = 0.5 (Taylor)	ε = 1 (Taylor)	ε = 1.5 (Taylor)
LPBF XY HT	0.2902	0.3928	0.1151	2.1288	3.6471	5.1626
LPBF XZ HT	0.2873	0.3982	0.1170	2.1139	3.7023	5.1586
LPBF XY NHT	0.3005	0.3825	0.1148	2.1923	3.7147	5.1753
LPBF XZ NHT	0.2795	0.4110	0.1194	2.1130	3.6349	5.0466
EB-PBF XY	0.2994	0.3963	0.1167	2.0285	3.5247	4.8956
EB-PBF XZ	0.2935	0.3851	0.1171	2.0923	3.5557	5.1285
DED XY	0.2761	0.3491	0.1118	2.1296	3.9260	5.5082
DED XZ	0.2800	0.4377	0.1334	2.0096	3.2098	4.5987

Abbreviations: DED: Directed energy deposition; EB-PBF: Electron beam powder bed fusion; LPBF: Laser powder bed fusion.

machining parameters. The prediction response is the specific cutting energy. Root mean square error (RMSE) is used as the evaluation metric to show the model's accuracy. The XGBoost model and linear regression model are applied in this study.

Five different feature combinations were designed: Machining parameters only (MP), machining parameters and EBSD features (MP + EBSD), machining parameters and residual stress (MP + XRD), machining parameters and SEM microstructure functions (MP + SEM), and all features (All). The rationale for this approach is to understand the individual and cumulative interaction effects of machining conditions, grain size, grain density, grain orientation, and residual stress on machining behavior.

The first condition in this study uses 14400 L-PBF data points as a training set, and the testing set is DED data. During the training process in the XGBoost model, the grid-search method was used for digging hyper-

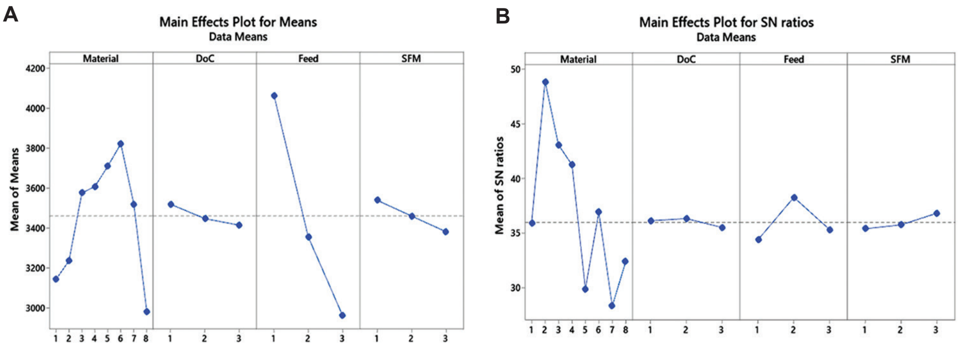

Figure 7. Main effects of the control parameters (A) and signal-to-noise ratio (B) indicate that AM-process induced microstructure greatly affects the resulting machining behavior.

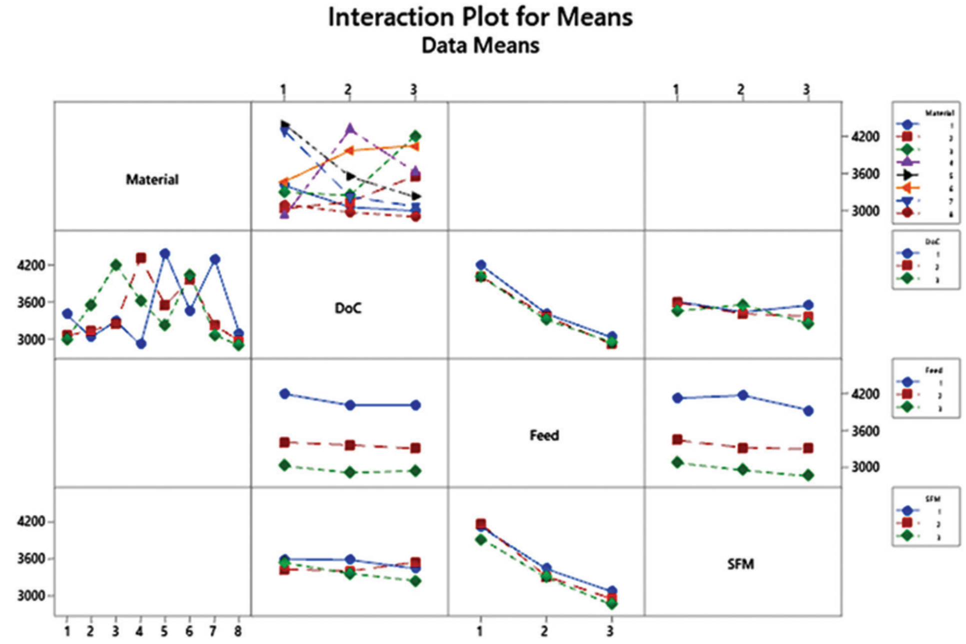

Figure 8. Mean and interaction effects of control factors on specific cutting energy.

Table 6. ANOVA results of the specific cutting energy consumed on the machining of Ti-6Al-4V

Variables	DoF	Sum of squares	Adj SS	Mean of square	*F*	*P*-value
Materials	7	7554173	7057373	1008196	34.27	0.000***
DoC	2	159581	33089	16545	0.56	0.574
Feed	2	17631530	4758353	2379176	80.86	0.000***
Speed	2	479466	369950	184975	6.29	0.004**
Material and DoC	14	4500947	4514152	322439	10.96	0.000***
DoC and feed	4	73329	50848	12712	0.43	0.785
DoC and speed	4	15547	14093	3523	0.12	0.975
Feed and speed	4	10677	10677	2669	0.09	0.985
Residual	44	1294626	1294626	29423	\	\
Total	83	31719875	\	\	\	\

*$P<0.05$, **$P<0.005$, ***$P<0.0005$.

Abbreviations: Adj SS: Adjusted sum of squares; DoC: Depth of cut; DoF: Degree of freedom.

parameters to minimize the error rate within the training set through cross-validation. After the training process, the testing set was applied to the best XGBoost estimator and linear model to validate the accuracy[90]. Figure 9A shows the RMSE results, where all features condition accuracy for the XGBoost model reaches 84.2%. The second condition in this study combined all L-PBF and DED datasets together, where randomly selected sets of training data (80%) and testing data (20%) were applied. It should be noted that when all features are used, the standard deviation for the XGBoost model is minimal (RMSE: 0.48 ± 0.026%).

To better understand the influence of machining parameters, microstructure functions, residual stress, and EBSD feature inputs on model accuracy; five different combinations of features were designed for training and testing. The first combination uses only machining parameters as the ML inputs (MP); the second combination considers machining parameters and EBSD features (MP + EBSD); the third combination considers machining parameters and residual stress (MP + XRD); the fourth design considers machining parameters and SEM microstructure functions (MP + SEM); and the last design integrates all the input features (All = MP + SEM + EBSD + XRD). The rationale for this approach is to understand the individual and interaction effects of machining conditions, grain size, grain density, grain orientation, and residual stress on machining behavior.

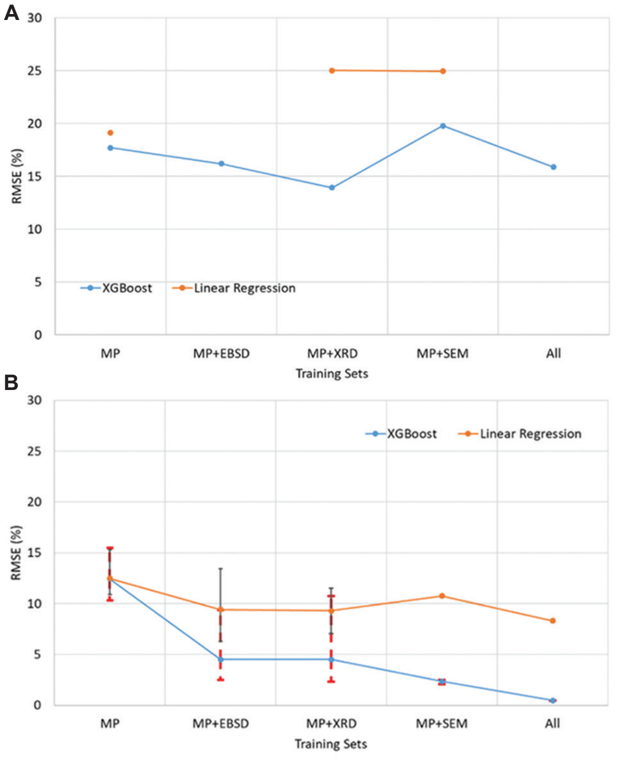

Figure 9. RMSE values in XGBoost and linear regressions for (A) DED Ti-6Al-4V prediction model and (B) PBF and DED Ti-6Al-4V prediction model.

Abbreviations: DED: Directed energy deposition; PBF: Powder bed fusion; RMSE: Root mean square error.

The first model run in this study is that all the EB-PBF and L-PBF datasets, in total, 14400 sample points were used as the training set, and the test set is the DED data. During the training process in the XGBoost model, the grid-search method was used for digging hyper-parameters, including the maximum depth of each subtree and the number of subtrees. The grid-search method is used to minimize the error rate within the training set by cross-validation and adjust the hyper-parameters. After the training process, the test set was applied to the best XGBoost estimator and linear model to validate the accuracy[66]. Figure 9A shows that the RMSE result, where all features used for the XGBoost ML model, is 84.2%.

The second model run in this study is that all EB-PBF, L-PBF, and DED datasets combined, where randomly selected sets of training data (80%) and test data (20%) were applied, as shown in Figure 9B. It should be noted that when all features are used, the standard deviation for the XGBoost ML model is minimal (RMSE: 0.48 ± 0.026%).

4. Discussion

In Figure 9A, there is no prediction in the linear regression model on MP+EBSD and ALL conditions. This shows the limitation of the classic linear regression model in that it cannot analyze the high dimensional, low sample size data. Predictors trained with only machining parameters achieve an 80 – 83% accuracy for both XGBoost and linear regression models, which demonstrates that the machining parameter combinations are significantly related to the specific cutting energy. However, in the linear regression model, when more features are added, the robust information acts as a detriment to the model prediction. This demonstrates that XGBoost is more favorable in building PSP linkages among metal AM materials. This can be observed in Figure 9A under MP + EBSD and MP + XRD conditions, as the model prediction accuracies increase to 83.8% and 86.1%.

However, when SEM microstructure information is added, the model prediction capability decreases massively to 80.2%; this phenomenon indicates that the testing features significantly differ from the training features[90-92]. For all SEM datasets, inverse-normal transformation data were generated from the CLDs for all these Ti-6Al-4V surfaces. For each microstructure data point, CLDs were fitted with the normal curve and calculated the mean value μ and variance σ^2, which show the grain size distribution. An ANOVA test was applied to analyze the microstructure difference based on Gaussian coefficients. Table 7 shows that materials selection, that is, AM processing condition, is statistically highly significant ($P = 0.000$), which proves that there is a significant difference among the microstructure information. This also shows that the LPBF_XZ samples have a significant difference compared with all other planes. In addition, the DED_XZ plane is the only surface showing a positive mean value, indicating that the average grain size in the DED sample is larger than the L-PBF material. The reason for the large negative mean value in the L-PBF sample could be due to the considerable number of tiny discontinuous β grains growing along the α or α' grain boundary. Therefore, the SEM features in the testing set could be outside of the training boundary. This leads to poor results in model prediction. To better understand the SEM microstructure among these materials, the normal distribution was used to represent CLDs, and the power functions were used to represent 2-point correlation functions. Tables 8 and 9 show a pairwise comparison analysis based on the materials' CLDs and 2-point representative coefficients.

The second condition could solve the above problem. In Figure 9B, when the model training from 80% of all data points was collected, the MP condition shows an 87% prediction accuracy, which decreased from 90% when only L-PBF materials were considered. However, when more feature information was added, the prediction results improved. When SFs and TFs were considered in the MP+EBSD condition, the XGBoost model's accuracy increased to 95.5% with a large variance, while the linear regression also increased to 90.5%. Through all five conditions, the XGBoost model proved superior to linear modeling. To analyze the importance of all features included in the new PSP linkages, feature importance analysis was employed to determine the feature impact. In the feature analysis, in addition to the machining parameters, all residual stresses play important roles in the XGBoost model training. This indicates that the near-surface residual stress heavily affects the specific cutting energy when machining AM Ti-6Al-4V samples. From this, SFs on basal slip systems, prismatic slip systems, and TFs form EBSD data measurement are shown in Figure 10.

The high-dimension SEM microstructure information significantly improves the PSP linkage accuracy. When combining all features, the high-dimension SEM data do not show a significant impact on the model. This may need future in-depth research to reveal the reason, obtain a better method to reduce dimension and extract additional microstructure data.

Table 7. ANOVA of SEM microstructure information among AM Ti-6AL-4V

Variables	Degree of freedom	Sum of squares	Adj SS	Mean of square	*F*	*P*-value
Materials	7	1328590541	1328590541	189798649	11.20	0.000
Number	89	1274031245	1274031245	14314958	0.84	0.839
Residual error	623	10555977115	10555977115	16943783	\	\
Total	719	13158598901	\	\	\	\

Abbreviations: Adj SS: Adjusted sum of squares; SEM: Scanning electron microscope.

Table 8. Comparison of *P*-values for AM Ti-6Al-4V CLDs coefficients

CLDs coefficient	EB-PBF XY	EB-PBF XZ	LPBFHT XY	LPBFHT XZ	LPBFNHT XY	LPBFNHT XZ	DED XY	DED XZ
EB-PBF XY	\	0.680	0.348	0.000	0.005	0.000	0.933	0.014
EB-PBF XZ	\	\	0.819	0.000	0.021	0.000	0.759	0.109
LPBFHT XY	\	\	\	0.000	0.019	0.000	0.508	0.004
LPBFHT XZ	\	\	\	\	0.172	0.264	0.000	0.000
LPBFNHT XY	\	\	\	\	\	0.038	0.010	0.001
LPBFNHT XZ	\	\	\	\	\	\	0.000	0.000
DED XY	\	\	\	\	\	\	\	0.096
DED XZ	\	\	\	\	\	\	\	\

Abbreviations: CLDs: Chord length distributions; DED: Directed energy deposition; EB-PBF: Electron beam powder bed fusion; LPBF: Laser powder bed fusion.

Table 9. Comparison of *P*-values for AM Ti-6Al-4V 2-point coefficients

2-Point coefficient	EB-PBF XY	EB-PBF XZ	LPBFHT XY	LPBFHT XZ	LPBFNHT XY	LPBFNHT XZ	DED XY	DED XZ
EB-PBF XY	\	0.021	0.046	0.001	0.063	0.005	0.025	0.078
EB-PBF XZ	\	\	0.591	0.019	0.170	0.005	0.088	0.378
LPBFHT XY	\	\	\	0.056	0.130	0.009	0.030	0.826
LPBFHT XZ	\	\	\	\	0.777	0.241	0.208	0.060
LPBFNHT XY	\	\	\	\	\	0.377	0.381	0.046
LPBFNHT XZ	\	\	\	\	\	\	0.020	0.013
DED XY	\	\	\	\	\	\	\	0.019
DED XZ	\	\	\	\	\	\	\	\

Abbreviations: DED: Directed energy deposition; EB-PBF: Electron beam powder bed fusion; LPBF: Laser powder bed fusion.

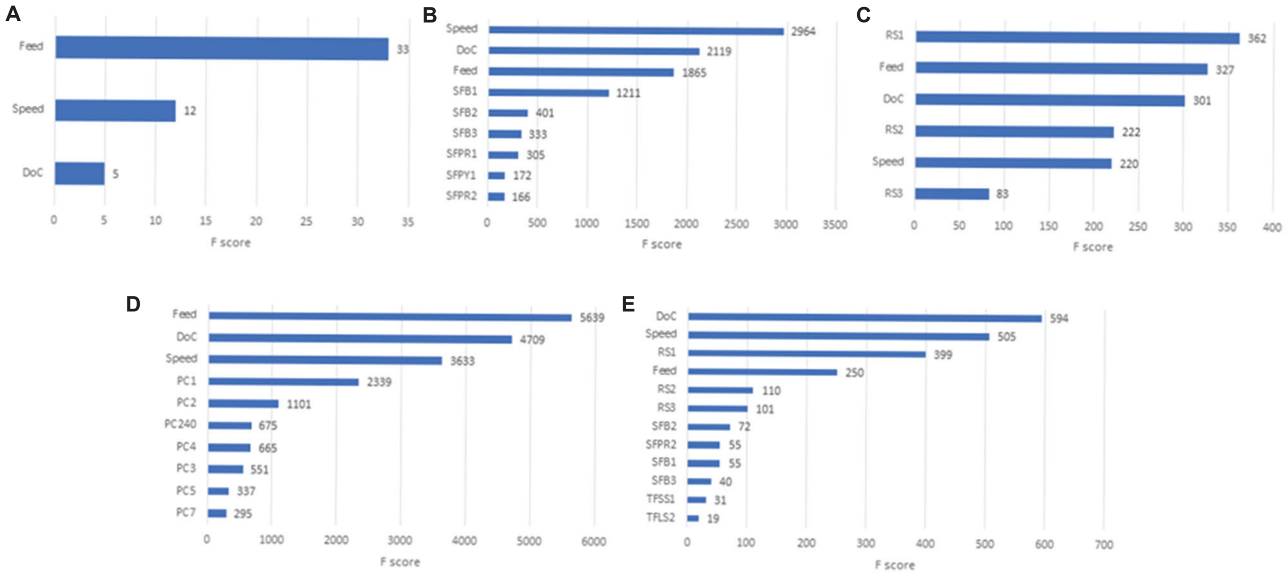

Figure 10. *F*-score for different training conditions: (A) MP, (B) MP + EBSD, (C) MP + XRD, (D) MP + SEM, and (E) all feature above.
Abbreviations: EBSD: Electron backscatter diffraction; MP: Machining parameters; SEM: Scanning electron microscope; XRD: X-ray diffraction.

5. Conclusion

A valid Ti-6Al-4V AM PSP linkage is presented herein. The PSP linkage focuses on connecting the AM Ti-6Al-4V structure information with post-processing machining behavior. This PSP linkage covers L-PBF, EB-PBF, and DED Ti-6AL-4V data, which expands the previous research version and overcomes the application limitation of the previous PBF Ti-6Al-4V PSP linkages.

To validate the Ti-6Al-4V PSP linkages established in the previous research based on the PBF dataset, wire feed plasma-based directed energy deposition Ti-6Al-4V materials were applied to evaluate the efficacy of the ML-based PSP linkage accuracy. Similar to a prior study[7], statistical methods were employed to define the properties of the material, and revised feature dimensionality reduction methods were applied to this study to save computational cost and time. Finally, the new PSP linkages, which include the most employed Ti-6Al-4V AM technologies (PBF and DED), were established through this study.

The key findings of this research are as follows:

(i) Established a validated statistical methodology to distinguish the microstructure difference among different AM processes fabricated Ti-6Al-4V alloys (L-PBF with/without heat treatment, EB-PBF, and DED).(ii) It was shown that due to inherently different grain morphologies across PBF and DED processes, the developed ML-based PSP linkages could be limited if one of the AM process categories (e.g., PBF) is used as a training set to predict the material response, that is, machining behavior of other AM process category (e.g., DED) in prediction accuracy.

(iii) On the other hand, cross-training datasets across AM process categories offer a wider training boundary and testing capability for AM Ti-6Al-4V materials with superior prediction accuracy. In addition, the workflow introduced in this research illustrates the robustness of ML-based PSP models with desired computational efficiency that is well suited for broader application in AM research (e.g., prediction of wear behavior and corrosion resistance)

(iv) Development of fully functional and computationally efficient PSP linkages of the AM Ti-6Al-4V to investigate metal AM materials properties and material response, that is, machining behavior. Previous work in this field is based on traditional PSP linkages that connect limited metal AM process parameters to minimal microstructure information, and few mechanical properties cannot predict material response as demonstrated in this study.

(v) The ML-based PSP linkage from this study was validated to accurately extract multiple structure information from metal AM parts under different manufacturing procedures and accurately predict the machining behavior during post-processing (>99% RMSE).

(vi) The workflow established in this research was shown to be robust across multiple AM surfaces (AM process, build orientation, and post-AM heat treatment) under a single framework time with extremely high prediction accuracy. For instance, over 1800 SVEs were involved in data analysis, and it was apparent that the workflow is robust and quite flexible to harness a variety of datasets, material systems, and material response, that is, machining behavior, in this research.

Although the PSP linkage demonstrated here showed high prediction accuracy (>99%), ongoing advancements in the AM industry will provide new AM technologies, and continuing to maintain these PSP linkage models will be essential. In the future, this PSP linkage can be expanded for other materials and can begin to consider additional machining responses such as tool wear behavior, surface finish, and tolerance analysis.

Acknowledgments

The authors would like to acknowledge the support from Norsk Titanium, Dr. Saurabh Basu, Kazi Shahed, and Dongrui Zeng.

Funding

Partial support for this study was provided by NIST AMTech (Grant no. 70NANB15H070), and the Manufacturing PA program.

Conflict of interest

The authors report no conflicts of interest.

Author contributions

Conceptualization: Xi Gong, Guha Manogharan

Formal analysis: Xi Gong, Guha Manogharan

Investigation: Xi Gong

Methodology: Xi Gong, Guha Manogharan

Resources: Guha Manogharan

Validation: Xi Gong

Visualization: All authors

Writing – original draft: Xi Gong, Guha Manogharan

Writing – review and editing: All authors

Ethics approval and consent to participate

Not applicable.

Consent for publication

Not applicable.

Availability of data

Data collected and analyzed in this work is available from the authors upon request.

References

1. Conner JW, Manogharan BP, Martof GP, *et al*., 2014, Making sense of 3-D printing: Creating a map of additive manufacturing products and services. *Addit Manuf*, 1: 64–76.

   https://doi.org/10.1016/j.addma.2014.08.005

2. Dutta B, (Sam) Froes FH, 2017, The additive manufacturing (AM) of titanium alloys. *Metal Powder Rep*, 72: 96–106.

   https://doi.org/10.1016/j.mprp.2016.12.062

3. Arthur NK, 2019, Laser based manufacturing of ti6al4v: A comparison of lens and selective laser melting. *Mater Sci Forum*, 950: 44–49.

   https://doi.org/10.4028/www.scientific.net/MSF.950.44

4. Frazier WE, 2014, Metal additive manufacturing: A review. *J Mater Eng Perform*, 23: 1917–1928.

   https://doi.org/10.1007/s11665-014-0958-z

5. Baufeld B, Brandl E, Van Der Biest O, 2011, Wire based additive layer manufacturing: Comparison of microstructure and mechanical properties of Ti-6Al-4V components fabricated by laser-beam deposition and shaped metal deposition. *J Mater Process Technol*, 211: 1146–1158.

https://doi.org/10.1016/j.jmatprotec.2011.01.018

6. Kruth JP, Leu MC, Nakagawa T, 1998, Progress in additive manufacturing and rapid prototyping. *Ann CIRP*, 47: 525–540.

   https://doi.org/10.1016/S0007-8506(07)63240-5

7. Gong X, Zeng D, Groeneveld-Meijer W, *et al*., 2022, Additive manufacturing: A machine learning model of process-structure-property linkages for machining behavior of Ti-6Al-4V. *Mater Sci Addit Manuf*, 1: 6.

   https://doi.org/10.18063/msam.v1i1.6

8. Liu Q, Wu H, Paul MJ, *et al*., 2020, Machine-learning assisted laser powder bed fusion process optimization for AlSi10Mg: New microstructure description indices and fracture mechanisms. *Acta Mater*, 201: 316–328.

   https://doi.org/10.1016/J.ACTAMAT.2020.10.010

9. Wang C, Chandra S, Huang S, *et al*., 2023, Unraveling process-microstructure-property correlations in powder-bed fusion additive manufacturing through information-rich surface features with deep learning. *J Mater Process Technol*, 311: 117804.

   https://doi.org/10.1016/J.JMATPROTEC.2022.117804

10. Goh GD, Huang X, Huang S, *et al*., 2023, Data imputation strategies for process optimization of laser powder bed fusion of Ti6Al4V using machine learning. *Mater Sci Addit Manuf*, 2: 50.

    https://doi.org/10.36922/msam.50

11. Mondal B, Mukherjee T, DebRoy T, 2022, Crack free metal printing using physics informed machine learning. *Acta Mater*, 226: 117612.

    https://doi.org/10.1016/J.ACTAMAT.2021.117612

12. Galati M, Iuliano L, 2018, A literature review of powder-based electron beam melting focusing on numerical simulations. *Addit Manuf*, 19: 1–20.

    https://doi.org/10.1016/J.ADDMA.2017.11.001

13. Biamino S, Penna A, Ackelid U, *et al*., 2011, Electron beam melting of Ti-48Al-2Cr-2Nb alloy: Microstructure and mechanical properties investigation. *Intermetallics (Barking)*, 19: 776–781.

    https://doi.org/10.1016/J.INTERMET.2010.11.017

14. Vayre B, Vignat F, Villeneuve F, 2012, Metallic additive manufacturing: State-of-the-art review and prospects. *Mech Ind*, 13: 89–96.

    https://doi.org/10.1051/MECA/2012003

15. Bhavar V, Kattire P, Patil V, *et al*., 2018, A review on powder bed fusion technology of metal additive manufacturing. In: Additive Manufacturing Handbook. United States: CRC Press. p. 251–253.

    https://doi.org/10.1201/9781315119106-15

16. Saboori A, Gallo D, Biamino S, *et al*., 2017, An overview of additive manufacturing of titanium components by directed energy deposition: Microstructure and mechanical properties. *Appl Sci* 7: 883.

    https://doi.org/10.3390/APP7090883

17. Bordin A, Sartori S, Bruschi S, *et al*., 2017, Experimental investigation on the feasibility of dry and cryogenic machining as sustainable strategies when turning Ti6Al4V produced by Additive Manufacturing. *J Clean Prod*, 142: 4142–4151.

    https://doi.org/10.1016/J.JCLEPRO.2016.09.209

18. Ding R, Guo ZX, Wilson A, 2002, Microstructural evolution of a Ti-6Al-4V alloy during thermomechanical processing. *Mater Sci Eng A*, 327: 233–245.

    https://doi.org/10.1016/S0921-5093(01)01531-3

19. Baufeld B, Van der Biest O, Gault R, 2010, Additive manufacturing of Ti–6Al–4V components by shaped metal deposition: Microstructure and mechanical properties. *Mater Des*, 31: S106–S111.

    https://doi.org/10.1016/J.MATDES.2009.11.032

20. Anwar S, Ahmed N, Abdo BM, *et al*., 2018, Electron beam melting of gamma titanium aluminide and investigating the effect of EBM layer orientation on milling performance. *Int J Adv Manuf Technol*, 96: 3093–3107.

    https://doi.org/10.1007/s00170-018-1802-7

21. Vayre B, Vignat F, Villeneuve F, 2013, Identification on some design key parameters for additive manufacturing: Application on electron beam melting. *Proc CIRP*, 7: 264–269.

    https://doi.org/10.1016/j.procir.2013.05.045

22. Murr LE, Johnson WL, 2017, 3D metal droplet printing development and advanced materials additive manufacturing. *J Mat Res Technol*, 6: 77–89.

    https://doi.org/10.1016/j.jmrt.2016.11.002

23. Antonysamy AA, Meyer J, Prangnell PB, 2013, Effect of build geometry on the β-grain structure and texture in additive manufacture of Ti6Al4V by selective electron beam melting. *Mater Charact*, 84: 153–168.

    https://doi.org/10.1016/J.MATCHAR.2013.07.012

24. Al-Bermani SS, Blackmore ML, Zhang W, *et al*., 2010, The origin of microstructural diversity, texture, and mechanical properties in electron beam melted Ti-6Al-4V. *Metall Mater Trans A Phys Metall Mater Sci*, 41: 3422–3434.

    https://doi.org/10.1007/s11661-010-0397-x

25. Murr LE, Gaytan SM, Medina F, *et al*., 2010, Characterization of Ti-6Al-4V open cellular foams fabricated by additive manufacturing using electron beam melting. *Mater Sci Eng A*, 527: 1861–1868.

https://doi.org/10.1016/j.msea.2009.11.015

26. Cheng B, Price S, Lydon J, *et al*., 2014, On process temperature in powder-bed electron beam additive manufacturing: Model development and validation. *J Manuf Sci Eng Trans ASME*, 136: 061019.

    https://doi.org/10.1115/1.4028484

27. King WE, Anderson AT, Ferencz RM, *et al*., 2015, Laser powder bed fusion additive manufacturing of metals; physics, computational, and materials challenges. *Appl Phys Rev*, 2: 041304.

    https://doi.org/10.1063/1.4937809

28. Loh LE, Chua CK, Yeong WY, *et al*., 2015, Numerical investigation and an effective modelling on the selective laser melting (SLM) process with aluminium alloy 6061. *Int J Heat Mass Transf*, 80: 288–300.

    https://doi.org/10.1016/J.IJHEATMASSTRANSFER.2014.09.014

29. Vilardell AM, Fredriksson G, Yadroitsev I, *et al*., 2019, Fracture mechanisms in the as-built and stress-relieved laser powder bed fusion Ti6Al4V ELI alloy. *Opt Laser Technol*, 109: 608–615.

    https://doi.org/10.1016/j.optlastec.2018.08.042

30. Heigel JC, Phan TQ, Fox JC, *et al*., 2018, Experimental investigation of residual stress and its impact on machining in hybrid additive/subtractive manufacturing. *Proc Manuf*, 26: 929–940.

    https://doi.org/10.1016/J.PROMFG.2018.07.120

31. Ming W, Chen J, An Q, *et al*., 2019, Dynamic mechanical properties and machinability characteristics of selective laser melted and forged Ti6Al4V. *J Mater Process Technol*, 271: 284–292.

    https://doi.org/10.1016/j.jmatprotec.2019.04.015

32. Vrancken B, Thijs L, Kruth JP, *et al*., 2012, Heat treatment of Ti6Al4V produced by selective laser melting: Microstructure and mechanical properties. *J Alloys Compd*, 541: 177–185.

    https://doi.org/10.1016/j.jallcom.2012.07.022

33. Ren S, Chen Y, Liu T, *et al*., 2019, Effect of build orientation on mechanical properties and microstructure of Ti-6Al-4V manufactured by selective laser melting. *Metall Mater Trans A Phys Metall Mater Sci*, 50: 4388–4409.

    https://doi.org/10.1007/s11661-019-05322-w

34. Thijs L, Vrancken B, Kruth JP, *et al*., 2013, The Influence of Process Parameters and Scanning Strategy on the Texture in Ti6Al4V Part Produced by Selective Laser Melting. In: Proceedings of the Advanced Materials, Processes and Applications for Additive Manufacturing, Vol. 1. p. 21–28.

35. Wanjara P, Brochu M, Jahazi M, 2007, Electron beam freeforming of stainless steel using solid wire feed. *Mater Des*, 28: 2278–2286.

    https://doi.org/10.1016/j.matdes.2006.08.008

36. Taminger K, Hafley R, 2003, Electron Beam Freeform Fabrication: A Rapid Metal Deposition Process. Proceedings of the 3rd Annual Automotive Composites Conference, 3, p. 9–10. Available from: https://ntrs.nasa.gov/citations/20040042496 [Last accessed on 2023 Aug 25].

37. Hofmann DC, Roberts S, Otis R, *et al*., 2014, Developing gradient metal alloys through radial deposition additive manufacturing. *Sci Rep*, 4: 5357.

    https://doi.org/10.1038/srep05357

38. Sun G, Zhou R, Lu J, *et al*., 2015, Mazumder, 'Evaluation of defect density, microstructure, residual stress, elastic modulus, hardness and strength of laser-deposited AISI 4340 steel. *Acta Mater*, 84: 172–189.

    https://doi.org/10.1016/j.actamat.2014.09.028

39. Zhang YN, Cao X, Wanjara P, *et al*., 2015, Tensile properties of laser additive manufactured Inconel 718 using filler wire. *J Mater Res*, 30: 2006–2020.

    https://doi.org/10.1557/jmr.2014.199

40. Derekar KS, 2018, A review of wire arc additive manufacturing and advances in wire arc additive manufacturing of aluminium. *Mater Sci Technol*, 34: 895–916.

    https://doi.org/10.1080/02670836.2018.1455012

41. McAndrew AR, Rosales MA, Colegrove PA, *et al*., 2018, Interpass rolling of Ti-6Al-4V wire + arc additively manufactured features for microstructural refinement. *Addit Manuf*, 21: 340–349.

    https://doi.org/10.1016/j.addma.2018.03.006

42. Guzanová A, Ižaríková G, Brezinová J, *et al*., 2017, Influence of build orientation, heat treatment, and laser power on the hardness of Ti6Al4V manufactured using the DMLS process. *Metals* (*Basel*), 7: 318.

    https://doi.org/10.3390/met7080318

43. Gorsse S, Hutchinson C, Gouné M, *et al*., 2017, Additive manufacturing of metals: a brief review of the characteristic microstructures and properties of steels, Ti-6Al-4V and high-entropy alloys. *Sci Technol Adv Mater*, 18: 584–610.

    https://doi.org/10.1080/14686996.2017.1361305

44. Neikter M, Åkerfeldt P, Pederson R, *et al*., 2018, Microstructural characterization and comparison of Ti-6Al-4V manufactured with different additive manufacturing processes. *Mater Charact*, 143: 68–75.

    https://doi.org/10.1016/j.matchar.2018.02.003

45. Li GC, Li J, Tian XJ, *et al*., 2017, Microstructure and properties of a novel titanium alloy Ti-6Al-2V-1.5Mo-0.5Zr-0.3Si manufactured by laser additive manufacturing. *Mater Sci Eng A*, 684: 233–238.

https://doi.org/10.1016/j.msea.2016.11.084

46. Lin JJ, Lv YH, Liu YX, 2016, Microstructural evolution and mechanical properties of Ti-6Al-4V wall deposited by pulsed plasma arc additive manufacturing. *Mater Des*, 102: 30–40.

    https://doi.org/10.1016/j.matdes.2016.04.018

47. Zhai Y, Galarraga H, Lados DA, 2016, Microstructure, static properties, and fatigue crack growth mechanisms in Ti-6Al-4V fabricated by additive manufacturing: LENS and EBM. *Eng Fail Anal*, 69: 3–14.

    https://doi.org/10.1016/j.engfailanal.2016.05.036

48. Liu S, Shin YC, 2019, Additive manufacturing of Ti6Al4V alloy : A review. *Mater Des*, 164: 107552.

    https://doi.org/10.1016/j.matdes.2018.107552

49. Bonaiti G, Parenti P, Annoni M, *et al.*, 2017, Micro-milling machinability of DED additive titanium Ti-6Al-4V. *Proc Manuf*, 10: 497–509.

    https://doi.org/10.1016/j.promfg.2017.07.104

50. Oyelola O, Crawforth P, M'Saoubi R, *et al.*, 2018, Machining of functionally graded Ti6Al4V/WC produced by directed energy deposition. *Addit Manuf*, 24: 20–29.

    https://doi.org/10.1016/j.addma.2018.09.007

51. Acharya R, Sharon JA, Staroselsky A, 2017, Prediction of microstructure in laser powder bed fusion process. *Acta Mater*, 124: 360–371.

    https://doi.org/10.1016/j.actamat.2016.11.018

52. Fergani O, Berto F, Welo T, *et al.*, 2017, Analytical modelling of residual stress in additive manufacturing. *Fatigue Fract Eng Mater Struct*, 40: 971–978.

    https://doi.org/10.1111/ffe.12560

53. Chen Q, Guillemot G, Gandin CA, *et al.*, 2017, Three-dimensional finite element thermomechanical modeling of additive manufacturing by selective laser melting for ceramic materials. *Addit Manuf*, 16: 124–137.

    https://doi.org/10.1016/j.addma.2017.02.005

54. Bostanabad R, Zhang Y, Li X, *et al.*, 2018, Computational microstructure characterization and reconstruction: Review of the state-of-the-art techniques. *Prog Mater Sci*, 95: 1–41.

    https://doi.org/10.1016/j.pmatsci.2018.01.005

55. Popova E, Rodgers TM, Gong X, *et al.*, 2017, Process-structure linkages using a data science approach: Application to simulated additive manufacturing data. *Integr Mater Manuf Innov*, 6: 54–68.

    https://doi.org/10.1007/s40192-017-0088-1

56. Pilania G, Wang C, Jiang X, *et al.*, 2013, Accelerating materials property predictions using machine learning. *Sci Rep*, 3: 1–6.

    https://doi.org/10.1038/srep02810

57. Ko H, Witherell P, Ndiaye NY, *et al.*, 2019, Machine learning based continuous knowledge engineering for additive manufacturing. In: IEEE International Conference on Automation Science and Engineering, p. 648–654.

    https://doi.org/10.1109/COASE.2019.8843316

58. Baumann FW, Sekulla A, Hassler M, *et al.*, 2018, Trends of machine learning in additive manufacturing. *Int J Rapid Manuf*, 7: 310.

    https://doi.org/10.1504/IJRAPIDM.2018.095788

59. Delli U, Chang S, 2018, Automated process monitoring in 3D printing using supervised machine learning. *Proc Manuf*, 26: 865–870.

    https://doi.org/10.1016/j.promfg.2018.07.111

60. Yao X, Moon SK, Bi G, 2017, A hybrid machine learning approach for additive manufacturing design feature recommendation. *Rapid Prototype J*, 23: 983–997.

61. ASME, 2019, ASME Y14.41-Digital Product Definition Data Practices: ASME Digital Standards. New York City: ASME, p. 128. Available: https://www.asme.org/codes-standards/find-codes-standards/y14-5-dimensioning-tolerancing [Last accessed on 2023 Sep 21].

62. Tilton M, Borjali A, Isaacson A, *et al.*, 2021, On structure and mechanics of biomimetic meta-biomaterials fabricated via metal additive manufacturing. *Mater Des*, 201: 109498.

    https://doi.org/10.1016/J.MATDES.2021.109498

63. Wang SQ, Liu JH, Chen DL, 2014, Effect of strain rate and temperature on strain hardening behavior of a dissimilar joint between Ti-6Al-4V and Ti17 alloys. *Mater Des*, 56: 174–184.

    https://doi.org/10.1016/j.matdes.2013.11.003

64. Rao PP, Tangri K, 1991, Yielding and work hardening behaviour of titanium aluminides at different temperatures. *Mater Sci Eng A*, 132: 49–59.

    https://doi.org/10.1016/0921-5093(91)90360-Y

65. Bystrzanowski S, Bartels A, Clemens H, *et al.*, 2008, Characteristics of the tensile flow behavior of Ti-46Al-9Nb sheet material-analysis of thermally activated processes of plastic deformation. *Intermetallics* (*Barking*), 16: 717–726.

    https://doi.org/10.1016/j.intermet.2008.02.008

66. Lu W, Li X, Lei Y, *et al.*, 2012, Study on the mechanical heterogeneity of electron beam welded thick TC4-DT joints. *Mater Sci Eng A*, 540: 135–141.

    https://doi.org/10.1016/j.msea.2012.01.117

67. Chiou ST, Tsai HL, Lee WS, 2007, Effects of strain rate and temperature on the deformation and fracture behaviour of titanium alloy. *Mater Trans*, 48: 2525–2533.

    https://doi.org/10.2320/MATERTRANS.MRA2007607

68. E. Committee of C, 2001, Aeronautical Materials, '中国航空材料手册 (China Aeronautical Materials Handbook). 2nd ed. Beijing: Standing Press China, p. 874.

69. Rafi HK, Karthik NV, Gong H, *et al.*, 2013, Microstructures and mechanical properties of Ti6Al4V parts fabricated by selective laser melting and electron beam melting. *J Mater Eng Perform*, 22: 3872–3883.

https://doi.org/10.1007/S11665-013-0658-0/FIGURES/14

70. Liu Q, Wang Y, Zheng H, *et al.*, 2016, Microstructure and mechanical properties of LMD-SLM hybrid forming Ti6Al4V alloy. *Mater Sci Eng A*, 660: 24–33.

https://doi.org/10.1016/j.msea.2016.02.069

71. Shi X, Ma S, Liu C, *et al.*, 2017, Selective laser melting-wire arc additive manufacturing hybrid fabrication of Ti-6Al-4V alloy: Microstructure and mechanical properties. *Mater Sci Eng A*, 684: 196–204.

https://doi.org/10.1016/j.msea.2016.12.065

72. Simonelli M, Tse YY, Tuck C, 2014, Effect of the build orientation on the mechanical properties and fracture modes of SLM Ti-6Al-4V. *Mater Sci Eng A*, 616: 1–11.

https://doi.org/10.1016/j.msea.2014.07.086

73. Tan X, Kok Y, Tan YJ, *et al.*, 2015, Graded microstructure and mechanical properties of additive manufactured Ti-6Al-4V via electron beam melting. *Acta Mater*, 97: 1–16.

https://doi.org/10.1016/j.actamat.2015.06.036

74. Murr LE, Esquivel EV, Quinones SA, *et al.*, 2009, Microstructures and mechanical properties of electron beam-rapid manufactured Ti-6Al-4V biomedical prototypes compared to wrought Ti-6Al-4V. *Mater Charact*, 60: 96–105.

https://doi.org/10.1016/j.matchar.2008.07.006

75. Wolff S, Lee T, Faierson E, *et al.*, 2016, Anisotropic properties of directed energy deposition (DED)-processed Ti-6Al-4V. *J Manuf Process*, 24: 397–405.

https://doi.org/10.1016/j.jmapro.2016.06.020

76. Qiu C, Adkins NJ, Attallah MM, 2013, Microstructure and tensile properties of selectively laser-melted and of HIPed laser-melted Ti-6Al-4V. *Mater Sci Eng A*, 578: 230–239.

https://doi.org/10.1016/j.msea.2013.04.099

77. Bordin A, Bruschi S, Ghiotti A, *et al.*, 2015, Analysis of tool wear in cryogenic machining of additive manufactured Ti6Al4V alloy. *Wear*, 328–329: 89–99.

https://doi.org/10.1016/j.wear.2015.01.030

78. Shunmugavel M, Polishetty A, Goldberg M, *et al.*, 2017, A comparative study of mechanical properties and machinability of wrought and additive manufactured (selective laser melting) titanium alloy-Ti-6Al-4V. *Rapid Prototype J*, 23: 1051–1056.

https://doi.org/10.1108/RPJ-08-2015-0105

79. Polishetty A, Shunmugavel M, Goldberg M, *et al.*, 2017, Cutting force and surface finish analysis of machining additive manufactured titanium alloy Ti-6Al-4V. *Proc Manuf*, 7: 284–289.

https://doi.org/10.1016/j.promfg.2016.12.071

80. Wu X, Jiang P, Chen L, *et al.*, 2014, Extraordinary strain hardening by gradient structure. *Proc Natl Acad Sci U S A*, 111: 7197–7201.

https://doi.org/10.1073/pnas.1324069111

81. Jiao Y, Stillinger FH, Torquato S, 2007, Modeling heterogeneous materials via two-point correlation functions: Basic principles. *Phys Rev E Stat Nonlin Soft Matter Phys*, 76: 1–15.

https://doi.org/10.1103/PhysRevE.76.031110

82. Berryman JG, Blair SC, 1986, Use of digital image analysis to estimate fluid permeability of porous materials: Application of two-point correlation functions. *J Appl Phys*, 60: 1930–1938.

https://doi.org/10.1063/1.337245

83. Corson PB, 1974, Correlation functions for predicting properties of heterogeneous materials. I. Experimental measurement of spatial correlation functions in multiphase solids. *J Appl Phys*, 45: 3159–3164.

https://doi.org/10.1063/1.1663741

84. Turner DM, Niezgoda SR, Kalidindi SR, 2016, Efficient computation of the angularly resolved chord length distributions and lineal path functions in large microstructure datasets. *Model Simul Mat Sci Eng*, 24: 075002.

https://doi.org/10.1088/0965-0393/24/7/075002

85. Fitzpatrick ME, Fry AT, Holdway P, *et al.*, 2005, Determination of residual stresses by X-ray diffraction-issue 2. In: A National Measurement Good Practice Guide. United Kingdom: National Physical Laboratory.

https://doi.org/10.1063/1.3525214

86. Luo Q, Yang S, 2017, Uncertainty of the X-ray diffraction (XRD) $\sin^2 \Psi$ technique in measuring residual stresses of physical vapor deposition (PVD) hard coatings. *Coatings*, 7: 128.

https://doi.org/10.3390/coatings7080128

87. Priddy MW, Paulson NH, Kalidindi SR, *et al.*, 2017, Strategies for rapid parametric assessment of microstructure-sensitive fatigue for HCP polycrystals. *Int J Fatigue*, 104: 231–242.

https://doi.org/10.1016/j.ijfatigue.2017.07.015

88. Bieler TR, Semiatin SL, 2002, The origins of heterogeneous deformation during primary hot working of Ti-6Al-4V. *Int J Plast*, 18: 1165–1189.

https://doi.org/10.1016/S0749-6419(01)00057-2

89. Hémery S, Villechaise P, 2018, Investigation of size effects in

slip strength of titanium alloys: α Nodule size dependence of the critical resolved shear stress. *Metall Mater Trans A Phys Metall Mater Sci*, 49: 4394–4397.

https://doi.org/10.1007/s11661-018-4678-0

90. Gong G, 1986, Cross-validation, the jack knife, and the bootstrap: Excess error estimation in forward logistic regression. *J Am Stat Assoc*, 81: 108–113.

    https://doi.org/10.1080/01621459.1986.10478245

91. Chen T, Guestrin C, 2016, XGBoost: A Scalable Tree Boosting System. KDD ’16, August 13-17, San Francisco, CA, USA, 2016.

92. Sundararaghavan V, Zabaras N, 2005, Classification and reconstruction of three-dimensional microstructures using support vector machines. *Comput Mater Sci*, 32: 223–239.

    https://doi.org/10.1016/j.commatsci.2004.07.004

93. Sun J, Guo YB, 2009, Material flow stress and failure in multiscale machining titanium alloy Ti-6Al-4V. Int J Adv Manuf Technol, 41: 651–659.

    https://doi.org/10.1007/s00170-008-1521-6

94. Ginting A, Nouari M, 2009, Surface integrity of dry machined titanium alloys. Int J Mach Tools Manuf, 49: 325–332.

    https://doi.org/10.1016/j.ijmachtools.2008.10.011

95. Pramanik A, 2014, Problems and solutions in machining of titanium alloys. Int J Adv Manuf Technol, 70: 919–928.

    https://doi.org/10.1007/s00170-013-5326-x

ACCSCIENCE PUBLISHING

Materials Science in Additive Manufacturing

ORIGINAL RESEARCH ARTICLE

3D-printed triaxial nozzles fabricated by stereolithography to prevent backflow in soft matter biofabrication

Hamed I. Albalawi[1,2,3,4], **Dana M. Alhattab**[1,2,3], **Aris P. Konstantinidis**[1,2,3,4], **Khadija B. Shirazi**[1,2,3,4], **Yousef Altayeb**[1], **and Charlotte A. E. Hauser**[1,2,3,4]*

[1]Laboratory for Nanomedicine, Bioengineering Program, Division of Biological and Environmental Science and Engineering (BESE), King Abdullah University of Science and Technology (KAUST), 23955-6900, Thuwal, Saudi Arabia

[2]Computational Bioscience Research Center (CBRC), King Abdullah University of Science and Technology (KAUST), 23955-6900, Thuwal, Saudi Arabia

[3]KAUST Smart Health Initiative (KSHI), King Abdullah University of Science and Technology (KAUST), 23955-6900, Thuwal, Saudi Arabia

[4]Red Sea Research Center (RSRC), King Abdullah University of Science and Technology (KAUST), 23955-6900, Thuwal, Saudi Arabia

Abstract

Three-dimensional (3D) bioprinting has a significant influence on tissue engineering by virtue of its capacity to produce complicated structures with complex geometries that are challenging to recreate using conventional manufacturing methods. However, the nozzle design and fabrication remain a limitation within extrusion-based 3D bioprinting, restricting and compromising the overall potential of this technology. The proposed nozzle design combines three Luer-Lok compatible inlets and an outlet within the printed body, eliminating manual assembly and enhancing fabrication consistency and quality. Furthermore, a finite element analysis of the fluid flow in the nozzle demonstrated the effectiveness of the nozzle to minimize backflow, in comparison with a traditional nozzle design. The tetrameric IIZK (Ac-Ile-Ile-Cha-Lys-NH_2) and IIFK (Ac-Ile-Ile-Phe-Lys-NH_2) peptide bioinks were used to 3D-print a variety of 3D scaffolds of varying complexity, with good resolution and gel continuity. Our work successfully demonstrated the fabrication of a novel design and its potential, and by means of 3D bioprinting, we assessed the biocompatibility and cell viability of the cell-laden constructs. This study highlights the capability of the novel design, which aids the field of tissue engineering, allowing 3D extrusion-based bioprinting to be utilized in the production of cell-incorporated constructions or scaffolds.

Keywords: 3D Bioprinting; 3D-Printed nozzles; Extrusion-based 3D printing; Backflow prevention; Disposable nozzles; Stereolithography

***Corresponding author:**
Charlotte A. E. Hauser
(charlotte.hauser@kaust.edu.sa)

Citation: Albalawi HI, Alhattab DM, Konstantinidis AP, *et al.*, 2023, 3D-printed triaxial nozzles fabricated by stereolithography to prevent backflow in soft matter biofabrication. *Mater Sci Add Manuf*, 2(3): 1786. https://doi.org/10.36922/msam.1786

Received: September 10, 2023

Accepted: September 24, 2023

1. Introduction

Additive manufacturing (AM), also widely known as three-dimensional (3D) printing, allows for the creation of 3D objects in a layer-by-layer fashion from digital computer-aided design (CAD) files. Fused deposition modeling, stereolithography (SLA), digital light processing, and selective laser sintering are the several types of 3D printing technologies[1,2]. These technologies were first employed for product design and development and fast prototyping as they exhibit significantly decrease in lead time and cost; in recent years, their applications have been broadened to high-value production and especially manufacturing. Numerous AM technologies have been created, enabling the use of a variety of materials for diverse sectors, including improved ceramics, composites, plastics, and metals[3]. AM technologies play an increasingly significant role in the biomedical industry, evidenced by the growing trend of AM application in the field of medicine and dentistry[4].

The selection of 3D printing materials is an important aspect for consideration because they have an immediate impact on the characteristics, appearance, and functionality of the finished product. A wide variety of materials have evolved with the quick development of 3D printing technology, each with distinctive properties and advantages. Polymeric materials are by far the most frequently used class of materials for 3D printing due to their ease of processing and low cost[5]. The development of 3D-printed polymeric materials is fueling this industry's expansion[6]. By using 3D extrusion printing, various polymer types, such as thermoplastics, thermosets, elastomers, and hydrogels, may be treated[5,7].

Moreover, an attractive feature of hydrophilic chains that swell in an aqueous environment to generate hydrogels is their polymeric 3D network. High water content, shape change, multi-stimuli responsiveness, and biocompatibility are some of their numerous material qualities and capabilities[8]. These materials are especially appealing for a wide range of uses, including soft actuators and sensors, as well as biological[9] and energy applications. As one of the most extensively studied polymeric materials for 3D printing applications, hydrogels are a result of the fast growth of AM in tissue engineering[10].

Hydrogels, due to their dynamic character of physical associations between monomers, are created by non-covalent interactions between their network-forming building blocks that make them suitable for 3D extrusion printing[11]. Such physical hydrogel systems exhibit shear-thinning behavior because the weak physical connection is quickly destroyed when pressure is applied. Due to their extremely mobile and ephemeral non-covalent network, hydrogels may also instantly return to their solid state if shear force is removed[12]. As biomaterials, hydrogels have been used for decades in 3D cell culture-based research applications. They act as scaffolds and can mimic various properties within tissues in the body, thus making them suitable candidates for tissue engineering[11-13].

In tissue engineering and regenerative medicine, 3D extrusion-based bioprinting is frequently utilized to produce cell-incorporated constructions or scaffolds[14]. Printability, or the capacity to create and sustain repeatable 3D scaffolds from bioink, is crucial in 3D extrusion-based bioprinting (a mixture of biomaterials and cells)[15]. Numerous variables or characteristics, such as those related to the bioink, printing method, and scaffold design, have been shown in the research to impact printability[14,15]. Soft matter bioinks, such as ultrashort self-assembling peptides, are desirable candidates to apply for 3D bioprinting due to their instantaneous gelation properties under physiological conditions, their biocompatibility, and nanofibrous topography resembling the natural extracellular matrix[16-19]. Our previous research explored the development of microfluidic syringe pump extrusion systems embedded with dual coaxial nozzles to accommodate the gelation nature of peptide bioink[20-22].

The capacity to create and maintain repeatable 3D scaffolds out of bioink using bioprinting technology is known as printability. The scaffolds' structure, which in turn impacts their mechanical and biological qualities, depends on their printability. The extrusion-based bioprinting approach can be used to create objects with live cells integrated into them. The high water content and cell-friendly environment of hydrogels make them ideal for this function. Hydrogels can be chemically or physically cross-linked to enable the production of a 3D-bioprinted structure.

Extrusion-based 3D bioprinting and customized 3D printed parts have been explored with respect to the construction of tissue scaffolds with distinctive characteristics. Khan *et al.* combined vat photopolymerization and extrusion-based 3D bioprinting to create a complex human-like ear structure. Furthermore, Abdelrahman *et al.* incorporated a hybrid 3D bioprinting and vat photopolymerization approach using dopaminergic neurons to model Parkinson's disease[23].

Hydrogel crosslinking may not happen instantaneously as the hydrogel may flow or spread, significantly deviating from the intended design. Moreover, hydrogels are challenging to print with, and printed scaffolds can even fall apart and fail to create a 3D structure. The issue of printability is crucial because the mechanical and biological qualities, such as mechanical strength and cell functions, of a printed scaffold might vary from an ideal design[24-26].

Over-extrusion- or under-extrusion-related flaws, including blobs or holes, are typical quality defects in such systems. A further extrusion failure known as annular backflow happens when the molten material can flow back up the annular zone between the filament and the liquefier wall, escape the heated area, and cool below its solid/fluid transition temperature. It is certain that these issues are a result of the interaction between the soft material/biomaterial's rheological qualities and the extrusion process parameters[27].

To prevent ink from one channel from flowing upstream into a nearby channel that houses a different ink, pressure-driven extrusion necessitates careful adjustment of the ink rheology, nozzle geometry, and printing pressure. In the event of backflow, the incorrect voxel composition is extruded right away after switching. Even the potential of a good biomaterial for 3D printing is compromised by this phenomenon. Therefore, additional fundamental studies are required for further comprehension of the underlying mechanisms and formulation of the best strategies to stop them, particularly backflow prevention. Skylar-Scott *et al.* made Y-junction nozzles and examined the ink flows in real-time[28]. With a symmetric single nozzle that alternates between two materials, the researchers essentially printed a two-material design. However, there has not been much progress made in terms of nozzle innovation and printing settings to prevent backflow, which underscores the importance of our work[28].

The nozzle design and fabrication method proposed are the key components of the novelty of this work. Conventionally, there is a distinction between the inlets, outlets, and their assembly separately from the nozzle setup, whereas in our work, the three inlets and outlets are integrated within the nozzle, eliminating the necessity of manual assembly using the connectors. This would otherwise result in the connectors being fragile, thus increasing the occurrence of issues including leaking, which compromise the printing capability. In addition, we modified the interior design of the inlet with backflow prevention features to remedy potential clogging problems. The nozzle design also incorporates an additional cell inlet, which enables cell extrusion right before the hydrogel extrusion from the nozzle outlet. This ensures better cell distribution within the extruded material. All of which ultimately improve the utilization and overall experience of 3D bioprinting in terms of user-friendliness, practicality, accessibility, and versatility in accommodating a wide range of materials.

2. Materials and methods

Using CAD design and SLA 3D printing, we designed and 3D-printed multiple nozzles that meet our bioink requirements. The newly designed nozzle was compatible with Luer-Lok, making it easy to print using our microfluidic syringe pump-based extrusion system with peptide and live cells. We conducted 3D bioprinting using the 3D-printed nozzles to evaluate gelation continuity, printability, biocompatibility, and shape fidelity. This section focuses on the methods applied to design, fabricate, and evaluate the 3D-printed nozzle for cellular 3D bioprinting with peptide bioinks.

2.1. Designing of the nozzle

The nozzles were designed using Siemens NX CAD software with millimeter measurements. Initially, the channels were designed, followed by the outer case of the nozzle. The channel design consists of three inlets and one outlet, as shown in Figure 1. The peptide and phosphate-buffered saline (PBS) channels incorporate features to prevent backflow, as illustrated in Figure 1. This design aims to delay any backflow that may occur at the mixing region where the two liquids (peptide and PBS) meet. The length of the mixing region, which met the requirements of our peptide hydrogels for 3D bioprinting, was derived from previous studies[29]. After mixing, the design focuses on maintaining a 90° angle for smooth flow. The inlet for cells was designed to extrude cells after the peptide and the PBS had mixed but before the materials had been extruded out of the nozzle outlet. Finally, the outer case of the nozzle was designed around the channels with a Luer-Lok design to ensure compatibility[20,21,30].

2.2. 3D Printing nozzle using vat photopolymerization

The nozzles were 3D-printed using FormLabs 3B 3D printer in the recommended settings of the white and clear polymer resin. It is important to note that the nozzle during the slicing must be placed vertically for the print plate to ensure the printability of the inner channels, as illustrated in Figure S1. Post-printing, the 3D-printed nozzles were washed with isopropanol for 30 min and then cured at 40°C for 65 min using the FormLabs Washer and Cure post-processing devices.

2.3. Finite element analysis of fluid flow in nozzle

A finite element analysis for the fluid flow in the nozzle was performed using the COMSOL Multiphysics software.

A 2D DXF domain, defined as the intersection of the 3D model with the frontal symmetry plane, was created from the nozzle 3D CAD model and divided into three different segments, one for each fluid (Figure S2A). The cells inlet was not included in the model, as the cells were extruded just before the outlet and after gelation had occurred, and the cell flow did not affect backflow or gel formation in any way. The first segment has the peptide solution properties (ρ = 1000 kg/m^3, μ = 0.1 Pa·s), the second segment has the PBS properties (ρ = 1000 kg/m^3, μ = 0.001 Pa·s), and the third segment has the hydrogel properties (ρ = 1000 kg/m^3,

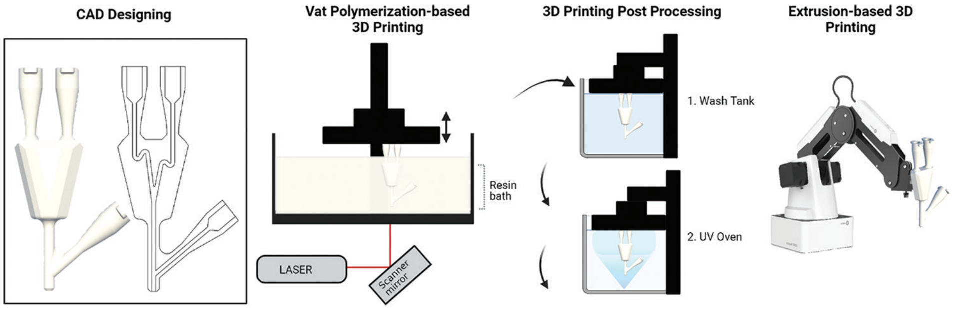

Figure 1. A schematic view of the nozzle fabrication process, including computer-aided design design, 3D printing of the nozzle using vat photopolymerization, post-3D printing processes, and extrusion-based 3D bioprinting using the fabricated nozzle.

μ = 1 Pa·s). The dynamic viscosity of the peptide solution and the hydrogel was obtained by rheology measurements performed in a previous study and was similar for both IIZK and IIFK peptides for the calculated shear rate applied in 3D bioprinting (γ = 29.7 rad/s)[30].

Two distinct 2D COMSOL laminar flow models were set up: one for backflow assessment and one for normal nozzle operation. PBS properties were used for the whole domain in the backflow assessment model; whereas the fluid properties were set to each area segment of the nozzle, as previously described, in the normal operation model (Figure S2B). The backflow assessment model had one inlet and two outlets, whereas the normal operation model had two inlets and one outlet. Both models were run with the inlets interchanged, to demonstrate potential differences between the two configurations. The boundary conditions were the velocity magnitude normal to the inlets and the pressure for the outlets. The input velocity for the inlets was determined by dividing the flow rate by the area of the inlet (0.005 m/s for the peptide solution, 0.00125 m/s for PBS). A flow rate of 60 μL/min was used for the backflow assessment model inlet, whereas the optimized flow rates of 60 μL/min and 15 μL/min for the peptide and PBS inlet, respectively, were used for the normal operation model. The outlet pressure was set to the atmospheric pressure (P = 101325 Pa). The mesh size was selected as medium (Figure S2C). The nozzle was evaluated based on the resulting flow profiles.

The same analysis was performed for an equivalent typical nozzle of the same dimensions, without the backflow prevention features, as demonstrated in Figures S2D-F. The two nozzle designs were compared based on the resulting flow profiles.

2.4. Parameter optimization for 3D bioprinting

For effective hydrogel bioink extrusion with the nozzle, parameter optimization experiments were performed using an in-house developed robotic arm 3D bioprinter, coupled with two microfluidic syringe pumps (one for each nozzle inlet). A version of the nozzle without the cell inlet was used. Two different bioinks were created – one using 10 mg/mL IIZK (Ac-Ile-Ile-Cha-Lys-NH_2) and one using 10 mg/mL IIFK (Ac-Ile-Ile-Phe-Lys-NH_2) peptide solutions – mixed with 5× PBS to accelerate crosslinking. A test to determine the optimal gelation parameters was conducted by running the pumps at a range of flow rates for peptide solution (45 – 60 μL/min) and PBS (15 – 25 μL/min) and observing the bioink thread extruded from the nozzle.

2.5. 3D Printing shape fidelity and resolution

To evaluate the shape fidelity achieved by the nozzle, cell-free constructs were printed with both peptide bioinks and observed for print resolution, dimensional accuracy, consistent formation of bioink thread, and layer deposition. Six-layer 15 × 15 × 1.2 mm^3 hollow cylinders, six-layer 20 × 20 × 1.2 mm^3 grids, and 50-layer 10 × 10 × 10 mm^3 hollow cylinders were printed, with the optimized flow rates of 60 μL/min for the peptide solution and 15 μL/min for 5× PBS.

2.6. Bioprinting of cell-laden constructs

2.6.1. Cell culture

Primary human bone marrow mesenchymal stem cells (hBM-MSCs) and bone marrow endothelial cells (BMECs) were used in the 3D bioprinting experiments. hBM-MSCs were provided as a gift from Prof. A. Awidi (Cell Therapy Center, The University of Jordan). BMECs (CRL-3421™) were purchased from ATCC.

Primary hBM-MSCs were expanded in culture, as described previously[31]. Briefly, the cells were cultured at a seeding density of 4 × 10^3 cells/cm^2 in T175 tissue culture flasks. When cultures reached 70 – 80% confluence, the cells were subcultured using 0.25% trypsin. Cells in passages 4 – 7 were used in the bioprinting experiments. The growth media for hBM-MSCs consisted of α-modified minimum essential medium (α-MEM) (GIBCO, ThermoFisher, USA) supplemented with 5% human platelet lysate (StemCell Technologies, USA), 2 mM L-glutamine, and 1% penicillin/streptomycin (GIBCO, ThermoFisher, USA).

BMECs were cultured at seeding of 2 × 10^4 cells/cm^2 in T175 tissue culture flasks and subcultured when cultures reached 80% confluence. The cells were maintained in complete growth media consisting of MCDB-131 media supplemented with 10% fetal bovine serum (FBS), 2 mM L-glutamine, and 1% penicillin/streptomycin (all from GIBCO, ThermoFisher, USA). Cells in passage 3 or 4 were used for bioprinting experiments.

2.6.2. Bioprinting

For bioprinting, the cells were mixed with 1× PBS solution to prepare cell suspensions with a final concentration of 10 × 10^6 cells/mL or 20 × 10^6 cells/mL, depending on whether hBM-MSCs or BMEC were used. Those cell concentrations were identified as the optimal density in terms of cell viability and cell-cell interaction after bioprinting. Subsequently, the microfluidic pumps of the robotic arm bioprinter were loaded with the cell solution. During the printing process, flow rates of 55 μL/min, 15 μL/min, and 15 μL/min were maintained for peptide solution, 5× PBS, and cells, respectively. Cuboid cell-laden structures with 10 mm edges and 2.6 mm height were printed. Following the printing process, the cell-laden constructs were incubated in the CO_2 incubator for 5 min, after which complete growth media were added. The printed cell-laden constructs were placed in standard conditions (37°C, 5% CO_2, and 95% relative humidity), and the media were changed every 3 days.

2.7. Assessment of cell-laden constructs

2.7.1. Cell viability assessment

The viability of 3D bioprinted cells was assessed using the LIVE/DEAD Viability/Cytotoxicity Kit (ThermoFisher, USA), in which calcein acetoxymethyl ester (Calcein-AM) is used to detect viable cells, and ethidium homodimer-I (EthD-I) is used to detect dead cells. The 3D cell-laden bioprinted constructs were washed twice with Dulbecco's phosphate-buffered saline (D-PBS). Then, a staining solution of 2 μM Calcein-AM and 4 μM of EthD-1 was added to the 3D cell-laden bioprinted constructs and incubated for 45 min in the CO_2 incubator. Subsequently, the staining solution was removed, and the 3D-bioprinted constructs were washed with 1× DPBS. The stained printed cell-laden constructs were imaged using an inverted immunofluorescent microscope (Evos, Invitrogen, ThermoFischer, USA). The assessment of cell viability was performed at days 3, 7, and 10 for hBM-MSCs and at days 5 and 10 for BMECs.

2.7.2. Cytoskeleton staining

The cell-laden constructs were first fixed with 4% formaldehyde solution for 30 min. Subsequently, the cells were permeabilized using a cold cytoskeleton buffer (consisting of 3 mM $MgCl_2$, 300 mM sucrose, and 0.5% Triton X-100 in PBS) for 5 min. Then, the permeabilized cells were incubated in a blocking buffer solution (comprising 5% FBS, 0.1% Tween-20, and 0.02% sodium azide in PBS) for 30 min at 37°C. To detect F-actin, rhodamine-phalloidin (1:300) was added to the cells for 1 h. Subsequently, the cells were treated with DAPI for 5 min to counterstain the nucleus. The cells were then observed and imaged using a laser scanning confocal microscope (Zeiss LSM 710 Inverted Confocal Microscope, Germany), and z-stack images of the samples were captured.

3. Results and discussion

This study highlights the benefits of using AM to produce customized 3D-printed nozzles for 3D bioprinting. Using resin-based 3D printing as a fabrication method for nozzles has several advantages, including precision and reproducibility. This new design for a 3D-printed nozzle addresses some of the limitations observed in previous designs[29], such as the complexities of the assembly process and the potential for backflow. Moreover, this nozzle design features a cell inlet that extrudes cells inside the nozzle, allowing for the introduction of cells into the bioink after gelation and before the final extrusion.

3.1. Design and fabrication of the nozzle

This nozzle was designed with three inlets and one outlet. The top two inlets are meant for the addition of the material to be mixed and gelled inside the nozzle, while the third inlet is used to extrude the cells just before the final extrusion of the materials (Figure 2A). This allows for the addition of cells to the gel once gelation occurs within the nozzle mixing region. In addition, the nozzle is compatible with the Luer-Lok for ease of use despite the larger diameter of the Luer-Lok compared to the desired interior diameter of our materials. To maintain optimal flow, the nozzle channels are kept at a consistent 1 mm inner diameter throughout the entire nozzle. A backflow prevention feature was also incorporated to prevent any backflow before the materials were mixed. The backflow issue was particularly prevalent in previous experiments we performed with other nozzles, where the different flow rates between peptide and PBS led to a difference in pressure. As the peptide flowed toward the PBS inlet, premature mixing occurred before reaching the intended mixing region, leading to clog formation and disrupting gel continuity.

After designing using NX CAD software, the 3D model was extruded as an STL file. The file was then uploaded to a

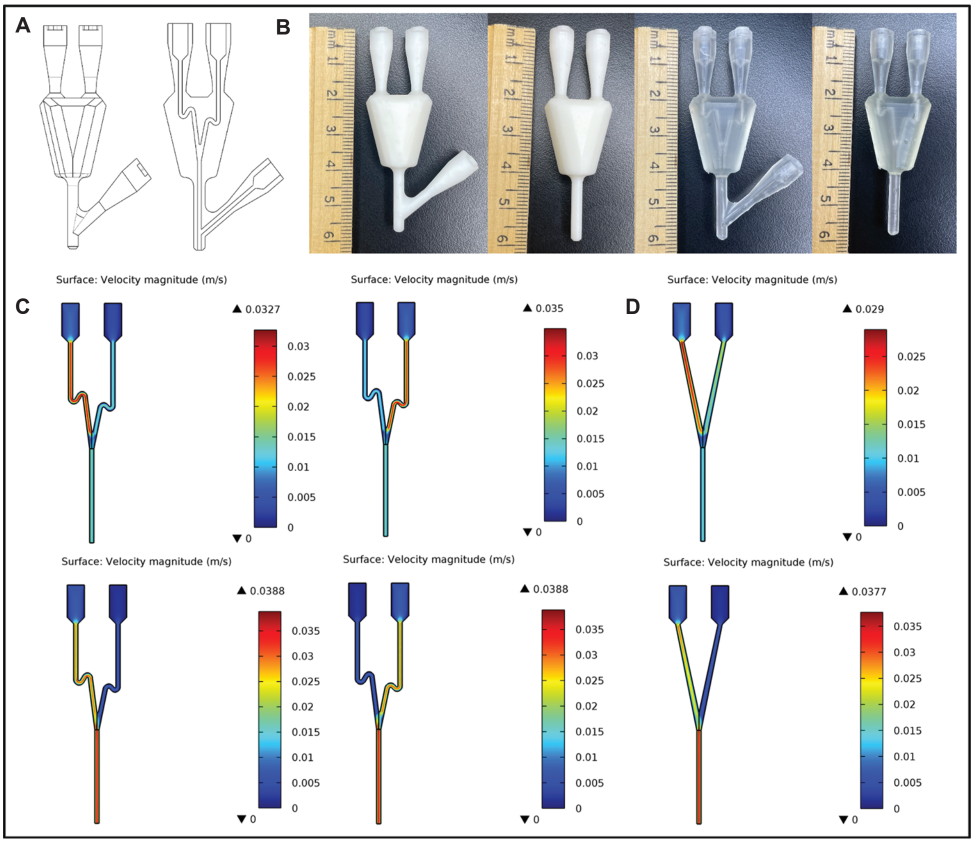

Figure 2. An illustration of the 3D CAD model of the nozzle (A), and visual representations of the 3D-printed nozzle using white and clear FormLabs materials (B). Backflow assessment (top) and normal operation (bottom) fluid velocity profiles for the nozzle (C) and typical nozzle (D) are presented.

PreForm slicing software for the FormLabs 3B 3D printer. Since the inner channel diameter was designed to be 1 mm, we experimented with different orientations when slicing the nozzle (Figure S1). Subsequently, the files were sent to the FormLabs 3B 3D printer for printing. On printing the nozzles, we discovered that the optimal slicing and printing orientation for these inner channels is vertical. Horizontal slicing did not result in printed channels inside the nozzle (Figure S1). Therefore, the selection of slicing orientation is crucial for successful nozzle printing using SLA 3D printing. Post-printing, the nozzles were washed and cured using the recommended settings on the FormLabs post-processing devices, specifically for the selected materials (white and clear resins in this case). The total time taken to print and cure a batch of five nozzles was estimated to be around 7h. The printed nozzles are shown in Figure 2B.

FormLabs reported a shrinkage rate in the order of 1% for both clear and white resins after post-curing using the recommended settings. The PreForm software also took the estimated shrinkage into account and scales structures up accordingly to ensure the final product was as close to the nominal dimensions as possible. Our printed nozzles did not show deviation from that estimate in their external dimensions. The inner diameters were checked using a Nikon SMZ25 Stereo Microscope. As shown in Figures S3A, B, and D, the channels were dimensionally accurate in both the inlet and outlet areas, consistent with the 1% shrinkage estimate. These deviations were not deemed to have a significant effect on the experimental results. However, in the case of the cell inlet, a reduction in diameter of around 30% could be observed (Figure S3B). The deviation can be attributed to the angled placement of the inlet, as opposed to the vertical placement of the other inlets and outlet. This reduction in diameter does not affect printability. Small localized defects could be observed in the outermost part of the outlet in some nozzles due to the support touchpoints (Figure S3C). These defects can be avoided by placing the touchpoints further away from the channel, or using smaller touchpoints.

3.2. Finite element analysis of fluid flow in nozzle

The velocity profiles for each inlet configuration in the nozzle and for the typical nozzle are demonstrated in Figures 2C and D.

No significant difference was observed in terms of backflow between the inlet configurations of the nozzle, showing that the inlets can be used interchangeably. In both configurations, a velocity magnitude in the range of 0.0150 m/s was calculated in the outlet segment, compared to a slightly lower magnitude in the range of 0.0125 m/s, which represents the backflow. A slightly higher maximum velocity magnitude was calculated for the inlet where the bend was placed lower (0.0350 m/s compared to 0.0327 m/s) due to the sharper bend and the longer vertical part of the segment. Conversely, for the typical nozzle, the backflow was significantly larger, with the velocity magnitude reaching values in the range of 0.0180 m/s, considerably higher than the 0.0110 m/s magnitude for the outlet. These results clearly indicate that the nozzle features are effective in minimizing backflow compared to a nozzle design without them.

In the normal operation model, the velocity profiles were comparable for both configurations of the nozzle. The maximum velocity (0.0388 m/s) was observed at the outlet segment, and the velocity magnitude for the peptide inlet was in the range of 0.0325 m/s for both configurations, which further attests to the interchangeability of the nozzle inlets for 3D bioprinting. For the typical nozzle, a similar profile was observed, with the exception of the velocity magnitude for the peptide inlet being lower, in the range of 0.0300 m/s. This difference is expected, given the absence of the bends in the inlet segments.

3.3. Parameter optimization for 3D printing

Gelation time for the formation of a stable bioink thread was found to be approximately 30 seconds for both peptides, significantly faster than previous nozzle designs[29]. In terms of gelation continuity, the best flow rate profile was found to be 60 µL/min and 15 µL/min for the peptide solution and 5× PBS, respectively, for both IIZK and IIFK peptides. The extruded hydrogel thread for the aforementioned flow rates displayed both continuity and stiffness, a prime indicator for printability. Lower flow rates resulted in less viscous, softer gel, at times with notable PBS accumulation, whereas higher flow rates resulted in clog formation and segmented hydrogel extrusion. Hence, the optimal flow rates were set according to these observations to be used for further printability assessments.

3.4. 3D Printing shape fidelity and resolution

Six-layer 15 × 10 × 1.2 mm^3 rings were 3D-printed with both peptide bioinks (Figure 3A). For the IIZK bioink, the construct exhibited excellent resolution and dimensional accuracy with a defined thin wall. No clumps or clogs were observed during printing, attesting to the nozzle's effectiveness in controlling gelation. In addition, the hydrogel deposition on each of the construct's layers was seamless with no loss of continuity. For the IIFK bioink, the resolution was acceptable, but the ring wall was less defined. The gelation was sometimes inconsistent, yielding some clumps that resulted in a less homogenous hydrogel. These observations should not be collectively construed as deterrents to printing with IIFK using the nozzle, as they are mostly attributed to the properties of the bioink, which has previously been proven to be more challenging to achieve consistent gelation with[29].

Fine grid squares of 20 × 20 mm^2 were 3D-printed with both peptide bioinks. Figure 3B shows the formation of fine threads formed in different layers. For IIZK, the resolution of the grid was very good, with clear and continuous

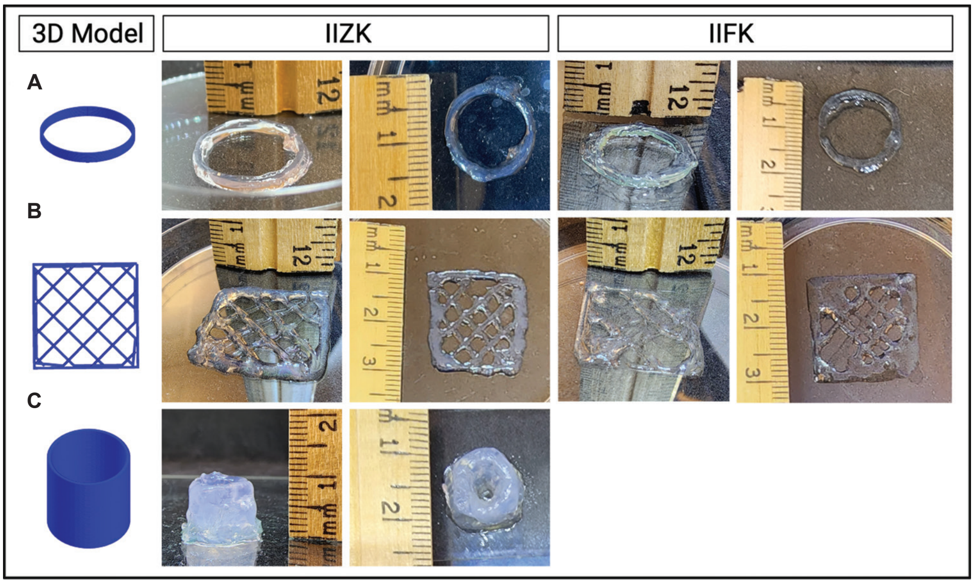

Figure 3. 3D-Printed peptide acellular scaffolds using the 3D-printed nozzle. These scaffolds demonstrated varying levels of shape complexity, including a hollow cylinder measuring 15 × 15 × 1.2 mm^3 (A), a grid measuring 20 × 20 mm^2 (B), and a tall hollow cylinder measuring 10 × 10 × 10 mm^3 (C).

lines. A few clumps were observed while printing the grid outline, without impact in the shape fidelity. For IIFK, the resolution was mediocre, with less defined segmented lines. The gelation was more inconsistent, with the presence of some clogs affecting thread continuity.

Furthermore, to assess the nozzle's capability to achieve continuous hydrogel deposition in taller constructs, a hollow cylinder of 10 × 10 × 10 mm^3 was printed using IIZK (Figure 3C). A continuous thread was formed during printing, suggesting the absence of clogs. The layers of the construct were seamlessly deposited, with no apparent sagging and loss of contact. According to these results, the nozzle shows promising potential to be used for hydrogel-based 3D bioprinting, since it enables, for the most part, continuous thread extrusion and forms 3D structures of varying dimensions, shapes, and complexity with good resolution for two distinct peptide bioinks.

3.5. 3D Bioprinting and biocompatibility studies

The viability of cells on 3D bioprinting is an essential parameter of a successful process in tissue engineering and regenerative medicine[32]. The availability of bioinks that support cellular growth and proliferation while allowing proper cell function is crucial for a successful bioprinting process[33]. In addition, the extrusion unit (nozzle) and its design are essential in having a high percentage of viable cells in the printed constructs[34]. This is partly due to the shear stress experienced by the cells during printing, significantly reducing the viability rate[33,35]. To assess the potential of our newly designed nozzle as an extrusion unit for 3D bioprinting, we assessed cell viability at different time points post-printing using live-dead staining. In addition, to demonstrate the feasibility of our newly designed nozzle, two different peptide bioinks were used in the 3D bioprinting process.

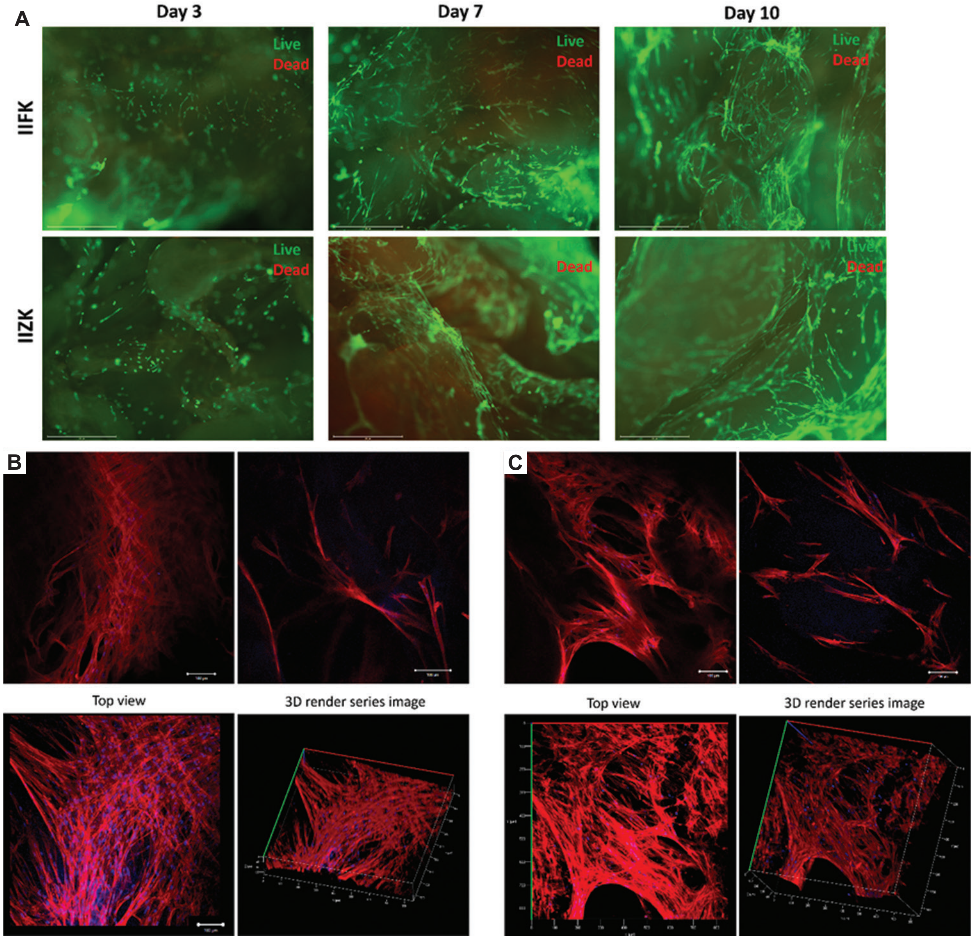

Figure 4. Biocompatibility assessment of human bone marrow mesenchymal stem cells (hBM-MSCs) after 3D bioprinting using our newly designed nozzle and IIFK and IIZK peptide bioinks. (A) Live/dead cell viability assessment post-printing using IIFK and IIZK peptide bioinks (days 3, 7, and 10 culture time). Cells were stained with Calcein-AM (green, live cells) and ethidium homodimer-1 (red, dead cells). Scale bar = 650 µm. (B and C) Cytoskeleton staining to detect morphology and 3D distribution of cells within printed constructs using IIFK peptide bioink (B) and IIZK peptide bioink (C). The lower panel presents the z-stack images, both top view and 3D render series images. F-actin was stained with phalloidin (red) and the nucleus with DAPI (blue). Scale bar = 100 µm.

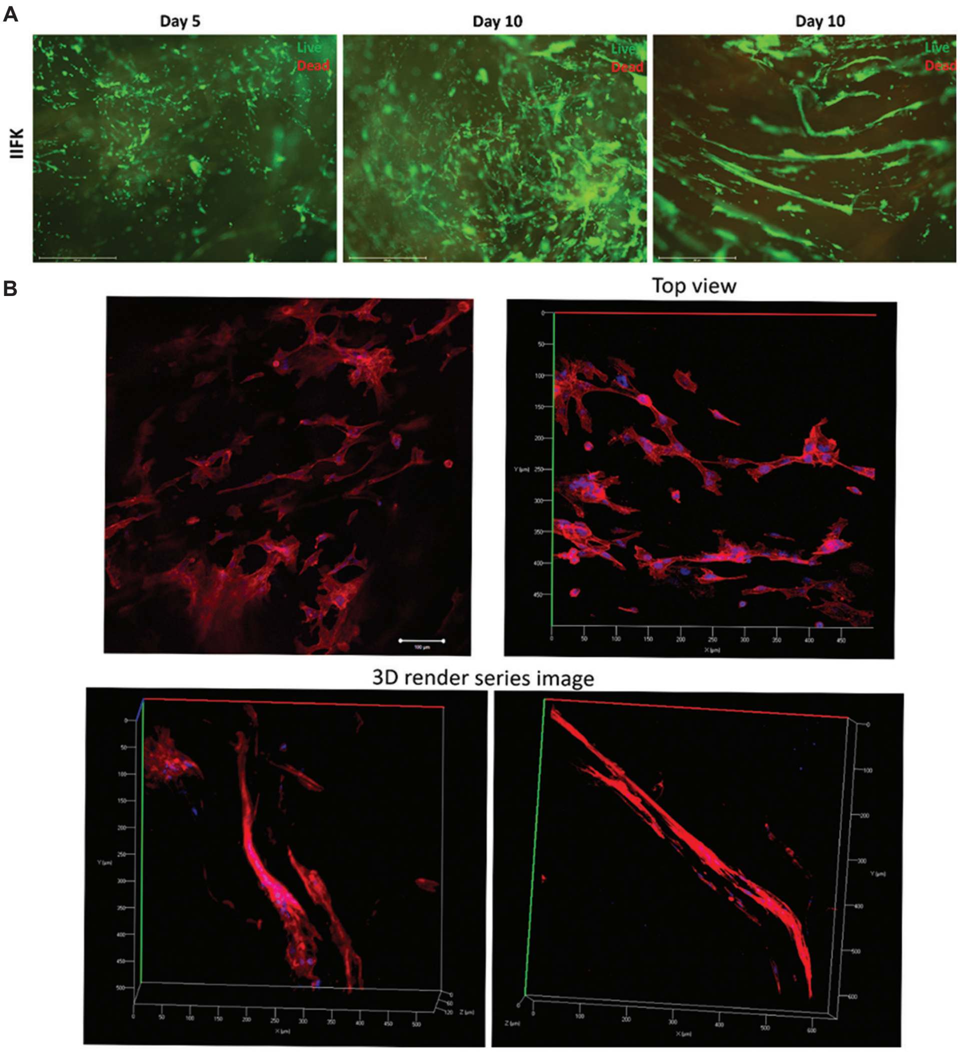

Figure 5. Biocompatibility assessment of human endothelial cells after 3D bioprinting using our newly designed nozzle with IIFK peptide bioink. (A) Live/dead cell viability assessment at days 5 and 10 post-printing. Cells were stained with Calcein-AM (green, live cells) and ethidium homodimer-1 (red, dead cells). Scale bar = 650 µm. (B) Cytoskeleton staining to detect morphology and 3D distribution of endothelial cells within printed constructs using IIFK peptide bioink. The z-stack images, both the top view and 3D render series images, show cell interconnections and cells' alignment into tube-like structures. F-actin was stained with phalloidin (red) and the nucleus with DAPI (blue). Scale bar = 100 µm.

Primary hBM-MSCs demonstrated a high cell viability rate post-printing at all measured time points up to 10 days of the observation period (Figure 4A). Furthermore, cell-laden constructs showed an increase in cell viability and density over days post-printing. The high cell viability rate and density indicate the biocompatibility of the peptide bioink and the suitability of the newly designed nozzle for bioprinting applications. The observed high cell viability rate was similar to our previous reports[36,37], further confirming the efficacy of the newly designed nozzle.

To evaluate the 3D distribution and morphology of cells within the printed cell-laden constructs, hBM-MSCs were 3D-bioprinted using IIZK and IIFK peptide bioink. Subsequently, the cell-laden constructs were stained for cytoskeleton, and z-stack 3D images were taken using confocal microscopy (Figure 4B and C). Cell distribution was evaluated at day 14 post-printing. The results indicated that hBM-MSCs retained their fibroblast-like morphology with well-defined actin fibers, and z-stack images demonstrated the 3D distribution of the cells throughout the printed structures. Cell elongation revealed the cytoplasmic extensions, cell-cell interaction, and cell-matrix interaction, indicating the high cytocompatibility of the peptide bioinks and the effectiveness of the newly designed nozzle in the bioprinting process.

To further demonstrate the effectiveness of our newly designed nozzle, 3D bioprinting of endothelial cells using

IIFK peptide bioink was performed. Endothelial cells and the vasculature are essential constituents of every tissue, and having a bioprinting system that maintains the viability and functionality of these cells is crucial for tissue engineering applications[38,39]. In this regard, cell viability was observed at days 5 and 10 post-printing using Live/Dead assay (Figure 5A). The results revealed a high percent of cell viability at all measured time points, indicating the peptide bioink's cytocompatibility and nozzle design's suitability toward more delicate cell types. Importantly, cytoskeleton staining of endothelial cell-laden constructs at day 12 post-printing revealed interesting results. Endothelial cells within the printed scaffold demonstrated morphological changes into elongated cells with cell-cell connections and interactions, indicating the establishment of cell differentiation and proliferation processes (Figure 5B). In addition, alignments of endothelial cells forming tube-like structures were found in different areas in the printed scaffolds (Figure 5B).

4. Conclusions

In this paper, an integrated 3D printing approach for the fabrication of 3D bioprinting nozzles for hydrogel bioink extrusion is proposed. The nozzle design integrates three Luer-Lok-compatible inlets and an outlet within the printed body, eliminating the need for manual assembly and improving the fabrication consistency and quality. Moreover, it incorporates backflow prevention features aimed at minimizing backflow at the mixing region, thus avoiding clogging caused by over-gelation. We also demonstrated its potential in 3D bioprinting applications by printing cell-laden constructs and proving biocompatibility and cell viability after 3D bioprinting.

Acknowledgments

The authors acknowledge the bioimaging and characterization core laboratories for confocal microscopy use.

Funding

This work was financially supported by King Abdullah University of Science and Technology under the KAUST-Smart Health Initiative (project number: REI/1/4938).

Conflict of interest

The authors declare that they have no conflicts of interest.

Author contributions

Conceptualization: Hamed I. Albalawi, Aris P. Konstantinidis, Dana M. Alhattab, Charlotte A. E. Hauser
Investigation: Hamed I. Albalawi, Dana M. Alhattab, Aris P. Konstantinidis, Yousef Altayeb
Methodology: Hamed I. Albalawi, Dana M. Alhattab, Aris P. Konstantinidis, Yousef Altayeb
Writing – original draft: Hamed I. Albalawi, Aris P. Konstantinidis, Dana M. Alhattab, Khadija B. Shirazi, Yousef Altayeb
Writing – review & editing: Dana M. Alhattab, KS, Charlotte A. E. Hauser

Ethics approval and consent to participate

Not applicable.

Consent for publication

Not applicable.

Availability of data

Raw data can be shared with the readers by contacting the corresponding author.

References

1. Kafle A, Luis E, Silwal R, *et al.*, 2021, 3D/4D printing of polymers: Fused deposition modelling (FDM), selective laser sintering (SLS), and stereolithography (SLA). *Polymers* (*Basel*), 13: 3101.

   https://doi.org/10.3390/polym13183101

2. Mirzaali MJ, Moosabeiki V, Rajaai SM, *et al.*, 2022, Additive manufacturing of biomaterials-design principles and their implementation. *Materials* (*Basel*), 15: 5457.

   https://doi.org/10.3390/ma15155457

3. Mehrpouya M, Dehghanghadikolaei A, Fotovvati B, *et al.*, 2019, The potential of additive manufacturing in the smart factory industrial 4.0: A review. *Appl Sci*, 9: 3865.

   https://doi.org/10.3390/app9183865

4. Prashar G, Vasudev H, Bhuddhi D, 2022, Additive manufacturing: Expanding 3D printing horizon in industry 4.0. *Int J Interact Des Manuf* (*IJIDeM*), 6:1–15.

   https://doi.org/10.1007/s12008-022-00956-4

5. Jiang Z, Diggle B, Tan ML, *et al.*, 2020, Extrusion 3D printing of polymeric materials with advanced properties. *Adv Sci* (*Weinh*), 7: 2001379.

   https://doi.org/10.1002/advs.202001379

6. Ligon SC, Liska R, Stampfl J, *et al.*, 2017, Polymers for 3D printing and customized additive manufacturing. *Chem Rev*, 117: 10212–10290.

   https://doi.org/10.1021/acs.chemrev.7b00074

7. Lin Q, Li L, Luo S, 2019, Asymmetric electrochemical catalysis. *Chemistry*, 25: 10033–10044.

   https://doi.org/10.1002/chem.201901284

8. Zhang YS, Khademhosseini A, 2017, Advances in

engineering hydrogels. *Science*, 356: eaaf3627.

https://doi.org/10.1126/science.aaf3627

9. Malda J, Visser J, Melchels FP, *et al.*, 2013, 25th anniversary article: Engineering hydrogels for biofabrication. *Adv Mater*, 25: 5011–5028.

   https://doi.org/10.1002/adma.201302042

10. Zhao F, Shi Y, Pan L, *et al.*, 2017, Multifunctional nanostructured conductive polymer gels: Synthesis, properties, and applications. *Acc Chem Res*, 50: 1734–1743.

    https://doi.org/10.1021/acs.accounts.7b00191

11. Ouyang L, Highley CB, Rodell CB, *et al.*, 2016, 3D printing of shear-thinning hyaluronic acid hydrogels with secondary cross-linking. *ACS Biomater Sci Eng*, 2: 1743–1751.

    https://doi.org/10.1021/acsbiomaterials.6b00158

12. Jungst T, Smolan W, Schacht K, *et al.*, 2016, Strategies and molecular design criteria for 3D printable hydrogels. *Chem Rev*, 116: 1496–1539.

    https://doi.org/10.1021/acs.chemrev.5b00303

13. Ouyang L, Highley CB, Sun W, *et al.*, 2017, A generalizable strategy for the 3D bioprinting of hydrogels from nonviscous photo-crosslinkable inks. *Adv Mater*, 29: 1604983.

    https://doi.org/10.1002/adma.201604983

14. Wang Y, Zhang S, Wang J, 2021, Photo-crosslinkable hydrogel and its biological applications. *Chin Chem Lett*, 32: 1603–1614.

    https://doi.org/10.1016/j.cclet.2020.11.073

15. Naghieh S, 2020, Extrusion Bioprinting of Hydrogel Scaffolds: Printability and Mechanical Behavior. Canada: University of Saskatchewan.

16. Hauser CA, Deng R, Mishra A, *et al.*, 2011, Natural tri- to hexapeptides self-assemble in water to amyloid beta-type fiber aggregates by unexpected alpha-helical intermediate structures. *Proc Natl Acad Sci U S A*, 108: 1361–1366.

    https://doi.org/10.1073/pnas.1014796108

17. Loo Y, Chan YS, Szczerbinska I, *et al.*, 2019, A chemically well-defined, self-assembling 3D substrate for long-term culture of human pluripotent stem cells. *ACS Appl Bio Mater*, 2: 1406–1412.

    https://doi.org/10.1021/acsabm.8b00686

18. Mishra A, Loo Y, Deng R, *et al.*, 2011, Ultrasmall natural peptides self-assemble to strong temperature-resistant helical fibers in scaffolds suitable for tissue engineering. *Nano Today*, 6: 232–239.

    https://doi.org/10.1016/j.nantod.2011.05.001

19. Wu EC, Zhang S, Hauser CA, 2012, Self-assembling peptides as cell-interactive scaffolds. *Adv Funct Mater*, 22: 456–468.

    https://doi.org/10.1002/adfm.201101905

20. Kahin K, Khan Z, Albagami M, *et al.*, 2019, Development of a Robotic 3D Bioprinting and Microfluidic Pumping System for Tissue and Organ Engineering. In: Proceedings of SPIE, Microfluidics, BioMEMS, and Medical Microsystems XVII, San Francisco, United States.

21. Khan Z, Kahin K, Rauf S, *et al.*, 2019, Optimization of a 3D bioprinting process using ultrashort peptide bioinks. *Int J Bioprinting*, 5: 173.

    https://doi.org/10.18063/ijb.v5i1.173

22. Khan Z, Kahin K, Hauser C, 2021, Time-dependent Pulsing of Microfluidic Pumps to Enhance 3D Bioprinting of Peptide Bioinks. In: Microfluidics, BioMEMS, and Medical Microsystems XIX, United States.

    https://doi.org/10.1117/12.2578830

23. Abdelrahman S, Alsanie WF, Khan ZN, *et al.*, 2022, A Parkinson's disease model composed of 3D bioprinted dopaminergic neurons within a biomimetic peptide scaffold. *Biofabrication*, 14: 044103.

    https://doi.org/10.1088/1758-5090/ac7eec

24. Domingos M, Intranuovo F, Russo T, *et al.*, 2013, The first systematic analysis of 3D rapid prototyped poly(ε-caprolactone) scaffolds manufactured through BioCell printing: The effect of pore size and geometry on compressive mechanical behaviour and *in vitro* hMSC viability. *Biofabrication*, 5: 045004.

    https://doi.org/10.1088/1758-5082/5/4/045004

25. Lee JW, Ahn G, Kim JY, *et al.*, 2010, Evaluating cell proliferation based on internal pore size and 3D scaffold architecture fabricated using solid freeform fabrication technology. *J Mater Sci Mater Med*, 21: 3195–3205.

    https://doi.org/10.1007/s10856-010-4173-7

26. Sobral JM, Caridade SG, Sousa RA, *et al.*, 2011, Three-dimensional plotted scaffolds with controlled pore size gradients: Effect of scaffold geometry on mechanical performance and cell seeding efficiency. *Acta Biomater*, 7: 1009–1018.

    https://doi.org/10.1016/j.actbio.2010.11.003

27. Schuller T, Fanzio P, Galindo-Rosales FJ, 2022, Analysis of the importance of shear-induced elastic stresses in material extrusion. *Addit Manuf*, 57: 102952.

    https://doi.org/10.1016/j.addma.2022.102952

28. Skylar-Scott MA, Mueller J, Visser CW, *et al.*, 2019, Voxelated soft matter via multimaterial multinozzle 3D printing. *Nature*, 575: 330–335.

    https://doi.org/10.1038/s41586-019-1736-8

29. Albalawi HI, Khan ZN, Rawas RH, *et al.*, 2023, 3D-printed disposable nozzles for cost-efficient extrusion-based 3D bioprinting. *Mater Sci Addit Manuf*, 2: 52.

    https://doi.org/10.36922/msam.52

30. Susapto HH, Alhattab D, Abdelrahman S, *et al.*, 2021, Ultrashort peptide bioinks support automated printing of large-scale constructs assuring long-term survival of printed tissue constructs. *Nano Lett*, 21: 2719–2729.

    https://doi.org/10.1021/acs.nanolett.0c04426

31. Alhattab D, Jamali F, Ali D, *et al.*, 2019, An insight into the whole transcriptome profile of four tissue-specific human mesenchymal stem cells. *Regen Med*, 14: 841–865.

    https://doi.org/10.2217/rme-2018-0137

32. Zhang Y, Liu Y, Xu Z, *et al.*, 2020, Nucleation-controlled growth of superior lead-free perovskite $Cs_3Bi_2I_9$ single-crystals for high-performance X-ray detection. *Nat Commun*, 11: 2304.

    https://doi.org/10.1038/s41467-020-16034-w

33. Gungor-Ozkerim PS, Inci I, Zhang YS, *et al.*, 2018, Bioinks for 3D bioprinting: An overview. *Biomater Sci*, 6: 915–946.

    https://doi.org/10.1039/c7bm00765e

34. Silva C, Cortés-Rodriguez CJ, Hazur J, *et al.*, 2020, Rational design of a triple-layered coaxial extruder system: *In silico* and *in vitro* evaluations directed toward optimizing cell viability. *Int J Bioprint*, 6: 282.

    https://doi.org/10.18063/ijb.v6i4.282

35. Shi J, Wu B, Li S, *et al.*, 2018, Shear stress analysis and its effects on cell viability and cell proliferation in drop-on-demand bioprinting. *Biomed Phys Eng Express*, 4: 045028.

    https://doi.org/10.1088/2057-1976/aac946

36. Alhattab DM, Khan Z, Alshehri S, *et al.*, 2023, 3D bioprinting of ultrashort self-assembling peptides to engineer scaffolds with different matrix stiffness for chondrogenesis. *Int J Bioprint*, 9: 719.

    https://doi.org/10.18063/ijb.719

37. Rauf S, Susapto HH, Kahin K, *et al.*, 2021, Self-assembling tetrameric peptides allow *in situ* 3D bioprinting under physiological conditions. *J Mater Chem B*, 9: 1069–1081.

    https://doi.org/10.1039/d0tb02424d

38. Daly AC, Prendergast ME, Hughes AJ, *et al.*, 2021, Bioprinting for the biologist. *Cell*, 184: 18–32.

    https://doi.org/10.1016/j.cell.2020.12.002

39. Sohn S, Van Buskirk M, Buckenmeyer MJ, *et al.*, 2020, Whole organ engineering: Approaches, challenges, and future directions. *Appl Sci*, 10: 4277.

    https://doi.org/10.3390/app10124277

ACCSCIENCE PUBLISHING

Materials Science in Additive Manufacturing

ORIGINAL RESEARCH ARTICLE

Maraging steel powder alteration caused by laser powder bed fusion printing process

Othmane Rayan[1]*, Jean Brousseau[1], Claude Belzile[2], and Abderrazak El Ouafi[1]

[1]Department of Mathematics, Computer Science and Engineering, Université du Québec à Rimouski, Rimouski, Quebec, Canada

[2]Institut des Sciences de la mer de Rimouski, Université du Québec à Rimouski, Rimouski, Quebec, Canada

(This article belongs to the *Special Issue: 3D Printing for Structural and Functional Integration*)

***Corresponding author:**
Othmane Rayan
(othmane.rayan@uqar.ca)

Citation: Rayan O, Brousseau J, Belzile C, *et al*., 2023, Maraging steel powder alteration caused by laser powder bed fusion printing process. *Mater Sci Addi Manuf*, 2(3): 1781. https://doi.org/10.36922/msam.1781

Received: September 8, 2023

Accepted: September 23, 2023

Abstract

Metallic additive manufacturing (AM) technologies have recently drawn a lot of interest, notably in the aerospace, automotive, and biomedical fields, as they allow a great degree of design flexibility, perform well mechanically, and reduce material waste. As long as the unfused powder is sieved and recycled for the next print, AM is a green and clean process. However, the recycled powder is prone to several modifications during the course of printing that may affect the mechanical properties of finished components. The study examines the phenomenon of powder degradation caused by laser powder bed fusion printing process and the reuse of the powder. Maraging steel was chosen because there are very few studies on the alteration of this type of powder. The effects of part location, distance between parts and lattice structure on powder characteristics were investigated. Results showed that powder particles were not uniformly distributed over the powder bed, coarsening toward the collecting bin. Nevertheless, the gas filtration system that transports spatters and fumes had no noticeable effect on the powder bed particle-size distribution (PSD). Analyses of the powder spread over the build plate revealed that the PSD shifted toward larger particles with a considerable drop in the percentage of fine particles as the spacing between printed parts was decreased. Printing lattice structures had a substantial impact on the PSD of the powder bed. The size of the particles increased remarkably as the lattice cell became tighter, while the powder morphology showed a huge amount of spatters, aggregates, "clip-clap," elongated particles, broken particles, shattered, and deformed particles. Taken together, the study showed that the PSD of the powder became coarser and the particle morphology was altered as the number of reuses increased.

Keywords: Additive manufacturing; Laser-powder-bed fusion process; Powder reuse; Powder morphology; Particle-size distribution; Lattice parts

1. Introduction

Additive manufacturing (AM) is a novel technique used to create three-dimensional (3D) products from virtual 3D models by layering the component until the part is complete. The earliest AM concept was a topographical map produced at the end of the 19th-century[1]. At present, AM knowledge and technologies are widely developed and advanced. These technologies allow us to produce innovative components that were previously impossible to make. In the biomedical sector, surgeons currently replace various human body components with 3D parts[1,2].

Laser powder bed fusion (L-PBF) and electron beam melting (EBM) are the most commonly used metallic AM technologies, and both use the same printing process[1]. They begin by spreading a fine layer of powder across the build plate. Then, either a laser or an electron beam melts the powder. Next, the build platform descends to allow the next layer of powder to be spread and melted, and this cycle repeats until the 3D part is complete. The difference between these two technologies is the energy source: L-PBF uses a laser to melt the powder, whereas EBM requires an electron beam[1]. The main methods used to produce AM powders are gas atomization, induction melted bar atomization, plasma atomized wire, plasma rotating electrode atomization and water atomization, among others. Each process has advantages and disadvantages in terms of powder properties. For example, water atomization produces particles with irregular shapes and wetness[3-5]. Herzog *et al.*[6] also reported an increase in oxygen content associated with powder produced by water atomization, whereas the gas atomization process reduces the risk of oxidation and contamination[6-8]. Plasma atomized wire produces a high-quality powder with a high ratio of spherical particles, high powder density, and low porosity[3,9].

The printing process itself has a significant impact on powder features, particularly the particle-size distribution (PSD), chemical composition, and morphology. When a laser melts the powder, it produces spatters and heat-affected particles, which deposit on the powder bed, affecting the nearby portion of the powder bed[10,11]. This is especially the case when printing lattice parts, which offer the multiple advantages of energy absorption, lightweight construction, excellent mechanical and thermal properties, and reduction of material consumption[12]. However, it has been argued that printing this type of structure accelerates powder bed contamination and degradation by producing a considerable number of spatters[13].

Anwar and Pham[14] studied the effects of inert gas flow velocity and scanning direction on the formation and accumulation of spattered powder. Their research showed that flow velocity affects the accumulation of spatters on the build plate. They also underline that scanning in the direction of the gas flow significantly decreases the accumulation of spatters over the powder bed. The presence of spatters on the powder bed must be minimized as much as possible since it not only increases the percentage of porosity within the printed component, but is also responsible for modifying the morphology of recycled powder[15]. The mechanical deformation of particle shape is largely caused by laser heat exposure that welds satellites to particles[16]. This result has also been confirmed by Park *et al.*[17] Furthermore, Popov *et al.*[16] claimed that satellites exist in virgin powder, but that the bonding of satellites with particles, which produces agglomerations, is induced by the sieving process.

Rock *et al.*[18] also investigated the impact of spatters on PSD and particle morphology. They concluded that the particle morphology of virgin powder differs significantly from that of powder recycled 10 times. They also discovered that, despite the fact that the sieving process removes the majority of spatters, some do infiltrate the feedstock powder. Consequently, the spatters are extremely likely to affect the powder and the mechanical properties of the manufactured part. Rock *et al.*[18] and Anwar and Pham[14] both claimed that despite the gas flow effect, spatters are candidates for melting and incorporation into a component if ejected into a laser pattern.

Moreover, according to Sutton *et al.*,[10] laser spatters and solidified particles, also known as ejecta or heat-affected powder, are responsible for compromising the morphological and chemical properties of reused powder. Spatters not only contaminate the powder bed when they are ejected, but also affect the mechanical properties of the next part printed when they are deposited over its laser pattern. Furthermore, the very small spatters traveling through the sieve device can influence the morphology of recycled powder and increase its oxygen concentration. In addition, Tan *et al.*[5] explained a defect called the balling effect that occurs in the L-PBF printing process when laser power is not properly adjusted. Balling affects melt pool formation and produces partially melted powder. Consequently, it enhances porosity inside parts and affects their surface roughness. Furthermore, Powell *et al.*[19] showed that the handling and removal procedure can impact powder properties. The unfused powder can be easily polluted by impurities such as fibers, dust, and other pollutants transported by ambient air during the handling, cleaning, and sieving processes. Thus, when sieve devices and procedures are not effective, the sieved powder can be polluted. Contamination can also be caused by the presence of foreign material in the dispenser. For example, after a material change, some particles of the previous material can be mixed with the newly loaded material. Soundarapandiyan *et al.*[20] reported a severe contamination scenario caused by the presence of Inconel 625 particles in the aluminum powder sample, which resulted in mechanical component failure. Storage techniques are also critical for preserving powder quality. When a reactive powder is not stored in an inert atmosphere, particles are more likely to come into contact with the ambient air. As a result, the powder is exposed to corrosion, oxidation, and contamination[19]. Aside from these factors, the chemical properties of the powder change significantly after multiple reuse cycles. Tang *et al.*[21] observed an increase in oxygen content while aluminum and vanadium percentages remained stable in Ti-6Al-4V powder after 21 printing cycles on an EBM machine. Popov *et al.*[16] also observed oxygen pickup in titanium powder, which exceeded the maximum ASTM F2924-14 (2014a) standard after 69 prints in an EBM process. Park *et al.*[17] validated prior findings for the same material in a selective laser melting process across 38 cycles, with an increase in oxygen and nitrogen content exceeding titanium Grade 23 standards. It is also worth noting the change in powder particle size that occurs due to reusing powder. O'Leary *et al.*[22] noticed a significant drop in the proportion of fine particles <15 μm in diameter and an increase in the number of larger particles over 45 μm in diameter after recycling Ti-6Al-4V powder 5 times in an L-PBF process. They also observed that powder surfaces became rougher and less spherical. Similar results were achieved with AISI 304L stainless steel powder by Sutton *et al.*[23] who revealed an increase in particle diameters after 5 reuse cycles.

Continuous refreshing or collective aging are two recycling techniques used in AM. In powder refreshing, the quality of recycled powder is determined by the percentages of virgin and reused powder utilized in the mix. Tan *et al.*[5] showed that combining 75% virgin powder with 25% reused powder results in an excellent flowability that is comparable to 100% virgin powder. In the collective aging technique, the depositing and mixing methodologies for combining dispenser powder with reused powder have a substantial impact on the quality of printed components.[24]

It is crucial to emphasize that changes in physical powder characteristics, specifically PSD and morphology, have an impact on both the rheological powder characteristics and the mechanical performances of completed parts[21,25,26]. Brika *et al.*[9] investigated the impact of geometrical particle characteristics on both rheological properties and mechanical performances of printed parts, and showed that using extremely spherical powders substantially improved powder flowability, powder density, and part density. It also increased mechanical properties, namely ultimate tensile strength, and yield strength, as well as surface roughness and dimension accuracy. Furthermore, Liu *et al.*[27] reported that variation in powder PSD was responsible for differences in powder quality and mechanical properties. Powder with a wide PSD provides better powder bed density, higher density parts under low laser energy intensity, and smoother surface finishing on components, while a powder with a narrower PSD has better flowability and produces components with optimal tensile properties and hardness. Moreover, it has been demonstrated that powder properties are not uniform throughout all regions of the powder bed. Pal *et al.*[28] investigated the evolution of L-PBF Ti-6Al-4V and Co-Cr-W-Mo powder characteristics and mechanical properties of specimens printed in two different locations over the build plate. For both materials, powder near the dispenser (position 1) had more fine particles and a better spherical shape than powder near the collecting bin (position 2). Parts printed in position 1 showed greater density and smaller pores, resulting in higher tensile properties than specimens printed in position 2.

The condition and properties of the powder have a significant impact on the quality of the printed part. According to recent studies[1,29], the spherical particle shape is ideal for metal AM because it improves powder flowability. Mechanical properties such as tensile strength, yield strength, surface roughness, and dimensional accuracy are also improved by the spherical shape. Liu *et al.*[27] found that powder with a wide PSD improved powder bed density, part density, and surface finish, while powder with a narrower PSD produced parts with higher tensile properties and hardness. Zhang *et al.*[30] reported that Er (erbium)-modified 7075 aluminum alloy powders prepared by ball milling reduced crack failure. However, the Er particles present in the melt pool drastically affected the flowability and increased the porosity of the part. The aforementioned studies revealed changes in powder characteristics and mechanical qualities of manufactured components caused by the AM process itself, particularly powder degradation induced by laser heat exposure and powder reuse cycles[11,13,31-36].

However, in the literature published to date, the influence of the geometry of printed parts as well as their positions over the build plate on the evolution of powder characteristics remains unclear and sparsely discussed. Therefore, this study investigated the influence of part geometry, part location and proximity of the printed parts on the contamination of the powder bed and on the recycled powder. The study also examined the extent to which lattice structures speed up powder degradation. Maraging steel powder was mainly used in the experiments because very few studies had been conducted to investigate the contamination and recycling of this material.

2. Materials and methods

2.1. Materials

The powder used was EOS Maraging Steel MS1 (18% Ni Maraging 300). The material data concerning its composition is shown in Table 1 (EOS art-no.9011-0016) [37]. The parts were printed on an EOS M290 400W machine in a nitrogen atmosphere with <1.3% oxygen concentration, with a gas flow differential pressure of 0.7 mbar and a chamber temperature of 40°C. The MS1 040 performance M291 2.00 EOSPRINT template was used: laser power = 285 W, beam offset = 20 µm, laser speed = 960 mm/s, layer thickness = 40 µm, hatch space = 110 µm, and laser pattern = stripes rotated at a 47° angle with a 30° restriction angle at each of the next layers.

After each print, the powder was sieved manually through an 80 µm mesh sieve and fed into the dispenser. The powder samples were analyzed with a Malvern Panalytical Mastersizer 3000 particle-size analyzer equipped with a Hydro LV module. The stirrer speed was set to 3000 rpm, a speed sufficient to keep the particles in suspension. Before the measurements, the sample was subjected to processing using Hydro LV ultrasounds at 25% power for 60 s to help disintegrate aggregates. Three consecutive measurements of 30 s each (20 s with the red laser, and 10 s with the blue LED) were collected for each sample. The average statistics of the three measurements were computed (the coefficient of variation in Dv10, Dv50, and Dv90 of the three measurements was always <1%), indicating a good sample dispersion. The Mastersizer general-purpose optical model for nonspherical particles with a refractive index of 2.757 and absorption 1.0 for stainless steel (values taken from the Malvern Panalytical database included with Mastersizer 3000 software) was employed. Instrument performance was confirmed using Malvern Panalytical's QAS4002 Quality Audit Standard and two silica powder secondary standards with median diameters of 70 µm and 270 µm. In addition, the powder morphology was analyzed with a NanoImage SNE 4500M scanning electron microscope.

2.2. Experiments

We conducted three experiments to investigate alterations in powder PSD throughout the L-PBF printing process, studying the effects on PSD of gas flow transporting spatters, powder distance from the printed part, and geometrical properties of lattice cylinders. The builds were not repeated to obtain replicates. However, the repeatability of the measurements was evaluated by analyzing three powder samples for each zone of experiment 2B and four powder samples of each lattice structure of the experiment 3.

2.2.1. Experiment 1: PSD variation caused by the powder spread process

The first experiment examines the PSD of the powder spread over the build plate during a printing cycle at different locations. We compared the PSD of powder loaded in the dispenser (before printing), powder at 16 different sites (matrix) over the powder bed, powder accumulated in the collector bin, and powder after sieving. To do so, we printed at x = 125 mm and y = 10 mm to produce a small vertical cylinder of Ø = 10 mm and h = 20 mm. The cylinder was located outside the sample matrix and close to the gas outlet, as shown in Figure 1.

2.2.2. Experiment 2: PSD variation depending on the position of printed part

2.2.2.1. Experiment 2A: Single contamination

In Experiment 2A, we evaluated the PSD based on horizontal and vertical distances from a centrally located printed cylinder with a diameter of 50 mm and a height of 20 mm. The printing process generates spatters and smoke that contaminate the power bed. As shown in Figure 2, the 12 samples collected are 40 mm apart.

2.2.2.2. Experience 2B: Double contamination

To study double contamination, we printed four concentric cylinders and analyzed the PSD of the powder collected in four different zones as shown in Figure 3.

2.2.3. Experiment 3: PSD changes when printing lattice structures of different cell sizes

The third experiment highlights the evolution of PSD and morphology of powder depending on the area and volume ratios of printed parts. For this experiment, lattice cylinders were designed using nTopology software. First, we defined the area and volume ratios of a lattice cylinder as follows:

$$R_A = A_{lattice}/A_{filled} \quad \text{(I)}$$

$$R_v = V_{lattice}/V_{filled} \quad \text{(II)}$$

where R_A is area ratio; A_{filled} and $A_{lattice}$ are, respectively, the total area of filled or lattice cylinders of equal diameter and height; R_V is volume ratio; and V_{filled} and $V_{lattice}$ are, respectively, the total volume of filled or lattice cylinders of equal diameter and height.

Eventually, we investigated the PSD of powder trapped inside 4 lattice structures. The cylinders had the same

Table 1. The chemical composition MS1 virgin powder (in weight %)

Element	Fe	Ni	Co	Mo	Ti	Al	Cr	Cu	C	Mn	Si	P	S
Max (%)	Balance	19	9.5	5.2	0.8	0.15	0.5	0.5	0.03	0.1	0.1	0.01	0.01
Min (%)		17	8.5	4.5	0.6	0.05	-	-	-	-	-	-	-

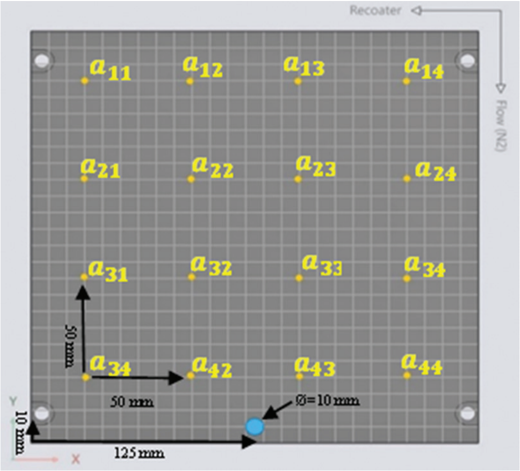

Figure 1. Particle-size distribution samples collected in different positions (matrix) over the build plate.

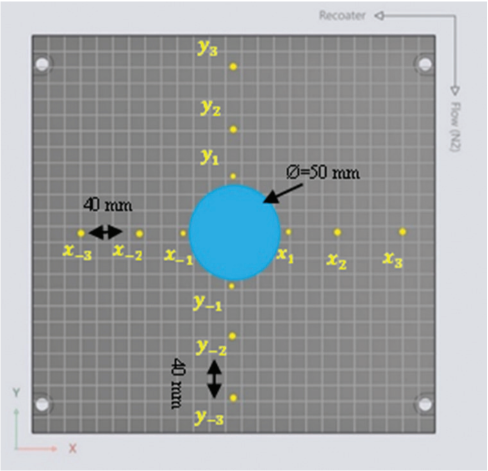

Figure 2. Particle-size distribution samples relative to position of printed cylinder.

diameter of Ø = 50 mm but four different cell sizes: 2 mm, 3 mm, 4 mm, and 5 mm for cylinders 1, 2, 3, and 4, respectively (Figure 4). The lattice cylinders were created with nTopology software using a cube edge structure with fillet radius of 2.1 mm and thickness of 0.5 mm. It is important to note that when the cell size was increased from 2 mm to 5 mm, the area and volume ratios dropped. Table 2 presents the characteristics of the four lattice cylinders.

3. Results and discussion

3.1. Results of experiment 1: PSD analyzed during printing cycle

Two samples of powder were collected from the dispenser before printing, two after printing and sieving, and two more from the collector bin, which contained the excess powder displaced by the recoater. The powder in the collector and

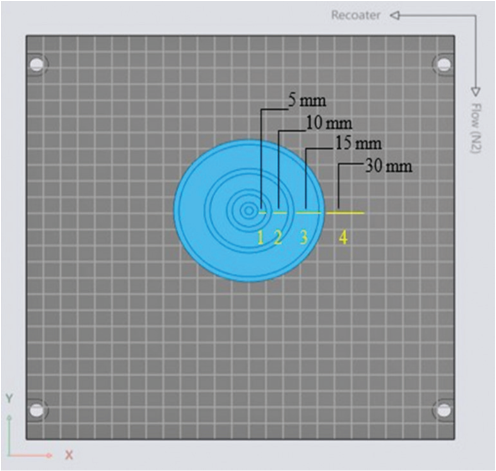

Figure 3. Four concentric cylinders with increasing distance spacing.

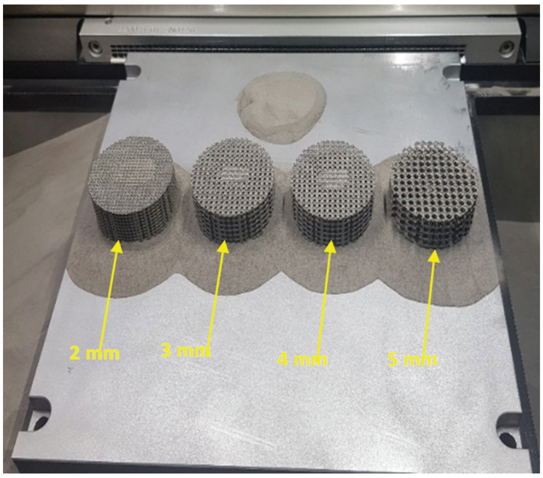

Figure 4. Lattices with different cell sizes.

Table 2. Lattice dimension parameters

Lattice cylinder	Cell size C (mm)	Area ratio, R_A	Volume ratio, R_V
1	2	8.4	0.49
2	3	5.7	0.42
3	4	3.6	0.26
4	5	2.4	0.18

the unfused powder on the build plate were sieved and placed in the dispenser. As shown in Figure 5, the PSD of the three samples is very similar, but it can be observed that the dispenser PSD moves slightly to the left in the direction of smaller particles after printing and sieving, while the PSD measured in the collector is located between the other two PSD arcs. Figure 6 shows that after the sieving process, the diameter D-values of the dispenser powder D90, D50, and

D10 decrease by 3.7%, 4%, and 6.8%, respectively, while the D-values of the collector powder appear to be quite similar to the D-values of the dispenser powder before printing. Consequently, the powder size in the dispenser during a printing cycle remains approximately constant when a small part is being printed. This change can be partly attributed to the fact that the powder is poured through a sieve with an 80 µm mesh, so that coarse particles (>80 µm) are retained in the sieve and eliminated from the process[25]. It should also be noted that during the printing process, splashes can weld particles together. Some particle agglomerations do not pass through the sieve mesh, which changes the PSD of the powder. We also collected powder samples from 16 locations (matrix) over the powder bed (Figure 7). Figures 8 and 9 present the PSD and D-values, respectively, along the horizontal line i = 1. As can be observed, along the horizontal line, the PSD slightly displaces left toward the fine particles as we move from the collector to the dispenser. These results become more apparent in the D-values graphs, which show that the D90, D50, and D10 values gradually decline as they move horizontally rightward toward the dispenser. The results are similar for the other three lines. The D50 value, for example, varies for each horizontal line (i = 1, 2, 3, 4) by −9.8%, −10.8%, −9.6%, and −14.6%, respectively. However, from the top to the bottom of the powder bed, the vertical columns show a mild reduction in D-values with the exception of column j = 4 (Table 3). For example, the variations in D50 for vertical columns j = 1, 2, 3, and 4 are −4.5%, +1.6%, −4.8%, and −9.5%, respectively.

Since the powder in the dispenser before printing contained a mixture of fine and larger particles, the recoater spread more particles smaller than the layer thickness (40 µm) at the beginning of the powder bed (a_{14}, a_{24}, a_{34}, a_{44}), while coarser particles, bigger than 40 µm,

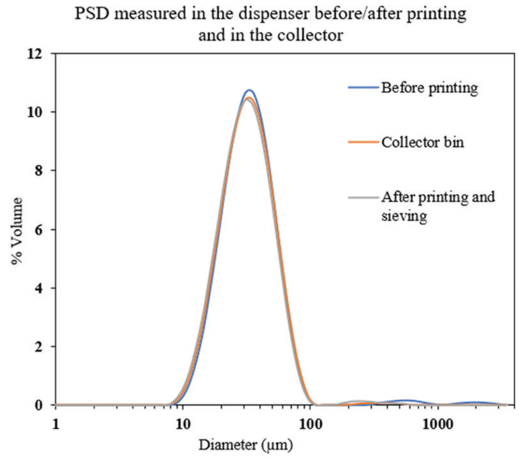

Figure 5. Particle-size distribution during printing cycle.

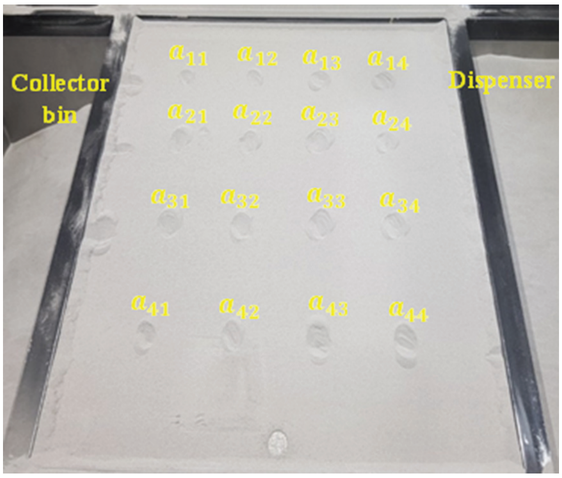

Figure 7. Particle-size distribution samples collected in different positions (matrix) over the build plate.

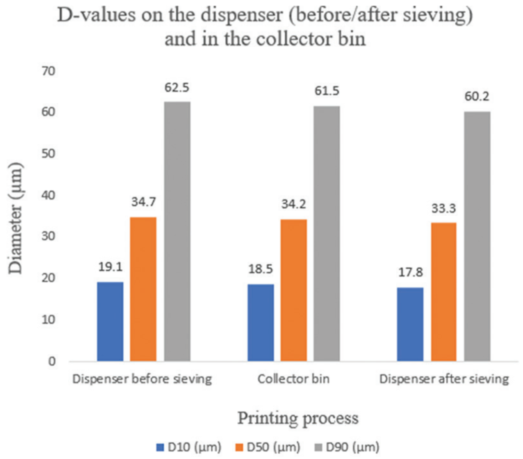

Figure 6. D-values during a printing cycle.

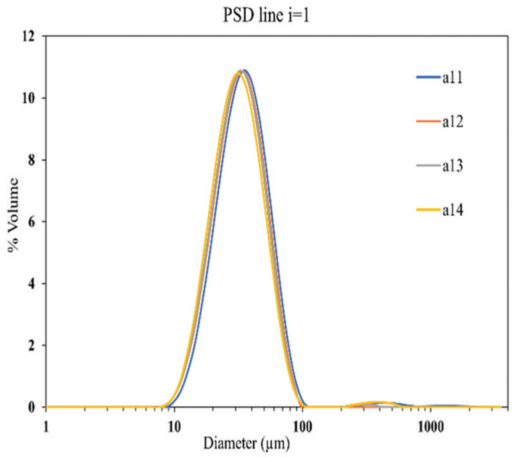

Figure 8. Particle-size distribution measured in line i=1.

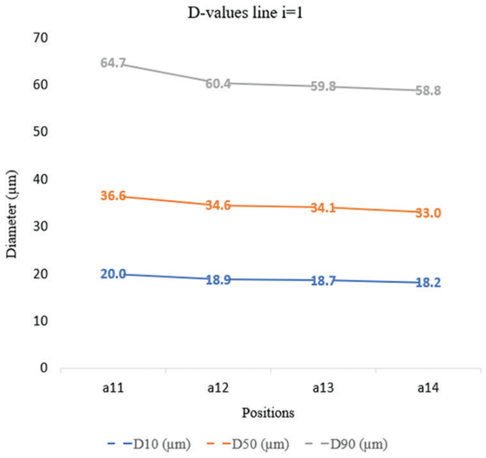

Figure 9. D-values for line i=1.

are dragged further away. This result is also reported by Carrion *et al.*[25] Moreover, Pal *et al.*[28] reported that the bulk density of the powder bed drops near the collector bin. It was also observed that near the dispenser, the D05, D50, and D10 values were slightly lower than those measured near the collector bin, whereas D90 and D95 showed an increase of 1.2 µm and 1.5 µm, respectively, near the dispenser[23]. However, the decrease in particle diameters along the columns remains unjustified and is not discussed in the literature.

3.2. Results of experiment 2: Evolution of PSD depending on position relative to a printed part

3.2.1. Results of single contamination

Figure 10 shows the locations of 6 powder samples collected along the horizontal X-axis, and 6 samples collected along the vertical Y-axis. Figures 11 and 12 show that the cumulative PSD and the PSD of samples positioned in negative abscissas x_{-1}, x_{-2}, x_{-3} (near the collector bin) are greater than those located in the positive abscissas x_1, x_2, x_3 (near the dispenser), indicating the same result as the first experiment, which demonstrated that the PSD in the graph is displaced progressively left toward fine particles as the sample location moves rightward on the build plate. In addition, the diameter values D90, D50, and D10 decrease by 5.1%, 12.1%, and 18%, respectively, toward the positive abscissas (Figure 13). Yet, the PSDs of samples taken on the Y-axis are superposed, and their diameter values remain approximately stable (Figure 14). As also shown in Figure 10, the powder bed area located below the printed cylinder shows a substantial amount of fine black particles as compared to the top area. The black particles are most likely spatters generated during printing of the solid cylinder and carried by the inert gas flowing from the top of the build plate toward the bottom[14]. However, their impact on powder size along the Y-axis is negligible.

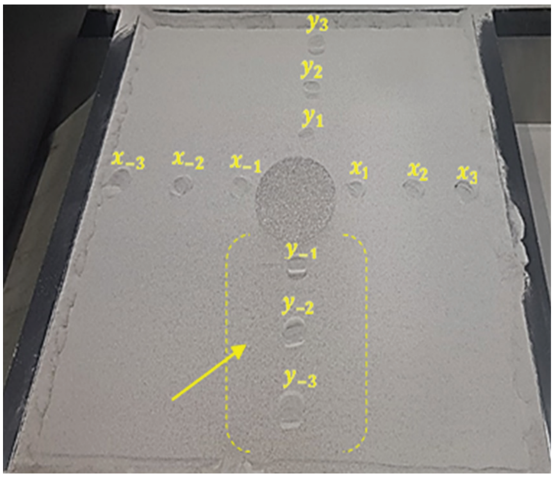

Figure 10. Location of powder samples collected along horizontal X-axis and vertical Y-axis.

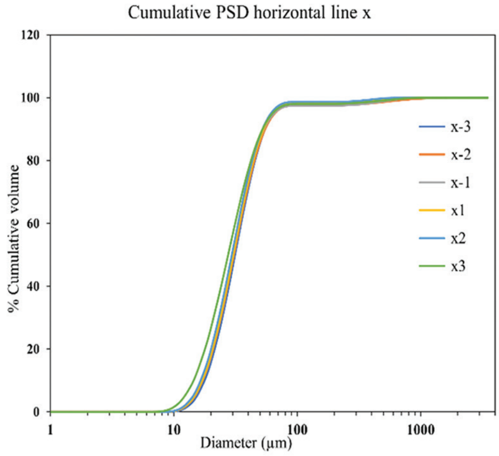

Figure 11. Cumulative particle-size distribution horizontal line.

Table 3. Diameter D-values variation along lines (toward right) and columns (toward bottom)

	Position	Δ D10 (µm)	Δ D50 (µm)	Δ D90 (µm)
Line	i=1	-9.0%	-9.8%	-9.1%
	i=2	-12.1%	-10.8%	-8.0%
	i=3	-6.3%	-9.6%	-10.9%
	i=4	-14.1%	-14.6%	-12.2%
Column	j=1	-4.9%	-4.5%	-3.5%
	j=2	0.8%	1.6%	5.2%
	j=3	-5.6%	-4.8%	-3.9%
	j=4	-10.0%	-9.5%	-6.9%

Figure 10 also shows that spatters are not visible in the powder bed along the X-axis. Changes to the PSD along this axis are comparable to the recoater effect identified in the first experiment.

3.2.2. Results of double contamination

Figure 15 illustrates the four concentric cylinders printed for Experiment 2B to study what happens when parts are printed in close proximity. As shown in Figure 16, the cumulative PSD shifts gradually rightward toward bigger particles, followed by a significant drop in the proportion of fine particles with the gradual movement from zone 4 to zone 1. This implies that zone 1 includes more coarse particles and less fine particles than zones 2, 3, or 4.

Figure 17 shows that the PSD moved rightward and became narrower from zone 4 to zone 1. Likewise, the percentage of smaller particles was significantly reduced. As shown in Figure 18, the particles average diameters D90, D50, and D10 increase gradually by 8%, 16%, and 24%, respectively, as we move from zone 4 to zone 1. The coefficients of variation on the measurements of the three samples taken in each zone are <0.4%, <0.3%, and <0.6% on Dv90, Dv50, and Dv10, respectively.

As can be observed in this experiment, reducing the distance between melted parts increases the proportion of coarse particles and significantly reduces the percentage of fine particles in the area. Powder located at a distance from the melt pool remains unaffected, with a PSD quite similar to that measured in the dispenser.

This change could be attributed to the fact that laser melting creates spatters and larger particles. This condensation occurs due to the vaporization of melted particles[5,23]. Furthermore, they may agglomerate into bigger particles to create satellites. Soundarapandiyan *et al.*[11] reported that powder particles located near the melt zone are not only coarser with a wider PSD than particles away from the melt pool, but they also demonstrate

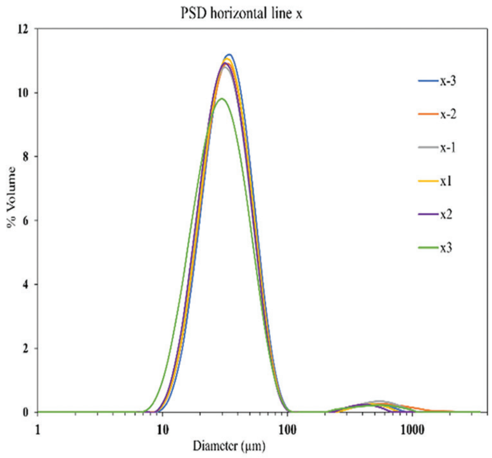

Figure 12. Particle-size distribution horizontal line.

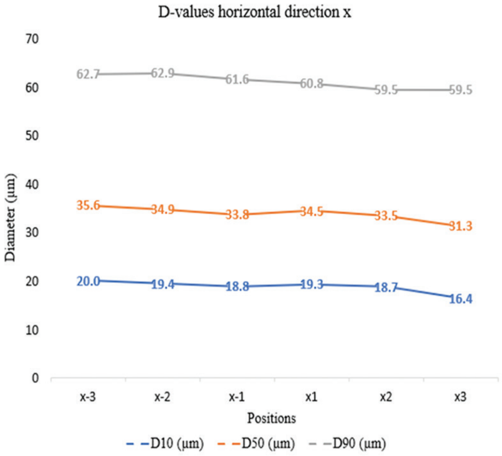

Figure 13. D-values horizontal line (X-axis).

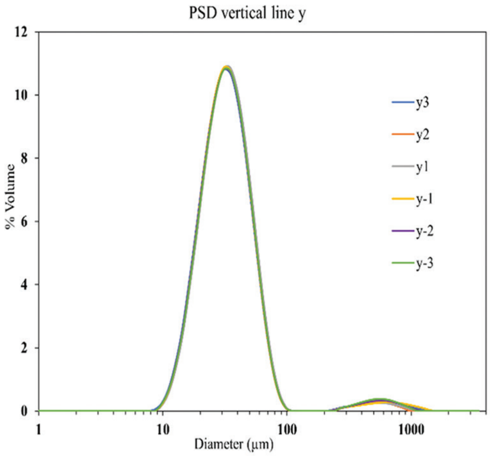

Figure 14. Particle-size distribution vertical line.

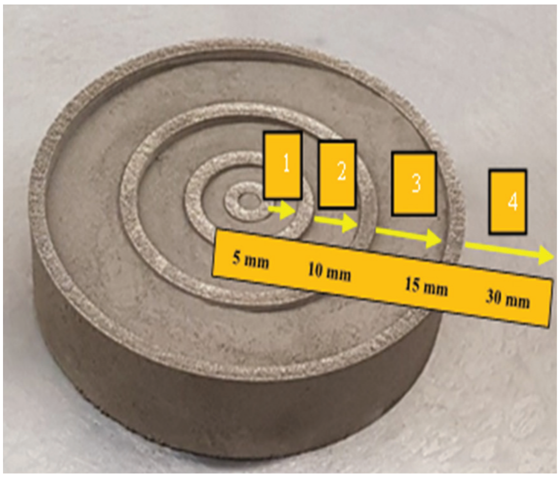

Figure 15. Part with four concentric cylinders with increasing distance of spacing.

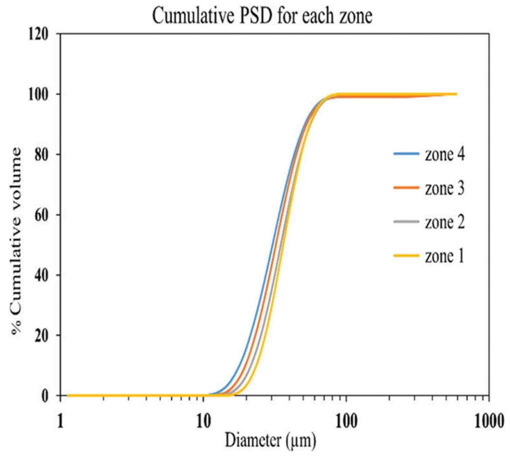

Figure 16. Cumulative particle-size distribution measured for each zone.

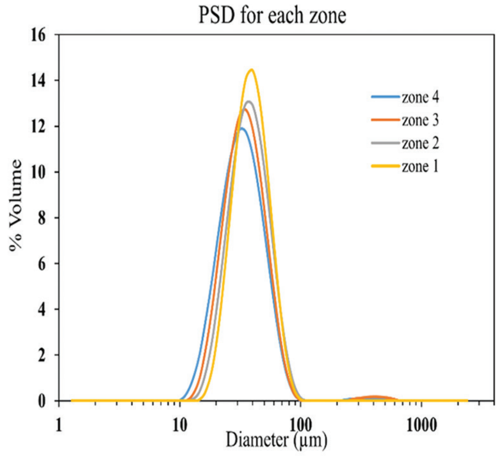

Figure 17. Particle-size distribution measured for each zone (first replicate for each zone).

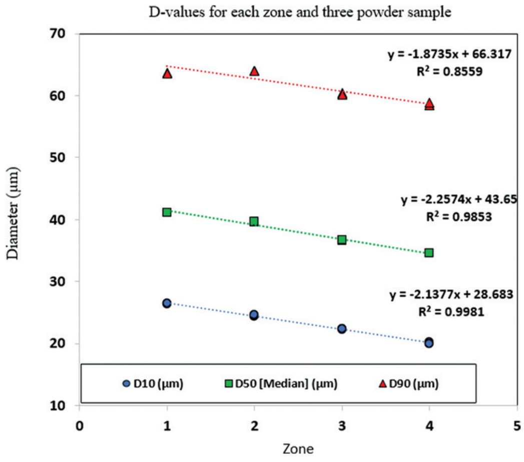

Figure 18. D-values for each zone.

a dramatic degradation in their morphology: partial melting, hard sintering, and agglomerations. The results of this experiment had also been confirmed by Sutton *et al.*[10] who concluded that heat affects particles located near the melt pool (zone 1). Consequently, heat-affected particles become irregular in shape and coarser than particle coming from unused powder. Recent studies[10,11,22,34,36,38] on the effects of reusing powder show that the PSD shifts rightward toward large particles after reuse cycles. In addition, the proportion of fine particles drops, whereas the proportion of bigger particles grows. Consequently, we can establish a similarity between the powder alteration caused by the proximity of printed parts and reuse cycles; the smaller the distance between printed parts, the more the powder is altered. Many authors[1,5,25,27] claim that the reduction in fine particles minimizes agglomeration effects, which improves powder flowability. However, a decrease in the smallest particles and the presence of coarser particles may be responsible for an increase in the percentage of void within the powder bed so that the printed part can be impacted by a lack of fusion[5,11].

3.3. Results of experiment 3: PSD changes when printing lattice structures of different cell sizes

Figure 4 shows the four lattice cylinders printed with varying cell sizes of 2 mm, 3 mm, 4 mm, and 5 mm. The powder samples are extracted from the lattices at the locations indicated by the yellow arrows. As mentioned above, and to evaluate the repeatability of the measurements, four samples of the powder trapped in each lattice structure were analyzed.

The PSD of the four different lattice cell sizes is not superposed, as shown in Figure 19. The PSD of powder trapped in the 2-mm-cell lattice shows a lower proportion of tiny particles than in the 5-mm-cell lattice. This finding is similar to the results of experiment 2, which reported a relevant decrease in small particles as the distance of spacing between parts was reduced.

Changing the cell size of the lattice, as described in Table 2, varied the area and volume ratios of the printed lattice cylinders. Figure 20 illustrates that increasing the cell size from 2 mm to 5 mm decreased the average diameter D-values D90, D50, and D10 by 6%, 12%, and 16%, respectively. The coefficients of variation on the measurements of the four samples for each lattice cell are <3.9%, <3.0%, and <4.2% on Dv90, Dv50, and Dv10, respectively.

When printing the lattice cylinders, the powder had already been recycled 11 times. Figure 21 illustrates the evolution of powder diameter values when comparing the diameter values of new powder with the diameter

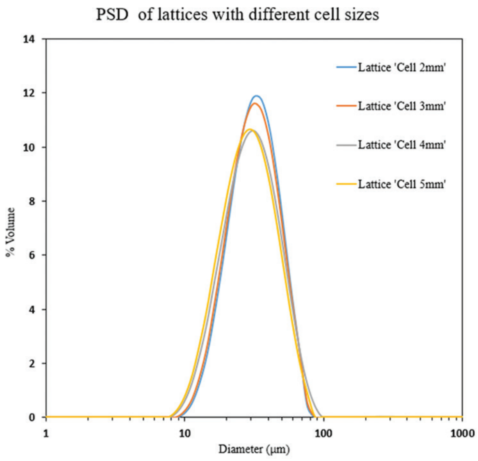

Figure 19. Particle-size distribution of lattices parts with different cell sizes (fourth replicate for each cell size).

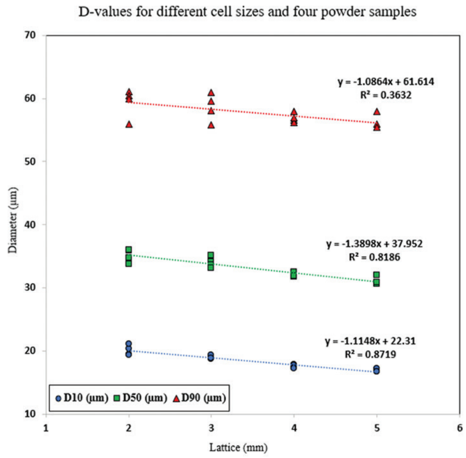

Figure 20. D-values of lattices depending on cell sizes.

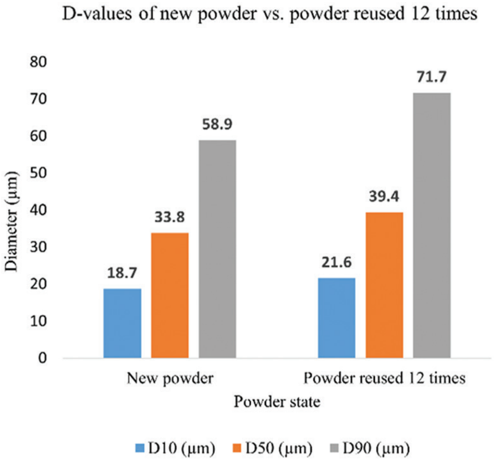

Figure 21. D-values of new powder versus powder reused 12 times.

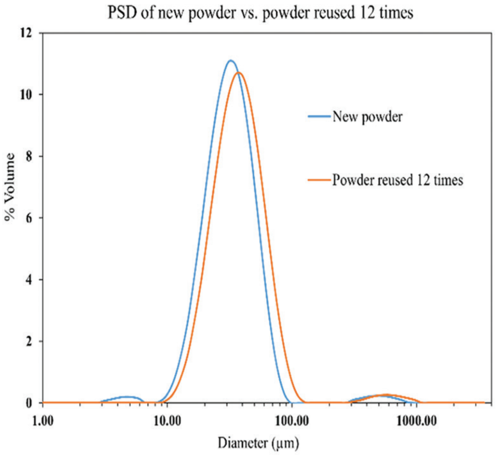

Figure 22. Particle-size distribution of new powder versus powder reused 12 times.

values of powder reused 12 times. Significant increases could be observed in D90, D50, and D10, of 21.7%, 16.6%, and 15.5%, respectively. The PSD moved larger particles rightward, followed by a slight drop in fine particles and a relevant increase in the proportion of large particles (Figure 22). This result has also been reported by many researchers studying the effects of reuse cycles on powder size characteristics[10,11,25,34,36,38-41]. For example, Soundarapandiyan *et al.*[11] and Richard and O'Leary *et al.*[22] observed the same behavior of the Ti-6Al-4V powder PSD, which shifted rightward after five reuse cycles. In another study, we confirmed the similar PSD behavior after reusing maraging steel powder 8 times[36].

Figure 20 shows that D-values D10 and D50 increased by 16.2% and 9%, respectively, while the D90 decreased by 13% when the area ratio was increased from 2.4 to 8.4. As a result, we can deduce that increasing the area and volume ratio of printed components in these lattice cylinders changes the PSD of the powder trapped in the lattice structure. This outcome might be caused by a variety of circumstances. The balling defect might be responsible for the increase in powder diameter to 500 µm due to the creation of partially melted particles[5]. Furthermore, formation of spatters could be the primary reason for the increase in PSD. Soundarapandiyan *et al.*[11,42] and Sutton *et al.*[10] observed that powder near the melt pool was coarser due to the presence of spatters, partially melted particles, hard sintering, and agglomerations.

A small proportion of large particles in the diameter range of 200–1000 µm (Figures 5, 8, 12, 14, and 22) were likely aggregates in the PSDs samples analyzed by the Mastersizer 3000, since particles in this size range were not observed using the electron microscope.

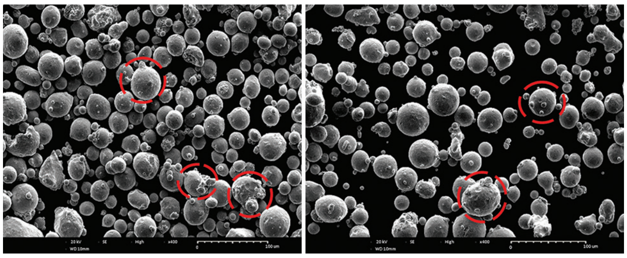

Figure 23. Morphologies of new powder.

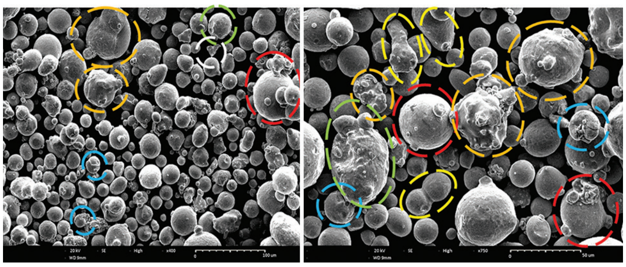

Figure 24. Morphologies of powder reused 12 times.

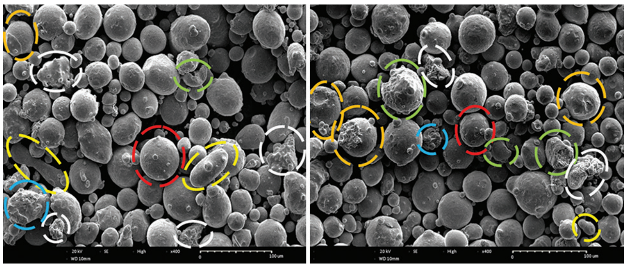

Figure 25. Powder confined within 3-mm-cell lattice.

As shown in Figure 23, the morphology of new powder is globally spherical with the presence of satellites and aggregates particles (indicated with red circles), which are formed during the powder production process. However, Figure 24 shows that the powder recycled 12 times exhibits the presence of satellites, deformed particles (indicated with orange circles), "clip-clap" (indicated with blue circles), and elongated particles (indicated with yellow circles). Furthermore, as shown in Figure 25, the powder inside the 3-mm-cell lattice shows a high shape degradation. The particles are deformed and exhibit a relevant amount of aggregates, elongated particles, broken particles (indicated with green circles), and shattered particles (indicated with white circles). Finally, Figure 26 shows spatters and heat-affected particles that are trapped within the 80-µm-mesh sieve device. The particles exhibit a wide scale of aggregate particles in addition to the presence of spherical larger particles "super ball" (indicated by purple circles).

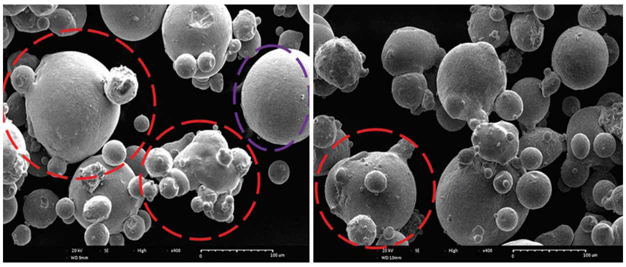

Figure 26. Heat-affected powder trapped in sieve device.

Many researches have reported the morphology of degraded particles after reusing cycles, especially the presence of defects such as broken particles, "clip-clap," shattered particles, deformed particles, elongated particles, aggregates, and particles with molten specks. This powder alteration is attributed to the effect of melting and sintering process[11,16,23,35,36,42,43].

4. Conclusion

In this study, we examined the evolution of PSD throughout the printing cycle and recycling of the L-PBF process, as well as the influence of printed component geometry on powder size and morphology. The conclusions from the different experiments are summarized as follows:

In experiment 1, we examined how powder was spread on the bed. The results showed that the powder is not uniformly spread over the build plate. Therefore, the PSD changed more along horizontal lines than along vertical lines, due to the recoater effect and powder flowability. When moving horizontally toward the collector, the diameter D-values D90, D50, and D10 progressively increased. For example, the D50 increased by 9.8%, 10.8%, 9.6%, and 14.6% for the four different lines. However, moving from the top to the bottom of the powder bed through the vertical columns j = 1, 2, 3, and 4, the diameters D-values mildly reduced.

In experiment 2A, we printed a filled cylinder in the middle of the build plate. The printing process produced spatters that were deposited in the inferior region of the powder bed due to the effect of gas flow, but their influence on PSD along the vertical axis (Y-axis) was negligible. Nevertheless, the powder samples obtained along the horizontal line (X-axis) showed an increase in PSD in the direction of the recoater, as measured in experiment 1. In experiment 2B, we examined the influence of part distance spacing on PSD. We conclude that decreasing the spacing between parts narrows and shifts the PSD toward larger particles.

Finally, in experiment 3, we examined a printing situation with significant potential for powder alteration. We printed lattice structures of different cell sizes and analyzed the PSD and the morphology of the powder trapped within the lattices. The PSD was quite different for each cell size. We observed that the smaller the cell size, the lower the percentage of small particles. The particles diameters D-values increased as the lattice cell size became smaller. The morphology of the particles stuck inside the lattice cylinders was impacted, accompanied by the formation of aggregates, elongated, broken, "clip-clap" and shattered particles.

Both experiments 2 and 3 confirmed that when the space between printed parts is reduced, the powder bed particles become coarser and the proportion of fines particles reduces.

From these results, we confirm the printing process generating spatters and particle agglomerations causes the degradation and alteration of the powder bed PSD and morphology. After significant courses of recycling, the PSD of the powder showed more coarse particles and less fine particles, as well as a relevant increase in the proportion of large particles and significant presence of aggregates, deformed and elongated particles within the recycled powder.

Acknowledgments

The authors would like to express their appreciation for the support provided by Jonathan Coudé, Karel J. Uhlir, Loubert Suzie, Charles-André Fraser, Dany Morin, and Richard Lafrance for their assistance in this project.

Funding

This research was funded by NSERC, grant CDEPJ/507533.

Conflict of interest

The authors declare no conflicts of interest.

Author contributions

Conceptualization: Othmane Rayan, Jean Brousseau
Formal analysis: Othmane Rayan, Jean Brousseau, Claude Belzile
Investigation: Othmane Rayan, Jean Brousseau, Claude Belzile
Methodology: Othmane Rayan, Jean Brousseau
Writing – original draft: Othmane Rayan
Writing – review and editing: Othmane Rayan, Jean Brousseau, Claude Belzile, Abderazak El Ouafi.

Ethics approval and consent to participate

Not applicable.

Consent for publication

Not applicable.

Availability of data

Raw data are available from the corresponding author on reasonable request.

References

1. Diegel O, Nordin A, Motte D, 2019, A Practical Guide to Design for Additive Manufacturing. Berlin: Springer.
2. Singh S, Prakash C, Singh R, 2020, 3D Printing in Biomedical Engineering. Berlin: Springer.
3. Dawes J, Bowerman R, Trepleton R, 2015, Introduction to the additive manufacturing powder metallurgy supply chain. *Johnson Matthey Technol Rev*, 59: 243–256.

   https://doi.org/10.1595/205651315x688686
4. Pasebani S, Ghayoor M, Badwe S, *et al.*, 2018, Effects of atomizing media and post processing on mechanical properties of 17-4 PH stainless steel manufactured via selective laser melting. *Addit Manuf*, 22: 127–137.

   https://doi.org/10.1016/j.addma.2018.05.011
5. Tan JH, Wong WLE, Dalgarno KW, 2017, An overview of powder granulometry on feedstock and part performance in the selective laser melting process. *Addit Manuf*, 18: 228–255.

   https://doi.org/10.1016/j.addma.2017.10.011
6. Herzog D, Seyda V, Wycisk E, *et al.*, 2016, Additive manufacturing of metals. *Acta Mater*, 117: 371–392.

   https://doi.org/10.1016/j.actamat.2016.07.019
7. Kelkar RM, 2019, High Quality Spherical Powders for Additive Manufacturing Processes Along with Methods of their Formation. Google Patents.
8. Li R, Shi Y, Wang Z, *et al.*, 2010, Densification behavior of gas and water atomized 316L stainless steel powder during selective laser melting. *Appl Surf Sci*, 256: 4350–4356.

   https://doi.org/10.1016/j.apsusc.2010.02.030
9. Brika SE, Letenneur M, Dion CA, *et al.*, 2020, Influence of particle morphology and size distribution on the powder flowability and laser powder bed fusion manufacturability of Ti-6Al-4V alloy. *Addit Manuf*, 31: 100929.

   https://doi.org/10.1016/j.addma.2019.100929
10. Sutton AT, Kriewall CS, Karnati S, *et al.*, 2020, Evolution of AISI 304L stainless steel part properties due to powder recycling in laser powder-bed fusion. *Addit Manuf*, 36: 101439.

    https://doi.org/10.1016/j.addma.2020.101439
11. Soundarapandiyan G, Johnston C, Khan RHU, *et al.*, 2021, The effects of powder reuse on the mechanical response of electron beam additively manufactured Ti6Al4V parts. *Addit Manuf*, 46: 102101.

    https://doi.org/10.1016/j.addma.2021.102101
12. Nagesha BK, Dhinakaran V, Varsha Shree M, *et al.*, 2020,

Review on characterization and impacts of the lattice structure in additive manufacturing. *Mater Today Proc*, 21: 916–919.

https://doi.org/10.1016/j.matpr.2019.08.158

13. Del Re F, Contaldi V, Astarita A, *et al*., 2018, Statistical approach for assessing the effect of powder reuse on the final quality of AlSi10Mg parts produced by laser powder bed fusion additive manufacturing. *Int J Adv Manuf Technol*, 97: 2231–2240.

    https://doi.org/10.1007/s00170-018-2090-y

14. Anwar AB, Pham QC, 2016, Effect of Inert Gas Flow Velocity and Unidirectional. Canning on the Formation and Accumulation of Spattered Powder During Selective Laser Melting. In: Proceedings of the 2nd International Conference on Progress in Additive Manufacturing (Pro-AM 2016).

15. Szost B, Wang X, Johns D, *et al*., 2018, Spatter and oxide formation in laser powder bed fusion of Inconel 718. *Addit Manuf*, 24: 446–456.

16. Popov VV Jr., Katz-Demyanetz A, Garkun A, *et al*., 2018, The effect of powder recycling on the mechanical properties and microstructure of electron beam melted Ti-6Al-4V specimens. *Addit Manuf*, 22: 834–843.

    https://doi.org/10.1016/j.addma.2018.06.003

17. Renishaw Plc., 2016, Investigating the Effects of Multiple Re-use of Ti6Al4V Powder in Additive Manufacturing. United Kingdom: Renishaw Plc. p1–10.

18. Rock C, Ledford C, Garcia-Avila M, *et al*., 2021, The influence of powder reuse on the properties of nickel super alloy ATI 718™ in laser powder bed fusion additive manufacturing. *Metallurgical Mater Trans B*, 52: 676–688.

    https://doi.org/10.1007/s11663-020-02040-2

19. Powell D, Rennie AEW, Geekie L, *et al*., 2020, Understanding powder degradation in metal additive manufacturing to allow the upcycling of recycled powders. *J Clean Prod*, 268: 122077.

    https://doi./org/10.1016/j.jclepro.2020.122077

20. Soundarapandiyan G, Johnston C, Khan RHU, *et al*., 2021, A technical review of the challenges of powder recycling in the laser powder bed fusion additive manufacturing process. *J Eng*, 2021: 97–103.

    https://doi.org/10.1049/tje2.12013

21. Tang HP, Qian M, Liu N, *et al*., 2015, Effect of powder reuse times on additive manufacturing of Ti-6Al-4V by selective electron beam melting. *JOM*, 67: 555–563.

    https://doi.org/10.1007/s11837-015-1300-4

22. O'Leary R, Setchi R, Prickett P, *et al*., 2016, An investigation into the recycling of Ti-6Al-4V powder used within SLM to improve sustainability. *J Innov Impact*, 8: 377.

23. Sutton AT, Kriewall CS, Karnati S, *et al*., 2020, Characterization of AISI 304L stainless steel powder recycled in the laser powder-bed fusion process. *Addit Manuf*, 32: 100981.

24. Lutter-Günther M, Gebbe C, Kamps T, *et al*., 2018, Powder recycling in laser beam melting: Strategies, consumption modeling and influence on resource efficiency. *Prod Eng*, 12: 377–389.

    https://doi.org/10.1007/s11740-018-0790-7

25. Carrion PE, Soltani-Tehrani A, Phan N, *et al*., 2018, Powder recycling effects on the tensile and fatigue behavior of additively manufactured Ti-6Al-4V parts. *JOM*, 71: 963–973.

    https://doi.org/10.1007/s11837-018-3248-7

26. Quintana OA, Alvarez J, McMillan R, *et al*., 2018, Effects of reusing Ti-6Al-4V powder in a selective laser melting additive system operated in an industrial setting. *JOM*, 70: 1863–1869.

    https://doi.org/10.1007/s11837-018-3011-0

27. Liu B, Wildman R, Tuck C, *et al*., 2011, Investigation the Effect of Particle Size Distribution on Processing Parameters Optimisation in Selective Laser Melting Process. United States: University of Texas at Austin.

28. Pal S, Gubeljak N, Bončina T, *et al*., 2021, The effects of locations on the build tray on the quality of specimens in powder bed additive manufacturing. *Int J Adv Manuf Technol*, 112: 1159–1170.

    https://doi.org/10.1007/s00170-020-06563-5

29. Brika SE, Letenneur M, Dion CA, *et al*., 2020, Influence of particle morphology and size distribution on the powder flowability and laser powder bed fusion manufacturability of Ti-6Al-4V alloy. *Addit Manuf*, 31: 100929.

30. Zhang X, Xiao Z, Yu W, *et al*., 2022, Influence of erbium addition on the defects of selective laser-melted 7075 aluminium alloy. *Virtual Phys Prototyp*, 17: 406–418.

31. Sun H, Chu X, Liu Z, *et al*., 2021, Selective laser melting of maraging steels using recycled powders: A comprehensive microstructural and mechanical investigation. *Metallurgical Mater Trans A*, 52: 1714–1722.

    https://doi.org/10.1007/s11661-021-06180-1

32. Asgari H, Baxter C, Hosseinkhani K, *et al*., 2017, On microstructure and mechanical properties of additively manufactured AlSi10Mg_200C using recycled powder. *Mater Sci Eng A*, 707: 148–158.

    https://doi.org/10.1016/j.msea.2017.09.041

33. Soltani-Tehrani A, Pegues J, Shamsaei N, 2020, Fatigue behavior of additively manufactured 17-4 PH stainless steel: The effects of part location and powder re-use. *Addit Manuf*, 36: 101398.

34. Contaldi V, Del Re F, Palumbo B, *et al*., 2019, Mechanical characterisation of stainless steel parts produced by direct

metal laser sintering with virgin and reused powder. *Int J Adv Manuf Technol*, 105: 3337–3351.

https://doi.org/10.1007/s00170-019-04416-4

35. Ahmed F, Ali U, Sarker D, *et al.*, 2020, Study of powder recycling and its effect on printed parts during laser powder-bed fusion of 17-4 PH stainless steel. *J Mater Process Technol*, 278: 116522.

    https://doi.org/10.1016/j.jmatprotec.2019.116522

36. Rayan O, Brousseau J, Belzile C, *et al.*, 2023, Maraging steel powder recycling effect on the tensile and fatigue behavior of parts produced through the laser powder bed fusion (L-PBF) process. *Int J Adv Manuf Technol*, 127: 1737–1754.

    https://doi.org/10.1007/s00170-023-11522-x.

37. Systems EG-EO, 2017, EOS MaragingSteel MS1 DATA SHEET. p1–5.

38. Ardila LC, Garciandia F, González-Díaz JB, *et al.*, 2014, Effect of IN718 recycled powder reuse on properties of parts manufactured by means of selective laser melting. *Phys Procedia*, 56: 99–107.

    https://doi.org/10.1016/j.phpro.2014.08.152

39. Seyda V, Kaufmann N, Emmelmann C, 2012, Investigation of aging processes of Ti-6Al-4 V powder material in laser melting. *Phys Procedia*, 39: 425–431.

    https://doi.org/10.1016/j.phpro.2012.10.057

40. Yi F, Zhou Q, Wang C, *et al.*, 2021, Effect of powder reuse on powder characteristics and properties of Inconel 718 parts produced by selective laser melting. *J Mater Res Technol*, 13: 524–533.

    https://doi.org/10.1016/j.jmrt.2021.04.091

41. Mohd Yusuf S, Choo E, Gao N, 2020, Comparison between virgin and recycled 316L SS and AlSi10Mg powders used for laser powder bed fusion additive manufacturing. *Metals*, 10: 1625.

42. Soundarapandiyan G, Johnston C, Khan RH, *et al.*, 2021, A technical review of the challenges of powder recycling in the laser powder bed fusion additive manufacturing process. *J Eng*, 2021: 97–103.

43. Shanbhag G, Vlasea M, 2020, The effect of reuse cycles on Ti-6Al-4V powder properties processed by electron beam powder bed fusion. *Manuf Lett*, 25: 60–63.

    https://doi.org/10.1016/j.mfglet.2020.07.007

Materials Science in Additive Manufacturing

Special Issue Alerts

Invitation for Special Issue Proposals

Organizing and editing for a Special Issue helps Guest Editors gain editorial experience and improve academic profile, in addition to being a part of organizing scientific communication of contemporary topics.

If you are published researcher and have an idea for a Special Issue, please write in via email to our Managing Editor (msam.office@accscience.sg). Please provide your CV, professional profile page and a topic of interest in your email. Our colleague will guide you in the process of writing a Special Issue proposal.

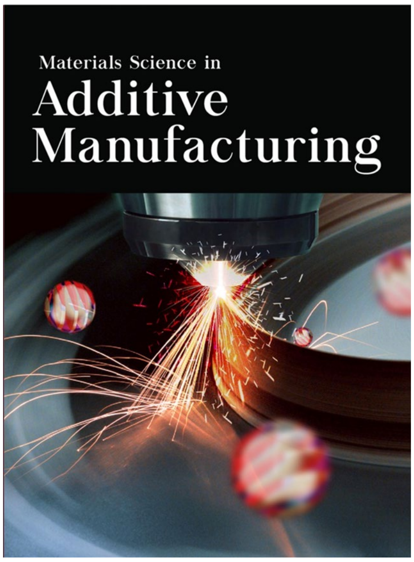

Frequently Asked Questions

1. **Are Special Issue submissions processed in the same way how Regular Issue papers are being pre-screened and reviewed?**
   Yes, all full-length article submissions to a Special Issue will go through the same editorial and peer-review process. The distinct difference here is that the Guest Editors will replace the usual editors and get involved in the making professional decisions on papers after peer review. Note that the specific roles of a Guest Editor could vary across Special Issues.

2. **How many Guest Editors are required to organize a Special Issue?**
   There is no fixed number; however, we suggest no more than 4 Guest Editors per Special Issue. More importantly, all Guest Editors should have excellent publication track records and demonstrated expertise in the topic(s) being proposed.

3. **Is the Special Issue governed by important deadlines?**
   Yes.

Benefits of Being A Guest Editor

- A chance to get involved in the conception and development of a specialty, contemporary topic that is of interest to the readers
- A chance to expand your professional network to the scholars and researchers who are similarly involved in the research of specialty topic
- A chance to hone your editorial skills
- A chance to gain first-hand experience of editing a thematic issue publication, which is a very valuable experience for those who aspire to edit their own journal in future
- A chance to improve your academic profile and help establish your academic influence within your discipline

ACCSCIENCE PUBLISHING

OUR JOURNALS

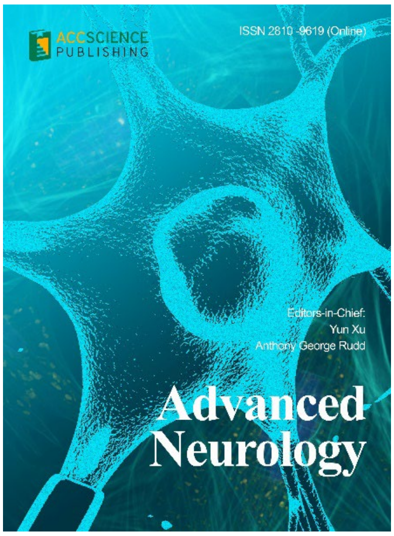

Advanced Neurology is a peer-reviewed and open-access journal that aims to publish and disseminate novel research in the breadth of neurology and neuroscience. The journal aims to advance our understanding in the nervous system and provide a platform to neuroscientists and physicians to showcase their findings in original fundamental and clinical research as well as to present new ideas that highlight the changes in the neurological clinical practice.

Advanced Neurology covers subject areas, including but not limited to the following:

- Neurological disorders
- Neurodegenerative disease
- Cerebrovascular disease
- Epilepsy and movement disorders
- Neuroimmune disease
- Neurological infections
- Muscle disease
- Molecular and cellular neuroscience
- Systems neuroscience
- Cognitive neuroscience
- Computational modeling of nervous system

Gene & Protein in Disease publishes rigorously peer-reviewed and high quality original articles and authoritative reviews that focus on the latest development in multidisciplinary areas in biology and biomedicine, with an emphasis on gene and protein research. The journal has worldwide authorship, and a broad scope in basic and translational biomedical research of genetics, biochemistry, biophysics, oncology, immunology, cell biology, molecular biology, developmental biology, microbiology, neuroscience, stem cell, protein science, structural biology, regenerative medicine and translational medicine.

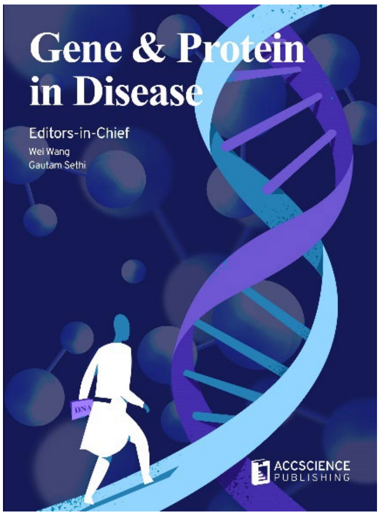

Start a new journal

Write to us via email if you are interested to start a new journal with AccScience Publishing. Please attach your CV, professional profile page and a brief pitch proposal in your email. We shall inform you of our decision whether we are interested to collaborate in starting a new journal.

Contact: info@accscience.com

ACCSCIENCE
PUBLISHING

Access Science Without Barriers

Contact

www.accscience.com
8 Burn Road, #15-03 Trivex, Singapore 369977
Email: editorial@accscience.com
Phone: +65 8182 1586